Quantification en imagerie moléculaire. Des aspects méthodologiques aux applications cliniques

Thomas Carlier

UNIVERSITÉ DE NANTES
FACULTÉ DE MEDECINE

ÉCOLE DOCTORALE BIOLOGIE-SANTÉ

Habilitation à diriger des recherches (HDR)

Quantification en imagerie moléculaire. Des aspects méthodologiques aux applications cliniques

Présentée par

Le 06 juin 2017

Thomas Carlier

Centre Hospitalier Universitaire de Nantes, Service de Médecine Nucléaire, Nantes
CRCINA, UMR 1232 INSERM, ERL CNRS, Université de Nantes, Nantes

Rapporteur	**Mathieu Hatt**, CR INSERM, Brest
Rapporteur	**Sébastien Jan**, Ingénieur chercheur, Orsay
Rapporteur	**Dominique Thers**, Maître assistant, Nantes
Examinateur	**Michel Chérel**, PU-PH, Nantes
Examinateur	**Françoise Kraeber-Bodéré**, PU-PH, Nantes
Examinateur	**Pierre Vera**, PU-PH, Rouen

2017

Comment exprimer simplement l'absence
Par ces petits mots, il me sera sans doute possible de discerner votre présence discrète

Papa. Mon phare dans la tempête
Jean-Baptiste. Mon cousin qui aurait mérité, plus que moi, d'être à ma place

Table des matières

Chapitre 1

Curriculum Vitae

1.1 État civil

Nom :	Thomas Carlier
Date de naissance :	31 juillet 1973 à Paris XIV
Nationalité :	Française
Situation de famille :	Marié, 3 enfants
Adresse professionnelle :	Centre Hospitalier Universitaire de Nantes
	Service de Médecine Nucléaire
	Place Alexis Ricordeau
	44093 Nantes Cedex
	☎ : + 33 240 08 41 36
	✉ : thomas.carlier@chu-nantes.fr

1.2 Expériences professionnelles

1997	Stage volontaire (2 mois) de maîtrise de physique (Université de Rennes I) à l'Université d'Exeter (Angleterre) dans le groupe d'imagerie par résonance magnétique
2005-2009	Doctorant au sein de l'équipe 13 du Centre de Recherche en Cancérologie Nantes-Angers (CRCINA INSERM U1232) sous la supervision du Pr F. Kraeber-Bodéré et du Dr J. Barbet • Sujet : Reconstruction 3D complète par modélisation Monte Carlo de la matrice système. Apport aux approches quantitatives à l'iode 131
Depuis septembre 2001	Physicien médical dans le service de Médecine Nucléaire du Centre Hospitalier Universitaire de Nantes
Depuis septembre 2011	Porteur du projet "Physique médicale et imagerie quantitative" au sein de l'équipe 13 du CRCINA dirigée par le Pr F. Kraeber-Bodéré et le Pr M. Chérel

1.3 Formation

2009	**Docteur** de l'Université de Nantes dans la spécialité Physique médicale • Sujet : Reconstruction 3D complète par modélisation Monte Carlo de la matrice système. Apport aux approches quantitatives à l'iode 131
2001	**Diplôme de Qualification en Physique Radiologique et Médicale** (Institut des Sciences et Techniques Nucléaires, Saclay)
1999	**Diplôme d'Étude Approfondie en Physique Radiologique et Médicale** de l'Université de Toulouse III
1998	Admissibilité à **l'Agrégation de Sciences Physiques option Physique** (Université de Rennes I)
1997	**Maîtrise de Physique** de l'Université de Rennes I Mention assez-bien
1996	**Licence de Physique** de l'Université de Rennes I Mention assez-bien
1993-1994	**Mathématiques supérieures et Mathématiques Spéciales option P**
1992	**Baccalauréat C** Mention Bien
1991	**Baccalauréat D** Mention assez-bien

1.4 Activités d'enseignements

Depuis 2005 — Master 2 Rayonnements Ionisants et Applications (Faculté des Sciences, Université de Nantes)

- Cours magistral : Théorie de la résonance magnétique nucléaire (3h/an) + Classification en imagerie médicale (3h/an)
- Travaux dirigés : Analyse et traitement d'images (8h/an) + Reconstruction tomographique (4h/an)
- Travaux pratiques : Simulation Monte Carlo à partir de GATE (10h/an)

Depuis 2005 — Master 1 de Sciences Biologiques et Médicales (Faculté de Médecine, Université de Nantes)

- Cours magistral : Technologie des systèmes d'imagerie monophotonique (1h/an) + Quantification en SPECT (1h/an) + Transformée de Fourier (1h/an)

Depuis 2011 — DFGSM2 (Faculté de Médecine, Université de Nantes)

- Cours magistral : Imagerie TEP et applications cliniques (1,5h/an) + Imagerie numérique (1h/an)

Depuis 2015 — Diplôme de Qualification en Physique Radiologique et Médicale (INSTN, Saclay)

- Cours magistral : Quantification en SPECT (3h/an) + Quantification en PET (3h/an)

Depuis 2016 — École Centrale de Nantes

- Cours magistral : Bases de la reconstruction tomographique en TEP (1h/an)
- Travaux dirigés : Reconstruction tomographique en TEP avec STIR (3h/an)

Depuis 2016 — DES Médecine Nucléaire (optionnel)

- Cours magistral : Métriques quantitatives pour l'évaluation thérapeutique en oncologie (1h/an)

Depuis 2004 — Institut de Formation des Préparateurs en Pharmacie de Tours

- Cours magistral : Bases mathématiques (3,5h/an)

2004-2012 — Master 2 de Modélisation et Simulation (Faculté des Sciences, Université de Rennes I)

- Cours magistral : Simulation Monte-Carlo en Médecine Nucléaire (3h/an)
- Travaux pratiques : Simulation Monte Carlo à partir de GATE (6h/an)

1.5 Activités d'encadrements

1.5.1 Encadrement de doctorant

1. 2011-2014

   (a) Matthieu Moreau : Reconstruction tomographique 3D complète par modélisation Monte Carlo de la matrice système en TEP pré-clinique à l'iode 124. Co-encadrement (50%) avec le Pr M. Chérel (50%). Thèse soutenue le 05 décembre 2014. Ce travail a donné lieu à plusieurs présentations orales et affichées dans des congrès internationaux ainsi qu'à une publication :

   - M. Moreau, I. Buvat, L. Ammour, N. Chouin, F. Kraeber-Bodéré, M. Chérel, **T. Carlier**, Assessment of a fully 3D Monte Carlo reconstruction method for preclinical PET with iodine-124, *Phys. Med. Biol.*, **60** (2015) 2475-2491

1.5.2 Encadrement de Master 2 (6 mois)

1. 2016

   (a) Rodolphe Leforestier : Évaluation de la valeur pronostique de l'analyse de texture tumorale par imagerie TEP chez les patients atteints de myélome multiple (Université de Rennes I). Encadrement 100%

   (b) Valentin Vielzeuf : Simulation et reconstruction de données de tomographie à émission de positons dans un cadre de très basses statistiques (École Centrale de Nantes). Encadrement 100%

2. 2015

   (a) Jean-Baptiste Tillard : Identification et évaluation de nouveaux paramètres quantitatifs en Immuno-TEP dans le cadre du cancer médullaire de la thyroïde et du cancer du sein (Université de Nantes). Co-encadrement (50%) avec le Dr H. Necib (50%)

3. 2014

   (a) Pierre-François Cléry : Identification et évaluation de nouveaux paramètres quantitatifs en Immuno-TEP dans le cadre du cancer médullaire de la thyroïde et du cancer du sein (Université de Rennes I). Co-encadrement (50%) avec le Dr H. Necib (50%)

4. 2013

(a) Luis Ammour : Reconstruction tomographique en TEP pré-clinique. Développement et calcul des matrices systèmes par des approches analytique et de type Monte Carlo (Université de Rennes I). Co-encadrement (50%) avec le Dr M. Moreau (50%). Ce travail a donné lieu à plusieurs présentations orales et affichées dans des congrès internationaux ainsi qu'à une publication :

- M. Moreau, I. Buvat, L. Ammour, N. Chouin, F. Kraeber-Bodéré, M. Chérel, **T. Carlier**, Assessment of a fully 3D Monte Carlo reconstruction method for preclinical PET with iodine-124, *Phys. Med. Biol.*, **60** (2015) 2475-2491

(b) Brice Hénaff : Suivi longitudinal en TEP au ^{18}F-FDG par imagerie paramétrique (Université de Nantes). Co-encadrement (50%) avec le Dr H. Necib (50%). Ce travail a donné lieu à une publication :

- D. Goulon, H. Necib, B. Hénaff, C. Rousseau, **T. Carlier**, F. Kraeber-Bodéré, Quantitative evaluation of therapeutic response by FDG-PET in metastatic breast cancer, *Front. Med.*, **3** (2016) 19

5. 2012

(a) Hugo Le Mée : Modélisation de la fonction de réponse du taux de comptage en imagerie TEP à l'aide de données cliniques. Applications (Université de Nantes). Encadrement 100%. Ce travail a donné lieu à une publication :

- **T. Carlier**, L. Ferrer, H. Necib, C. Bodet-Milin, C. Rousseau, F. Kraeber-Bodéré, Clinical NECR in 18F-FDG PET scans: optimization of injected activity and variable acquisition time. Relationship with SNR, *Phys. Med. Biol.*, **59** (2014) 6417-6430

6. 2011

(a) Hugues Loizeau : Optimisation des paramètres d'acquisition en imagerie TEP par modélisation de la NECR clinique (Université de Nantes). Encadrement 100%. Ce travail a donné lieu a une publication :

- **T. Carlier**, L. Ferrer, H. Necib, C. Bodet-Milin, C. Rousseau, F. Kraeber-Bodéré, Clinical NECR in 18F-FDG PET scans: optimization of injected activity and variable acquisition time. Relationship with SNR, *Phys. Med. Biol.*, **59** (2014) 6417-6430

7. 2007

(a) Maxime Moisan : Modélisation d'un système de détection SPECT par simulation Monte-Carlo (Université de Rennes I). Encadrement 100%. Ce travail a donné lieu à une présentation affichée dans un congrès international

8. 2005

   (a) Aurélien Vasseur : Simulation sous GATE d'un nouveau concept de Tomographe à Émissions de Positrons basé sur un milieu de détection au xénon liquide (Université de Toulouse III). Encadrement 100%. Ce travail a donné lieu à un acte complet de colloque :

   - C. Grignon, A. Breskin, **T. Carlier**, O. Couturier, J.P. Cussonneau, L. Ferrer, L. Luquin, V. Métivier, V. Peskov, F. Pheron, N. Servagent, D. Thers, A. Vasseur, Simulation of a high performance γ-camera concept for PET based on liquid xenon and gaseous photomultiplier, *Proceedings of the 15th IEEE International Conference on Dielectric Liquids* (2005) 357-360 (Coimbra, Portugal)

1.5.3 Encadrement de Master 1 (2 mois)

1. 2016

   (a) Marta Freire Lopez-Fernando : Calcul dosimétrique pour des traitements par radioembolisation de carcinome hépatocellulaire et cholangiocarcinome : comparaison entre les données d'entrée ^{99m}Tc-MAA TEMP et ^{90}Y micro-sphères TEP (Université de Nantes). Encadrement 100%

   (b) Coralie Haumont : Développement et évaluation d'approches multi-segmentation pour la détermination de volume en imagerie fonctionnelle (Institut National des Sciences Appliquées de Rennes). Encadrement 100%

2. 2015

   (a) Solène Couespel : Évaluation de la robustesse des métriques de texture en TEP à partir de données cliniques (Université de Rennes I). Encadrement 100%. Ce travail a donné lieu à une publication :

   - C. Bailly, C. Bodet-Milin, S. Couespel, H. Necib, F. Kraeber-Bodéré, C. Ansquer, **T. Carlier**, Revisiting the robustness of PET-based textural features in the context of multi-centric trials, *PLoS ONE*, **11** (2016) e0159984

3. 2014

   (a) Laëtitia Lechippey : Analyse quantitative de la TEP/TDM au 68Ga-DOTANOC dans le bilan des tumeurs endocrines Gastro-entéro-pancréatiques. Étude préliminaire (Université de Rennes I). Encadrement 100%. Ce travail a donné lieu à une présentation orale dans un congrès international et une présentation affichée dans un congrès national

4. 2012

   (a) Maxime Mauguet : Évaluation d'une méthode bootstrap non-paramétrique sur des données TEP temps-de-vol (stage volontaire ingénieur INSA Rennes). Encadrement 100%. Ce travail a donné lieu à une présentation affichée dans un congrès international

   (b) Luis Ammour : Modélisation Monte Carlo du système de détection TEP Biograph mCT 40 de Siemens à l'aide de l'outil de simulation GATE (Université de Nantes). Encadrement 100%

5. 2011

   (a) Jonathan Le Gouestre : Évaluation expérimentale de l'effet de volume partiel pour le système TEP Siemens mCT Biograph (Université de Nantes). Encadrement 100%

6. 2010

   (a) Caroline Noblet : Détermination de l'impact du bruit et de la résolution spatiale en SPECT dans les données d'entrée pour des simulations "hyper-réalistes" (Université de Nantes). Encadrement 100%. Ce travail a donné lieu à une publication :

   - S. Stute, **T. Carlier**, K. Cristina, C. Noblet, A. Martineau, B. Hutton, A. Barnden, I. Buvat, Monte Carlo simulations of clinical PET and SPECT scans: impact of the input data on the simulated images, *Phys. Med. Biol.*, **56** (2011) 6441-6457

7. 2008

   (a) Stéphanie Lapierre : Caractérisation des performances d'un système de Tomographie par Émission de Positons petit animal : Calcul de la fraction de diffusés suivant la nouvelle norme NEMA NU 4-2008 (Université de Nantes). Encadrement 100%

1.6 Activités éditoriales, Sociétés scientifiques, Financements, Distinction, Partenariats

1.6.1 Activités éditoriales

1. Editeur associé de *Frontiers in Nuclear Medicine*

2. Relecteur pour

   - *Physics in Medicine and Biology*
   - *Medical Physics*

- *Nuclear Medicine Communications*
- *European Journal of Nuclear Medicine and Molecular Imaging Research*
- *Frontiers in Cancer Imaging and Diagnosis*
- *Annals of Nuclear Medicine*
- *Médecine Nucléaire*
- Conférence "IEEE Medical Imaging Conference"

1.6.2 Sociétés scientifiques

1. Membre of Society of Nuclear Medicine (SNM)
2. Membre de la Société Française de Médecine Nucléaire (SFMN)
3. Membre de la Société Française de Physique Médicale (SFPM)

1.6.3 Financements obtenus

1. 2017 : Financement Université de Nantes dans le cadre de l'AAP Interdisciplinaires - Phase "exploratoire"
   - Titre : Imagerie TEP quantitative par reconstruction tomographique dans des conditions de basses statistiques après injection intra-artérielle de microsphères chargées à l'yttrium 90
   - Partenaire : Laboratoire des Sciences du Numérique de Nantes (Pr S. Moussaoui, Dr J. Idier)
2. 2014 : Financement INCa dans le cadre du plan Cancer 2014-2017
   - Titre : MILADY : MIcrosphere Liver Absorbed Dose assessment from Y90-PET
   - Durée : 3 ans
   - Partenaires : Centre de Recherche Bichat-Beaujon (Dr A. Dieudonné) et CEA/I2BM/Service Hospitalier Frédéric Joliot (Dr I. Buvat)
   - Personnel recruté : Dr J. Strydhorst (1,5 an en post-doctorat partagé entre notre laboratoire et le SHFJ)
3. 2012 : Financement INCa dans le cadre du plan Cancer 2009-2013
   - Titre : 3 gamma imaging with a liquid xenon Compton telescope
   - Durée : 2 ans
   - Partenaire : Laboratoire SUBATECH (Dr J.P. Cussonneau)
   - Personnel recruté : Dr N. Beaupère (1 an en post-doctorat au sein de notre laboratoire)

1.6.4 Distinction

1. Médaille Rotblat 2015 de la revue "Physics in Medicine and Biology" pour l'article le plus cité dans la période 2010-2014 (publication 19 de la partie 1.7.1)

1.6.5 Partenariats académiques et industriels

1.6.5.1 Partenariats académiques

- **Laboratoire SUBATECH** (École des Mines de Nantes - IN2P3/CNRS - Université de Nantes), Nantes, France
  - Sujet : Développement d'un détecteur TEP au xénon liquide (XEMIS2)
  - Contacts principaux : Dr Dominique Thers & Dr Jean-Pierre Cussonneau
- **Commissariat à l'Énergie Atomique et aux énergies alternatives** (Service Hospitalier Frédéric Joliot - Unité Imagerie Moléculaire In Vivo - UMR 1023 Inserm/CEA/Université Paris Sud, ERL 9218 CNRS), Orsay, France
  - Sujet : Imagerie quantitative basse statistique
  - Contact principal : Dr Irène Buvat
- **Centre de Recherche Bichat-Beaujon**, Paris, France
  - Sujet : Dosimétrie des traitements par radioembolisation
  - Contact principal : Dr Arnaud Dieudonné
- **Laboratoire de Traitement de l'Information Médicale** (INSERM U1101), Brest, France
  - Sujet : Reconstruction tomographique, Analyse de texture en TEP
  - Contact principal : Dr Mathieu Hatt & Dr Dimitris Visvikis

1.6.5.2 Partenariats industriels

Les partenariats industriels cités ont fait l'objet d'une convention de partenariat dûment signée par les directions respectives.

- **Société SIEMENS**, Knoxville, USA
  - Sujets : Imagerie phénotypique au ^{68}Ga, Imagerie TEP au ^{90}Y, Quantification dans le suivi thérapeutique en TEP
  - Contact principal : Dr Maurizio Conti

  - Durée : 2010 - 2016

- **Société DOSISOFT**, Cachan, France
  - Sujets : Dosimétrie des traitements par radioembolisation, Développement de paramètres quantitatifs pour le suivi thérapeutique en TEP
  - Contact principal : Dr Sébastien Vauclin
  - Durée : 2014 - 2017

1.7 Publications et communications

Nous rapportons en préambule le dernier "5-year impact factor" (dénoté par la suite IF) disponible sur le dernier "Journal Citation Reports®" (http://thomsonreuters.com/en/products-services/scholarly-scientific-research/research-management-and-evaluation/journal-citation-reports.html) des deux meilleurs journaux spécialisés pour les deux catégories dans lesquelles mon travail s'inscrit :

1. Catégorie principale (méthodologie) :
   (a) Physics in Medicine and Biology : **IF = 3,051**
   (b) Medical Physics : **IF = 2,889**
2. Catégorie secondaire (applications cliniques) :
   (a) Journal of Nuclear Medicine : **IF = 5,795**
   (b) European Journal of Nuclear Medicine and Molecular Imaging : **IF = 5,145**

Certains journaux, souvent compagnons de journaux de référence, mais récemment lancés, ne disposent pas encore d'IF. Ils seront mentionnés comme : (**non référencé**).

1.7.1 Articles originaux dans des journaux internationaux avec comité de lecture

1. M. Conti, L. Eriksson, H. Rothfuss, T. Sjoeholm, D. Townsend, G. Rosenqvist, **T. Carlier**, Characterization of 176Lu background in LSO-based PET scanners, *Phys. Med. Biol.*, accepted (**IF = 3,051**)

2. J. Strydhorst, **T. Carlier**, A. Dieudonné, M. Conti, I. Buvat, A GATE evaluation of the sources of error in quantitative ^{90}Y PET, *Med. Phys.*, **43** (2016) 5320-5329 (**IF = 2,889**)

3. C. Bailly, C. Bodet-Milin, S. Couespel, H. Necib, F. Kraeber-Bodéré, C. Ansquer, **T. Carlier**, Revisiting the robustness of PET-based textural features in the context of multi-centric trials, *PLoS ONE*, **11** (2016) e0159984 (**IF = 3,535**)

4. C. Bodet-Milin, A. Faivre-Chauvet, **T. Carlier**, A. Rauscher, M. Bourgeois, E. Cerato, V. Rohmer, O. Couturier, D. Drui, D.M. Goldenberg, R.M. Sharkey, J. Barbet, F. Kraeber-Bodéré, Immuno-PET using anti-carcinoembryonic antigen bispecific antibody and ^{68}Ga-labeled peptide in metastatic medullary thyroid carcinoma: clinical optimization of the pretargeting parameters in a First-in Human trial, *J. Nucl. Med.*, **57** (2016) 1505-1511 (**IF = 5,795**)

5. D. Goulon, H. Necib, B. Hénaff, C. Rousseau, **T. Carlier**, F. Kraeber-Bodéré, Quantitative evaluation of therapeutic response by FDG-PET in metastatic breast cancer, *Front. Med.*, **3** (2016) 19 (**non référencé**)

6. M.O. Habert, S. Marie, H. Bertin, M. Reynal, J.B. Martini, M. Diallo, A. Kas, **the CATI Nuclear Medicine network**, R. Trébossen, Optimization of brain PET imaging for a multicentre trial: the French CATI experience, *EJNMMI Physics*, **3** (2016) 6 (**non référencé**)

7. **T. Carlier**, K. Willowson, E. Fourkal, D.L. Bailey, M. Doss, M. Conti, ^{90}Y-PET imaging: exploring limitations and accuracy under conditions of low counts and high random fraction, *Med. Phys.*, **42** (2015) 4295-4309 (**IF = 2,889**)

8. M. Moreau, I. Buvat, L. Ammour, N. Chouin, F Kraeber-Bodéré, M. Chérel, **T. Carlier**, Assessment of a fully 3D Monte Carlo reconstruction method for preclinical PET with iodine-124, *Phys. Med. Biol.*, **60** (2015) 2475-2491 (**IF = 3,051**)

9. K. Willowson, M. Tapner, **The QUEST Investigator Team**, D.L. Bailey, A multicentre comparison of quantitative 90Y PET/CT for dosimetric purposes after radioembolization with resin microspheres, *Eur. J. Nucl. Med. Mol. Imaging*, **42** (2015) 1202-1222 (**IF = 5,145**)

10. D. Rusu, **T. Carlier**, M. Colombié, D. Goulon, V. Fleury, N. Rousseau, D. Berton-Rigaud, I. Jaffre, F. Kraeber-Bodéré, L. Campion, C. Rousseau, Clinical and survival impact of FDG PET in patients with suspicion or recurrent ovarian cancer: a 6-year follow-up, *Front. Med.*, **2** (2015) 46 (**non référencé**)

11. C. Mathieu, L. Ferrer, **T. Carlier**, M. Colombié, D. Rusu, F. Kraeber-Bodéré, L. Campion, C. Rousseau, Assessment of lymph nodes and prostate status using early dynamic curves with 18F-choline PET/CT in prostate cancer, *Front. Med.*, **2** (2015) 67 (**non référencé**)

12. L. Gallego, S. Bassetto, N. Beaupere, P. Briend, **T. Carlier**, M. Chérel, J.P. Cussonneau, J. Donnard, M. Gorski, R. Hamanishi, F. Kraeber-Bodéré, P. Le Ray, O. Lemaire, J. Masbou, S. Mihara, A.F. Mohamad Hadi, E. Morteau, L. Scotto Lavina, J.S Stutzmann, T. Tauchi, D. Thers, XEMIS: A liquid xenon detector for medical imaging, *Nucl. Instr. and Meth. A*, **787** (2015) 89-93 (**IF = 1,102**)

13. **T. Carlier**, L. Ferrer, H. Necib, C. Bodet-Milin, C. Rousseau, F. Kraeber-Bodéré, Clinical NECR in 18F-FDG PET scans: optimization of injected activity and variable acquisition time. Relationship with SNR, *Phys. Med. Biol.*, **59** (2014) 6417-6430 (**IF = 3,051**)

14. **T. Carlier**, T. Eugène, C. Bodet-Milin, E. Garin, C. Ansquer, C. Rousseau, L. Ferrer, J. Barbet, F. Schoenahl, F. Kraeber-Bodéré, Assessment of acquisition protocols for routine imaging of Y-90 using PET/CT, *EJNMMI Research*, **3** (2013) 11 (**IF = 2,131**)

15. F. Kraeber-Bodéré, **T. Carlier**, V. Meresse Naegelen, E. Shochat, J. Lumbroso, C. Trampal, J. Nagarajah, S. Chua, F. Hugonnet, M. Stokkel, F. Gleeson, J. Tessier, Differences in the biological activity of two novel MEK inhibitors revealed by ^{18}F-fluorodeoxyglucose positron emission tomography: Analysis of imaging data from two phase I trials, *J. Nucl. Med*, **53** (2012) 1836-1846 (**IF = 5,795**)

16. T. Eugène, N. Corradini, **T. Carlier**, B. Dupas, C. Leux, C. Bodet-Milin, ^{18}F-FDG-PET/CT in initial staging and assessment of early response to chemotherapy of pediatric rhabdomyosarcomas, *Nucl. Med. Commun.*, **33** (2012) 1089-1095 (**IF = 1,454**)

17. N. Anizan, **T. Carlier**, C. Hindorf, J. Barbet, M. Bardiès, Acquisition setting optimization and quantitative imaging for 124I studies with the Inveon microPET-CT system, *EJNMMI Res.*, **2** (2012) 7 (**IF = 2,131**)

18. S. Stute, **T. Carlier**, K. Cristina, C. Noblet, A. Martineau, B. Hutton, A. Barnden, I. Buvat, Monte Carlo simulations of clinical PET and SPECT scans: impact of the input data on the simulated images, *Phys. Med. Biol.*, **56** (2011) 6441-6457 (**IF = 3,051**)

19. S. Jan, D. Benoit, E. Becheva, **T. Carlier**, F. Cassol, P. Descourt, T. Frisson, L. Grevillot L. Guigues, L. Maigne, C. Morel, Y. Perrot, N. Rehfeld, D. Sarrut, D. R. Schaart, S. Stute, U. Pietrzyk, D. Visvikis, N. Zahra, I. Buvat, GATE V6: a major enhancement of the GATE simulation platform enabling modelling of CT and radiotherapy, *Phys. Med. Biol.*, **56** (2011) 881-901 (**IF = 3,051**)

20. P. Descourt, **T. Carlier**, Y. Du, X. Song, I. Buvat, E.C. Frey, M. Bardiès, B.M.W. Tsui, D. Visvikis, Implementation of Angular Response Function modeling in SPECT simulations with GATE, *Phys. Med. Biol.*, **55** (2010) N253-N266 (**IF = 3,051**)

21. **T. Carlier**, A. Oudoux, E. Mirallié, A. Seret, I. Daumy, C. Leux, C. Bodet-Milin, F. Kraeber-Bodéré, C. Ansquer, ^{99m}Tc-MIBI pinhole SPECT in primary hyperparathyroidism: comparison with conventional SPECT, planar scintigraphy and ultrasonography, *Eur. J. Nucl. Med. Mol. Imaging*, **35** (2008) 637-643 (**IF = 5,145**)

22. F. Haddad, L. Ferrer, A. Guertin, **T. Carlier**, N. Michel, J. Barbet, J.F. Chatal, ARRONAX, a high energy and high intensity cyclotron for nuclear medicine, *Eur. J. Nucl. Med. Mol. Imaging*, **35** (2008) 1377-1387 (**IF = 5,145**)

23. C. Ansquer, E. Mirallié, **T. Carlier**, H. Abbey-Huguenin, F. Aubron, F. Kraeber-Bodéré, Preoperative localization of parathyroid lesions: interest of ^{99m}TC-MIBI tomography and factors influencing detectability, *Nuklearmedizin*, **47** (2008) 158-162 (**IF = 1,160**)

24. C. Grignon, J. Barbet, M. Bardiès, **T. Carlier**, J.F. Chatal, O. Couturier, J.P. Cussonneau, A. Faivre, L. Ferrer, S. Girault, T. Haruyama, P. Leray, L. Luquin, S. Lupone, V. Métivier, E. Morteau, N. Servagent, D. Thers, Nuclear medical imaging using $\beta^+\gamma$ coincidences from ^{44}Sc radio-nuclide with liquid xenon as detection medium, *Nucl. Instr. and Meth. A*, **571** (2007) 142-145 (**IF = 1,102**)

25. C. Curtet, **T. Carlier**, E. Mirallié, C. Bodet-Milin, C. Rousseau, J. Barbet, F. Kraeber-Bodéré, Prospective comparison of two gamma probes for intraoperative detection of ^{18}F-FDG: In vitro assessment and clinical evaluation in differentiated thyroid cancer patients with iodo negative recurrence, *Eur. J. Nucl. Med. Mol. Imaging*, **34** (2007) 1556-1562 (**IF = 5,145**)

26. F. Valette, S. Querellou, A. Oudoux, **T. Carlier**, B. Dupas, J.F. Chatal, O. Couturier, Comparison of positron emission tomography and lymphangiography in the diagnosis of infradiaphragmatic Hodgkin's disease, *Acta Radiol.*, **48** (2007) 59-63 (**IF = 1,758**)

27. **T. Carlier**, P.Y. Salaun, M.B. Cavarec, F. Valette, A. Turzo, M. Bardiès, Y. Bizais, O. Couturier, Optimized radioiodine therapy of Graves' disease : two MIRD-based models for the computation of patient-specific therapeutic iodine-131 activity, *Nucl. Med. Commun.*, **27** (2006) 559-566 (**IF = 1,454**)

28. P.Y. Salaun, S. Querellou, J.M. Nguyen, C. Bodet-Milin, **T. Carlier**, A. Turzo, Y. Bizais, O. Couturier, Comparison of gastric emptying scintigraphy based on the geometric mean of the gastric proportion of the abdominal radioactivity or on the geometric mean of the intragastric radioactivity, *Nuc. Med. Commun.*, **27** (2006) 431-437 (**IF = 1,454**)

29. C. Bodet-Milin, S. Querellou, A. Oudoux, A. Haloun, D. Horeau-Langlard, **T. Carlier**, Y. Bizais, O. Couturier, Delayed gastric emptying scintigraphy in Cystic Fibrosis patients

before and after lung transplantation, *J. Heart Lung Transplant.*, **25** (2006) 1077-1083 (**IF = 5,627**)

30. S. Querellou, F. Valette, C. Bodet-Milin, A. Oudoux, **T. Carlier**, J.L. Harousseau, J.F. Chatal, O. Couturier, FDG-PET/CT predicts outcome in patients with aggressive non-Hodgkin's lymphoma and Hodgkin's disease, *Ann. Hematol.*, **85** (2006) 759-767 (**IF = 2,751**)

31. O. Couturier, C. Bodet-Milin, S. Querellou, **T. Carlier**, A. Turzo, Y. Bizais, Gastric scintigraphy with a liquid-solid radiolabeled meal : performances of solid and liquid parameters, *Nucl. Med. Commun.* **25** (2004) 1143-1150 (**IF = 1,454**)

1.7.2 Articles de revues dans des journaux internationaux avec comité de lecture

1. C. Bailly, R. Leforestier, B. Jamet, **T. Carlier**, M. Bourgeois, F. Guérard, C. Touzeau, P. Moreau, M. Chérel, F. Kraeber-Bodéré, C. Bodet-Milin, PET imaging for initial staging and therapy assessment in Multiple Myeloma patients, *Int. J. Mol. Sci.*, accepted

2. C. Bailly, P.F. Cléry, A. Faivre-Chauvet, M. Bourgeois, F. Guérard, F. Haddad, J. Barbet, M. Chérel, F. Kraeber-Bodéré, **T. Carlier**, C. Bodet-Milin, Immuno-PET for clinical theranostic approaches, *Int. J. Mol. Sci.*, **18** (2017) 57 (**IF = 3,213**)

3. **T. Carlier**, C. Bailly, State-of-the-art and recent advances in quantification for therapeutic follow-up in oncology using PET, *Front. Med.*, **2** (2015) 18 (**non référencé**)

4. F. Kraeber-Bodéré, C. Rousseau, C. Bodet-Milin, C. Mathieu, F. Guérard, E. Frampas, **T. Carlier**, N. Chouin, F. Haddad, J.F. Chatal, A. Faivre-Chauvet, M. Chérel, J. Barbet, Tumor immunotargeting using innovative radionuclides, *Int. J. Mol. Sci.*, **16** (2015) 3932-3954 (**IF = 3,213**)

5. F. Kraeber-Bodéré, C. Bodet-Milin, C. Rousseau, T. Eugène, A. Pallardy, E. Frampas, **T. Carlier**, L. Ferrer, J. Gaschet, F. Davodeau, A. Faivre-Chauvet, M. Chérel, J. Barbet, Radioimmunoconjugates for the treatment of cancer, *Semin. Oncol.*, **41** (2014) 613-622 (**IF = 3,847**)

6. O. Couturier, S. Supiot, M. Degraef-Mougin, A. Faivre-Chauvet, **T. Carlier**, J.F. Chatal, F. Davaudeau, M. Cherel, Cancer radioimmunotherapy with alpha-emitting nuclides, *Eur. J. Nucl. Med. Mol. Imaging*, **32** (2005) 601-614 (**IF = 5,145**)

1.7.3 Articles originaux dans des journaux nationaux avec comité de lecture

1. C. Bailly, M. Hatt, S. Le Gouill, F. Kraeber-Bodéré, D. Visvikis, C. Bodet-Milin, **T. Carlier**, Étude de la robustesse des paramètres d'hétérogénéité en TEP-FDG des lymphomes du manteau inclus dans l'étude LyMa, *Médecine Nucléaire*, **40** (2016) 297-306 (**IF = 0,093**)

2. C. Mathieu, L. Ferrer, **T. Carlier**, M. Colombié, D. Rusu, F. Kraeber-Bodéré, L. Campion, C. Rousseau, Évaluation du statut ganglionnaire et prostatique à la phase dynamique précoce de la TEP à la ^{18}F-choline dans le cancer de prostate, *Médecine Nucléaire*, **39** (2015) 138-147 (**IF = 0,093**)

3. D. Goulon, C. Rousseau, H. Necib, **T. Carlier**, B. Hennaff, D. Rusu, M. Lacombe, M. Colombié, F. Kraeber-Bodéré, Comparaison de différents indices métaboliques et de la méthode SULTAN dans l'évaluation de la réponse thérapeutique par TEP au ^{18}FDG dans le cancer du sein métastatique, *Médecine Nucléaire*, **38** (2014) 408-418 (**IF = 0,093**)

4. **T. Carlier**, H. Loizeau, E. Gaudin, C. Ansquer, C. Bodet-Milin, C. Rousseau, T. Eugène, L. Ferrer, F. Kraeber-Bodéré, Modélisation du taux de comptage en TEP à partir de données cliniques : une voie robuste pour l'optimisation des paramètres d'acquisition ?, *Médecine Nucléaire*, **36** (2012) 209-214 (**IF = 0,093**)

5. T. Eugène, C. Ansquer, A. Oudoux, N. Corradini, **T. Carlier**, C. Thomas, B. Dupas, F. Kraeber-Bodéré, C. Bodet-Milin, Apport de la TEP/TDM au 18FDG dans la stadification initiale et l'évaluation précoce de la réponse thérapeutique des rhadomyosarcomes pédiatriques, *Médecine Nucléaire*, **34** (2010) 655-663 (**IF = 0,093**)

6. A. Oudoux, **T. Carlier**, E. Mirallié, C. Bodet-Milin, A. Seret, F. Aubron, I. Daumy, C. Leux, F. Kraeber-Bodéré, C. Ansquer, Tomographie sténopéïque au ^{99m}Tc-MIBI dans l'hyperparathyroïdie primaire, *Médecine Nucléaire*, **31** (2007) 553-561 (**IF = 0,093**)

7. O. Couturier, F. Leost, M. Campone, **T. Carlier**, J.F. Chatal, R. Hustinx, Is 3'-deoxy-3'-[18F] fluorothymidine ([18F]-FLT) the next tracer for routine clinical PET after R [18F]-FDG, *Bull. Cancer*, **92** (2005) 1021-1025 (**IF = 0,580**)

8. C. Bodet-Milin, S. Querellou, A. Oudoux, A. Haloun, D. Horeau-Langlard, **T. Carlier**, Y. Bizais, O. Couturier, Delayed gastric emptying before and after lung transplantation in patients suffering from cystic fibrosis, *Médecine Nucléaire*, **29** (2005) 827-835 (**IF = 0,093**)

9. **T. Carlier**, A. Lisbona, F. Kraeber-Bodéré, C. Ansquer, O. Couturier, Practical recommandations for outpatients after differentiated thyroid carcinoma treatment with iodine-131, *Radioprotection*, **39** (2004) 481-492 (**IF = 0,510**)

1.7.4 Actes de colloques et communications orales et affichées dans des conférences internationales

La liste complète des actes, communications orales ou affichées dans des colloques internationaux et des conférences invitées dans des colloques nationaux est donnée dans l'annexe A.

1.7.5 Chapitre de livre

1. F. Kraeber-Bodéré, C. Bodet-Milin, C. Rousseau, **T. Carlier**, L. Ferrer, N. Chouin, F. Haddad, F. Davodeau, J.F. Chatal, A. Faivre-Chauvet, J.F. Gestin, M. Chérel, J. Barbet, New advances in radioimmunotherapy for the treatment of cancers in *Cancer immunology: bench to bedside immunotherapy of cancers*. Ed : N. Rezaei (2015)

1.7.6 Conférences invitées nationales

1. Optimisation en TEP FDG. (Congrès de la SFPM, Nancy, 2016)
2. Apport de la NECR clinique en 18F-FDG. (Réunion APRAMEN, Paris, 2015)
3. Quantification dans l'évaluation thérapeutique. Outils disponibles et applications cliniques. (Atelier FORAMEN de la SFMN, Paris, 2013)
4. SPECT & PET : quelle algorithmie implémentée chez Siemens ? (EPU "Nouvelles technologies en Médecine Nucléaire", Marseille, 2012)
5. Modélisation du taux de comptage en TEP à partir de données cliniques : une voie robuste pour l'optimisation des paramètres d'acquisition ? (Congrès de la SFMN, Montpellier, 2012)
6. Optimisation des paramètres d'acquisition à l'aide des données cliniques en TEP (Symposium des utilisateurs de Biograph Siemens, Paris, 2012)
7. Avancées et perspectives en SPECT et PET (Congrès de la SMNO, Belle-Ile-en-mer, 2010)

1.7.7 Publications représentatives

La reproduction des 7 publications les plus significatives est donnée en annexe B.

1.7.8 Organisation de conférence nationale

1. Workshop "TEP : Aspects physiques et quantitatifs" du 18 au 20 juin 2014 à Paris. Co-organisateur avec le Dr Antoine Martineau (Hôpital Saint Louis, Paris) avec le soutien de la SFMN et de la SFPM

Chapitre 2

Activités de recherches antérieures

2.1 Introduction

Mon activité de recherche s'est d'abord inscrite pleinement dans le cadre de l'activité d'un physicien médical exerçant en Médecine Nucléaire. A ce titre, plusieurs travaux de développements ont vu le jour au fur et à mesure de mon implication dans l'activité clinique du service de Médecine Nucléaire du Centre Hospitalier Universitaire (CHU) de Nantes. Ces travaux ont donné lieu à des publications suivies d'applications cliniques concrètes détaillées brièvement dans les parties suivantes dans le but essentiel d'améliorer les performances diagnostiques et donc la prise en charge du patient dans son parcours de soin. Ces premiers travaux m'ont poussé naturellement à entreprendre un travail de recherche plus fondamentale au travers d'une thèse de doctorat soutenue en décembre 2009.

Parallèlement à ce travail essentiellement axé sur des problématiques propres à la Médecine Nucléaire et compte tenu de ma formation initiale en physique fondamentale, j'ai saisi dès 2005 l'opportunité d'accompagner un projet d'instrumentation TEP très innovant porté par le laboratoire SUBATECH (École des Mines de Nantes - CNRS/IN2P3 - Université de Nantes). J'ai donc essayé de mettre à profit des compétences acquises en simulation/reconstruction pour abonder ce travail et construire une collaboration entre le CHU de Nantes, l'équipe 13 du CRCINA (INSERM U1232) et SUBATECH.

Enfin, sensible à l'importance croissante des aspects de médecine personnalisée notamment au travers de la caractérisation tumorale, du pronostic, de l'évaluation thérapeutique et de la maladie résiduelle, je suis en train de développer un axe de recherche permettant l'adaptation de

méthodologie originale quantitative dans un contexte clinique.

Finalement, le projet de physique médicale en Médecine Nucléaire porté depuis quelques années s'articule autour de trois piliers fondamentaux qui sont les soubassements essentiels de la Médecine Nucléaire :

1. Méthodologie

2. Applications cliniques d'outils méthodologiques

3. Instrumentation

Ces trois piliers vont constituer l'architecture de présentation de mes travaux de recherche passés et actuels (Figure 2.1).

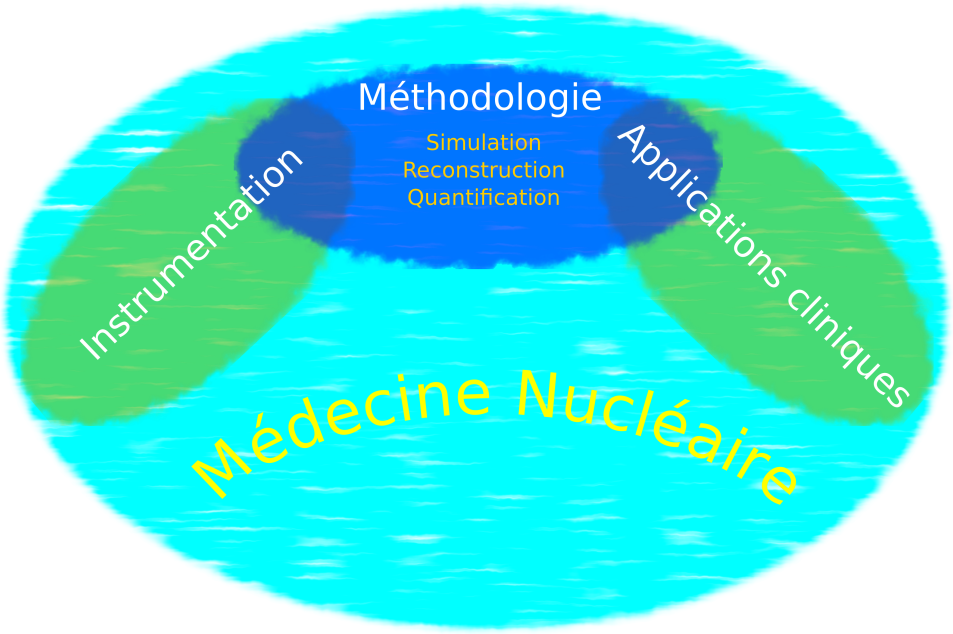

FIGURE 2.1 – Thématiques principales liées au développement de mon axe de recherche en Médecine Nucléaire

2.2 Méthodologie

2.2.1 Simulation Monte Carlo et Reconstruction tomographique

2.2.1.1 Développements effectués durant la thèse

Mon sujet de thèse s'est attaché à essayer d'apporter des éléments de réponse au problème de l'obtention d'une information quantitative la moins biaisée possible dans le cadre de l'imagerie monophotonique (SPECT) utilisant l'iode 131 comme radioélément. Je suis parti d'un travail pilote mené par D. Lazaro [1] qui a évalué la pertinence de modéliser l'ensemble des phénomènes physiques (qu'ils soient relatifs au patient ou au système de détection) dans la matrice système utilisée dans des algorithmes de reconstruction itérative. La construction du modèle repose sur une approche de simulation Monte Carlo des interactions de photons dans la matière. Ces simulations ont été menées grâce à l'environnement de simulation GATE [2, 3] pour lequel notre équipe est partenaire de la collaboration internationale depuis son lancement en 2004. Une des difficultés majeures qui s'est naturellement offerte a été la gestion du temps de simulation qui devient particulièrement prohibitif pour des particules créant de nombreuses interactions dans la matière (et spécialement dans le collimateur) comme c'est le cas pour l'iode 131. Pour répondre à cette problématique, nous nous sommes tournés vers deux solutions complémentaires. La première a consisté à utiliser un environnement parallèle au travers du projet EGEE (Enabling Grid for E-sciencE) mettant à disposition des ressources de calcul et de stockage importantes indépendamment de leur localisation géographique. D'un point de vue global, la grille de calcul EGEE représentait environ 240 sites répartis sur 45 pays, mettant à disposition plus de 50000 CPUs au moment du développement de mes travaux. La deuxième approche a consisté à implémenter une méthode originale développée par l'équipe de Baltimore [4] dans le "framework" de GATE. Elle repose sur le calcul préalable d'une fonction de réponse angulaire (ARF) qui est dépendante de l'énergie incidente du photon, de sa position d'interaction relative à sa position d'émission, de la fenêtre spectrométrique de détection et de la résolution en énergie du détecteur (figure 2.3). Elle s'exprime par la relation suivante :

$$F^{arf}(\theta,\phi) = \frac{N_1(E,W,R,\theta,\phi)}{N_2(\theta,\phi)} \tag{2.1}$$

où E est l'énergie incidente du photon, W la fenêtre spectrométrique d'enregistrement des évènements, R la résolution en énergie du détecteur, N_1 la contribution des photons détectés dans l'angle solide infinitésimal $\Delta\Omega(\theta,\phi)$ et N_2 le nombre total de photons dont le vecteur incident est compris dans le même angle solide $\Delta\Omega(\theta,\phi)$. Si N_0 exprime le nombre total de photons dans

la sphère de 4π stéradians, alors N_2 s'exprime par :

$$N_2(\theta, \phi) = \frac{N_0 \Delta\Omega(\theta, \phi)}{4\pi} \tag{2.2}$$

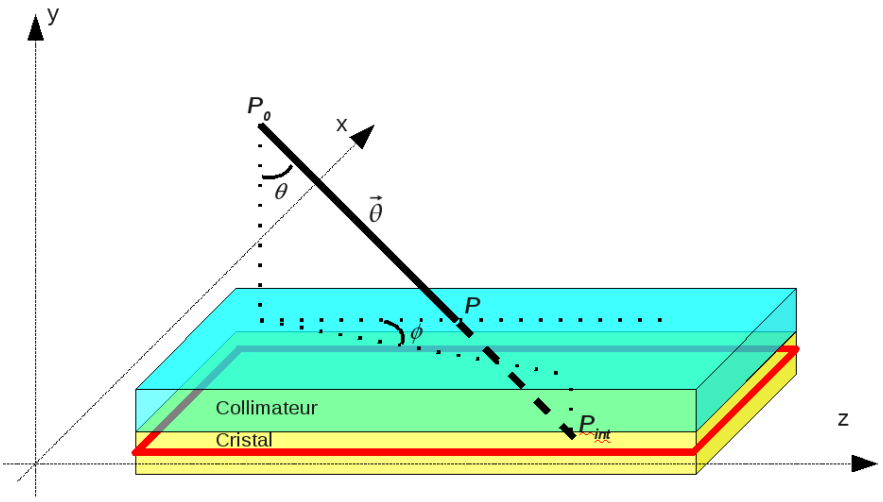

FIGURE 2.2 – Illustration du système de coordonnées utilisé dans la fonction de réponse angulaire. Un photon est repéré par ces coordonnées de départ $\vec{P_0}$ et son vecteur incident $\vec{\theta}$. Le point d'intersection avec le plan d'entrée du collimateur est donné par $\vec{P}$ et le point d'intersection entre la direction incidente θ et le plan situé au milieu du cristal (en rouge) est $\vec{P}_{int}$

Ce développement, sa validation et son évaluation ont été menés en étroite collaboration avec P. Descourt (LaTIM, Brest). Nous avons ainsi obtenu, à qualité de signal équivalent et en comparaison avec une simulation GATE standard, une accélération du temps de simulation de 140 pour un milieu de propagation composé uniquement d'air, proche de 100 en considérant un volume diffusant [5, 6]. Un exemple d'utilisation de l'approche ARF en comparaison d'une simulation GATE standard est donné dans la figure 2.3.

Ce développement a été incorporé à partir de la version 6.0 de GATE [3].

2.2.1.2 Exploitation des développements

Cette possibilité de significativement accélérer les simulations Monte Carlo pour de l'imagerie SPECT à l'iode 131 a été mise à profit en s'intéressant à la thématique de production de données simulées "hyper-réalistes". La plupart des études utilisant des données simulées par des codes Monte Carlo se basent en effet sur des volumes géométriques plus ou moins complexes mais avec l'approximation d'une activité uniforme par organe d'intérêt considéré dans le modèle [7, 8] . Cette hypothèse invalide conduit à des différences notables entre données simulées et cliniques

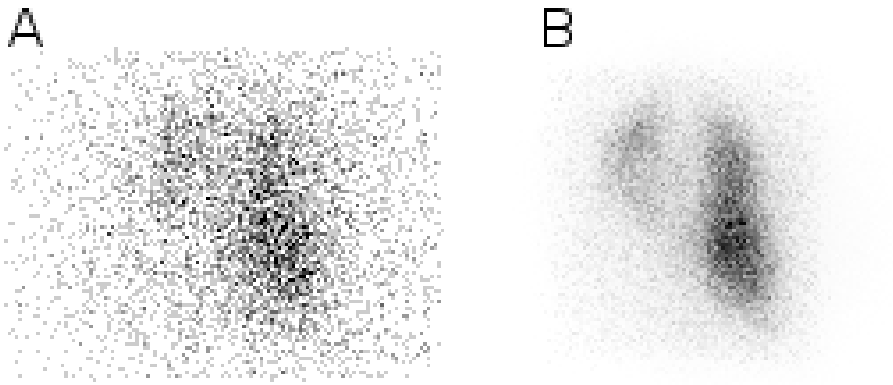

FIGURE 2.3 – Simulation d'une projection d'un patient injecté avec du Lipiocis (^{131}I) en utilisant la version standard de GATE (A) et l'approche ARF (B). Le même nombre de particules a été simulé (82×10^6) pour un temps total d'environ 26000 s pour le cas illustré en (A) et 10000 s pour le cas (B)

en terme d'hétérogénéité intrinsèque des organes. L'évaluation d'approches de segmentation [9], d'algorithmes de reconstruction (notamment sur la détectabilité [10, 11]) ou bien de métriques quantitatives obtenues sur ces données simulées [12] est ainsi rendue plus difficile par rapport à la réalité clinique. Si l'on ne s'intéresse pas à la problématique et à l'impact du mouvement des organes, il nous est donc apparu nécessaire d'établir les conditions nécessaires de production de données simulées indiscernables de données cliniques. Nous avons donc collaboré avec S. Stute (SHFJ, Orsay) pour caractériser les propriétés des données d'entrée voxelisées à une simulation Monte Carlo pour obtenir des données "hyper-réalistes" [13]. Ce travail a montré dans un premier temps que le bruit dans les données reconstruites est indépendant du bruit présent dans les données d'entrée de simulation. D'autre part, nous avons mis en évidence qu'il fallait utiliser de préférence des données d'entrée avec une résolution spatiale la plus importante possible, et donc avec un niveau de bruit corollairement important pour créer des images reconstruites à partir d'une simulation indiscernable d'acquisition réelle. Une illustration de comparaison entre des données réelles et simulées est présentée sur les figures 2.4 et 2.5 pour des projections SPECT réalisées à partir d'iode 131.

La méthodologie développée durant mon travail de thèse a conduit à envisager une extension de ce travail en l'appliquant à la problématique de la reconstruction PET à partir de radioéléments présentant des schémas de désintégrations complexes et donc susceptibles de rendre le processus de quantification difficile. L'équipe INSERM dans laquelle je m'inscris développe une thématique de radioimmunothérapie [14], en particulier à partir d'émetteur α [15]. L'astate 211 a été identifié comme étant un isotope d'intérêt par notre équipe et figure dans la liste des radioéléments devant

FIGURE 2.4 – Projections cardinales acquises (A) et simulées (B) d'un patient traité par Lipiocis (^{131}I). Les traits noirs représentent la position des deux profils tracés dans la figure 2.5

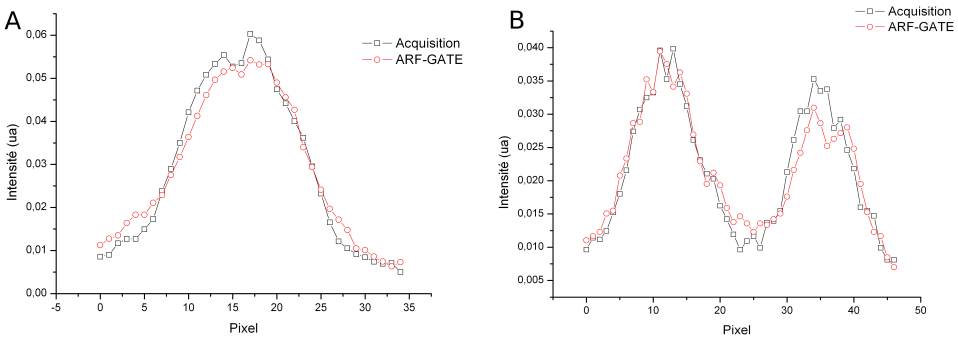

FIGURE 2.5 – Profils de l'acquisition et de la simulation ARF-GATE pour la première projection (A) et la dernière projection (B). Les emplacements des profils sont donnés sur la figure 2.4

être produits par le cyclotron ARRONAX [16]. Néanmoins, l'^{211}At ne peut être directement utilisé pour produire une image possédant une information quantitative la moins biaisée possible. L'iode 124 (émetteur β^+) peut lui être substitué afin d'obtenir une cartographie de distribution du radiopharmaceutique. L'iode 124 présente un spectre d'émission complexe comprenant en particulier deux émissions β^+ de haute énergie et plusieurs émissions de photons simples émis d'une part en cascade avec les particules β^+ et d'autre part avec une énergie compatible avec la mise en coïncidence de photons d'annihilation (figure 2.6).

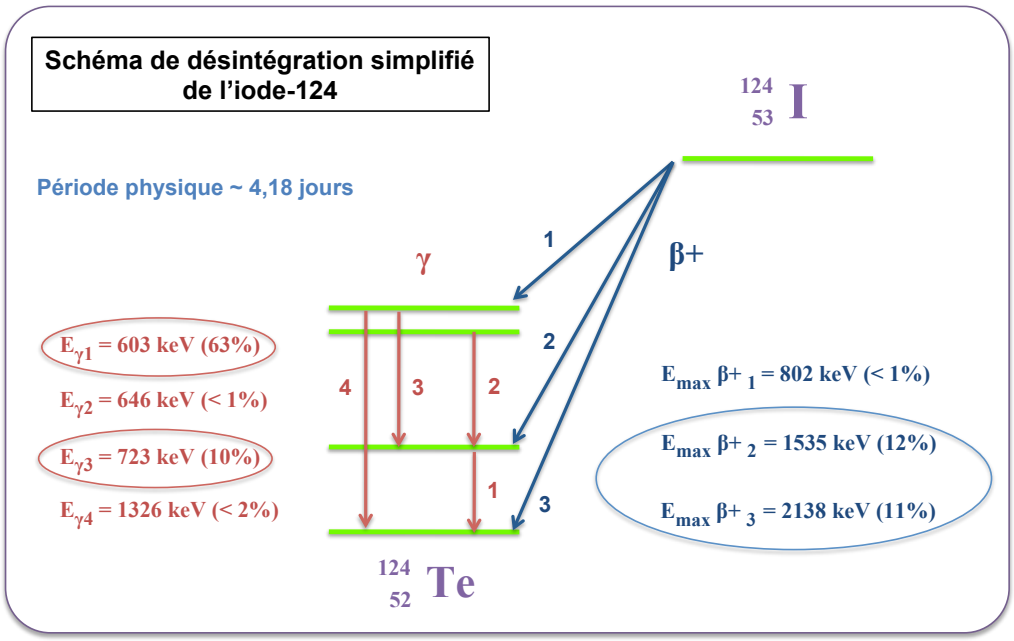

FIGURE 2.6 – Schéma de désintégration simplifié de l'iode-124. Seuls les rayonnements d'intensité proche ou supérieure à 1% sont représentés. Les rayonnements encerclés sont ceux responsables de la dégradation des images reconstruites lors de l'utilisation de cet isotope (d'après le manuscrit de thèse de M. Moreau)

Plusieurs stratégies de corrections analytiques reposant sur des hypothèses plus ou moins fortes ont été proposées sans résoudre de façon satisfaisante cette problématique complexe [17, 18, 19]. La plupart de ces approches nécessitent une estimation préalable de la distribution d'activité et/ou ne prennent en compte qu'une partie de la problématique liée à l'utilisation de l'iode 124 en TEP (photons simples émis en cascade et parcours du β^+).

Ainsi, dans la continuité de mes travaux de thèse, nous avons proposé d'étudier l'approche de reconstruction où toutes les corrections sont incorporées dans la matrice système [20]. Cette étude a fait l'objet d'un travail de thèse (réalisé par Matthieu Moreau) de 2011 à 2014 que j'ai officiellement co-encadré avec le Pr Chérel. Ce travail a été réalisé à partir d'un modèle numérique

du système PET Inveon de Siemens en utilisant une version modifiée pour nos besoins de GATE (v6.1) [1]. L'objectif principal de ce travail a été d'étudier le bénéfice de tenir compte ou non de l'ensemble des processus physiques pour la modélisation de la matrice système ainsi que l'impact des propriétés statistiques de cette dernière sur les images reconstruites. L'algorithme Maximum Likelihood Expectation Maximisation (MLEM) [21] a été implémenté en utilisant chacune des lignes de réponses (LOR : Line Of Response) sous leur forme "histogrammée" :

$$f_j^{n+1} = f_j^n \frac{1}{\sum_{i=0}^{I} R_{ij}} \sum_{i=0}^{I} R_{ij} \frac{LOR_i}{\sum_{j=0}^{J} R_{ij} f_j^n} \tag{2.3}$$

avec f_j^n une estimation du voxel j à l'itération n, R_{ij} la matrice système et LOR_i le nombre d'événements enregistré dans la LOR i. Un des principaux résultats obtenus montre qu'il n'est, *a priori*, pas nécessaire de tenir compte de toute la complexité des processus physiques pour obtenir les meilleurs résultats quantitatifs notamment dans les régions à convergence lente (figure 2.7) lorsque l'activité est localisée dans des structures de densité équivalente au tissu mou. En revanche, une fixation dans des tissus hétérogènes (de faible densité à forte densité comme les structures osseuses) est plus correctement prise en charge par une modélisation complète de la matrice système. Une des raisons principales (en même temps qu'une difficulté en terme de temps de calcul) est la grande variance des éléments de la matrice système, très souvent calculés à partir d'un seul événement (figure 2.8). La complexité croissante de modélisation de la matrice système se fait donc au prix d'une plus grande incertitude sur le calcul de chacun de ces éléments et donc d'une amélioration modeste des résultats finaux. Un compromis doit donc être trouvé en fonction de la situation explorée.

Ces développements nous ont motivé pour comparer nos travaux avec une approche (appelée IRIS : Iterative Random IDRF Sampling) développée au Laboratoire de Traitement de l'Information Médicale (INSERM U1101) de Brest également basée sur une simulation Monte Carlo préalable de la réponse du système pour une reconstruction mode-liste [23]. Les différences ont été trouvées modestes (figure 2.9) en utilisant un objet normalisé de type NEMA NU-4 2008 adapté pour l'évaluation des systèmes pré-cliniques. Ce travail a fait l'objet de deux actes de conférence [24, 25].

1. Compte tenu des ressources de calculs requises très importantes, il a été nécessaire d'installer, de paramétrer et d'utiliser un environnement de calcul parallèle local composé de 336 cœurs cadencés à 2,4 GHz.

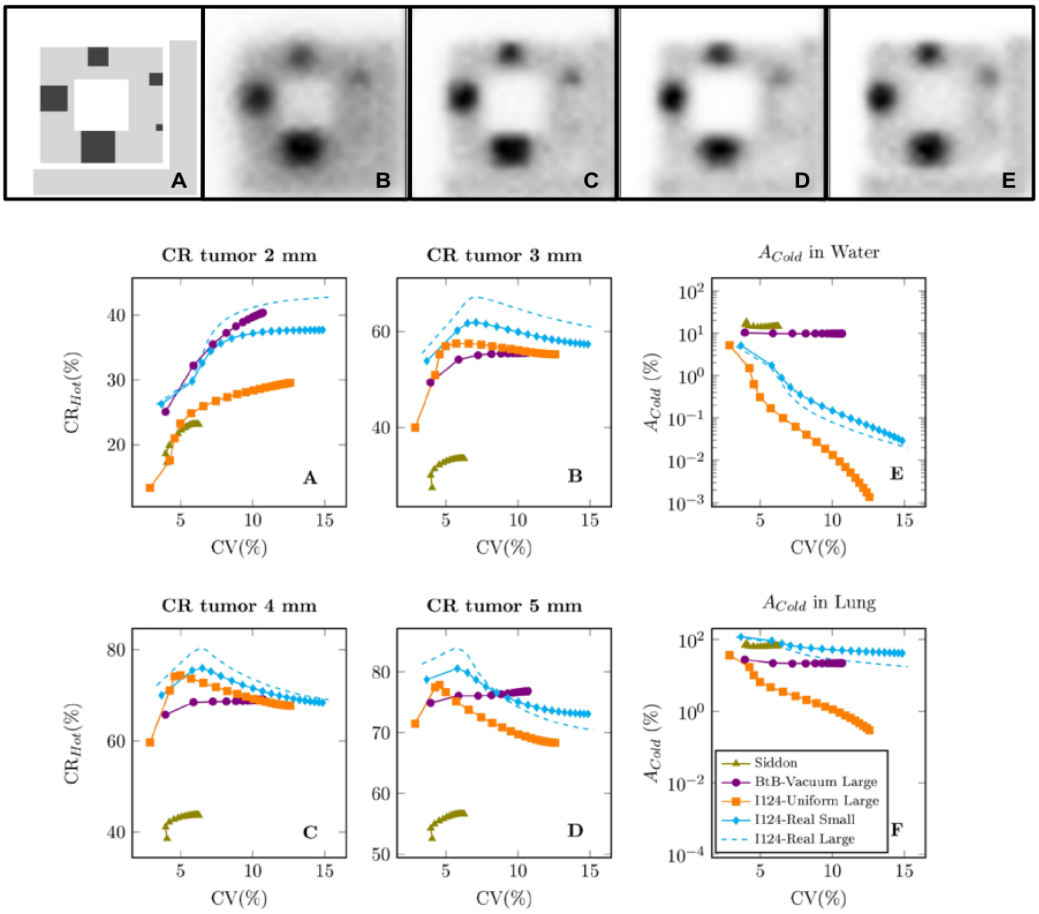

FIGURE 2.7 – Récupération de contraste pour différentes tailles de lésion en fonction du bruit dans l'image (CV : coefficient of variation). Plusieurs matrices systèmes sont évaluées : projecteur de Siddon (Siddon), projecteur calculé par Monte Carlo en considérant un milieu vide et deux photons à 180° (BtB-Vacuum Large), projecteur calculé par Monte Carlo en considérant un milieu uniforme (tissu mou) et toute la complexité de désintégration de l'iode 124 (I124-Uniform Large) et projecteur calculé par Monte Carlo en considérant un milieu hétérogène et toute la complexité de désintégration de l'iode 124 avec une matrice à grande variance (I124-Real Small) et faible variance (I124-Real Large). D'après [22]

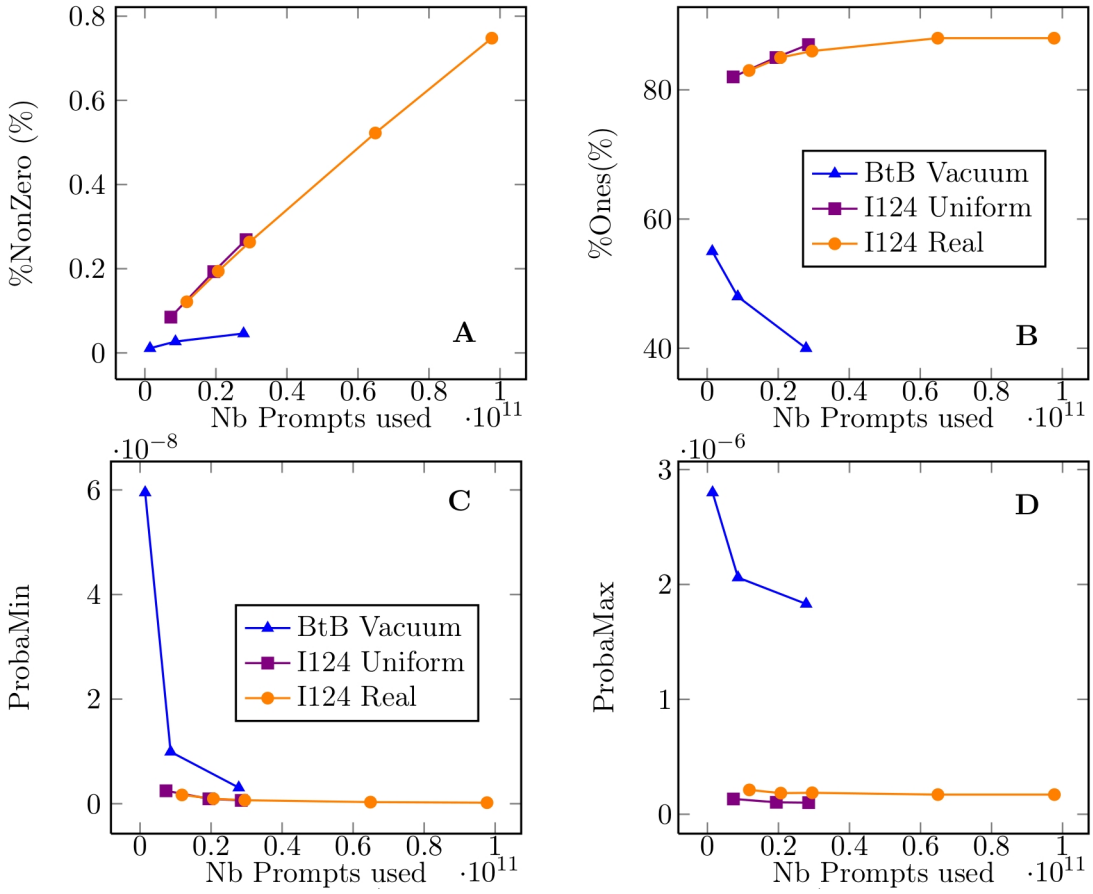

FIGURE 2.8 – Nombre d'éléments non-nuls (a), nombre d'éléments non-nuls calculés à partir d'un seul événement (b), et probabilité minimale (c) et maximale (d) en fonction du nombre de prompts utilisés pour calculer chaque matrice système. D'après [22]

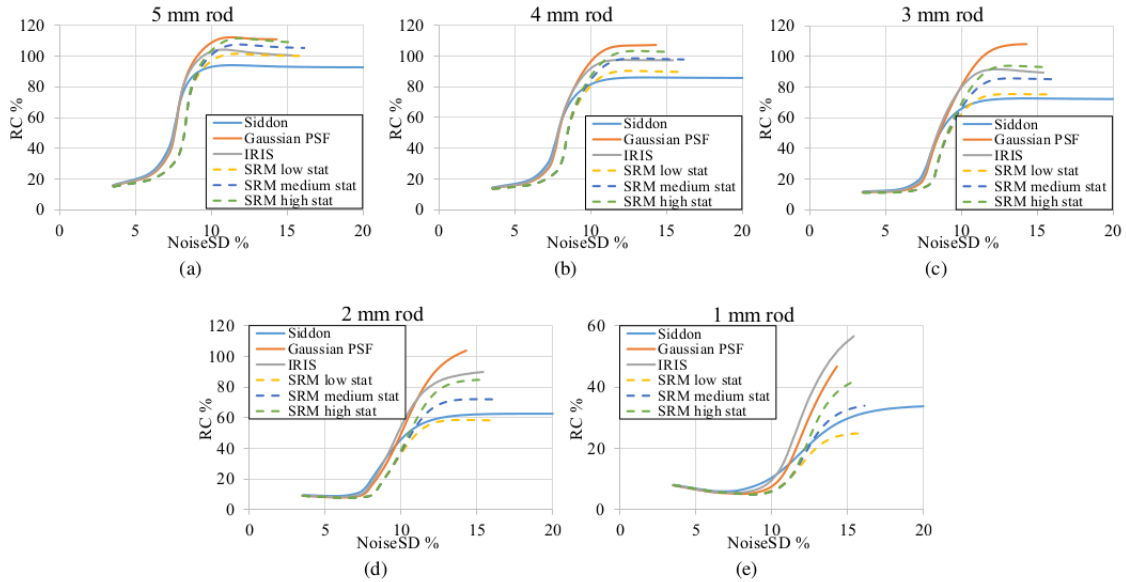

FIGURE 2.9 – Récupération de contraste des 5 barres du fantôme NEMA NU-4 2008 en fonction du bruit (NoiseSD) en utilisant 3 projecteurs (Siddon, Gaussian et IRIS) et 3 projecteurs calculés par Monte Carlo avec une basse, moyenne et haute statistique. D'après [24]

2.2.2 Caractérisation du signal TEP pour des approches quantitatives optimales utilisant des isotopes complexes

L'obtention d'une information quantitative la moins biaisée possible passe en premier lieu par des conditions d'acquisition adaptées tant au système TEP utilisé qu'au radiopharmaceutique (par l'intermédiaire de l'isotope essentiellement) choisi. Compte tenu des thématiques développées dans notre équipe et liées à l'immuno-TEP [26, 27] ou à la radio-immunothérapie [28, 29], nous avons étudié les caractéristiques de réponse des systèmes TEP et les conditions d'acquisition et de reconstruction optimales pour des applications pré-cliniques utilisant de l'iode 124 [30] et cliniques dans un contexte de thérapie interne sélective (SIRT) avec des microsphères chargées à l'yttrium 90 [31].

La caractérisation du signal TEP en utilisant de l'iode 124 sur un système pré-clinique a été menée durant le travail de thèse de Nadège Anizan. Ce travail effectué dans notre laboratoire a été conduit officieusement pour une très large majorité avec mon aide. Il a été montré à partir de données acquises, puis dans un second temps simulées par GATE, que les paramètres permettant de maximiser le Noise Equivalent Count Rate (NECR) tout en minimisant la fraction de diffusé et la fraction de photon simple, étaient différents suivant l'objet [30]. En particulier, un petit volume (typiquement une souris) devait être acquis en utilisant une fenêtre en énergie spécifique

(400-590 keV) tandis qu'un plus gros volume (rat) requiert une fenêtre en énergie différente (390-550 keV).

Cette volonté de correctement appréhender les signaux TEP dans des conditions complexes nous a également conduit à développer une connaissance approfondie des propriétés du signal TEP collecté dans le cadre d'acquisition liée à la SIRT avec des microsphères chargées à l'yttrium 90. En effet, depuis la prédiction théorique dans les années 50 par Ford [32] (figure 2.10), la première image publiée par Lhommel en 2009 [33] et les études pilotes sur ce sujet [34, 35], nous avons été l'une des premières équipes françaises à s'intéresser aux propriétés de ce type d'imagerie [36].

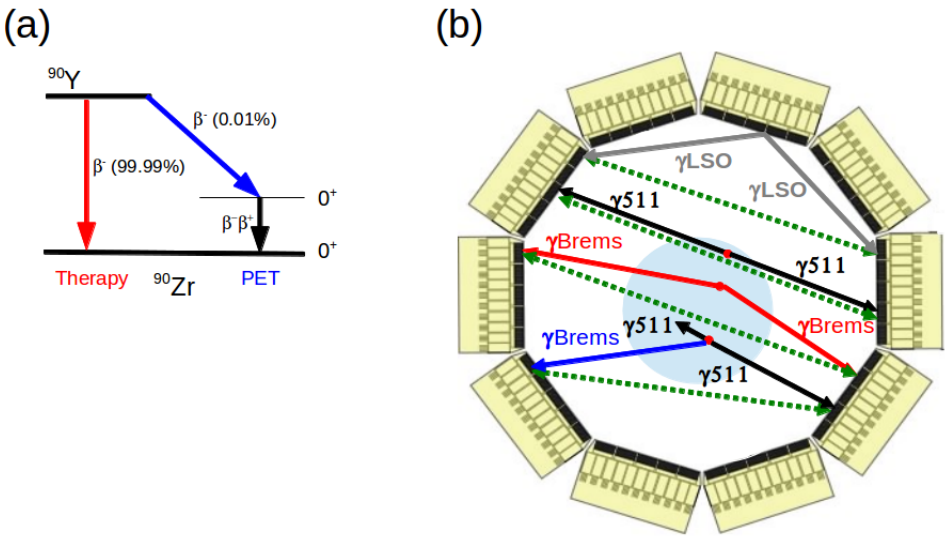

FIGURE 2.10 – Schéma simplifié de décroissance de l'yttrium 90. D'après [31]

Nous avons ainsi noué une collaboration avec le groupe de physique de Siemens (Knoxville, Tennessee, USA) afin de renseigner précisément les caractéristiques du signal TEP pour des systèmes Siemens. Ce travail a associé également deux équipes américaines (Allegheny General Hospital à Pittsburgh et Fox Chase Cancer Center à Philadelphie, Pennsylvania) et une équipe australienne (University of Sydney, Camperdown, New South Wales). Nous avons principalement montré que les performances quantitatives n'étaient ni affectées par la fraction d'événements fortuits (très importante dans ce type d'acquisition à très bas flux de comptage : entre 70 et 90% suivant l'activité présente dans le champ de vue) ni par celui des événements vrais (très faibles : entre 10^5 et 10^6). Par contre, les algorithmes itératifs "soustractifs" de type AW-OSEM donnaient les moins bonnes performances et ne doivent pas être utilisés en routine clinique pour ce type d'acquisition. Un exemple d'images reconstruites d'un fantôme de type IEC est donné dans

la figure 2.11. Ces caractérisations sont indispensables si l'on souhaite réduire le biais du calcul dosimétrique utile pour enrichir la connaissance de la réponse au traitement. C'est à cette fin que nous avons obtenu en collaboration avec l'équipe de Beaujon (Dr Arnaud Dieudonné) et l'équipe du SHFJ (Dr Irène Buvat) un financement INCa Physicancer sur 3 ans (2014-2017). Les premiers résultats intéressants de ce travail ont été récemment soumis [37]. En particulier, nous montrons pour la première fois la contribution relative de chaque processus physique au signal final collecté. Nos résultats suggèrent que la contribution du rayonnement freinage et des événements fortuits ont un impact extrêmement marginal sur le biais quantitatif (<5% en comparaison des données reconstruites en ne tenant compte que des événements vrais). De même, la composante diffusée a été trouvée mineure sur la quantification (<4%). C'est donc plutôt dans le champ de l'algorithme de reconstruction (en tenant compte du biais positif introduit par les approches MLEM) qu'une perspective d'amélioration de la valeur quantitative des données ^{90}Y-TEP est susceptible d'être envisagée.

2.3 Applications cliniques d'outils méthodologiques

Les développements et compétences acquises au travers de sujets de recherche méthodologique peuvent trouver des applications cliniques concrètes d'autant plus "facilement" que, d'une part, mon travail s'inscrit au sein du service de Médecine Nucléaire du Centre Hospitalier Universitaire de Nantes et, que d'autre part, l'équipe clinique soutient de façon indéfectible ce travail translationnel. Nous présentons donc ici quelques applications dans le domaine de la reconstruction tomographique, de la quantification en imagerie moléculaire, de la caractérisation de la texture tumorale en imagerie TEP et de la détection per-opératoire.

2.3.1 Application en reconstruction tomographique

L'hyperparathyroïdie primaire est souvent causée par un adénome solitaire. La résection de cet adénome peut se faire par un abord bi-latéral souvent considéré comme long et responsable de co-morbidité. La scintigraphie au ^{99m}Tc-MIBI planaire et l'échographie permettent d'augmenter la sensibilité de détection de cet adénome et donc autorise une chirurgie mini-invasive unilatérale. Il a été montré également que l'utilisation d'un collimateur sténopé en condition d'acquisition planaire avait également un grand intérêt dans la détection des petits adénomes parathyroïdiens [38]. Par ailleurs, la généralisation des acquisitions tomographiques et dernièrement couplées à un scanner (SPECT/CT) a permis également d'augmenter encore cette sensibilité [39]. Nous avons donc proposé en 2008 d'évaluer l'apport de la réalisation d'une tomographie avec un collimateur sténopé dans la détection des adénomes en comparaison des techniques conventionnelles disponibles à ce moment de l'étude (scintigraphie planaire, SPECT et échographie). L'acquisition et

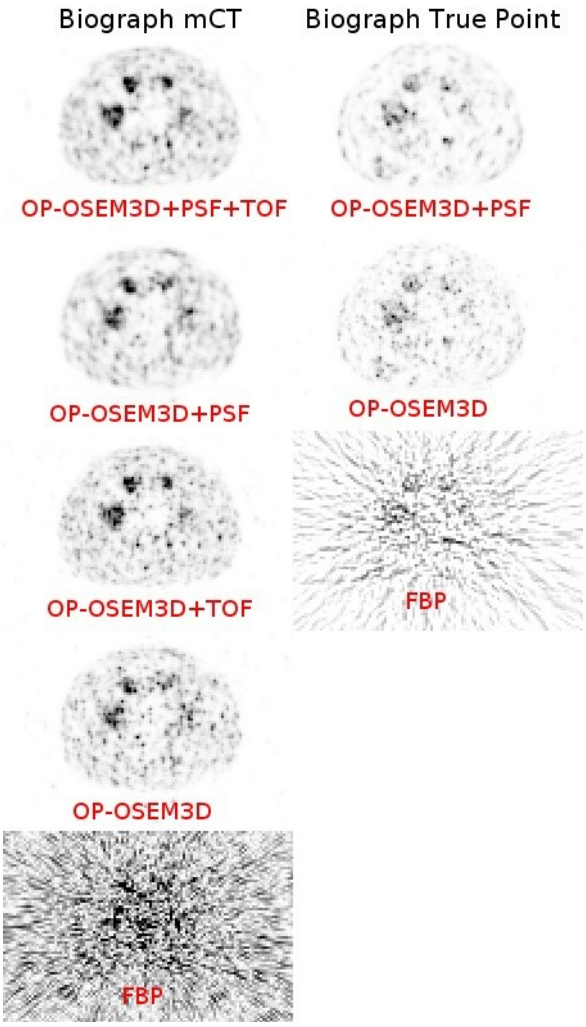

FIGURE 2.11 – Images reconstruites d'un fantôme de type IEC pour deux systèmes TEP Siemens (Biopgraph mCT et Biograph True Point) à partir de différents algorithmes de reconstructions. Chaque sinogramme contenait 4×10^5 événements vrais. D'après [31]

la reconstruction en géométrie sténopé sont deux problèmes difficiles que nous avons levés en collaboration avec le Pr Alain Seret (Université de Liège, Belgique) [40] sur la base des travaux de Vanhove [41].

Un code de reconstruction tomographique sténopé a donc été adapté à notre problématique et nous avons montré qu'une combinaison de la scintigraphie planaire avec la tomographie sténopé permettait d'augmenter la sensibilité de l'examen ainsi que l'indice de confiance accordé au diagnostic [42]. La figure 2.12 illustre le gain substantiel obtenu en qualité de détection d'un adénome orthotopique droit en comparaison d'une scintigraphie planaire et d'une tomographie parallèle.

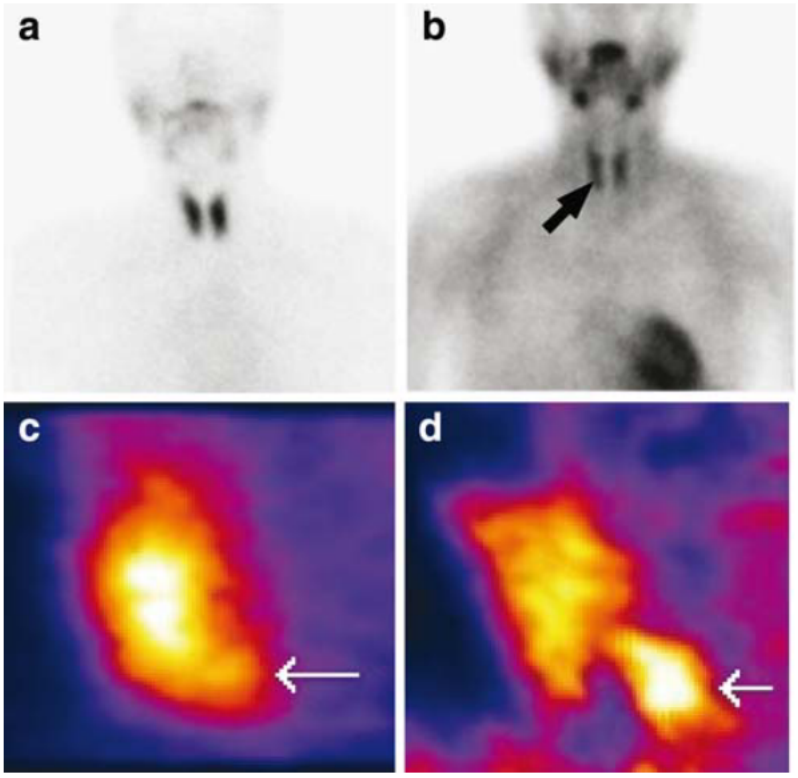

FIGURE 2.12 – Foyer très douteux sur la scintigraphie planaire (b) au ^{99m}Tc-MIBI (score de confiance = 1 sur une échelle de 0 à 3), évident (c) sur les images reconstruites de la tomographie parallèle (score de confiance = 2) et indiscutable (d) sur les images reconstruites de la tomographie sténopé (score de confiance = 3). D'après [42]

2.3.2 Application en quantification et en optimisation

Nous avons déjà abordé le travail méthodologique développé autour de la caractérisation du signal TEP collecté dans le cadre de l'imagerie post-thérapeutique de la SIRT à l'yttrium 90 dans la partie 2.2.2. Une de nos premières motivations dans ce cadre a été de déterminer si nous pouvions utiliser également cette approche pour réaliser une imagerie post-thérapeutique de patients souffrant de lymphome B traités par anti-CD20 Zevalin® ou anti-CD22 epratuzumab marqués à l'yttrium 90. Cette évaluation revient à calculer la concentration minimale de radiopharmaceutique nécessaire pour qu'il puisse être visualisé par détection TEP. Nous avons ainsi déterminé qu'il fallait au minimum une concentration de l'ordre de 1 MBq.mL^{-1} et l'utilisation de l'information temps de vol pour qu'une lésion puisse être détectée [36]. Cette concentration est rarement atteinte dans le cadre d'injection systémique dans le cadre de la radioimmunothérapie mais par contre très souvent rencontrée en SIRT. Cette modalité est ainsi systématiquement utilisée en routine clinique à Nantes après une SIRT pour, d'une part, cartographier précisément la distribution d'activité en comparaison de la cartographie prescrite et visualisée en pré-thérapie par injection de ^{99m}Tc-MAA et pour, d'autre part, calculer précisément l'activité réelle injectée dans le lobe hépatique traité. Bien évidemment, cette imagerie peut être également mise à profit pour réaliser un calcul dosimétrique post-thérapie. Nous reviendrons sur cette partie dans le chapitre 3.

Une seconde application très pratique en imagerie TEP a bénéficié d'un développement méthodologique autour de l'optimisation des paramètres d'acquisition. Nous sommes partis du constat qu'il n'existait pas de recommandations argumentées et rationnelles pour choisir l'activité injectée et le temps d'acquisition par position de lit pour des examens au ^{18}F-FDG. Nous avons alors développé, amélioré et appliqué une méthodologie proposée originellement par Watson [43] sur un nombre très large de patients (>500). Cette approche, se basant sur une relation de proportionnalité entre les propriétés du signal collecté (mesuré au travers du Noise Equivalent Count Rate [2]) et le rapport signal sur bruit dans l'image reconstruite, [44] consiste à modéliser la NECR à partir d'un seul point de mesure enregistré au moment de l'acquisition. Cette modélisation repose sur l'obtention de fonctions donnant la relation des événements simples, des événements vrais plus diffusés et des événements fortuits en fonction de l'activité présente dans le champ de vue. Ces fonctions dépendent d'autres fonctions propres au système de détection et déterminées une seule fois ainsi que de coefficients (eux aussi dépendant de l'activité dans le champ de vue) propres au patient. Nous avons vérifié que ce modèle donnait des résultats satisfaisants sur 60 patients avant de l'appliquer sur une population plus large. L'intérêt est donc de pouvoir déterminer, a

2.
$$NECR = \frac{T^2}{T + S_{in} + kR_{in}}$$
avec T le taux d'événements vrais, S_{in} et R_{in} le taux d'événements diffusés et fortuits à l'intérieur du patient, et k une constante comprise entre 1 et 2 tenant compte de la méthode de correction des événements fortuits

posteriori, quelle aurait été la réponse du système pour n'importe quelle activité injectée à un patient (figure 2.13).

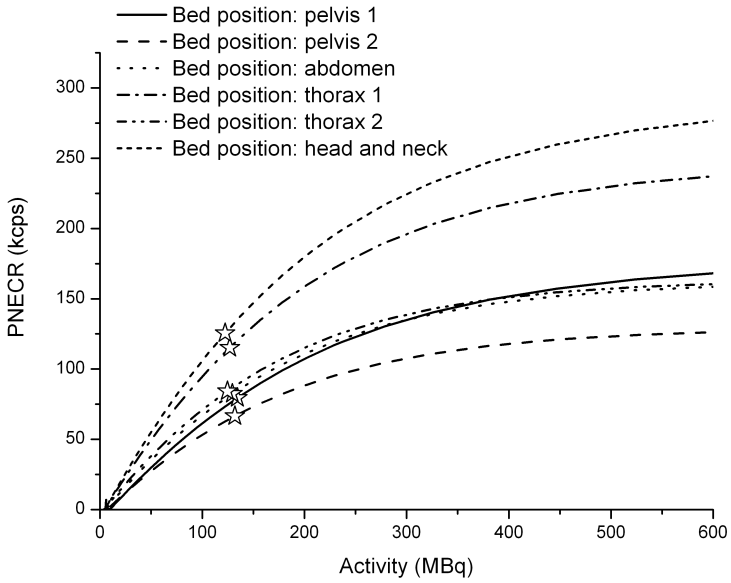

FIGURE 2.13 – Modélisation de la NECR pour plusieurs positions de lits. Les étoiles donnent le point de mesure utilisé comme paramètre d'entrée du modèle. D'après [45]

Nous en avons dérivé un schéma d'injection optimale pour le système ((a) de la figure 2.14) et un second harmonisé entre tous les patients ((b) de la figure 2.14) en fonction de leur indice de masse corporelle.

Nous avons également proposé d'adapter le temps par position de lit en fonction de la NECR correspondante à cette position. Cette nouvelle approche a permis d'optimiser le temps passé sur une région anatomique en fonction de son intérêt clinique et des propriétés des coïncidences collectées (figure 2.15). Ces différents résultats sont pris en compte et appliqués dans notre routine clinique.

2.3.3 Caractérisation de la texture tumorale en imagerie TEP

2.3.3.1 Préambule

Bien qu'il ne s'agisse pas, stricto sensu, d'une approche méthodologique ayant encore une application clinique de routine, nous mentionnons cette thématique en cours de développement dans cette partie en raison de son assise importante sur des protocoles de recherche clinique dont nous sommes promoteur ou investigateur principal.

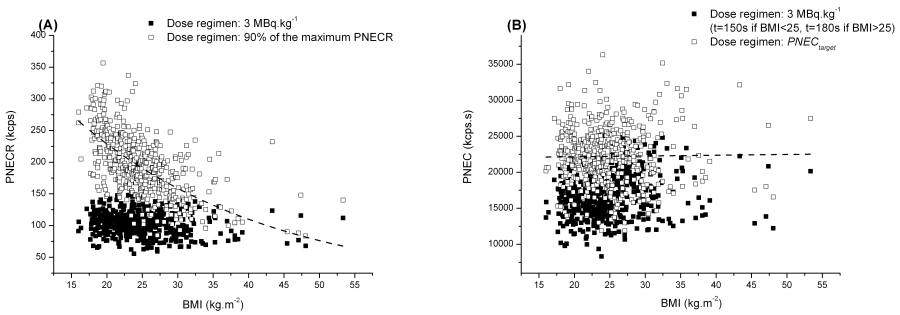

FIGURE 2.14 – NECR en fonction de la l'indice de masse corporelle (BMI). Le schéma d'injection maximisant les performances du système est représenté en (a) et celui harmonisant les propriétés du signal en fonction du patient est représenté en (b). Le schéma d'injection préconisé par Siemens (3 MBq.kg^{-1} est également mentionné par les carrés pleins noirs. D'après [45]

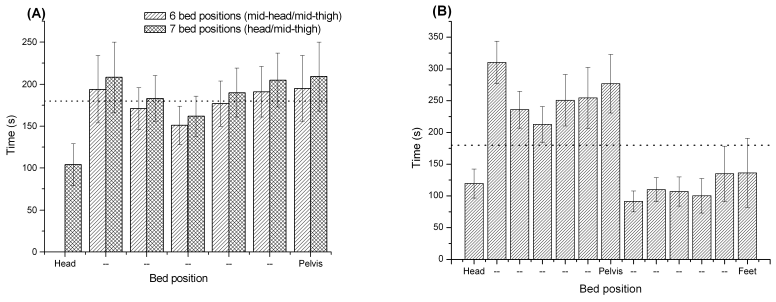

FIGURE 2.15 – Temps passé par position pour 6 et 7 pas (a) et une acquisition corps entier à 13 pas (b). Les valeurs sont ici montrées pour un seul indice de masse corporelle (BMI). D'après [45]

2.3.3.2 Texture tumorale en imagerie TEP

Les tumeurs présentent souvent une large hétérogénéité biologique, cellulaire et tissulaire. Les interactions des cellules cancéreuses avec leur microenvironnement ne sont pas uniformes dans la tumeur, et les propriétés de la trame conjonctivo-vasculaire qui constitue le stroma cancéreux ainsi que le remodelage de la matrice extracellulaire varient en fonction des régions de la tumeur. Par ailleurs certaines zones d'une tumeur sont moins bien vascularisées et oxygénées que d'autres et cette variation locale de l'angiogenèse et de l'hypoxie locale conduit, entre autres, à une modification du métabolisme énergétique. Ceci conditionne également l'agressivité de la tumeur et la résistance thérapeutique. Ainsi, les tumeurs avec une forte hétérogénéité intrinsèque ont un pronostic plus péjoratif. Or une méthode non invasive d'évaluation de l'hétérogénéité tumorale pourrait permettre d'extraire des caractéristiques utiles dans le cadre de l'évaluation tumorale et de mieux sélectionner les patients de mauvais pronostic pour une thérapie plus intensive. L'analyse de la distribution du traceur dans la tumeur pourrait ainsi apporter une caractérisation complémentaire des paramètres quantitatifs usuels tels que la SUV_{max} ou le volume métabolique tumoral. Sur la base de cette hypothèse, plusieurs travaux ont récemment montré le bénéfice de rapporter l'hétérogénéité tumorale au diagnostic dans un certain nombre de cancers solides, dont le cancer du sein [46], de l'œsophage [47, 48], de la sphère ORL [49, 50], du col utérin [51] et du poumon [52, 53]. Malgré des détails méthodologiques imparfaitement renseignés dans bon nombre d'études, c'est un domaine en pleine expansion en imagerie TEP [54, 55].

Nous avons récemment entrepris d'explorer ce champ de recherche dans un contexte d'étude multicentrique avec l'étude préalable des facteurs de perturbation des paramètres de texture dans le contexte où différents systèmes de détection avec différents paramètres d'acquisition et de reconstruction sont utilisés. Plusieurs résultats de corrélation entre paramètres de texture et métriques conventionnels [48, 56] ont été confirmés dans le contexte particulier du lymphome du manteau. Pour cette étude, la TEP-FDG initiale de 92 patients recrutés pour une étude ancillaire au protocole LyMa du groupe Lysa (the Lymphoma Study Association) ont été considérés [57]. Nous avons également conduit une étude visant à sélectionner les paramètres les plus robustes dans un contexte multicentrique en s'intéressant aux effets des paramètres d'acquisition et de reconstruction (algorithme utilisé, paramètres des algorithmes, taille des voxels et niveau de bruit dans les images). Ces effets avaient été en partie rapportées dans une étude récente [58] mais avec un nombre de lésions deux fois moins important et des métriques d'analyse différentes dans certains cas. Ces résultats (très souvent discordants avec l'étude de Yan & al) nous ont permis de ne rendre éligible que quelques paramètres suffisamment robustes qui seront considérés dans nos travaux futurs [59].

2.3.4 Détection per-opératoire

Nous avons caractérisé les performances de plusieurs sondes per-opératoires dans le contexte de détection de métastases iodo-négatives de cancers différenciés de la thyroïde. Cette détection se réalise après injection de ^{18}F-FDG étant donné les bonnes performances de sensibilité démontrées par imagerie. L'utilisation de sonde dans cette indication est rendue complexe de part l'émission de photons de haute énergie et la présence d'un bruit de fond important. Cette étude a permis, d'une part, de sélectionner une sonde appropriée à ce type de conditions et, d'autre part, de déterminer qu'un rapport signal sur bruit de fond de 1,5 (in vivo et ex vivo) permettait de correctement rendre compte du caractère malin de la lésion [60].

2.4 Instrumentation

2.4.1 Préambule

Une opportunité rare nous a été offerte de travailler sur un prototype innovant de système de détection TEP basé sur un milieu au Xénon liquide. C'est un projet porté par le groupe Xénon dirigé par le Dr Dominique Thers du laboratoire SUBATECH. Nous ne rentrerons pas trop dans les détails techniques du développement car nous ne faisons qu'accompagner le projet dont les idées et leurs mises en œuvre sont portées et réalisées essentiellement par le groupe Xénon. Nous mentionnerons brièvement le concept général de ce système et nos contributions à ce projet.

2.4.2 XEMIS

Nous avons commencé la collaboration avec le groupe Xénon dès le lancement de l'idée en 2005. Ce projet de détecteur TEP a pris ultérieurement le nom de XEMIS (XEnon Medical Imaging System). Initialement, l'idée des Dr Dominique Thers et Jean-Pierre Cussonneau était de réaliser un détecteur TEP basé sur un milieu de détection au xénon liquide afin d'augmenter significativement la résolution en énergie, la résolution spatiale et la sensibilité. Le concept d'utilisation du xénon liquide en imagerie TEP remonte à 1976 [61] mais l'utilisation conjointe du signal d'ionisation et de scintillation a été proposée en 1993 [62] et reprise par le groupe de Subatech. Cette mesure simultanée est rendue possible par l'utilisation d'une chambre à projection temporelle (ou TPC pour Time Projection Chamber) qui constitue l'élément primaire de cette technologie (figure 2.16). L'intérêt majeur de ce type d'approche est de pouvoir mesurer dans la TPC chaque vertex d'interaction. Il est donc possible de reconstruire toute la séquence Compton et donc de s'affranchir de façon élégante de l'effet de parallaxe. Ce procédé de détection est encore appelé télescope Compton.

Nous avons ainsi proposé dès 2005 de simuler un système clinique à l'aide de la plateforme

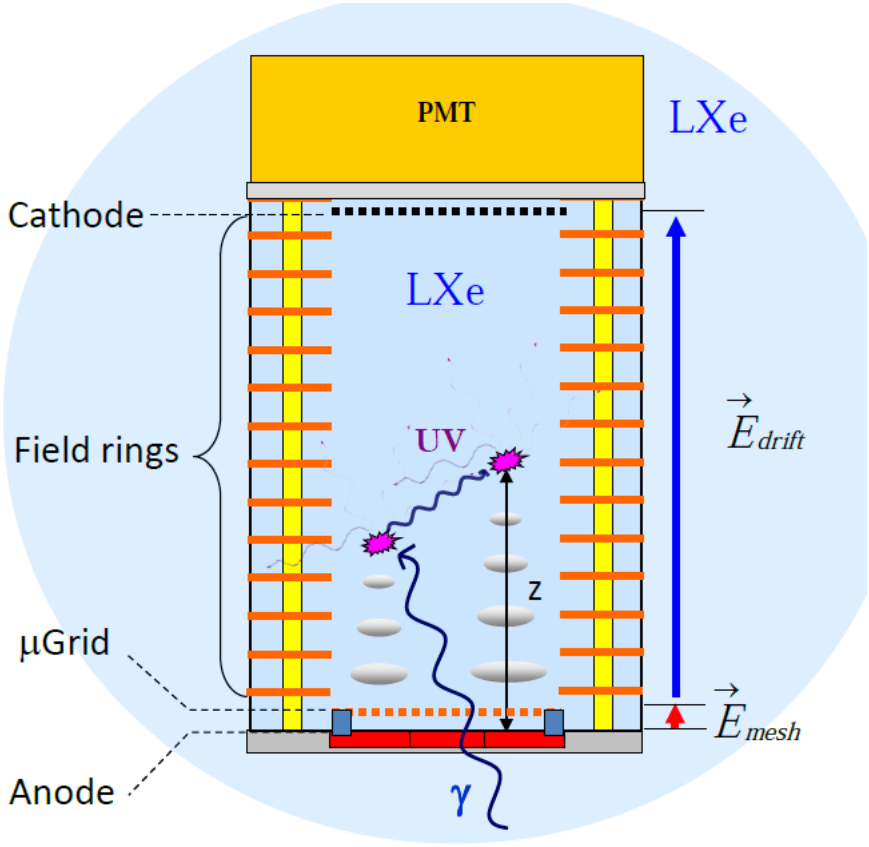

FIGURE 2.16 – Principe de la chambre à projection temporelle équipée du détecteur MICROMEGAS (grille, annotée μGrid sur le schéma + l'anode). Les nuages d'électrons sont représentés en tâches grises tandis que les photons de scintillation apparaissent en violet. D'après L. Gallego (SUBATECH)

GATE (en modifiant sensiblement le code pour les besoins très spécifiques à ce système original) afin d'évaluer le bénéfice de cette approche. Comme l'effet de parallaxe n'est plus une limitation, les dimensions du système simulé étaient de 60 cm de diamètre pour 60 cm de champ axial. Les données on été reconstruites grâce à une collaboration avec F. Lamare (LaTIM, Brest) et ont permis d'une part de montrer la très grande capacité résolutive du détecteur de l'ordre de 1,5 mm au centre du champ de vue (figure 2.17) et d'autre part d'atteindre un pourcentage d'événements calométrisés très élevé de l'ordre de 15 % au centre du champ de vue pour une résolution en énergie de l'ordre de 5 %. Ces résultats préliminaires simulés n'ont pas fait l'objet de publication.

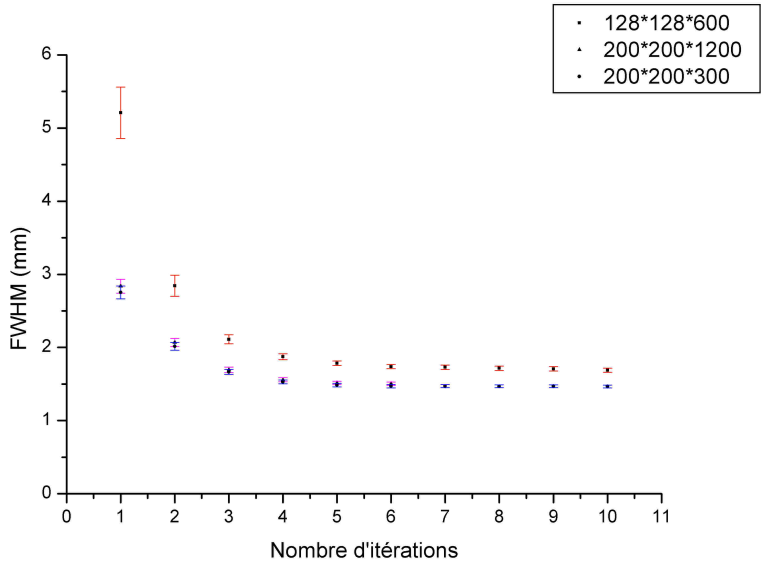

FIGURE 2.17 – Résolution spatiale mesurée à partir d'un point source au centre du champ de vue en fonction du nombre d'itérations pour différentes tailles de voxels reconstruits

Ce concept initial a très rapidement évolué vers une autre approche très originale (et brevetée en 2009) de détection à 3 photons. Le principe général est donné sur la figure 2.18. Il consiste en la détection simultanée des deux photons issus de l'annihilation du positron plus celle venant de l'émission d'un photon de haute énergie (> 1 MeV) en coïncidence temporelle avec les deux premiers photons. Parmi les quelques isotopes présentant cette propriété remarquable, c'est le scandium 44 qui a été retenu. Il émet un photon simple de 1,157 MeV environ 3 ps après le positron. Les premiers résultats expérimentaux sur une cellule élémentaire (appelée XEMIS1) ont été récemment rapportés [63]. Le gros avantage de cette approche est de permettre un positionnement de l'événement sur la LOR avec une précision de l'ordre de 1 cm. Cet ordre de grandeur est à comparer avec les technologies actuelles basées sur une détection par cristaux de

type LSO qui proposent une précision de l'ordre de 10 cm.

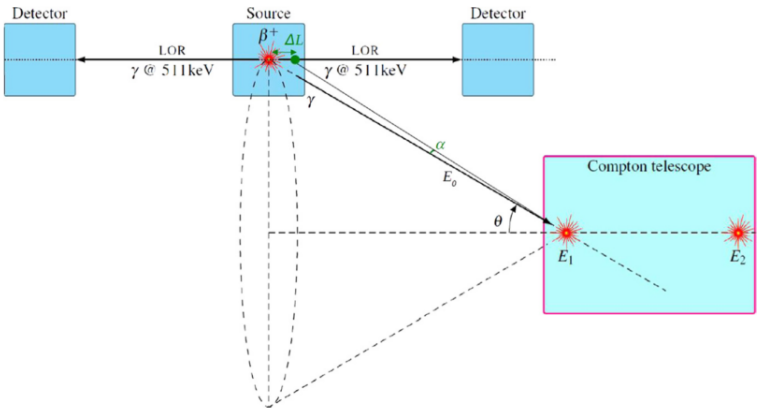

FIGURE 2.18 – Principe général de la détection 3 photons basé sur la détection des deux photons de 511 keV et d'un troisième photon de l'ordre de 1 MeV. Le croisement entre la LOR et le cône Compton donne le point d'émission avec une précision ΔL. D'après [63]

La preuve de concept à partir des premiers résultats expérimentaux nous a permis d'obtenir un financement INCa (Physicancer) en 2012 autour de la caractérisation d'un système de détection complet pour des applications pré-cliniques (figure 2.19). Nous avons pu ainsi développer toute la partie de simulation de ce système (appelé XEMIS2) et de développer de façon concomitante une approche originale de reconstruction par croisement de la LOR avec le cône Compton. Les premiers résultats nous laissent entrevoir la possibilité d'effectuer des acquisitions avec 100 fois moins d'activité que sur des systèmes conventionnels.

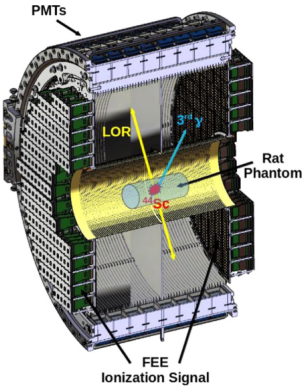

FIGURE 2.19 – Vue de la partie active du système pré-clinique XEMIS2. D'après [63]

Chapitre 3

Projet de recherche

Les différentes thématiques abordées ces dernières années se sont structurées principalement autour d'opportunité de développements, de rencontres scientifiques fructueuses, de curiosité dans un but d'application clinique plus ou moins immédiate mais aussi et surtout grâce au soutien précieux et indéfectible de l'équipe de Médecine Nucléaire du CHU de Nantes pilotée par le Pr Françoise Kraeber-Bodéré et de l'équipe Oncologie Nucléaire du CRCINA (INSERM U1232, Université de Nantes) pilotée par les Prs Françoise Kraeber-Bodéré et Michel Chérel. Ces différentes thématiques, pouvant sembler au demeurant erratiques, ont finalement convergé naturellement vers les trois piliers fondamentaux de la médecine nucléaire (en faisant abstraction du domaine primordial de la radiopharmacie) : méthodologie/reconstruction, applications cliniques et instrumentation. Ces trois points d'appuis sont maintenant au cœur du projet de recherche et nous envisageons d'abonder et d'approfondir ces thématiques avec des développements déjà débutés ou en projet. Ainsi, nous déclinerons dans cette partie les projets de recherche relatifs aux trois thématiques principales décrites au paragraphe 2.1 mais en s'attachant cette fois-ci à regrouper des projets partageant la même thématique sous une même partie qu'ils viennent d'aspect plutôt méthodologique ou plutôt clinique.

Nous aborderons donc trois axes principaux qui font parti de mon projet de recherche :

1. Reconstruction et quantification en imagerie TEP à l'yttrium 90

2. Paramètres quantitatifs avancés pour le pronostic et le suivi thérapeutique en imagerie moléculaire

3. Vers un détecteur au xénon liquide clinique

3.1 Reconstruction et quantification en imagerie TEP à l'yttrium 90

La radiothérapie interne sélective à l'aide de microsphères chargées à l'yttrium 90 est une technique faisant l'objet de nombreux travaux en particulier pour tous les aspects liés à l'imagerie et de plus en plus à la dosimétrie. La figure 3.1 donne l'évolution du nombre de publications trouvées dans PubMed se rapportant à cette technique de thérapie au cours des 12 dernières années. L'intérêt suscité par cette modalité de traitement est donc en très nette évolution depuis quelques années. La part consacrée à l'imagerie TEP par yttrium 90, la dosimétrie pré-traitement (et surtout post-traitement) ainsi que l'évaluation de la thérapie par des bio-marqueurs extraits d'examens TEP-FDG [64] attirent également beaucoup d'investigateurs dans un but de meilleur contrôle de la maladie.

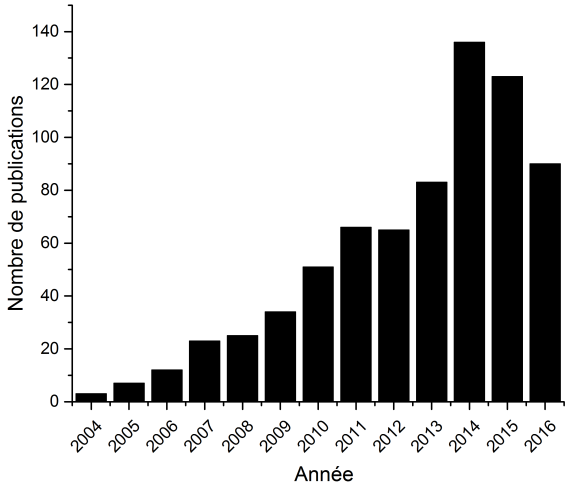

FIGURE 3.1 – Evolution du nombre de publications au cours des 12 dernières années sur la radiothérapie sélective par microsphères chargées à l'yttrium 90 d'après PubMed

Toutefois, il subsiste un champ important de recherche sur trois points :

1. Le biais quantitatif retrouvé sur les images reconstruites TEP à l'yttrium 90 ne peut, a priori, s'expliquer par des processus physiques mal corrigés comme nous l'avons récemment montré [37]. Nous avons donc débuté un travail autour de la reconstruction des données à faible statistique. En particulier, nous allons tenter d'appliquer des approches s'affranchissant du biais positif des algorithmes MLEM du type NEGML [65] ou ABML [66] étant donné les propriétés intéressantes déjà rapportées avec des objets analytiques [67]. Nous

avons ainsi très récemment intégré un projet collaboratif proposant de développer une plateforme de reconstruction pour des acquisitions SPECT et PET de façon la plus ouverte et modulable possible. Ce projet nommé CASToR (Customized and Advanced Software for Tomographic Reconstruction) et piloté par le Dr Dimitris Visvikis s'inscrit au sein du réseau France Life Imaging [68, 69]. Il agrège des équipes avec une très forte compétence en reconstruction tomographique, en particulier le Service Hospitalier Frédéric Joliot du Commissariat à l'Energie Atomique et aux Energies renouvelables (Dr Claude Comtat et Dr Simon Stute).

2. Le calcul dosimétrique sur la base des images TEP post-traitement représente une voie très prometteuse faisant l'objet d'une attention soutenue [70, 71] dans le but de mettre en relation l'efficacité du traitement et la quantité radioactive de microsphères injectés. Nous collaborons avec l'équipe de Beaujon (Dr Arnaud Dieudonné et Dr Manuel Sanchez) afin de tester une approche originale de déconvolution du signal directement sur les histogrammes dose-volume [72]. Bien que nous ne soyons pas moteur sur cet aspect particulier, nous sommes en charge de la production des données simulées afin d'appréhender les performances de ces approches. Ce travail se réalise actuellement dans le cadre collaboratif du plan Physicancer 2014 (projet MILADY 2014-2017). Nous appliquerons par la suite ces développements sur une base de données clinique homogène (cholangiocarcinome et/ou carcinome hepato-cellulaire) venant de nos deux institutions.

3. L'évaluation thérapeutique de ce type de traitement par imagerie fonctionnelle TEP-FDG (en particulier en utilisant les critères PERCIST [73]) suscite également beaucoup d'attention dans les indications telles que cholangiocarcinome [74] ou métastases hépatiques de différents cancers [71, 75]. C'est dans ce contexte que l'analyse de bio-marqueurs extraits de l'imagerie TEP-FDG a montré un intérêt préliminaire important. Nous ambitionnons d'étudier également ce type d'approche en mettant en relation le suivi thérapeutique par TEP-FDG avec le calcul dosimétrique à l'échelle du voxel et différents paramètres cliniques. Nous porterons dans ce contexte une étude particulière sur la segmentation tumorale guidée ou non par le scanner afin d'établir une relation la moins biaisée possible entre la réponse au traitement et le calcul dosimétrique.

3.2 Paramètres quantitatifs avancés pour le pronostic et le suivi thérapeutique en imagerie moléculaire

L'imagerie moléculaire est porteuse d'une information biologique extrêmement riche qu'il est possible d'exploiter à des fins de facteurs pronostiques ou d'évaluation à la réponse au traitement.

L'analyse visuelle a prouvé sa grande utilité dans les hémopathies et dans les tumeurs solides. Il est toutefois possible d'extraire plusieurs paramètres quantitatifs complémentaires afin de mieux caractériser la maladie [76, 55] comme mentionné dans le paragraphe 2.3.3. Nous avons ainsi débuté une thématique sur l'intérêt de l'utilisation de métriques quantitatives "avancées" pour la valeur pronostique, la stadification et la réponse au traitement.

3.2.1 Valeur pronostique et stadification

Les métriques utilisées sont basées, d'une part, sur la mesure de la texture tumorale par approche statistique [77, 78, 79] et, d'autre part, sur la mesure de paramètres de formes. Nous avons notamment débuté un travail de l'apport de ces métriques sur la valeur pronostique de la TEP initiale dans le myélome multiple (étude multicentrique IMAJEM : Imagerie Jeune Myélome) avec des premiers résultats semblant être très prometteurs. Une étude similaire portant sur la TEP initiale chez des enfants atteints de sarcome (ostéosarcome et sarcome d'Ewing) est également conduite dans notre équipe. Les premiers résultats vont être présentés au congrès européen de Médecine Nucléaire 2016 [80]. A cette faveur, nous étudions également l'impact des méthodes de ré-échantillonnage et notamment l'intérêt d'utiliser une égalisation d'histogramme avant ou après cette étape de ré-échantillonnage [81].

Nous nous intéressons également au développement de nouvelles métriques de caractérisation de l'hétérogénéité tumorale [81, 82, 83]. Certaines de ces métriques sont actuellement en cours d'investigation, en particulier pour l'étude IMAJEM. Ces métriques, calculées directement sur l'image sans passer par des matrices intermédiaires, présentent probablement un intérêt dans le cadre de lésions nécrotiques. Ainsi, nous envisageons de les employer sur une population de patients atteints de phéochromocytome à partir de la TEP initiale avant chirurgie. Les données anathomopathologiques seront disponibles et permettront de mesurer l'intérêt de ces métriques et plus généralement de la TEP-FDG en fonction des mutations génétiques.

Il faut cependant noter que, généralement dans les cas qui nous intéressent, le nombre de patients dans chacune de ces cohortes est relativement faible face au nombre de paramètres testés. Cela peut entraîner des faux positifs sur la valeur pronostique [55, 84]. Une attention particulière sera portée pour correctement tenir compte de ces tests multiples et du choix des seuils optimaux dans les analyses de survie. Dans la mesure du possible, une cohorte prospective de validation sera utilisée.

3.2.2 Réponse au traitement

Une approche originale, développée par le Dr Hatem Necib au cours de son doctorat [85], a été récemment employée sur une base de données de cancer du sein métastatique dans le but d'établir sa pertinence dans le contexte de la réponse au traitement à partir de séries d'images

TEP-FDG [86]. Nous prévoyons d'étendre cette méthodologie dans le champ de l'imagerie SPECT avec un appui technique de la société Dosisoft. Notre service développe en effet une activité de traitement chez les patients porteurs d'une tumeur endocrine gastro-entéro-pancréatique positive aux récepteurs à la somatostatine. Ces patients sont traités par 4 injections de ^{177}Lu-Octreotate espacées de 8 semaines. Il n'existe pas actuellement de moyen fiable d'évaluer la réponse précoce au traitement entre deux ou plusieurs cycles à l'aide des images SPECT/CT au ^{177}Lu-Octreotate enregistrées 24h après l'injection. Nous envisageons donc d'évaluer cette approche reposant sur l'analyse factorielle [87] afin de cartographier les évolutions de fixation au sein de la tumeur et d'en dériver une tendance sur la réponse au traitement. Ces conclusions seront confrontées au suivi clinique du patient par imagerie morphologique (critère RECIST1.1) ou fonctionnelle (imagerie au ^{68}Ga-DOTANOC) ; cette dernière étant déjà utilisée en routine dans notre service.

Il est également souvent difficile de procéder à la segmentation des lésions sur les examens TEP après traitement dans certaines hémopathies dans la mesure où les lésions sont parfois très difficilement discernables du bruit de fond loco-régional. Nous sommes actuellement en train de déployer une approche permettant de s'affranchir de ce problème dans la mesure où seule la segmentation de la lésion sur l'examen initial est requise. Cette méthode calcule une distance entre les histogrammes de la lésion avant et après traitement [88]. Il n'y a donc pas ici de notions de relations spatiales entre les voxels de la lésion mais l'ensemble des valeurs de SUV est prise en compte, a priori, plus finement que par comparaison de métrique plus classique comme la SUV_{mean} ou SUV_{peak}. Cette approche est en cours d'analyse sur la population IMAJEM.

3.2.3 Aide à la décision diagnostique à partir d'informations multiples

Avec, entre autres, la multiplication des métriques quantitatives (dont il faut s'assurer qu'elles ne sont pas corrélées entre elles), l'information disponible pour poser le diagnostic devient très importante. Une de nos ambitions est d'étudier le bénéfice d'utiliser des méthodes de classification automatique reposant sur des algorithmes tels que les réseaux neuronaux, l'approche "random forest", l'approche "support vector machine"... Ces méthodologies tirent parti des métriques extraites des images mais également de l'ensemble des informations cliniques disponibles au diagnostic. Quelques études très récentes [89, 90, 91], dont une sur les hémopaties [91], ont montré le potentiel de telles approches pour la caractérisation tumorale ou la valeur prédictive. Il apparaît très clairement que ce champ d'investigation devrait prendre à l'avenir une place grandissante afin de prédire et donc de sélectionner une thérapie adaptée au patient en tenant compte de toutes les données cliniques. Cependant, ces approches nécessitent une base de données pour l'apprentissage de l'algorithme et une autre pour sa validation avec dans les deux cas un nombre de patients suffisamment large. L'exploitation de données multicentriques ancillaires à des études cliniques sera alors nécessaire avec la difficulté de l'harmonisation des paramètres d'acquisition

et de reconstruction pour les métriques dérivées de l'imagerie fonctionnelle.

Nous envisageons d'aborder cette thématique à la faveur d'un rapprochement entre l'École Centrale de Nantes (notamment au travers de l'équipe SIMS du Laboratoire des Sciences du Numérique de Nantes) et le Centre Hospitalier Universitaire de Nantes. Les compétences développées à l'École Centrale de Nantes, en particulier sur les techniques d'apprentissage profond et le recrutement potentiel d'un enseignant chercheur à l'interface entre les deux institutions, devraient permettre de prendre en charge correctement cette thématique.

3.2.4 Imagerie multimodale

L'essor récent de l'imagerie multimodale simultanée TEP/IRM a ouvert des opportunités intéressantes de caractérisation tumorale [92, 93] et d'approches méthodologiques relatives à l'hétérogénéité tumorale [94] ou à la segmentation [95]. Bien que le bénéfice clinique réelle en oncologie d'examen simultané TEP/IRM ne soit pas encore pleinement établi [96, 97], il apparaît maintenant plus ou moins nettement qu'un des premiers apports significatifs se situerait dans le champ d'extraction de métriques multi-modales et multi-paramétriques [98].

Le Centre Hospitalier Universitaire de Nantes va accueillir prochainement un Centre d'Imagerie Multimodale Appliqué (CIMA) sous l'égide de l'équipe l'équipe Oncologie Nucléaire du CRCINA (INSERM U1232, Université de Nantes). Ce centre hébergera trois équipements dédiés à la recherche pré-clinique :

- un système TEP/TDM (Inveon, Siemens),
- le prototype XEMIS2 développé par le laboratoire Subatech
- un système TEP/IRM simultané

L'acquisition du système pré-clinique TEP/IRM va nous permettre d'explorer les approches multi-paramétriques dans le contexte de développement de nouveaux radiopharmaceutiques propres à notre équipe d'Oncologie Nucléaire (immuno-TEP). Il serait par exemple intéressant de mettre en rapport une mesure de cellularité par IRM avec un signal TEP d'un radiopharmaceutique spécifique développé par notre équipe dans le contexte du myélome multiple avec comme cible l'antigène CD138 (éventuellement avec des Affitins marquées au ^{89}Zr ou ^{64}Cu).

3.3 Vers un détecteur au xénon liquide clinique

Le détecteur au xénon liquide adapté à des expériences pré-cliniques (XEMIS2) va être installé dans les locaux du Centre Hospitalier Universitaire de Nantes en 2017 comme indiqué dans le paragraphe 3.2.4. A partir de ce moment, un travail important de caractérisation du détecteur en

terme de fonctionnement et de performances va être mené entre l'équipe de Subatech et l'équipe INSERM. Ce travail sera conduit jusqu'en 2018 où les premières images d'animaux injectés avec de très faibles activités de ^{44}Sc devraient être disponibles. Avant cette étape finale très importante pour XEMIS2, il sera nécessaire de continuer le développement de la reconstruction cône-LOR évoquée au paragraphe 2.4.2.

Les premiers résultats de caractérisation du détecteur devraient nous permettre de déduire certains paramètres utiles afin de simplifier la simulation du système tout en restant aussi proche que possible de son fonctionnement réel. Ces paramétrisations ouvriront en retour la voie de la simulation d'un système avec des dimensions adaptées à des acquisitions cliniques corps entier (champ de vue axial de 2m) à l'instar d'un projet développé par l'université de Californie à Davis [99]. Par ailleurs, l'excellente résolution en énergie du système (autour de 5% mesuré à 511 keV pour un champ de 1 kV/cm sur XEMIS1) associé au processus de reconstruction Compton devrait également permettre de conserver des événements avec de faibles angles de diffusion afin d'augmenter la sensibilité.

Bibliographie

[1] D. Lazaro, Z. El Bitar, V. Breton, D. Hill, and I. Buvat, "Fully 3D Monte Carlo reconstruction in SPECT: a feasibility study," *Phys Med Biol*, vol. 50, pp. 3739–54, 2005.

[2] S. Jan, G. Santin, D. Strul, S. Staelens, K. Assie, D. Autret, S. Avner, R. Barbier, M. Bardies, P. Bloomfield, D. Brasse, V. Breton, P. Bruyndonckx, I. Buvat, A. Chatziioannou, Y. Choi, Y. Chung, C. Comtat, D. Donnarieix, L. Ferrer, S. Glick, C. Groiselle, D. Guez, P. Honore, S. Kerhoas-Cavata, A. Kirov, V. Kohli, M. Koole, M. Krieguer, D. van der Laan, F. Lamare, G. Largeron, C. Lartizien, D. Lazaro, M. Maas, L. Maigne, F. Mayet, F. Melot, C. Merheb, E. Pennacchio, J. Perez, U. Pietrzyk, F. Rannou, M. Rey, D. Schaart, C. Schmidtlein, L. Simon, T. Song, J. Vieira, D. Visvikis, R. Van de Walle, E. Wieers, and C. Morel, "GATE: a simulation toolkit for PET and SPECT," *Phys Med Biol*, vol. 49, pp. 4543–4561, 2004.

[3] S. Jan, D. Benoit, E. Becheva, T. Carlier, F. Cassol, P. Descourt, T. Frisson, L. Grevillot, L. Guigues, L. Maigne, C. Morel, Y. Perrot, N. Rehfeld, D. Sarrut, D. Schaart, S. Stute, U. Pietrzyk, D. Visvikis, N. Zahra, and I. Buvat, "GATE V6: a major enhancement of the GATE simulation platform enabling modelling of CT and radiotherapy," *Phys Med Biol*, vol. 56, pp. 881–901, 2011.

[4] X. Song, W. Segars, Y. Du, B. Tsui, and E. Frey, "Fast modelling of the collimator-detector response in Monte Carlo simulation of SPECT imaging using the angular response function," *Phys Med Biol*, vol. 50, pp. 1791–804, 2005.

[5] T. Carlier, P. Descourt, L. Maigne, D. Visvikis, M. Bardies, and I. Buvat, "Efficient simulations of iodine 131 SPECT scans using gate," in *Nuclear Science Symposium Conference Record (NSS/MIC), 2009 IEEE*, pp. 3412–3414, 2009.

[6] P. Descourt, T. Carlier, Y. Du, X. Song, I. Buvat, E. Frey, M. Bardies, B. Tsui, and D. Visvikis, "Implementation of angular response function modeling in SPECT simulations with GATE," *Phys Med Biol*, vol. 55, pp. N253–266, 2010.

[7] B. He, Y. Du, X. Song, W. P. Segars, and E. Frey, "A Monte Carlo and physical phantom evaluation of quantitative In-111 SPECT," *Phys Med Biol*, vol. 50, pp. 4169–4185, 2005.

[8] W. Segars, J. Bond, J. Frush, S. Hon, C. Eckersley, C. Williams, J. Feng, D. Tward, J. Ratnanather, M. Miller, D. Frush, and E. Samei, "Population of anatomically variable 4D XCAT adult phantoms for imaging research and optimization," *Med Phys*, vol. 40, p. 043701, 2013.

[9] http://aapm.org/org/structure/default.asp?committee_code=TG211.

[10] G. El Fakhri, S. Surti, C. Trott, J. Scheuermann, and J. Karp, "Improvement in lesion detection with whole-body oncologic time-of-flight PET," *J Nucl Med*, vol. 52, pp. 347–353, 2011.

[11] S. Surti, J. Scheuermann, G. El Fakhri, M. Daube-Witherspoon, R. Lim, N. Abi-Hatem, E. Moussallem, F. Benard, D. Mankoff, and J. Karp, "Impact of time-of-flight PET on whole-body oncologic studies: a human observer lesion detection and localization study," *J Nucl Med*, vol. 52, pp. 712–719, 2011.

[12] P. Papadimitroulas, G. Loudos, A. Le Maitre, M. Hatt, F. Tixier, N. Efthimiou, G. Nikiforidis, D. Visvikis, and G. Kagadis, "Investigation of realistic PET simulations incorporating tumor patient's specificity using anthropomorphic models: creation of an oncology database," *Med Phys*, vol. 40, p. 112506, 2013.

[13] S. Stute, T. Carlier, K. Cristina, C. Noblet, A. Martineau, B. Hutton, L. Barnden, and I. Buvat, "Monte Carlo simulations of clinical PET and SPECT scans: impact of the input data on the simulated images," *Phys Med Biol*, vol. 56, pp. 6441–6457, 2011.

[14] F. Kraeber-Bodéré, C. Rousseau, C. Bodet-Milin, L. Ferrer, A. Faivre-Chauvet, L. Campion, J. Vuillez, A. Devillers, C. Chang, D. Goldenberg, J. Chatal, and J. Barbet, "Targeting, toxicity, and efficacy of 2-step, pretargeted radioimmunotherapy using a chimeric bispecific antibody and 131I-labeled bivalent hapten in a phase I optimization clinical trial," *J Nucl Med*, vol. 47, p. 247–255, 2006.

[15] M. Chérel, S. Gouard, J. Gaschet, C. Sai-Maurel, F. Bruchertseifer, A. Morgenstern, M. Bourgeois, J. F. Gestin, F. Kraeber-Bodéré, J. Barbet, P. Moreau, and F. Davodeau, "^{213}Bi radioimmunotherapy with an anti-mCD138 monoclonal antibody in a murine model of multiple myeloma," *J Nucl Med*, vol. 54, pp. 1597–1604, 2013.

[16] F. Haddad, L. Ferrer, A. Guertin, T. Carlier, N. Michel, J. Barbet, and J. Chatal, "ARRONAX, a high energy and high intensity cyclotron for nuclear medicine," *Eur J Nucl Med Mol Imaging*, vol. 35, pp. 1377–1387, 2008.

[17] L. Jødal, C. Le Loirec, and C. Champion, "Positron range in PET imaging: an alternative approach for assessing and correcting the blurring," *Phys Med Biol*, vol. 57, pp. 3931–3943, 2012.

[18] F. A. Kotasidis, G. Angelis, J. Anton-Rodriguez, J. Matthews, A. Reader, and H. Zaidi, "Isotope specific resolution recovery image reconstruction in high resolution PET imaging," *Med Phys*, vol. 41, p. 052503, 2014.

[19] R. Laforest and X. Liu, "Cascade removal and microPET imaging with 76Br," *Phys Med Biol*, vol. 54, pp. 1503–1531, 2009.

[20] C. Floyd, R. Jaszczak, K. Greer, and R. Coleman, "Inverse Monte Carlo as a unified reconstruction algorithm for ECT," *J Nucl Med*, vol. 27, pp. 1577–1585, 1986.

[21] L. Shepp and Y. Vardi, "Maximum likelihood reconstruction for emission tomography," *IEEE Trans Med Imaging.*, vol. MI-1, pp. 113–121, 1982.

[22] M. Moreau, I. Buvat, L. Ammour, N. Chouin, F. Kraeber-Bodéré, M. Chérel, and T. Carlier, "Assessment of a fully 3D Monte Carlo reconstruction method for preclinical PET with iodine-124," *Phys Med Biol*, vol. 60, no. 6, pp. 2475–2491, 2015.

[23] A. Autret, J. Bert, O. Strauss, and D. Visvikis, "Projector with realistic detector scatter modelling for PET list-mode reconstruction," in *Nuclear Science Symposium Conference Record (NSS/MIC), 2012 IEEE*, pp. 3333–3336, 2012.

[24] A. Autret, M. Moreau, T. Carlier, J. Bert, O. Strauss, and D. Visvikis, "Detector modeling in pet list-mode reconstruction: comparison between pre-calculated and on-the-fly computed system matrix," in *Proc International Meeting on Fully Three-Dimensional Image Reconstruction in Radiology and Nuclear Medicine*, 2015.

[25] A. Autret, M. Moreau, T. Carlier, J. Bert, O. Strauss, and D. Visvikis, "Detector modeling in pet list-mode reconstruction: Comparison between pre-calculated and on-the-fly computed system matrices," in *Nuclear Science Symposium Conference Record (NSS/MIC), 2015 IEEE*, 2015.

[26] F. Kraeber-Bodéré, C. Rousseau, C. Bodet-Milin, C. Mathieu, F. Guerard, E. Frampas, T. Carlier, N. Chouin, F. Haddad, J. Chatal, A. Faivre-Chauvet, M. Chérel, and J. Barbet, "Tumor immunotargeting using innovative radionuclides," *Int J Mol Sci*, vol. 16, pp. 3932–3954, 2015.

[27] F. Kraeber-Bodéré, C. Rousseau, C. Bodet-Milin, E. Frampas, A. Faivre-Chauvet, A. Rauscher, R. Sharkey, D. Goldenberg, J. Chatal, and J. Barbet, "A pretargeting system for tumor PET imaging and radioimmunotherapy," *Front Pharmacol*, vol. 6, p. 54, 2015.

[28] F. Kraeber-Bodéré, J. Barbet, and J. Chatal, "Radioimmunotherapy: From Current Clinical Success to Future Industrial Breakthrough ?," *J Nucl Med*, vol. 57, pp. 329–331, 2016.

[29] F. Kraeber-Bodéré, C. Bodet-Milin, C. Rousseau, T. Eugene, A. Pallardy, E. Frampas, T. Carlier, L. Ferrer, J. Gaschet, F. Davodeau, J. Gestin, A. Faivre-Chauvet, J. Barbet, and M. Chérel, "Radioimmunoconjugates for the treatment of cancer," *Semin Oncol*, vol. 41, no. 5, pp. 613–622, 2014.

[30] N. Anizan, T. Carlier, C. Hindorf, J. Barbet, and M. Bardies, "Acquisition setting optimization and quantitative imaging for 124I studies with the Inveon microPET-CT system," *EJNMMI Res*, vol. 2, p. 7, 2012.

[31] T. Carlier, K. P. Willowson, E. Fourkal, D. L. Bailey, M. Doss, and M. Conti, "(90)Y - PET imaging: Exploring limitations and accuracy under conditions of low counts and high random fraction," *Med Phys*, vol. 42, pp. 4295–4309, 2015.

[32] K. Ford, "Predicted 0+ level of Zr90," *Phys Rev*, vol. 98, p. 1516, 1955.

[33] R. Lhommel, P. Goffette, M. Van den Eynde, F. Jamar, S. Pauwels, J. I. Bilbao, and S. Walrand, "Yttrium-90 TOF PET scan demonstrates high-resolution biodistribution after liver SIRT," *Eur J Nucl Med Mol Imaging*, vol. 36, p. 1696, 2009.

[34] R. Lhommel, L. van Elmbt, P. Goffette, M. Van den Eynde, F. Jamar, S. Pauwels, and S. Walrand, "Feasibility of 90Y TOF PET-based dosimetry in liver metastasis therapy using SIR-Spheres," *Eur J Nucl Med Mol Imaging*, vol. 37, pp. 1654–1662, 2010.

[35] V. L. Gates, A. A. Esmail, K. Marshall, S. Spies, and R. Salem, "Internal pair production of 90Y permits hepatic localization of microspheres using routine PET: proof of concept," *J Nucl Med*, vol. 52, pp. 72–76, 2011.

[36] T. Carlier, T. Eugene, C. Bodet-Milin, E. Garin, C. Ansquer, C. Rousseau, L. Ferrer, J. Barbet, F. Schoenahl, and F. Kraeber-Bodéré, "Assessment of acquisition protocols for routine imaging of Y-90 using PET/CT," *EJNMMI Res*, vol. 3, p. 11, 2013.

[37] J. Strydhorst, T. Carlier, M. Conti, A. Dieudonné, and I. Buvat, "A GATE evaluation of the sources of error in quantitative ^{90}Y PET," *Med Phys*, in press.

[38] A. K. Arveschoug, H. Bertelsen, and B. Vammen, "Presurgical localization of abnormal parathyroid glands using a single injection of Tc-99m sestamibi: comparison of high-resolution parallel-hole and pinhole collimators, and interobserver and intraobserver variation," *Clin Nucl Med*, vol. 27, pp. 249–254, 2002.

[39] W. P. Kluijfhout, W. M. Vorselaars, M. R. Vriens, I. H. Borel Rinkes, G. D. Valk, and B. de Keizer, "Enabling minimal invasive parathyroidectomy for patients with primary hyperparathyroidism using Tc-99m-sestamibi SPECT-CT, ultrasound and first results of (18)F-fluorocholine PET-CT," *Eur J Radiol*, vol. 84, pp. 1745–1751, 2015.

[40] A. Seret, M. Defrise, and D. Blocklet, "180 degree pinhole SPET with a tilted detector and OS-EM reconstruction: phantom studies and potential clinical applications," *Eur J Nucl Med*, vol. 28, pp. 1836–1841, 2001.

[41] C. Vanhove, M. Defrise, P. R. Franken, H. Everaert, F. Deconinck, and A. Bossuyt, "Interest of the ordered subsets expectation maximization (OS-EM) algorithm in pinhole single-photon emission tomography reconstruction: a phantom study," *Eur J Nucl Med*, vol. 27, pp. 140–146, 2000.

[42] T. Carlier, A. Oudoux, E. Mirallié, A. Seret, I. Daumy, C. Leux, C. Bodet-Milin, F. Kraeber-Bodéré, and C. Ansquer, "99mTc-MIBI pinhole SPECT in primary hyperparathyroidism : comparison with conventional SPECT, planar scintigraphy and ultrasonography," *Eur J Nucl Med Mol Imaging*, vol. 35, pp. 637–643, 2008.

[43] C. C. Watson, M. E. Casey, B. Bendriem, J. P. Carney, D. W. Townsend, S. Eberl, S. Meikle, and F. P. Difilippo, "Optimizing injected dose in clinical PET by accurately modeling the counting-rate response functions specific to individual patient scans," *J Nucl Med*, vol. 46, pp. 1825–1834, 2005.

[44] C. C. Watson, "Count rate dependence of local signal-to-noise ratio in positron emission tomography," *IEEE Trans Nucl Sci*, vol. 51, pp. 2670–2680, 2004.

[45] T. Carlier, L. Ferrer, H. Necib, C. Bodet-Milin, C. Rousseau, and F. Kraeber-Bodere, "Clinical NECR in 18F-FDG PET scans : optimization of injected activity and variable acquisition time. Relationship with SNR," *Phys Med Biol*, vol. 59, pp. 6417–6430, 2014.

[46] M. Soussan, F. Orlhac, M. Boubaya, L. Zelek, M. Ziol, V. Eder, and I. Buvat, "Relationship between tumor heterogeneity measured on FDG-PET/CT and pathological prognostic factors in invasive breast cancer," *PLoS ONE*, vol. 9, p. e94017, 2014.

[47] F. Tixier, C. C. Le Rest, M. Hatt, N. Albarghach, O. Pradier, J. P. Metges, L. Corcos, and D. Visvikis, "Intratumor heterogeneity characterized by textural features on baseline 18F-FDG PET images predicts response to concomitant radiochemotherapy in esophageal cancer," *J Nucl Med*, vol. 52, pp. 369–378, 2011.

[48] M. Hatt, M. Majdoub, M. Vallieres, F. Tixier, C. C. Le Rest, D. Groheux, E. Hindie, A. Martineau, O. Pradier, R. Hustinx, R. Perdrisot, R. Guillevin, I. El Naqa, and D. Visvikis, "18F-FDG PET uptake characterization through texture analysis : investigating the complementary nature of heterogeneity and functional tumor volume in a multi-cancer site patient cohort," *J Nucl Med*, vol. 56, pp. 38–44, 2015.

[49] N. M. Cheng, Y. H. Fang, L. Y. Lee, J. T. Chang, D. L. Tsan, S. H. Ng, H. M. Wang, C. T. Liao, L. Y. Yang, C. H. Hsu, and T. C. Yen, "Zone-size nonuniformity of 18F-FDG PET regional textural features predicts survival in patients with oropharyngeal cancer," *Eur J Nucl Med Mol Imaging*, vol. 42, pp. 419–428, 2015.

[50] J. S. Oh, B. C. Kang, J. L. Roh, J. S. Kim, K. J. Cho, S. W. Lee, S. B. Kim, S. H. Choi, S. Y. Nam, and S. Y. Kim, "Intratumor Textural Heterogeneity on Pretreatment (18)F-FDG PET Images Predicts Response and Survival After Chemoradiotherapy for Hypopharyngeal Cancer," *Ann Surg Oncol*, vol. 22, pp. 2746–2754, 2015.

[51] W. Mu, Z. Chen, Y. Liang, W. Shen, F. Yang, R. Dai, N. Wu, and J. Tian, "Staging of cervical cancer based on tumor heterogeneity characterized by texture features on (18)F-FDG PET images," *Phys Med Biol*, vol. 60, pp. 5123–5139, 2015.

[52] T. Pyka, R. A. Bundschuh, N. Andratschke, B. Mayer, H. M. Specht, L. Papp, N. Zsoter, and M. Essler, "Textural features in pre-treatment [F18]-FDG-PET/CT are correlated with risk of local recurrence and disease-specific survival in early stage NSCLC patients receiving primary stereotactic radiation therapy," *Radiat Oncol*, vol. 10, p. 100, 2015.

[53] F. Tixier, M. Hatt, C. Valla, V. Fleury, C. Lamour, S. Ezzouhri, P. Ingrand, R. Perdrisot, D. Visvikis, and C. C. Le Rest, "Visual versus quantitative assessment of intratumor 18F-FDG PET uptake heterogeneity : prognostic value in non-small cell lung cancer," *J Nucl Med*, vol. 55, pp. 1235–1241, 2014.

[54] M. Hatt, F. Tixier, L. Pierce, P. E. Kinahan, C. C. Le Rest, and D. Visvikis, "Characterization of PET/CT images using texture analysis : the past, the present... any future ?," *Eur J Nucl Med Mol Imaging*, in press.

[55] S. S. Yip and H. J. Aerts, "Applications and limitations of radiomics," *Phys Med Biol*, vol. 61, pp. R150–166, 2016.

[56] F. Orlhac, M. Soussan, J. A. Maisonobe, C. A. Garcia, B. Vanderlinden, and I. Buvat, "Tumor texture analysis in 18F-FDG PET : relationships between texture parameters, histogram indices, standardized uptake values, metabolic volumes, and total lesion glycolysis," *J Nucl Med*, vol. 55, pp. 414–422, 2014.

[57] C. Bailly, M. Hatt, S. Le Gouill, F. Kraeber-Bodéré, D. Visvikis, C. Bodet-Milin, and T. Carlier, "Etude de la robustesse des paramÃ¨tres d'hÃ©tÃ©rogÃ©nÃ©itÃ© en TEP-FDG des lymphomes du manteau inclus dans l'Ã©tude LyMa," *Médecine Nucléaire*, pp. 297–306, 2016.

[58] J. Yan, J. L. Chu-Shern, H. Y. Loi, L. K. Khor, A. K. Sinha, S. T. Quek, I. W. Tham, and D. Townsend, "Impact of Image Reconstruction Settings on Texture Features in 18F-FDG PET," *J Nucl Med*, vol. 56, pp. 1667–1673, 2015.

[59] C. Bailly, C. Bodet-Milin, S. Couespel, H. Necib, F. Kraeber-Bodéré, C. Ansquer, and T. Carlier, "Revisiting the robustness of PET-based textural features in the context of multi-centric trials," *PLoS ONE*, vol. 11, p. e0159984, 2016.

[60] C. Curtet, T. Carlier, E. Mirallie, C. Bodet-Milin, C. Rousseau, J. Barbet, and F. Kraeber-Bodere, "Prospective comparison of two gamma probes for intraoperative detection of 18F-FDG: in vitro assessment and clinical evaluation in differentiated thyroid cancer patients with iodine-negative recurrence," *Eur J Nucl Med Mol Imaging*, vol. 34, pp. 1556–1562, 2007.

[61] L. Lavoie, "Liquid xenon scintillators for imaging of positron emitters," *Med Phys*, vol. 3, pp. 283–293, 1976.

[62] V. Chepel, "A new liquid xenon scintillation detector for positron emission tomography," *Nucl Tracks Radiat Meas*, vol. 21, pp. 47–51, 1993.

[63] L. Gallego Manzano, S. Bassetto, N. Beaupère, P. Briend, T. Carlier, M. Chérel, J. Cussonneau, J. Donnard, M. Gorski, R. Hamanishi, F. Kraeber-Bodéré, P. Le Ray, O. Lemaire, J. Masbou, S. Mihara, E. Morteau, L. Scotto Lavina, J. Stutzmann, T. Tauchi, and D. Thers, "XEMIS: A liquid xenon detector for medical imaging," *Nucl Instr Meth Physics Research A*, vol. 787, pp. 89–93, 2015.

[64] O. Bagni, L. Filippi, and O. Schillaci, "18F-FDG PET-derived parameters as prognostic indices in hepatic malignancies after 90Y radioembolization : is there a role ?," *Eur J Nucl Med Mol Imaging*, vol. 42, pp. 367–369, 2015.

[65] J. Nuyts, S. Stroobants, P. Dupont, S. Vleugels, P. Flamen, and L. Mortelmans, "Reducing loss of image quality because of the attenuation artifact in uncorrected PET whole-body images," *J Nucl Med*, vol. 43, pp. 1054–1062, 2002.

[66] C. Byrne, "Iterative algorithms for deblurring and deconvolution with constraints," *Inverse Problem*, vol. 14, pp. 1455–1467, 1998.

[67] K. Van Slambrouck, S. Stute, C. Comtat, M. Sibomana, F. H. van Velden, R. Boellaard, and J. Nuyts, "Bias reduction for low-statistics PET : maximum likelihood reconstruction with a modified Poisson distribution," *IEEE Trans Med Imaging*, vol. 34, pp. 126–136, 2015.

[68] http://castor-project.org/.

[69] T. Merlin, S. Stute, D. Benoit, J. Bert, T. Carlier, C. Comtat, F. Lamare, and D. Visvikis, "CASToR: a generic data organization and processing code framework for multi-modal and multi-dimensional tomographic reconstruction," in *Nuclear Science Symposium Conference Record (NSS/MIC), 2016 IEEE*, accepted.

[70] A. S. Pasciak, A. C. Bourgeois, and Y. C. Bradley, "A microdosimetric analysis of absorbed dose to tumor as a function of number of microspheres per unit volume in 90Y radioembolization," *J Nucl Med*, vol. 57, pp. 1020–1026, 2016.

[71] A. F. van den Hoven, C. E. Rosenbaum, S. G. Elias, H. W. de Jong, M. Koopman, H. M. Verkooijen, A. Alavi, M. A. van den Bosch, and M. G. Lam, "Insights into the dose-response relationship of radioembolization with resin 90Y-microspheres: a prospective cohort study in patients with colorectal cancer liver metastases," *J Nucl Med*, vol. 57, pp. 1014–1019, 2016.

[72] M. Sanchez-Garcia, J. Strydhorst, H. Levillain, I. Gardin, P. Buyssens, T. Carlier, R. Lebtahi, I. Buvat, and A. Dieudonné, "Partial volume effect and noise compensation of dose-volume histograms for Y90-PET based dosimetry by means of region sub-segmentation," in *Nuclear Science Symposium Conference Record (NSS/MIC), 2016 IEEE*, accepted.

[73] R. L. Wahl, H. Jacene, Y. Kasamon, and M. A. Lodge, "From RECIST to PERCIST: evolving considerations for PET response criteria in solid tumors," *J Nucl Med*, vol. 50 Suppl 1, pp. 122S–150S, 2009.

[74] L. Filippi, G. Pelle, R. Cianni, F. Scopinaro, and O. Bagni, "Change in total lesion glycolysis and clinical outcome after (90)Y radioembolization in intrahepatic cholangiocarcinoma," *Nucl Med Biol.*, vol. 42, pp. 59–64, 2015.

[75] A. Sabet, C. Meyer, A. Aouf, A. Sabet, S. Ghamari, C. C. Pieper, K. Mayer, H. J. Biersack, and S. Ezziddin, "Early post-treatment FDG PET predicts survival after 90Y microsphere radioembolization in liver-dominant metastatic colorectal cancer," *Eur J Nucl Med Mol Imaging*, vol. 42, pp. 370–376, 2015.

[76] T. Carlier and C. Bailly, "State-of-the-art and recent advances in quantification for therapeutic follow-up in oncology using PET," *Front Med (Lausanne)*, vol. 2, p. 18, 2015.

[77] R. Haralick, K. Shanmugam, and I. Dinstein, "Textural features for image classification," *IEEE Trans Syst Man Cybern*, vol. SMC-3, pp. 610–621, 1973.

[78] G. Thibault, B. Fertil, C. Navarro, S. Pereira, P. Cau, N. Levy, J. Sequeira, and J. Mari, "Shape and texture indexes application to cell nuclei classification," *Int J Pattern Recognit Artif Intell*, vol. 27, p. 1357002, 2013.

[79] A. Laine and J. Fan, "Texture classification by wavelet packet signatures," *IEEE Trans Pattern Anal Mach Intell*, vol. 15, pp. 1186–1191, 1993.

[80] C. Bailly, L. Campion, E. Thebaud, N. Corradini, A. Moreau, D. Dansette, F. Kraeber-Bodéré, C. Bodet-Milin, and T. Carlier, "Prognosis value of SUV-based metrics, textural and shape features derived from initial FDG-PET in paediatric patients with Ewing sarcoma and osteosarcoma.," in *Eur J Nucl Med Mol Imaging [abstracts]*, accepted.

[81] F. Brooks and P. Grigsby, "Low-order non-spatial effects dominate second-order spatial effects in the texture quantifier analysis of 18F-FDG-PET images," *PLoS ONE*, vol. 10, p. e0116574, 2015.

[82] P. Wang, W. Xu, J. Sun, C. Yang, G. Wang, Y. Sa, X. H. Hu, and Y. Feng, "A new assessment model for tumor heterogeneity analysis with [18]F-FDG PET images," *EXCLI J*, vol. 15, pp. 75–84, 2016.

[83] A. Rahmim, C. R. Schmidtlein, A. Jackson, S. Sheikhbahaei, C. Marcus, S. Ashrafinia, M. Soltani, and R. M. Subramaniam, "A novel metric for quantification of homogeneous and heterogeneous tumors in PET for enhanced clinical outcome prediction," *Phys Med Biol*, vol. 61, pp. 227–242, 2016.

[84] A. Chalkidou, M. J. O'Doherty, and P. K. Marsden, "False discovery rates in PET and CT studies with texture features: a systematic review," *PLoS ONE*, vol. 10, p. e0124165, 2015.

[85] A. Necib, *Caractérisation de l'évolution tumorale au cours d'une thérapie au moyen d'examens TEP/TDM*. PhD thesis, Université Paris-sud XI, 2010.

[86] D. Goulon, H. Necib, B. Henaff, C. Rousseau, T. Carlier, and F. Kraeber-Bodere, "Quantitative evaluation of therapeutic response by FDG-PET-CT in metastatic breast cancer," *Front Med (Lausanne)*, vol. 3, p. 19, 2016.

[87] H. Benali, I. Buvat, F. Frouin, J. Bazin, and R. Di Paola, "Information processing in medical imaging foundations of factor analysis of medical image sequences: a unified approach and some practical implications," *Image Vision Comput*, vol. 12, pp. 375–385, 1994.

[88] S. Tan, H. Zhang, Y. Zhang, W. Chen, W. D. D'Souza, and W. Lu, "Predicting pathologic tumor response to chemoradiotherapy with histogram distances characterizing longitudinal changes in 18F-FDG uptake patterns," *Med Phys*, vol. 40, p. 101707, 2013.

[89] C. Parmar, P. Grossmann, J. Bussink, P. Lambin, and H. J. Aerts, "Machine learning methods for quantitative radiomic biomarkers," *Sci Rep*, vol. 5, p. 13087, 2015.

[90] H. Zhang, S. Tan, W. Chen, S. Kligerman, G. Kim, W. D. D'Souza, M. Suntharalingam, and W. Lu, "Modeling pathologic response of esophageal cancer to chemoradiation therapy using spatial-temporal 18F-FDG PET features, clinical parameters, and demographics," *Int J Radiat Oncol Biol Phys*, vol. 88, pp. 195–203, 2014.

[91] C. Lartizien, M. Rogez, E. Niaf, and F. Ricard, "Computer-aided staging of lymphoma patients with FDG PET/CT imaging based on textural information," *IEEE J Biomed Health Inform*, vol. 18, pp. 946–955, 2014.

[92] O. M. Henriksen, V. A. Larsen, A. Muhic, A. E. Hansen, H. B. Larsson, H. S. Poulsen, and I. Law, "Simultaneous evaluation of brain tumour metabolism, structure and blood volume using [(18)F]-fluoroethyltyrosine (FET) PET/MRI : feasibility, agreement and initial experience," *Eur J Nucl Med Mol Imaging*, vol. 43, pp. 103–112, 2016.

[93] S. Leibfarth, U. Simoncic, D. Monnich, S. Welz, H. Schmidt, N. Schwenzer, D. Zips, and D. Thorwarth, "Analysis of pairwise correlations in multi-parametric PET/MR data for biological tumor characterization and treatment individualization strategies," *Eur J Nucl Med Mol Imaging*, vol. 43, pp. 1199–1208, 2016.

[94] M. Vallières, C. R. Freeman, S. R. Skamene, and I. El Naqa, "A radiomics model from joint FDG-PET and MRI texture features for the prediction of lung metastases in soft-tissue sarcomas of the extremities," *Phys Med Biol*, vol. 60, pp. 5471–5496, 2015.

[95] S. Leibfarth, F. Eckert, S. Welz, C. Siegel, H. Schmidt, N. Schwenzer, D. Zips, and D. Thorwarth, "Automatic delineation of tumor volumes by co-segmentation of combined PET/MR data," *Phys Med Biol*, vol. 60, pp. 5399–5412, Jul 2015.

[96] L. Mansi and A. Ciarmiello, "Perspectives on PET/MR imaging: are we ready for clinical use?," *J Nucl Med*, vol. 55, pp. 529–530, 2014.

[97] H. Sotoudeh, A. Sharma, K. J. Fowler, J. McConathy, and F. Dehdashti, "Clinical application of PET/MRI in oncology," *J Magn Reson Imaging*, vol. 44, pp. 265–276, 2016.

[98] D. L. Bailey, B. J. Pichler, B. Guckel, H. Barthel, A. J. Beer, J. Bremerich, J. Czernin, A. Drzezga, C. Franzius, V. Goh, M. Hartenbach, H. Iida, A. Kjaer, C. la Fougere, C. N.

Ladefoged, I. Law, K. Nikolaou, H. H. Quick, O. Sabri, J. Schafer, M. Schafers, H. F. Wehrl, and T. Beyer, "Combined PET/MRI: multi-modality multi-parametric imaging is here: summary report of the 4th international workshop on PET/MR imaging; february 23-27, 2015, Tübingen, Germany," *Mol Imaging Biol*, vol. 17, pp. 595–608, 2015.

[99] http://explorer.ucdavis.edu/.

Annexe A

A.1 Actes de colloques internationaux avec comité de lecture

1. T. Merlin, S. Stute, D. Benoit, J. Bert, **T. Carlier**, C. Comtat, F. Lamare, D. Visvikis, CASToR: evaluation of an efficient generic data organization and processing code framework for multi-modal and multi-dimensional tomographic teconstruction, *Proc International Meeting on Fully Three-Dimensional Image Reconstruction in Radiology and Nuclear Medicine*, (2017) accepted

2. L. Virone, N. Beaupère, P. Briend, J. Butterworth, **T. Carlier**, M. Chérel, J.P. Cussonneau, L. Gallego, P. Le Ray, J. Masbou, E. Morteau, M. Staempflin, J.S. Stutzmann, D. Thers, New cryogenic processes implemented for 3γ imaging with liquid xenon, *Proceedings of the 14th Cryogenis IIR International Conference*, (2017) accepted

3. L. Gallego Manzano, S. Acounis, S. Bassetto, S. Bouvier, N. Beaupere, J. Butterworth, **T. Carlier**, J.P. Cussonneau, P. Le Ray, F. Lefevre, O. Lemaire, J. Masbou, E. Morteau, L. Scotto Lavina, M. Staempflin, J.S Stutzmann, L. Virone, D. Thers, Low dose 3γ medical imaging for small animals with the XEMIS2 single-phase liquid xenon Compton Camera, *Proc IEEE Nuclear Science Symp Medical Imaging Conf*, (2016) accepted

4. T. Merlin, S. Stute, D. Benoit, J. Bert, **T. Carlier**, C. Comtat, F. Lamare, D. Visvikis, CASToR: a generic data organization and processing code framework for multi-modal and multi-dimensional tomographic reconstruction, *Proc IEEE Nuclear Science Symp Medical Imaging Conf*, (2016) accepted

5. M. Sanchez-Garcia, J. Strydhorst, H. Levillain, I. Gardin, P. Buyssens, **T. Carlier**, R. Lebtahi, I. Buvat, A. Dieudonné, Partial volume effect and noise compensation of dose-volume histograms for Y90-PET based dosimetry by means of region sub-segmentation,

Proc IEEE Nuclear Science Symp Medical Imaging Conf, (2016) accepted

6. J. Strydhorst, **T. Carlier**, A. Dieudonné, I. Buvat, Evaluation of the random fraction contribution to error in quantitative Y-90 PET, *Proc IEEE Nuclear Science Symp Medical Imaging Conf*, (2015) accepted

7. A. Autret, M. Moreau, **T. Carlier**, J. Bert, O. Strauss, D. Visvikis, Detector modeling in PET list-mode reconstruction: comparison between pre-calculated and on-the-fly computed system matrix, *Proc International Meeting on Fully Three-Dimensional Image Reconstruction in Radiology and Nuclear Medicine*, (2015) accepted

8. A. Autret, M. Moreau, **T. Carlier**, J. Bert, O. Strauss, D. Visvikis, Detector Modeling in PET List-Mode Reconstruction: Comparison Between Pre-Calculated and On-the-Fly Computed System Matrices, *Proc IEEE Nuclear Science Symp Medical Imaging Conf*, (2015) accepted

9. L. Gallego Manzano, S. Acounis, S. Bassetto, S. Bouvier, N. Beaupere, P. Briend, **T. Carlier**, M. Cherel, J.P. Cussonneau, R. Hamanishi, F. Kraeber-Bodéré, P. Le Ray, F. Lefevre, O. Lemaire, S. Manen, J. Masbou, H. Matez, S. Mihara, E. Morteau, D. Roy, L. Royer, L. Scotto Lavina, M. Staempflin, J.S. Stutzmann, T. Tauchi, L. Virone, D. Thers, 3γ imaging with liquid xenon: from XEMIS1 to XEMIS2, *Proc IEEE Nuclear Science Symp Medical Imaging Conf*, (2015) accepted

10. M. Conti, V. Panin, I. Hong, **T. Carlier**, K. Parodi, Monitoring hadron and Y90 therapies: PET reconstruction at extremely low counts, *Proc IEEE Nuclear Science Symp Medical Imaging Conf*, (2015) accepted

11. J. Masbou, J.P. Cussonneau, J. Donnard, L. Gallego-Manzano, P. Le Ray, A.F.M. Hadi, E. Morteau, L. Scotto Lavina, J.S. Stutzmann, D.Thers, S. Bassetto, P. Briend, M. Gorski, N. Beaupère, **T. Carlier**, M. Chérel, F. Kraeber-Bodéré, XEMIS: A new Compton camera with liquide xenon, *Proceedings of the 18th IEEE International Conference on Dielectric Liquids* (2014) 1-4

12. **T. Carlier**, L. Ferrer, H. Necib, C. Bodet-Milin, C. Rousseau, F. Kraeber-Bodéré, Clinical NECR in 18F-FDG PET Scans: Optimization of Patient Specific Activity and Variable Acquisition Time. Relationship with SNR, *Proc IEEE Nuclear Science Symp Medical Imaging Conf*, (2013) 1-4

13. **T. Carlier**, P. Descourt, L. Maigne, D. Visvikis, M. Bardiès, I. Buvat, Efficient simulations of iodine 131 SPECT scans using GATE, *Proc IEEE Nuclear Science Symp Medical Imaging Conf*, (2009) 3412-14

14. **T. Carlier**, L. Ferrer, J.B. Berruchon, R. Cuissard, A. Martineau, P. Loonis, O. Couturier, Quality controls for gamma-cameras and PET cameras: development of a free open-source ImageJ program, *Proc. SPIE* **5745** (2005) 1237-1246

15. C. Grignon, A. Breskin, **T. Carlier**, O. Couturier, J.P. Cussonneau, L. Ferrer, L. Luquin, V. Métivier, V. Peskov, F. Pheron, N. Servagent, D. Thers, A. Vasseur, Simulation of a high performance γ-camera concept for PET based on liquid xenon and gaseous photomultiplier, *Proceedings of the 15th IEEE International Conference on Dielectric Liquids* (2005) 357-360

A.2 Communications orales internationales avec comité de lecture

1. C. Bailly, **T. Carlier**, M. Meignan, F. Kraeber-Bodéré, S. Le Gouill, C. Bodet-Milin, Prognosis value of FDG-PET Parameters at Diagnosis and after Induction in Patients with Mantle Cell Lymphoma, Interim Results from the LyMa-PET Project, a LYSA study, [abstract] *Eur. J. Nucl. Med. Mol. Imaging*, **43** (2016) S202

2. **T. Carlier**, C. Bailly, M. Hatt, F. Kraeber-Bodéré, D. Visvikis, S. Le Gouill, C. Bodet-Milin, Quantification of intratumor heterogeneity derived from baseline FDG PET/CT in untreated mantle cell lymphoma patients enrolled in a prospective phase III trial of the LYSA group: preliminary results, [abstract] *J. Nucl. Med. Meeting Abstracts*, **56** (2015) 429

3. C. Bodet-Milin, C. Bailly, M. Meignan, A. Beriollo-Riedinger, A. Devillers, O. Hermine, **T. Carlier**, M. Hatt, F. Kraeber-Bodéré, S. Le Gouill, Prognosis value of quantitative indices derived from initial FDG PET/CT in untreated mantle cell lymphoma patients enrolled in the Lyma trial, a LYSA study. Preliminary results, [abstract] *J. Nucl. Med. Meeting Abstracts*, **56** (2015) 659

4. B. Jamet, **T. Carlier**, E. Bompas, M. Colombié, D. Rusu, D. Goulon, V. Fleury, F. Kraeber-Bodéré, C. Rousseau, Initial FDG PET/CT predicts survival in adults ewing sarcoma family of tumors, [abstract] *Eur. J. Nucl. Med. Mol. Imaging*, **42** (2015) S188

5. C. Bodet-Milin, C. Bailly, M. Meignan, A. Beriollo-Riedinger, R. Casasnovas, A. Devillers, T. Lamy, M. Santiago-Ribeiro, E. Gyan, C. Gallazzini-Crepin, R. Gressin, **T. Carlier**, F. Kraeber-Bodéré, O. Hermine, S. Le Gouill, Predictive power of FDG-PET parameters at diagnosis and after induction in patients with mantle cell lymphoma, interim results from the LyMa-PET project, conducted on behalf of the Lysa group, [abstract] *Blood*, **126** (2015) 335

6. **T. Carlier**, L. Lechippey, A. Rauscher, A. Faivre-Chauvet, C. Mathieu, D. Rusu, O. Couturier, C. Ansquer, Impact of time acquisition and delay on quantitative results of 68Ga-DOTANOC PET/CT in neuroendocrine tumors: A preliminary basic investigation, *Nuclear Technologies for Health Symposium* (2015)

7. C. Mathieu, L. Ferrer, **T. Carlier**, M. Colombié, D. Rusu, F. Kraeber-Bodéré, L. Campion, C. Rousseau, Assessment of lymph nodes and prostate status with early dynamic curves PET/CT 18F-choline (FCH) in prostate cancer, *Nuclear Technologies for Health Symposium* (2015)

8. D. Rusu, **T. Carlier**, L. Campion, M. Colombié, D. Goulon, F. Kraeber-Bodéré, C. Rousseau, Clinical impact and prognostic value of FDG PET/CT in suspected recurrence ovarian cancer patients. Results and clinical implications after 6 years follow-up, *Nuclear Technologies for Health Symposium* (2015)

9. C. Bodet-Milin, C. Rousseau, L. Rbah-Vidal, A. Rauscher, D. Masson, A. Faivre-Chauvet, P. Baumgartner, **T. Carlier**, L. Ferrer, D.M. Goldenberg, R.M. Sharkey, F. Kraeber-Bodéré, J. Barbet, Pharmacokinetic modelling and optimization of pretargeting using anti-carcinoembryonic antigen (CEA) bispecific antibody and 68Ga-, 111In- or 177Lu-labeled peptide in CEA-positive tumour patients, *Nuclear Technologies for Health Symposium* (2015)

10. C. Bodet-Milin, L. Ferrer, A. Rauscher, **T. Carlier**, A. Faivre-Chauvet, C. Rousseau, J. Hureaux, O. Couturier, P.Y. Salaun, D.M. Goldenberg, R.M. Sharkey, J. Barbet, F. Kraeber-Bodéré, 111In-labelled images predict 177Lu-IMP288 distribution and estimate absorbed doses in patients with CEA-expressing relapsing lung cancer included in a prospective pretargeted radioimmunotherapy (PRAIT) phase I/II optimization study using anti-CEA x anti-HSG TF2 Bispecific Antibody (bsMAb) and 177Lu-IMP-288 peptide: Preliminary results of the dosimetric study, *Nuclear Technologies for Health Symposium* (2015)

11. M. Moreau, N. Chouin, F. Kraeber-Bodéré, M. Chérel, **T. Carlier**, Assessment of a fully 3D Monte Carlo reconstruction method for preclinical PET with Iodine-124 in heterogeneous media, [abstract] *J. Nucl. Med. Meeting Abstracts*, **55** (2014) 373

12. D. Rusu, **T. Carlier**, L. Campion, M. Colombié, D. Goulon, F. Kraeber-Bodéré, C. Rousseau, Clinical impact and prognostic value of FDG PET/CT in suspected recurrence ovarian cancer patients. Results and clinical implications after 6 years follow up, [abstract] *Eur. J. Nucl. Med. Mol. Imaging*, **41** (2014) S201

13. L. Ferrer, T. Eugène, **T. Carlier**, P. Chevalier, N. Varmenot, W.A. Wegener, D.M. Goldenberg, F. Kraeber-Bodéré, Absorbed doses estimations for patients with B-acute lymphoblastic leukaemia treated by radioimmunotherapy with 90Y-epratuzumab tetraxetan, [abstract] *Eur. J. Nucl. Med. Mol. Imaging*, **41** (2014) S141

14. C. Rousseau, A. Faivre-Chauvet, A. Rauscher, **T. Carlier**, L. Ferrer, P. Baumgartner, C. Bodet-Milin, D.M. Goldenberg, R.M. Sharkey, J. Barbet, F. Kraeber-Bodéré, Feasibility of pretargeted immuno-PET using an anti-CEA bispecific antibody and a 68Ga-labeled hapten-peptide in metastatic breast patients (BC): preliminary results, [abstract] *Eur. J. Nucl. Med. Mol. Imaging*, **41** (2014) S226

15. C. Rousseau, M. Campone, A. Rauscher, A. Faivre-Chauvet, **T. Carlier**, L. Ferrer, P. Baumgartner, C. Bodet-Milin, D.M. Goldenberg, R.M. Sharkey, J. Barbet, Pretargeted immuno-PET with an anti-carcinoembryonic antigen (CEA) bispecific antibody and a 68Ga-labeled hapten-peptide compared to conventional imaging and FDG-PET in metastatic breast cancer patients (BC): preliminary results, [abstract] *Eur. J. Nucl. Med. Mol. Imaging*, **41** (2014) S226

16. C. Bodet-Milin, C. Rousseau, C. Ansquer, A. Faivre-Chauvet, A. Rauscher, **T. Carlier**, L. Ferrer, D. Masson, V. Rohmer, O. Couturier, D. Drui, D.M. Goldenberg, R.M. Sharkey, J. Barbet, F. Kraeber-Bodéré, Pretargeted immuno-PET using anti-carcinoembryonic antigen (CEA) bispecific antibody and 68Ga-labeled peptide in metastatic medullary thyroid carcinoma (MTC) patients: preliminary results of an optimization clinical study, [abstract] *Eur. J. Nucl. Med. Mol. Imaging*, **41** (2014) S315

17. C. Bodet-Milin, C. Rousseau, C. Ansquer, A. Faivre-Chauvet, A. Rauscher, **T. Carlier**, L. Ferrer, D. Masson, V. Rohmer, O. Couturier, D. Drui, D.M. Goldenberg, R.M. Sharkey, J. Barbet, F. Kraeber-Bodéré, High sensitivity of pretargeted immuno-PET using anti-carcinoembryonic antigen (CEA) bispecific antibody and 68Ga-labeled peptide in metastatic medullary thyroid carcinoma (MTC) patients, [abstract] *Eur. J. Nucl. Med. Mol. Imaging*, **41** (2014) S314

18. M. Moreau, N. Chouin, F. Kraeber-Bodéré, M. Chérel, **T. Carlier**, Development of a fully 3D Monte Carlo Reconstruction method for Preclinical PET with Iodine-124 (ReS_PET): efficiency in heterogeneous media, *Nuclear Technologies for Health Symposium* (2014)

19. L. Ferrer, T. Eugene, N. Varmenot, **T. Carlier**, F. Kraeber-Bodéré, Absorbed dose estimations for patients with B-acute lymphoblastic leukemia treated by 90Y-epratuzumab (hLL2) radioimmunotherapy, *Nuclear Technologies for Health Symposium* (2014)

20. A. Pallardy, S. Evain, T. Lebouvier, **T. Carlier**, M. Verceletto, P. Derkinderen, F. Kraeber-Bodéré, C. Boutoleau-Bretonnière, Relationship between clinical features of Lewy pathology and dopaminergic function throughout the alsheimer disease dementia with Lewy bodies spectrum, *Nuclear Technologies for Health Symposium* (2014)

21. C. Rousseau, A. Faivre-Chauvet, A. Rauscher, P. Baumgartner, **T. Carlier**, L. Ferrer, C. Bodet-Milin, D. Goldenberg, R. Sharkey, J. Barbet, F. Kraeber-Bodéré, Feasability of pretargeted immuno-PET using an anti-CEA bispecific antibody and a ^{68}Ga-labeled hapten-peptide in metastatic breast and medullary thyroid carcinoma patients: preliminary results, *Nuclear Technologies for Health Symposium* (2014)

22. **T. Carlier**, T. Eugène, A. Faivre-Chauvet, F. Kraeber-Bodéré, R. Lebtahi, I. Gardin, A. Dieudonné, Impact of 90Y-PET reconstruction parameters on dose volume histograms in post-implantation dosimetry of selective intravascular radionuclide therapy (SIRT), [abstract] *J. Nucl. Med. Meeting Abstracts*, **54** (2013) 30P

23. T. Eugène, **T. Carlier**, A. Faivre-Chauvet, F. Kraeber-Bodéré, R. Lebtahi, I. Gardin, A. Dieudonné, Absorbed doses distributions from 99mTc-MAA-SPECT and 90Y-PET in selective intravascular radionuclide therapy (SIRT): a phantom and patient study, [abstract] *Eur. J. Nucl. Med. Mol. Imaging*, **40** (2013) S174

24. M. Moreau, N. Chouin, F. Kraeber-Bodéré, J. Abadie, M. Chérel, **T. Carlier**, Preliminary assessment of iodine-124 degrading factors in pre-clinical PET using Monte Carlo simulation, *Nuclear Technologies for Health Symposium* (2012)

25. **T. Carlier**, L. Ferrer, E. Garin, C. Bodet-Milin, C. Rousseau, C. Ansquer, F. Schoenahl, S. Laffont, F. Kraeber-Bodéré, Is ^{90}Y-PET feasible with systemic injection ?, [abstract] *J. Nucl. Med. Meeting Abstracts*, **52** (2011) 205

26. L. Ferrer, **T. Carlier**, A. Lisbona, M. Bardiès, An ImageJ plugin to create whole body transmission scan using CT scanner: a validation study, [abstract] *Eur. J. Nucl. Med. Mol. Imaging*, **34** (2007) S198

27. **T. Carlier**, P. Salaun, M.B. Cavarec, F. Valette, A. Turzo, M. Bardiès, Y. Bizais, O. Couturier, Assessment of two new MIRD-based models for the computation of patient-specific therapeutic iodine-131 activity in Graves' disease, *J. Nucl. Med. Meeting Abstracts*, **47** (2006) 157P

28. F. Haddad, L. Ferrer, A. Guertin, N. Michel, **T. Carlier**, J. Barbet, J.F. Chatal, Evaluation of potential innovative positron-emitting radionuclides for PET applications, [abstract] *Eur. J. Nucl. Med. Mol. Imaging*, **33** (2006) S228

29. F. Valette, S. Querellou, A. Oudoux, C. Bodet-Milin, **T. Carlier**, B. Dupas, J.F. Chatal, O. Couturier, Respective Value of PET using 18F-fluorodeoxyglucose and Lymphangiography in Staging Hodgkin's disease patients with negative abdomino-pelvic CT, [abstract] *Eur. J. Nucl. Med. Mol. Imaging*, **33** (2006) S85

30. C. Bodet-Milin, S. Querellou, A. Oudoux, A. Haloun, D. Horeau-Langlard, **T. Carlier**, Y. Bizais, O. Couturier, Delayed gastric emptying scintigraphy in Cystic Fibrosis patients before and after lung transplantation, [abstract] *Eur. J. Nucl. Med. Mol. Imaging*, **33** (2006) S87

31. C. Ansquer, E. Mirallié, A. Oudoux, C. Bodet-Milin, M. Defrise, A. Seret, I. Daumy, F. Aubron, F. Kraeber-Bodéré, **T. Carlier**, Improvement of parathyroid lesion visualization in primary hyperparathyroidism with 99mTc-MIBI pinhole SPECT: comparison with conventional SPECT and planar scintigraphy, [abstract] *Eur. J. Nucl. Med. Mol. Imaging*, **33** (2006) S100

32. A. Breskin, **T. Carlier**, R. Chechik, O. Couturier, J.P. Cussonneau, L. Ferrer, C. Grignon, L. Luquin, V. Métivier, V. Peskov, F. Pheron, N. Servagent, D. Thers, A proposal High performance γ-camera concept based on liquid xenon converter and a gaseous photomultiplier for PET in *Proceedings of the 2nd international workshop on application of rare gas xenon to science and technology* (2005) Waseda Mediamix Publishing Co.

33. J.P Cussonneau, C. Grignon, L. Luquin, V. Metivier, F. Pheron, N. Servagent, **T. Carlier**, O. Couturier, L. Ferrer, D. Thers, Simulation and evaluation of a new PET design based on liquid xenon as detection medium in *Proceedings of the 2nd international workshop on application of rare gas xenon to science and technology* (2005) Waseda Mediamix Publishing Co.

34. **T. Carlier**, E. Mirallié, F. Kraeber-Bodéré, C. Curtet, Prospective comparison of two gamma probes for intraoperative detection of 18F-FDG in malignancy. A feasibility study, [abstract] *Eur. J. Nucl. Med. Mol. Imaging* **32** (2005) S112

35. S. Chiavassa, I. Aubineau-Lanièce, **T. Carlier**, L. Ferrer, A. Lisbona, M. Bardiès, Effect of patient morphology on dosimetric estimation, [abstract] *Eur. J. Nucl. Med. Mol. Imaging* **32** (2005) S110

36. C. Curtet, **T. Carlier**, E. Mirallié, B. Bridji, C. Rousseau, F. Kraeber-Bodéré, ^{18}F-FDG radioguided surgery (RS): Evaluation of 2 gamma probes in differentiated thyroid cancer (DTC) patients with ^{131}I negative locoregional recurrence, [abstract] *J. Nucl. Med.* **46** (2005) 132P

37. **T. Carlier**, M. Bardiès, L. Ferrer, C. Ansquer, F. Kaeber-Bodéré, J.F. Chatal, O. Couturier, A general method to compute activity in Graves' disease treatment by radioiodine based on the MIRD formalism. Preliminary results [abstract] *Eur. J. Nucl. Med. Mol. Imaging* **31** (2004) S241

38. L. Ferrer, Y. Grealou, D. Autret, S. Gaudaire, G. Brunet, G. Delpon, A. Lisbona, B. Bridji, I. Resche, C. Rousseau, **T. Carlier**, M. Bardiès, A new ImageJ plugin to correct for partial volume effect [abstract] *Eur. J. Nucl. Med. Mol. Imaging* **31** (2004) S241

A.3 Communications affichées internationales avec comité de lecture

1. **T. Carlier**, S. Gouard, C. Bailly, M. Colombié, C. Sai-Maurel, F. Kraeber-Bodéré, M. Chérel, Are macroscopic PET textural features representative of microscopic heterogeneity ? A preliminary simple and direct comparison between PET and digital autoradiography, [abstract] *J. Nucl. Med. Meeting Abstracts*, **57** (2016), 1407

2. A. Pallardy, O. Pauline, **T. Carlier**, T. Lebouvier, S. Le Dily, H. Courtemanche, F. Kraeber-Bodéré, C. Boutoleau-Bretonnière, Dementia with Lewy body and Alzheimer's disease : a continuum ? First results of a striatal [18F]Fluorodopa Positron Emission Tomography pilot study, [abstract] *Eur. J. Nucl. Med. Mol. Imaging*, **43** (2016), S622

3. C. Bailly, L. Campion, E. Thebaud, N. Corradini, A. Moreau, D. Dansette, F. Kraeber-Bodéré, **T. Carlier**, C. Bodet-Milin, Volumetric FDG-PET indices for the assessment of histological response to neoadjuvant chemotherapy and outcome in paediatric patients with Ewing sarcoma and osteosarcoma, [abstract] *Eur. J. Nucl. Med. Mol. Imaging*, **43** (2016), S257

4. C. Bailly, L. Campion, E. Thebaud, N. Corradini, A. Moreau, D. Dansette, F. Kraeber-Bodéré, C. Bodet-Milin, **T. Carlier**, Prognosis value of SUV-based metrics, textural and shape features derived from initial FDG-PET in paediatric patients with Ewing sarcoma and osteosarcoma, [abstract] *Eur. J. Nucl. Med. Mol. Imaging*, **43** (2016), S257

5. M. Sanchez-Garcia, J. Strydhorst, H. Levillain, I. Gardin, P. Buyssens, **T. Carlier**, R. Lebtahi, I. Buvat, A. Dieudonné, Improved dose-volume histograms for Y90-PET based dosimetry with partial volume effect and noise compensations by means of region subsegmentation, [abstract] *Eur. J. Nucl. Med. Mol. Imaging*, **43** (2016), S225

6. B. Jamet, C. Bailly, L. Planche, **T. Carlier**, T. Eugène, C. Touzeau, C. Ansquer, P. Moreau, F. Kraeber-Bodéré, C. Bodet-Milin, FDG-PET/CT at relapse predicts survival in multiple myeloma, [abstract] *Eur. J. Nucl. Med. Mol. Imaging*, **43** (2016), S126

7. M. Sanchez-Garcia, J. Strydhorst, I. Buvat, **T. Carlier**, R. Lebtahi, A. Dieudonné, Partial volume effect and noise compensation for improved Dose Volume Histogram in 90Y-SIRT PET based dosimetry, *J. Nucl. Med. Meeting Abstracts*, **57** (2016), 1013

8. **T. Carlier**, L. Campion, D. Rusu, M. Colombié, D. Goulon, F. Kraeber-Bodéré, C. Rousseau, Correlation and usefulness of textural metrics in ovarian carcinoma using PET imaging: preliminary results, [abstract] *Eur. J. Nucl. Med. Mol. Imaging*, **41** (2014) S366

9. J. Barbet, C. Bodet-Milin, C. Rousseau, A. Rauscher, D. Masson, A. Faivre-Chauvet, P. Baumgartner, **T. Carlier**, L. Ferrer, D.M. Goldenberg, R.M. Sharkey, F. Kraeber-Bodéré, Pharmacokinetic modelling and optimization of pretargeting using anti-carcinoembryonic antigen (CEA) bispecific antibody and 68Ga, 111In or 177Lu-labeled peptide in CEA-positive tumour patients, [abstract] *Eur. J. Nucl. Med. Mol. Imaging*, **41** (2014) S349

10. **T. Carlier**, T. Eugène, A. Faivre-Chauvet, F. Kraeber-Bodéré, R. Lebtahi, I. Gardin, A. Dieudonné, Similarity of absorbed doses distributions from 99mTc-MAA-SPECT and 90Y-PET in selective intravascular radionuclide therapy (SIRT): a phantom study, [abstract] *J. Nucl. Med. Meeting Abstracts*, **54** (2013) 513P

11. **T. Carlier**, M. Mauguet, H. Necib, F. Schoenahl, C. Rousseau, C. Bodet-Milin, M. Chérel, F. Kraeber-Bodéré, Feasibility of non-parametric bootstrap resampling with clinical TOF PET sinograms, [abstract] *J. Nucl. Med. Meeting Abstracts*, **54** (2013) 499P

12. **T. Carlier**, L.Ferrer, H. Necib, L. Le Meunier, F. Schoenahl, C. Bodet-Milin, C. Rousseau, F. Kraeber-Bodéré, Optimization of acquisition parameters for 18F-FDG PET scans using the clinical NECR, [abstract] *J. Nucl. Med. Meeting Abstracts*, **54** (2013) 509P

13. D. Goulon, **T. Carlier**, C. Rousseau, C. Bailly, F. Kraeber-Bodéré, H. Necib, Comparison of different indices for metastatic breast cancer therapy assessment, [abstract] *J. Nucl. Med. Meeting Abstracts*, **54** (2013) 318P

14. D. Goulon, C. Rousseau, **T. Carlier**, H. Necib, F. Kraeber-Bodéré, Comparison of different indices for metabolic PET assessment according to PERCIST in metastatic breast cancer, [abstract] *J. Nucl. Med. Meeting Abstracts*, **54** (2013) 318P

15. H. Necib, D. Goulon, C. Rousseau, **T. Carlier**, F. Kraeber-Bodéré, I. Buvat, Comparison of parametric imaging with PERCIST to assess tumor response in metastatic breast cancer, [abstract] *J. Nucl. Med. Meeting Abstracts*, **54** (2013) 510P

16. D. Goulon, Brice Hénaff, Hatem Necib, **T. Carlier**, C. Rousseau, F. Kraeber-Bodéré, Comparison of different metabolic indices for therapeutic response evaluation by PET assessment in metastatic breast cancer, [abstract] *Eur. J. Nucl. Med. Mol. Imaging*, **40** (2013) S416

17. H. Necib, T. Eugène, **T. Carlier**, F. Kraeber-Bodéré, Feasibility of parametric imaging for longitudinal monitoring by FDG PET/CT in Diffuse Large B Cell Lymphoma (DLBCL) *International workshop on PET in Lymphoma* (2012)

18. C. Mathieu, L. Ferrer, **T. Carlier**, M. Lacombe, L. Campion, D. Rusu, F. Kraeber-Bodéré, C. Rousseau Assessment of lymph nodes and prostate pathological status with early dynamic curves PET/CT 18F-Choline (FCH) in prostate cancer: preliminary results [abstract] *Eur. J. Nucl. Med. Mol. Imaging*, **39** (2012) S461

19. S. Stute, **T. Carlier**, K. Cristina, B. Hutton, I. Buvat, Making simulated PET images indistinguishable from real PET images for evaluation purposes, [abstract] *J. Nucl. Med. Meeting Abstracts*, **52** (2011) 1985

20. **T. Carlier**, L. Ferrer, Experimental comparison of SUV measurement between two generations of PET scanners, [abstract] *J. Nucl. Med. Meeting Abstracts*, **52** (2011) 1977

21. M. Lacombe, M. Mothy, T. Eugène, C. Ansquer, F. Kraeber-Bodéré, **T. Carlier**, T. Guillaume, P. Chevallier, J. Delaunay, C. Bodet-Milin, FDG-PET/CT for the detection of gastrointestinal graft-versus-host disease (GVHD) after allogeneic hematopoietic stem cell transplantation (allo-HSCT), [abstract] *J. Nucl. Med. Meeting Abstracts*, **52** (2011) 1877

22. I. Souillac, F. Kraeber-Bodéré, O. Bouchot, J. Rigaud, **T. Carlier**, C. Ansquer, 18FDG-PET/CT in the assessment of lymph node involvement in patients with invasive penile carcinoma, [abstract] *J. Nucl. Med. Meeting Abstracts*, **52** (2011) 1905

23. N. Anizan, **T. Carlier**, C. Hindorf, M. Bardiès, Optimisation of I-124 acquisition parameters with the NEMA NU 4-2008 performances assessment for the Inveon PET system [abstract] *Eur. J. Nucl. Med. Mol. Imaging*, **37** (2010) S334

24. N. Dartial, **T. Carlier**, M. Fuselier, J. Desfontis, D. Visvikis, M. Bardiès, C. Hindorf, Monte-Carlo simulation of the Inveon microPET system using GATE, *J. Nucl. Med. Meeting Abstracts*, **50** (2009) 1487 (SNM congress, Toronto, USA)

25. N. Dartial, **T. Carlier**, M. Fuselier, J. Desfontis, D. Visvikis, M. Bardiès, C. Hindorf, Validation of the Inveon small animal PET system model using GATE, [abstract] *Eur. J. Nucl. Med. Mol. Imaging*, **36** (2009) S411

26. **T. Carlier**, M. Moisan, L. Ferrer, F. Kraeber-Bodéré, J. Barbet, M. Bardiès, Validation of a GATE model of the Siemens Symbia system for 99mTc, 111In and 131I acquisitions, *J. Nucl. Med. Meeting Abstracts*, **49** (2008) 405P

27. N. Dartial, **T. Carlier**, D. Visvikis, S. Jan, M. Fuselier, J.C. Desfontis, J. Barbet, M. Bardiès, Performance evaluation of the Siemens Inveon microPET system, *J. Nucl. Med. Meeting Abstracts*, **49** (2008) 404P

28. C. Curtet, **T. Carlier**, F. Kraeber-Bodéré, Intraoperative gamma probes evaluation for 18F-FDG detection in patients recurrences, *J. Nucl. Med. Meeting Abstracts*, **48** (2007) 432P

29. **T. Carlier**, C. Bodet-Milin, A. Oudoux, M. Defrise, A. Seret, O. Couturier, F. Kraeber-Bodéré, C. Ansquer, Technical feasibility of pinhole SPECT acquisition in primary hyperparathyroidism: phantoms and patients studies, *J. Nucl. Med. Meeting Abstracts*, **47** (2006) 378P

30. J.M. Vrigneaud, **T. Carlier**, Comparison of two spreadsheets for calculation of radiation exposures following hyperthyroidism treatment with iodine-131, *Proceedings of the 2nd european IRPA congress on radiation protection* (2006) P-122

31. P.Y. Salaun, S. Querellou, C. Bodet-Milin, **T. Carlier**, A. Turzo, Y. Bizais, O. Couturier, Comparison of gastric emptying scintigraphy based on the geometric mean of the gastric proportion of the abdominal radioactivity or on the geometric mean of the intragastric, *J. Nucl. Med. Meeting Abstracts*, **47** (2006) 336P

32. S. Querellou, F. Valette, A. Oudoux, C. Bodet-Milin, **T. Carlier**, N. Juge-Morineau, J. Chatal, O. Couturier, FDG-PET/CT predicts outcome in patients with aggressive non-Hodgkin's lymphoma and Hodgkin's disease, *J. Nucl. Med. Meeting Abstracts*, **47** (2006) 451P

33. C. Ansquer, E. Mirallié, A. Oudoux, C. Bodet-Milin, M. Defrise, A. Seret, F. Kraeber-Bodéré, **T. Carlier**, Clinical evaluation of iterative versus analytic reconstruction for parathyroid lesions vizualisation in primary hyperparathyroidism with 99mTc-MIBI pinhole SPECT, [abstract] *Eur. J. Nucl. Med. Mol. Imaging*, **33** (2006) S355

34. C. Curtet, **T. Carlier**, F. Kraeber-Bodéré, Evaluation of 2 intraoperative gamma probes for radiodetection of 18F-FDG, [abstract] *Eur. J. Nucl. Med. Mol. Imaging*, **33** (2006) S322

35. E. Mirallié, C. Bodet-Milin, **T. Carlier**, C. Curtet, B. Cariou, B. Bridji, F. Dravet, C. Rousseau, I. Resche, F. Kraeber-Bodéré, Feasibility of 18F-FDG-guided surgery in the

management of metastases from differentiated thyroid carcinoma with negative 131I uptake, [abstract] *J. Nucl. Med.* **46** (2005) 310P

36. F. Valette, C. Bodet-Milin, A. Oudoux, **T. Carlier**, J. Hélias, O. Couturier, Results obtained by combined PET/CT in the staging Hodgkin's disease are not affected by iodized contrast medium used for lymphangiography, [abstract] *Eur. J. Nucl. Med. Mol. Imaging* **32** (2005) S147

37. O. Couturier, C. Bodet-Milin, S. Querellou, **T. Carlier**, A. Turzo, Y. Bizais, Gastric scintigraphy with a liquid-solid radiolabeled meal: performances of solid and liquid parameters [abstract] *Eur. J. Nucl. Med. Mol. Imaging* **31** (2004) S230

Annexe B

B.1 Reproduction des 5 publications les plus significatives

Eur J Nucl Med Mol Imaging (2008) 35:637–643
DOI 10.1007/s00259-007-0625-9

ORIGINAL ARTICLE

^{99m}Tc-MIBI pinhole SPECT in primary hyperparathyroidism: comparison with conventional SPECT, planar scintigraphy and ultrasonography

Thomas Carlier · Aurore Oudoux · Eric Mirallié · Alain Seret · Isabelle Daumy · Christophe Leux · Caroline Bodet-Milin · Françoise Kraeber-Bodéré · Catherine Ansquer

Received: 4 July 2007 / Accepted: 28 September 2007 / Published online: 25 October 2007

Abstract
Purpose A pinhole collimator is routinely used to increase the resolution of scintigraphy. This prospective study was conducted to determine the interest of ^{99m}Tc-MIBI pinhole single-photon emission computed tomography (SPECT) for the preoperative localisation of parathyroid lesions in primary hyperparathyroidism.
Methods All patients underwent a neck ultrasonography (US), $^{99m}TcO_4^-$ and ^{99m}Tc-MIBI planar images and two consecutive SPECT with a parallel (C-SPECT) and a pinhole collimator (P-SPECT). P-SPECT was performed with a tilted detector equipped with a pinhole collimator and reconstructed with a dedicated OSEM algorithm. A diagnostic confidence score (CS) was assigned to each procedure considering intensity and extra-thyroidal location of suspected lesions: 0=negative, 1=doubtful, 2=moderately positive, 3=positive. The results of these preoperative localisation studies were compared with surgical, pathological and 6-month biological findings.
Results Fifty-one patients cured after surgery were included. Surgery revealed 55 lesions (median weight 0.5 g, 11 in ectopy). Sensitivities of US, planar imaging, C-SPECT and P-SPECT were, respectively, 51, 76, 82 and 87%. Nine glands were only detected by tomography and five glands only by P-SPECT. $^{99m}Tc-MIBI/^{99m}TcO_4^-$ planar scans and P-SPECT were complementary and, when combined together, showed the highest sensitivity (93%). Compared with planar imaging and C-SPECT, P-SPECT increased CS for 42 and 53% of lesions, respectively, and contributed to markedly reduce the number of uncertain results.
Conclusions A combination of planar $^{99m}Tc-MIBI/^{99m}TcO_4^-$ scintigraphy and P-SPECT appears to be a highly accurate preoperative imaging procedure in primary hyperparathyroidism.

Keywords Hyperparathyroidism · Pinhole SPECT · ^{99m}Tc-sestamibi · Preoperative localisation · Parathyroid scintigraphy · Parathyroid adenoma

T. Carlier · A. Oudoux · C. Bodet-Milin · F. Kraeber-Bodéré · C. Ansquer (✉)
Nuclear Medicine Department, Hôtel Dieu University Hospital, Nantes, France
e-mail: catherine.ansquer@chu-nantes.fr

T. Carlier · C. Bodet-Milin · F. Kraeber-Bodéré · C. Ansquer
INSERM CRCNA,
Nantes, France

E. Mirallié
Surgery Department, Hôtel Dieu University Hospital,
Nantes, France

A. Seret
Experimental Medical Imaging, University of Liège,
Institute of Physics,
Liège, Belgium

I. Daumy
Ultrasonography Center,
Nantes, France

C. Leux
PIMESP, Saint Jacques University Hospital,
Nantes, France

Introduction

Primary hyperparathyroidism (pHPT), characterised by an elevated serum level of calcium and inappropriate or elevated parathyroid hormone (PTH) is most likely (80%)

caused by a solitary adenoma [1]. The conventional surgical approach is a parathyroidectomy with bilateral neck exploration. However, it is time-consuming and can be responsible for morbidity. After the generalisation of ^{99m}Tc-MIBI parathyroid scintigraphy as well as ultrasonography (US) to identify and localise the parathyroid lesion(s) preoperatively, minimally invasive parathyroidectomy has become possible [2]. The sensitivity of US depends on the size of the hyperfunctioning gland and its location (a mediastinal gland cannot be localised) [1]. The sensitivity of ^{99m}Tc-MIBI scintigraphy depends almost on the number of mitochondria, the oxyphil cell density and the solid or cystic nature of the gland [3, 4]. Recently, more and more patients with mild pHPT (characterised by moderate hypercalcemia and a moderately elevated PTH level) are operated on because a parathyroidectomy significantly improves their quality of life [5]. The glands responsible for mild pHPT are generally small with a demonstrated correlation between PTH level and weight [6, 7]. As a consequence, conventional scintigraphy should be improved to localise these small glands to allow minimally invasive surgery.

It has been proven that single-photon emission computed tomography (SPECT) increases the sensitivity of ^{99m}Tc-MIBI scintigraphy [6, 8–11]. However, the use of a pinhole collimator, instead of a parallel hole collimator, has also proved to improve the sensitivity of planar scintigraphy, especially for the detection of small parathyroid adenomas [12]. Only two studies evaluated P-SPECT in HPT [13, 14].

Our group conducted a prospective study to assess the additional value of pinhole SPECT (P-SPECT) compared with conventional scintigraphic procedures (planar and conventional SPECT ^{99m}Tc-MIBI images) and ultrasound (US) for the preoperative localisation of parathyroid lesions in patients with an established diagnosis of sporadic pHPT. This study is the first comparing P-SPECT and consecutive SPECT (C-SPECT).

Materials and methods

Patients

From October 2004 to August 2006, 66 consecutive patients suffering from pHPT underwent preoperatively a P-SPECT in addition to the conventional procedures performed routinely in our institution, including a planar double-phase $^{99m}TcO_4^- / ^{99m}Tc-MIBI$, a conventional SPECT (C-SPECT) and a neck US.

Of these 66 patients, we excluded seven patients not operated on, two patients not cured after surgery and six patients with multiple endocrine neoplasia type 1 syndrome or familial history of HPT. The 51 patients whose calcium and PTH levels had returned to normal 6 months after surgery were selected for this study. The diagnosis of pHPT was based on elevated levels of calcium and elevated or unadapted PTH levels.

Bilateral or unilateral surgical neck exploration was performed on each patient by experienced parathyroid surgeons. The choice of the surgical technique was based on preoperative localisation studies, preoperative findings and/or surgeon's practice.

Acquisition protocol

Planar images and C-SPECT were performed on a single-head gamma camera equipped with a low-energy, high-resolution, large field-of-view parallel-hole collimator (SOPHY DSX, France). Anterior planar views centered on the cervical and thoracic areas were recorded 20 min after intravenous injection of 74 MBq of $^{99m}TcO_4^-$, and 15 min and at least 2 h after injection of 925 MBq of ^{99m}Tc-MIBI (Cardiolite®, Bristol-Meyers-Squibb). The time acquisition was 10 min per view.

C-SPECT centered on neck and thorax was performed 30 min after injection of ^{99m}Tc-MIBI. C-SPECT acquisition was acquired over 180° with 32 equally spaced angular projections of 30 s.

P-SPECT was performed on the same gamma camera 60 min after the injection of ^{99m}Tc-MIBI. Thirty-two projections were acquired over 180° with a circular orbit. The acquisition time per step was set to 40 s. The main characteristics of the pinhole collimator were a 3-mm aperture and an inner focal length of 205 mm. The pinhole collimator was tilted (15.7°±5.8°) to increase both resolution and sensitivity [15, 16], but care was taken to ensure that the thyroid was always in the field of view whatever the angular step.

Tomographic reconstruction

The C-SPECT data were reconstructed by iterative reconstruction (OSEM, three iterations, ten subsets) using the algorithm provided by the Mirage workstation version 4.339a (Segami, Columbia, USA). Scatter, attenuation and distance-dependent camera resolution were not modelled in the algorithm.

P-SPECT data were reconstructed with a dedicated OSEM algorithm which uses a ray-driven forward projector and a voxel-driven backprojector that do not model the finite dimension of the pinhole aperture, the attenuation and the scatter [17]. The algorithm allows independent specification of all geometrical parameters of the pinhole-tilted geometry. The spatial resolution and noise in reconstructed slices were previously determined [18] to optimise the reconstruction parameters (two iterations and eight subsets). The θ angle dependence sensitivity of pinhole acquisition

(where θ is the incidence angle between the detected gamma ray and the perpendicular direction to the detector) was corrected by acquiring a 20-MBq point source at different horizontal offset as suggested by Smith and Jaszczak [19]. The measured data were fitted to a $\sin^n\theta$ function and the best fit was obtained for n=4.5. The projections were corrected by applying a $\sin^{4.5}\theta$ factor.

Image analysis

^{99m}Tc-MIBI and $^{99m}TcO_4^-$ planar images were visually compared. A focus of increased ^{99m}Tc-MIBI uptake without technetium focus was considered positive for a parathyroid lesion on either early and/or late planar views, independently of the intensity of the uptake (cf. following confidence score). An evident nodular formation or irregularity of the posterior side of the thyroid was considered compatible with a parathyroid lesion on SPECT.

A diagnostic confidence score (CS) was assigned to each scintigraphic procedure considering intensity and extra-thyroidal location of suspected lesions and was defined as follows: 0=no focus, 1=doubtful focus, 2=moderately positive focus, 3=positive focus.

A combined analysis of scintigraphic procedures (planar + SPECT) was performed: A focus of increased ^{99m}Tc-MIBI uptake on planar images and/or SPECT was considered positive for parathyroid lesion.

All the various scintigraphic procedures were interpreted independently by two experienced nuclear medicine specialists without reference to the results of US. Discrepancies in interpretation between observers were resolved by consensus.

US method

US was performed by experienced radiologists for all patients using high-resolution (7 to 12 MHz) transducers to examine the anterior neck and upper mediastinum: Aloka 5000 (Aloka) or Voluson 730 (General Electric). A US examination showing one or more hypoechogenic nodule(s) distinct from the thyroid gland was considered indicative of one or more parathyroid abnormal gland(s). The radiologists were unaware of the results of the scintigraphic procedures.

Results analysis

Statistical analyses were carried out using the software R version 2.4.1(http://lib.stat.cmu.edu/R/CRAN, accessed on March 28, 2007) to compare the results of US and scintigraphic procedures. The gold standard was histology and follow-up at 6 months (normal PTH level and calcemia). Adenomatous, carcinomatous or hyperplastic parathyroid glands were considered true-positive findings. Normal parathyroid glands were considered true-negative findings. Accumulation in a non-parathyroid lesion and especially in a thyroid nodule was considered false-positive (FP) finding. A parathyroid lesion confirmed by a pathological analysis and which had not been previously detected by imaging procedures was considered false-negative (FN) result. Sensitivity and specificity were calculated on a per-parathyroid-gland basis for each imaging modality. The chi-square test, Mac Nemar test or Wilcoxon test were used for comparison. The tests were considered statistically significant at $p<0.05$.

Results

Characteristics of the population

Thirteen men and 38 women were studied with a median age of 56 years (range, 20–93). Median PTH was 125 pg/ml (normal<70; range, 68–790). Twenty-two patients (43%) had thyroid nodules. None of the patients had previously undergone thyroid or parathyroid surgery.

Bilateral surgical neck exploration was performed on 28 patients and minimally invasive neck surgery on 23 patients. In six patients, parathyroidectomy was associated with isthmo-lobectomy for thyroid nodules.

Among the 55 parathyroid lesions resected, there were 45 adenomas, 6 hyperplasias, 1 adenocarcinoma and 3 lesions difficult to classify as either adenoma or hyperplasia. Most of the lesions were solitary except in two patients who had two and three pathological parathyroid glands, respectively. The median maximum diameter was 16 mm (range, 6–55). The median weight was 0.5 g (range, 0.1–18) with 33 (60%) glands ≤0.5 g. Eleven glands were in ectopic location: six in posterior ectopy, three within the thyrothymic ligament, one intra-mediastinal and one intra-thyroidal.

Imaging findings

The sensitivities of US and scintigraphic procedures are reported in Table 1. US showed the lowest sensitivity compared with all scintigraphic procedures ($p<0.05$), detecting only 28 of 55 lesions (51%). Of the 27 FN for US imaging, 21 glands (78%) were ≤0.5 g, and seven glands were ectopic (64% of all ectopic glands).

Planar scintigraphy identified 42 of 55 lesions (76%), whereas C-SPECT and P-SPECT detected, respectively, 45 of 55 (82%) and 48 of 55 (87%) of the abnormal glands. Of the 13 FN for planar scintigraphy, ten concerned glands ≤0.5 g and ten of these lesions were solitary. Imaging by C-SPECT and especially by P-SPECT improved the detection rate, with detection of 4 of 13 and 9 of 13 of these lesions, respectively.

Table 1 Sensitivities and specificities of US and scintigraphic procedures, alone or combined

Imaging modalities	Sensitivity (%)	Specificity (%)
US	51[a]	91
Planar scintigraphy	76	95
C-SPECT	82	95
P-SPECT	87[b]	91
Combination of planar and C-SPECT	84	95
Combination of planar and P-SPECT	93	91

[a] Significantly lower than other imaging modalities: $p<0.05$ (Mac Nemar test)
[b] Including the two parathyroid lesions outside the field of view of the pinhole collimator

The five adenomas detected only by P-SPECT ranged from 0.3 to 1.9 g (four glands weighing ≤0.6 g) and measured from 13 to 27 mm in diameter (median, 18 mm). Four lesions were not detected by planar and tomographic (C-SPECT and P-SPECT) images. Three of these lesions were hyperplastic lesions with weights of 0.1–0.2 g associated with identified others lesions. The fourth lesion not detected by scintigraphy was an inferior adenoma of 3 g located in the continuity of the thyroid lobe and considered as thyroidal by planar scintigraphy, C-SPECT and P-SPECT.

All ectopic lesions were detected by both planar scintigraphy and C-SPECT, whereas P-SPECT was negative in 2 of 11 cases. In the first case, a deep mediastinal lesion was not in the field of view of the pinhole, and in the second, a misalignment of the pinhole collimator relative to the thyroid was responsible for the non-visualisation of the pathological gland. Except for these two cases, the use of parallel hole collimator (C-SPECT) instead of pinhole collimator (P-SPECT) did not yield any additional information.

Despite a lower sensitivity compared with SPECT, planar scintigraphy and US detected one additional lesion each and gave additional information about thyroid morphology.

US and planar imaging showed, respectively, 14 and 8 FP. The number of FP was higher with P-SPECT than for C-SPECT acquisition (14 vs 8). Among these 14 FP, five showed a CS=2 and nine a CS=1. The FP with a CS=2 were visualised in four patients with concomitant nodular goiter and in one patient treated by amiodarone with poor thyroid uptake and rapid washout of ^{99m}Tc-MIBI.

The diagnostic CS assigned to each gland with the different scintigraphic modalities is reported in Table 2. P-SPECT showed the highest mean CS among the 55 pathologic glands compared with planar and C-SPECT ($p<0.001$). P-SPECT contributed to significantly reduce the number of negative or uncertain results (CS=0 or 1, $p<0.01$).

Table 3 summarises the variations of CS on a per gland basis with P-SPECT. P-SPECT increased CS for 42% of parathyroid lesions when compared with planar imaging and for 53% of parathyroid lesions when compared with C-SPECT. Figure 1 illustrates the case of a right inferior orthotopic adenoma (0.4 g, 13×7×8 mm^3) showing a very doubtful uptake on planar scintigraphy which appears clearly on SPECT and especially P-SPECT.

Table 2 Diagnostic CS of imaging modalities

CS of each gland (n=55)	Planar images	C-SPECT	P-SPECT
0	13	10	7[a]
1	14	16	7
2	11	20	13
3	17	9	28
Mean CS	1.58	1.51	2.13[b]

[a] Including the two parathyroid lesions outside the field of view of the pinhole collimator
[b] Mean CS significantly higher than the others mean CS: $p<0.001$ (Wilcoxon test)

However, the CS of six glands was inferior with P-SPECT compared with planar imaging. In three of six cases, the reduction of CS was mild (from 3 to 2) and did not modify final diagnosis. In one case, a focus was assigned to thyroidal origin because of its location in the continuity of the inferior thyroid lobe on P-SPECT and C-SPECT, but was correctly identified on dual tracer planar images. In the other two cases, the glands were not in the field of view of the pinhole collimator.

When the diagnosis is based on the CS value and a comparison between planar imaging and P-SPECT, the number of P-SPECT FP could be markedly reduced. Table 4 shows the CS assigned to each focus detected by P-SPECT and the results of comparison between P-SPECT and planar images. The probability of a parathyroid lesion visualisation increased with CS (in particular, all the foci with a CS=3 corresponded to a parathyroid lesion) and in the case of an agreement between P-SPECT and planar images (95 vs 43%

Table 3 Variations of diagnostic CS for each lesion with the additional use of P-SPECT

Variations of CS	P-SPECT vs planar images (55 glands)	P-SPECT vs C-SPECT (55 glands)
Increase of CS	23 (42%)	29 (53%)
0 or 1 to ≥ 2	16	14
0 to 1	3	3
2 to 3	4	12
CS unchanged	26 (47%)	24 (43%)
Decrease of CS	6 (11%)	2 (4%)
3 to 2	3	0
2 to 0	3[a]	2[a]

[a] Including the two parathyroid lesions outside the field of view of the pinhole collimator

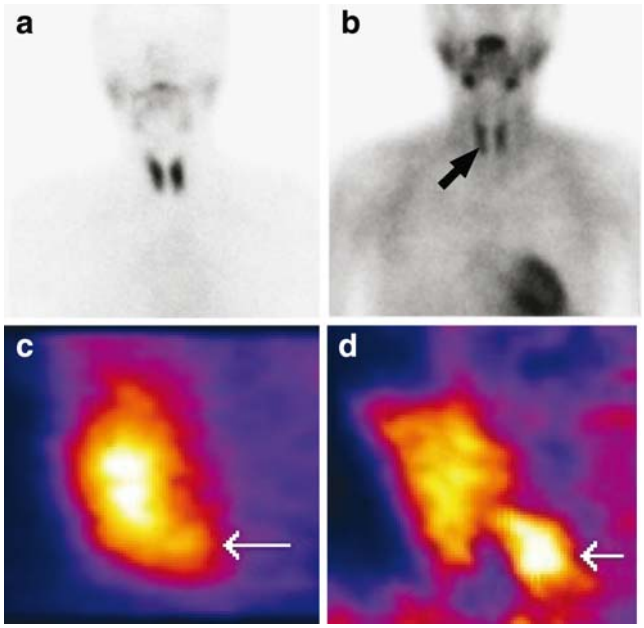

Fig. 1 Patient without nodular thyroid disease (**a**) suffering from pHPT (PTH=110 pg/ml) caused by a right inferior orthotopic adenoma. Very doubtful focus indicated by the *arrows* on ^{99m}Tc-MIBI planar scintigraphy (**b**, CS=1) and evident focus on C-SPECT (**c**, CS=2) and especially on P-SPECT sagittal slices (**d**, CS=3)

in case of discordance). In contrast, the probability of a P-SPECT FP was higher in the case of discordance between planar and P-SPECT, especially with CS=1 (80%).

Discussion

Parathyroidectomy significantly improves the quality of life of patients suffering from pHPT and even those with mild elevated PTH level [5]. Consequently, more and more patients with mild pHPT are operated on. As glands responsible for mild pHPT are generally small, conventional preoperative localisation studies should be improved to allow minimally invasive surgery.

A pinhole collimator is routinely used to increase spatial resolution and improve sensitivity of planar parathyroid scintigraphy [12]. SPECT could certainly be optimised by the use of these collimators. Several technical studies performed on thyroid phantoms showed the feasibility of such explorations [15, 16, 18, 20]. Clinical applications are rare because of the difficulties to use this method routinely.

Only two studies had evaluated P-SPECT in patients suffering from HPT. Profanter et al. [14] compared $^{99m}TcO_4^-/^{201}Tl$ pinhole subtraction SPECT and US in 15 patients and showed that P-SPECT was significantly more accurate than US in the detection of pathological parathyroid glands. P-SPECT showed a sensitivity of 80% and a specificity of 93% with only one case of FP reported. Spanu et al. [13] showed that P-SPECT was a highly sensitive method, identifying more lesions than planar scans in 67 patients. Interestingly, P-SPECT was the only positive procedure in 8.9% of these patients. For the 48 patients explored for pHPT, the sensitivity of P-SPECT reached 98% (vs 88% for planar scans). Sensitivities of P-SPECT and planar scans observed in our patients were slightly lower (87 and 76%), but glands were smaller in our series (60%≤0.5 g vs 30% in the series of Spanu). Spanu and collaborators used the filtered back-projection algorithm of Feldkamp, Davis and Kress which was shown to produce more artifacts compared to ML-EM based reconstruction for pinhole geometry [17]. Surprisingly, no FP results relative to artefacts were reported in their study. Unlike Spanu et al., we decided to consider accumulation in thyroidal structures or nodules as FP findings. FP were frequent with P-SPECT in our patients with a high prevalence of thyroid nodules (43%). With a higher spatial resolution compared with parallel collimation, irregularities of dystrophic thyroid lobes and thyroid nodules were easily detected due to the better definition of thyroid contours and could be falsely interpreted as parathyroid lesions especially in the case of heterogeneous and faint thyroid uptake. A faint focal uptake (CS=1), unilateral or bilateral, was frequently observed in the upper and inside face of thyroid lobes. This corresponds probably to a thickening resulting from fusion of the ultimobranchial body into the principal medial thyroid process (Zuckerkandl's tuberculum) [21].

Table 4 Probability occurrence of parathyroid lesion (PL) or FP for P-SPECT according to diagnostic CS and planar scans

	CS=1	CS=2	CS=3
Total number of P-SPECT foci	*n*=16	*n*=18	*n*=28
	PL: 7/16=44%	PL: 13/18=72%	PL: 28/28=100%
	FP: 9/16=56%	FP: 5/18=28%	FP: 0/28=0%
Concordant P-SPECT and planar foci	*n*=6	*n*=10	*n*=25
	PL: 5/6=83%	PL: 9/10=90%	PL: 25/25=100%
	FP: 1/6=17%	FP: 1/10=10%	FP: 0/25=0%
Discordant P-SPECT and planar foci	*n*=10	*n*=8	*n*=3
	PL: 2/10=20%	PL: 4/8=50%	PL: 3/3=100%
	FP: 8/10=80%	FP: 4/8=50%	FP: 0/3=0%

The higher level of FP due to the use of pinhole collimator for SPECT acquisition represents a potential drawback of P-SPECT interpretation. Nevertheless, FP could be reduced with a comparison between P-SPECT and planar imaging. The FP probability was only 10% in case of agreement with a CS=2 and reached 80% in cases of discordance with a CS=1. In practice, we concluded to a high probability of FP when a doubtful focus (CS=1) of P-SPECT was not confirmed by planar views and particularly when one another evident focus was detected elsewhere. If no another focus was detected, the possibility of a small parathyroid lesion detected only by P-SPECT remained possible, and a comparison with US was recommended.

Our study demonstrated a potential improvement of sensitivity of P-SPECT compared with conventional scintigraphic procedures. P-SPECT was able to confirm clearly doubtful results of C-SPECT or planar views. P-SPECT may, thus, replace C-SPECT, except in cases of major ectopy that could be previously detected on planar scintigraphy. A morphologic analysis of the thyroid (thyroid scintigraphy and US) remained useful. In particular, an US examination may reduce FP due to thyroid nodules [22] and FN caused by adenoma of a cystic nature or associated with concomitant hyperfunctioning thyroid nodules, which may be undetected by scintigraphy [11].

To our knowledge, this is the first study that compares SPECT acquisition with a parallel and a pinhole collimator for the same patient. For ethical reasons, we decided to perform the two studies after a single injection of ^{99m}Tc-MIBI; however, this leads to a different time delay between injection and acquisition for the two imaging procedures evaluated. C-SPECT was always performed before P-SPECT to minimise the time delay of the collimator change over 30 min and to not change the procedure performed routinely in our institution. This delay may have an impact on CS, as it may depend on relative uptake and retention of ^{99m}Tc-MIBI by parathyroid and thyroid. Nevertheless, if many authors recommend an early acquisition (15–30 min) to avoid rapid washout of adenomas [1, 23], a significant difference between a 30- and 60-min p.i SPECT imaging has not been yet demonstrated. As a consequence, it would be useful in additional comparative studies to alternate the 30- and 60-min starting times for C-SPECT and P-SPECT.

From a practical point of view, owing to the presence of the patient's shoulders, the use of a tilted geometry is essential to optimise the distance between the thyroid and the pinhole collimator [15]. We should emphasise that this geometry is not possible with the current generation of gamma cameras and could limit clinical P-SPECT development in the future.

Furthermore, in our study, the algorithm used for P-SPECT is a straightforward implementation of the OSEM method for the pinhole geometry without any compensation for resolution recovery. This correction has been recently evaluated by two studies (using either a multi-ray approach [24] or a point-spread function based resolution recovery [25]) and was found to improve markedly the trade-off between spatial resolution and noise. This correction should be added in future algorithm development.

Conclusion

The use of a pinhole collimator for SPECT in pHPT increases the sensitivity of scintigraphy and is very useful to confirm doubtful results of conventional scintigraphy. P-SPECT gives additional topographic information of benefit to the surgeon. Combined with double phase $^{99m}\mathrm{Tc}-\mathrm{MIBI}/^{99m}\mathrm{TcO}_4^-$, planar scintigraphy and neck US, P-SPECT appears to be a highly accurate procedure to select patients for minimally invasive surgery.

Acknowledgements The authors are very grateful to Pr. Michel Defrise from the Vrije Universiteit Brussel for providing the reconstruction algorithm dedicated to pinhole geometry. We would like to thank also Dr. Samantha Warren for her very useful suggestions.

References

1. Mariani G, Gulec SA, Rubello D, Boni G, Puccini M, Pelizzo MR, et al. Preoperative localization and radioguided parathyroid surgery. J Nucl Med 2003;44:1443–58.
2. Henry JF, Iacobone M, Mirallie E, Deveze A, Pili S. Indications and results of video-assisted parathyroidectomy by a lateral approach in patients with primary hyperparathyroidism. Surgery 2001;130:999–1004.
3. Arbab AS, Koizumi K, Toyama K, Arai T, Arak T. Ion transport systems in the uptake of 99Tcm-tetrofosmin, 99Tcm-MIBI and 201Tl in a tumour cell line. Nucl Med Commun 1997;18:235–40.
4. Carpentier A, Jeannotte S, Verreault J, Lefebvre B, Bisson G, Mongeau CJ, et al. Preoperative localization of parathyroid lesions in hyperparathyroidism: relationship between technetium-99m-MIBI uptake and oxyphil cell content. J Nucl Med 1998;39:1441–4.
5. Caillard C, Sebag F, Mathonnet M, Gibelin H, Brunaud L, Loudot C, et al. Prospective evaluation of quality of life (SF-36v2) and nonspecific symptoms before and after cure of primary hyperparathyroidism (1-year follow-up). Surgery 2007;141:153–9.
6. Moka D, Voth E, Dietlein M, Larena-Avellaneda A, Schicha H. Technetium 99m-MIBI-SPECT: a highly sensitive diagnostic tool for localization of parathyroid adenomas. Surgery 2000;128:29–35.
7. Biertho LD, Kim C, Wu HS, Unger P, Inabnet WB. Relationship between sestamibi uptake, parathyroid hormone assay, and nuclear morphology in primary hyperparathyroidism. J Am Coll Surg 2004;199:229–33.
8. Sharma J, Mazzaglia P, Milas M, Berber E, Schuster DM, Halkar R, et al. Radionuclide imaging for hyperparathyroidism (HPT): which is the best technetium-99m sestamibi modality? Surgery 2006;140:856–63.
9. Lorberboym M, Minski I, Macadziob S, Nikolov G, Schachter P. Incremental diagnostic value of preoperative 99mTc-MIBI SPECT in patients with a parathyroid adenoma. J Nucl Med 2003;44:904–8.

10. Billotey C, Sarfati E, Aurengo A, Duet M, Mundler O, Toubert ME, et al. Advantages of SPECT in technetium-99m-sestamibi parathyroid scintigraphy. J Nucl Med 1996;11:1773–8.
11. Ansquer C, Mirallie E, Sadot S, Couturier O, Valette F, Kraeber-Bodéré F. Comparison of 99mTc-MIBI / 99mTc dual planar scintigraphy, 99mTc-MIBI SPECT and ultrasound in preoperative localization of parathyroid lesions for primary hyperparathyroididsm [abstract]. Eur J Nucl Med Mol Imaging 2005;31(Suppl):S263.
12. Arveschoug AK, Bertelsen H, Vammen B. Presurgical localization of abnormal parathyroid glands using a single injection of Tc-99m sestamibi: comparison of high-resolution parallel-hole and pinhole collimators, and interobserver and intraobserver variation. Clin Nucl Med 2002;27:249–54.
13. Spanu A, Falchi A, Manca A, Marongiu P, Cossu A, Pisu N, et al. The usefulness of neck pinhole SPECT as a complementary tool to planar scintigraphy in primary and secondary hyperparathyroidism. J Nucl Med 2004;45:40–8.
14. Profanter C, Gabriel M, Wetscher GJ, Gadenstatter M, Mittermair R, Moncayo R, et al. Accuracy of preoperative pinhole subtraction single photon emission computed tomography for patients with primary and recurrent hyperparathyroidism in an endemic goiter area. Surg Today 2004;34:493–7.
15. Seret A, Defrise M, Blocklet D. 180 degree pinhole SPET with a tilted detector and OS-EM reconstruction: phantom studies and potential clinical applications. Eur J Nucl Mol Imaging 2001;28:1836–41.
16. Wanet PM, Sand A, Abramovici J. Physical and clinical evaluation of high-resolution thyroid pinhole tomography. J Nucl Med 1996;37:2017–20.
17. Vanhove C, Defrise M, Franken PR, Everaert H, Deconinck F, Bossuyt A. Interest of the ordered subsets expectation maximization (OS-EM) algorithm in pinhole single-photon emission tomography reconstruction: a phantom study. Eur J Nucl Med Mol Imaging 2000;27:140–6.
18. Carlier T, Bodet-Milin C, Oudoux A, Defrise M, Seret A, Couturier O, et al. Technical feasibility of pinhole SPECT acquisition in primary hyperparathyroidism: phantoms and patients studies [abstract]. J Nucl Med 2006;47(Suppl):378P.
19. Smith MF, Jaszczak RJ. Penetration and angle-dependent sensitivity for pinhole collimation. Med Phys 1997;24:1701–9.
20. Palmer J, Wollmer P. Pinhole emission computed tomography: method and experimental evaluation. Phys Med Biol 1990;35: 339–50.
21. Chevallier JM, Martelli H, Wind P. Surgical discovery of parathyroid glands and the recurrent laryngeal nerve. Application of well known embryological concepts in the operating room. Ann Chir 1995;49:296–304.
22. Freudenberg LS, Frilling A, Sheu SY, Görges R. Optimizing preoperative imaging in primary hyperparathyroidism. Langenbecks Arch Surg 2006;391:551–6.
23. Rubello D, Gross MD, Mariani G, Al-Nahhas A. Scintigraphic techniques in primary hyperparathyroidism: from pre-operative localisation to intra-operative imaging. Eur J Nucl Med Mol Imaging 2007;926–33.
24. Vanhove C, Andreyev A, Defrise M, Nuyts J, Bossuyt A. Resolution recovery in pinhole SPECT based on multi-ray projections: a phantom study. Eur J Nucl Med Mol Imaging 2007;34:170–80.
25. Sohlberg A, Watabe H, Zeniya T, Iida H. Comparison of multi-ray and point-spread function based resolution recovery methods in pinhole SPECT reconstruction. Nucl Med Commun 2006;27:823–7.

Phys. Med. Biol. **55** (2010) N253–N266 doi:10.1088/0031-9155/55/9/N04

NOTE

Implementation of angular response function modeling in SPECT simulations with GATE

P Descourt[1], T Carlier[2,3], Y Du[4], X Song[4], I Buvat[5], E C Frey[4], M Bardies[2], B M W Tsui[4] and D Visvikis[1]

[1] INSERM, U650, LaTIM, IFR SclnBioS; Université de Brest; CHU Brest; Brest, F-29200, France
[2] CRCNA INSERM U892, Nantes, France
[3] Service de Médecine Nucléaire, Centre Hospitalier Universitaire, Nantes, France
[4] Department of Radiology, J Hopkins University, Baltimore, MD, USA
[5] IMNC–UMR 8165 CNRS Universités Paris 7 et Paris 11, Orsay, France

E-mail: dimitris@univ-brest.fr

Received 1 November 2009, in final form 11 March 2010
Published 14 April 2010
Online at stacks.iop.org/PMB/55/N253

Abstract

Among Monte Carlo simulation codes in medical imaging, the GATE simulation platform is widely used today given its flexibility and accuracy, despite long run times, which in SPECT simulations are mostly spent in tracking photons through the collimators. In this work, a tabulated model of the collimator/detector response was implemented within the GATE framework to significantly reduce the simulation times in SPECT. This implementation uses the angular response function (ARF) model. The performance of the implemented ARF approach has been compared to standard SPECT GATE simulations in terms of the ARF tables' accuracy, overall SPECT system performance and run times. Considering the simulation of the Siemens Symbia T SPECT system using high-energy collimators, differences of less than 1% were measured between the ARF-based and the standard GATE-based simulations, while considering the same noise level in the projections, acceleration factors of up to 180 were obtained when simulating a planar 364 keV source seen with the same SPECT system. The ARF-based and the standard GATE simulation results also agreed very well when considering a four-head SPECT simulation of a realistic Jaszczak phantom filled with iodine-131, with a resulting acceleration factor of 100. In conclusion, the implementation of an ARF-based model of collimator/detector response for SPECT simulations within GATE significantly reduces the simulation run times without compromising accuracy.

1. Introduction

Monte Carlo (MC) simulations play an important role in medical imaging and radiotherapy (Zaidi 1999, Rogers 2006, Visvikis *et al* 2006, Verhaegen and Seuntjens 2003). In medical

imaging, simulations are primarily used for the design and optimization of new and existing imaging devices, and for the assessment of acquisition and processing protocols. Among the MC codes available for simulations in emission tomography (Buvat and Castiglioni 2002), GATE, the Geant4 Toolkit for Emission Tomography, is a powerful, reliable and versatile tool for simulating PET and SPECT scans (Jan *et al* 2004). However, GATE simulations are often lengthy. One of the most significant reasons is the low efficiency of Geant4 for tracking photons in a geometry described as a large set of voxels. This limitation has been recently tackled by implementing fictitious interactions in GATE (Rehfeld *et al* 2009), or by separating the phantom and detector parts of the simulation, either within GATE (Descourt and Visvikis 2008) or combining GATE with SimSET/PHG so that the latter manages the photon tracking in the voxelized phantom before the propagation results are fed to GATE which manages the detector and associated electronics modeling (Chen *et al* 2008). A second reason for the long simulation times is the precise modeling of the collimator in SPECT, where photon tracking in the collimator is extremely time consuming. Because parallel hole collimators are composed of thousands of holes, the photon tracking accounting for septal penetration and interactions, such as Compton scattering, photo-electric absorption and x-ray fluorescence, is computationally very demanding. For realistic parallel hole collimators, roughly one 140 keV photon over 640 entering the collimator is detected for a low-energy high-resolution collimator (148 000 holes for a 53×39 cm^2 surface) in a 15% energy window and only one 364 keV photon over 1550 for a high-energy collimator (8000 holes for a 53×39 cm^2 surface). Yet, the precise modeling of the collimator/detector response is essential for accurate simulations of SPECT datasets, especially when septal penetration and scattering in the collimator are prominent (Dewaraja *et al* 2000, Rault *et al* 2007). For example collimator scatter could account for as much as 30% of the detected counts in a 20% window around 364 keV (Dewaraja *et al* 2000) for I-131 imaging. In this note, we address this specific issue of computationally demanding particle tracking in the collimator within the GATE MC simulation platform.

One approach to tackle this problem consists in using a tabulated modeling of the collimator/detector response instead of tracking each particle in the collimator. Early work regarding the tabulation of the detector point spread function (PSF) was proposed for the Utrecht Monte Carlo System (Beekman *et al* 1999). This idea was next incorporated in various MC codes using the concept of convolution-based forced detection (CFD) and validated for ^{99m}Tc (de Jong *et al* 2001, Liu *et al* 2008, De Beenhouwer *et al* 2008). However, these methods did not consider the septal penetration component, given that septal penetration can be neglected for the low-energy photons (140 keV) of ^{99m}Tc. More recently, a fast method was developed for incorporating the effects of septal penetrating photons and was validated for ^{201}Tl and ^{111}In (Staelens *et al* 2007), showing a reduction in computation time by up to four orders of magnitude associated with small accuracy losses (7% and 8% for ^{201}Tl and ^{111}I, respectively, considering an optimum, in terms of accuracy loss and speed improvement, object voxelization and detector pixelization). This approach has not been assessed in the context of ^{131}I and the use of high-energy collimators.

The method presented in this work and implemented in GATE is also based on the use of tabulated responses, namely angular response functions (ARF) (Frey and Tsui 2006). The ARF is a function of energy and direction of the incident photon. It represents the probability that a photon hitting the surface of the collimator will either interact with or pass through the collimator and be detected, with an energy included in a given energy range, at the intersection point of the photon direction vector and the detection plane. These functions once tabulated and computed for a given collimator/detector pair and energy window, may be subsequently used for any simulation involving this specific collimator/detector pair. Like in CFD, the use

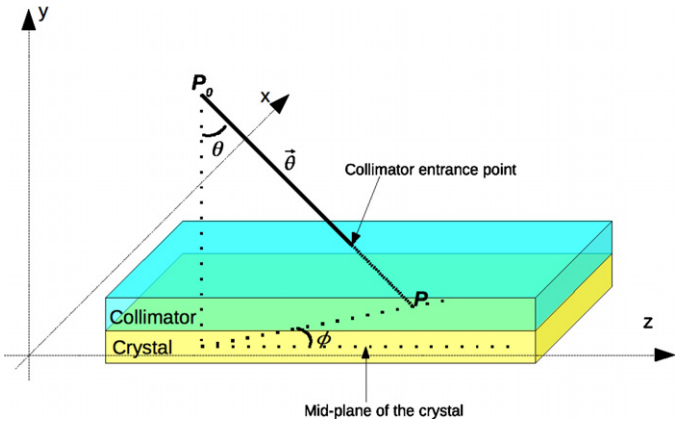

Figure 1. Angular parameterization of the ARF method. P_0 is the emission point. P is the geometric point of intersection of the photon, defined as the intersection of the line with direction $\vec{\theta}$ considering the mid-plane of the crystal.

of these functions removes the need for tracking the photons inside the collimator/detector volumes, which in turn yields significant reductions in run time.

In the implementation described here, an integrated solution is proposed in the sense that GATE manages both the generation of the ARF tables and their use in subsequent simulations. The model accuracy and associated run times are assessed for the elementary SPECT system used in the GATE SPECT benchmark and for a realistic clinical SPECT system.

2. Materials and methods

2.1. Angular response function

The angular response function refers to the spatial distribution of photons detected for a given point source position. It is related to the collimator/detector response function (CDRF) which is the image generated from a point source. The ARF is a function of the polar angle θ and azimuthal angle ϕ of incidence of a photon with respect to the collimator surface (figure 1), the incident energy, the energy window of interest and the energy resolution of the system.

The CDRF is the primary factor determining the image resolution in SPECT (Frey and Tsui 2006). It represents the probability that photons emitted at some point in space will be detected at a given position on the detection plane. This CDRF can be decomposed into four components: (1) the intrinsic response function (response of the scintillation camera without any collimator to a pencil beam of radiation), (2) the geometric response function (response to detected photons which travel through the collimator holes without interaction), (3) the septal penetration response function (response to photons which go through the collimator septa) and (4) the septal scatter response function (response to photons which scatter in the collimator septa).

As described in Song *et al* (2005), a key approximation of the ARF model is that a photon interacting with the collimator can be assumed to be detected at the geometric intersection point defined as the point where the incident photon direction vector intersects the detection plane usually taken halfway through the crystal thickness. The ARF should actually also depend on

the position of the incidence of the photon relative to the collimator surface. However, when the collimator septal thickness is small compared to the intrinsic resolution (including pixel size effects), the CDRF may be approximated as being spatially invariant over the collimator unit cell.

The value of the ARF table normalized to an incident photon for a given solid angle (θ, ϕ) is given by

$$P(\theta, \phi) = \frac{N_{\text{counts}}(E_{\text{in}}, R, E_T, E_u, \theta, \phi)}{N(\theta, \phi)} \tag{1}$$

where E_{in} is the photon incident energy, R is the detector energy resolution and the range $[E_T, E_u]$ defines the energy window of interest. The numerator N_{counts} is the contribution of all the photons which deposit energy in the infinitesimal solid angle $\Delta\Omega(\theta, \phi)$ and the denominator N denotes the number of photons whose incidence vector is located within this same solid angle $\Delta\Omega(\theta, \phi)$. If N_0 denotes the total number of simulated photons in a 4π steradian solid angle, we have

$$N(\theta, \phi) = \frac{\Delta\Omega(\theta, \phi)}{4\pi} \quad N_0. \tag{2}$$

2.2. ARF table computation within GATE

The strategy used in Song *et al* (2005) for the implementation of the ARF approach took advantage of the SIMSET/PHG simulation code to generate the list mode files from which the ARF tables were deduced using external programs. In our implementation, the data needed for calculating the ARF tables are produced with GATE and used within GATE to derive the CDRF tables. New C++ classes have been designed to handle all tasks with versatile GATE script commands that allow the user to generate and compute the tables (Descourt *et al* 2008). This new development is publicly available since the GATE version 5.0.0. The ARF computation process can be divided into two separate steps as are described below.

First, photons are emitted from a rectangular source in air within a given incident energy window. The source to collimator distance was set to 34 cm. This distance was chosen so that the rectangular source covered several holes to average out the effects of the collimator hole pattern (Song *et al* 2005). The photons undergoing photoelectric absorption in the crystal (after Compton interactions or not) are collected, and the deposited energy and corresponding incidence angles with respect to the collimator plane are stored into ROOT files (http://root.cern.ch/drupal).

In the second step, the collected data are used to generate the ARF table for a given incident energy or a small incident energy window. This ARF table is computed for a given energy resolution and energy window of interest. In this work, two different ARF tables were calculated for comparison purposes.

- The raw ARF table (denoted by ARF_r) is directly computed from equations (1) and (2),
- In addition to the solid angle binning used for the ARF_r, the emission point coordinates are subtracted from the detection point coordinates. The detected photons are subsequently binned on the detection plane to derive the CDRF. For each solid angle bin, the averaged sum in the CDRF table of all the bins inside a disk with a fixed radius is computed. The ARF tables are then deduced from the CDRF. These ARF tables are denoted as 'averaged tables' (ARF_a).

Table 1. Characteristics of the two SPECT systems simulated in this work.

SPECT system	Benchmark SPECT (scripted within GATE)	Clinical system (Siemens Symbia T)
Collimator		
Number of hexagonal parallel holes	18 000	8000
Hole length (mm)	30	59.7
Hole inner radius (mm)	1.5	2
Septal thickness (mm)	0.6	2
Transverse dimension (cm^2)	19×28	57×44
NaI(Tl) crystal thickness (mm)	10	9.5

2.3. Sampling of ARF tables

The ARF tables were calculated considering photons with energy between 364 and 365 keV for the simulations involving only a monoenergetic source of 364 keV. In this case, 10 billion photons were simulated to compute each of the ARF tables (one for the SPECT benchmark set-up and one for the clinical system, described in section 2.4 below). When considering simulations in a scattering medium for the iodine-131 source with several emission energies (364.5 keV, 637 keV and 723 keV for the main photopeaks), a set of 44 ARF_a tables were computed. The spectrum of iodine-131 was sampled in 10 keV wide energy intervals from 304 to 364 keV (6 intervals), 365 to 635 keV (27 intervals) and 639 to 709 keV (7 intervals). Three additional tables were computed for the three main emission photopeaks (ranges: 364–365 keV, 635–639 keV and 722–723 keV for the 364 keV, 637 keV and 723 keV, respectively). The last ARF table covered the range from 709 to 722 keV. Five billion up to 80 billion photons were simulated in 4π steradians for the simulation of each ARF table.

2.4. Validation

Two detector models were considered. The first was the hypothetical detector used in the SPECT benchmark provided with the GATE distribution (GATE user's guide, www.opengatecollaboration.org). The second was a model of the Siemens Symbia T system (Carlier *et al* 2008) equipped with a high-energy collimator. The main properties of these two systems are summarized in table 1. For both setups, all images were 128×128 (pixel size: 4.8×4.8 mm^2).

A point source was first simulated in air. Profiles across the point sources were drawn for visual comparison of the standard (sGATE) and ARF-based (ARF–GATE) GATE simulations. A root mean squared difference index (RMSD) was also calculated to measure the agreement between sGATE and ARF–GATE using

$$\mathrm{RMSD(ARF, sGATE)} = \sqrt{\frac{1}{N}\sum_{k=1}^{N}\left(B_k^{\mathrm{ARF}} - B_k^{\mathrm{sGATE}}\right)^2} \tag{3}$$

where B_k^{ARF} is the content of voxel k in ARF-simulated images $\left(B_k^{\mathrm{sGATE}}\right.$ is for the sGATE simulated images, respectively$\left.\right)$. For RMSD calculation, the images were first normalized to 1.0 and the computation was performed only for pixel values greater than 0.1.

A uniform planar source (30×30 cm^2) was also simulated in air with all photons forced in the solid angle of the detector plane. Profiles through the sGATE and ARF–GATE images were drawn, and RMSD was calculated. The acceleration factor resulting from ARF–GATE

was computed considering the same statistical quality between ARF–GATE and sGATE simulations. The statistical quality was defined as the standard deviation divided by the mean over a region of interest (ROI) including at least 400 pixels within the image of the uniform source.

The clinical SPECT system sensitivity (counts MBq^{-1} s^{-1}) was derived based on ten simulations (16 s each) of a point source (3 MBq in 4π sr). The count density in the images was computed and normalized by the activity and the time. Mean and standard deviations of total count density were derived from the ten independent simulations.

For the point source and planar source simulations, 364 keV photons were simulated to assess the use of ARF–GATE for simulations involving a monoenergetic source in air and a 15% energy window around 364 keV was considered for detection.

The computational efficiency was also estimated for a realistic Jaszczak phantom (diameter: 21.6 cm; length: 18.6 cm) uniformly filled with iodine-131 and centered in the field of view. SPECT simulations involving four heads of the Siemens Symbia T system with 64 projections (16 steps per head; projection matrix size: $64 \times 64 \times 64$; pixel size: 9.6×9.6 mm^2) were performed using sGATE and ARF–GATE. The simulation results were compared by calculating the RMSD for the two sets of 64 projections. The acceleration factor was calculated when reaching the same noise level in the projections for the two simulations. The noise level was calculated first in each projection, as the standard deviation divided by the mean over a region of interest (ROI) including at least 400 pixels and then averaged over all projections. This noise level is not intended to be a reliable measurement of noise partly because of the spatially dependent attenuation effect but rather as an index of comparison between two datasets corresponding to the same set-up.

3. Results

For the GATE SPECT benchmark, the ARF tables are shown in figure 2. The averaged table, ARF_a (figure 2(B)), is computed from the smooth CDRF (figure 3(A)). The hole effect pattern seen in figure 3(B) is removed in ARF_a (figure 2(B)). The ARF_r and ARF_a tables computed for the clinical SPECT camera are shown in figure 4.

The ARF profile for the 0° polar angle is shown in figure 2 for the GATE SPECT benchmark and in figure 4 for the clinical SPECT camera. The noisy nature of the ARF_r table compared to the ARF_a tables is clearly demonstrated, as well as the 'wavy' behavior at a low azimuthal angle induced by the hole pattern effect. This effect at low incidence angles may come from the septal thickness that modifies the CRDF by introducing the honeycomb structure from the collimator hexagonal holes (see figure 3(B)).

Figure 5 shows the projections obtained using the GATE SPECT benchmark and the clinical SPECT system for the point source simulations using the ARF_r, ARF_a tables and sGATE simulations. The ARF–GATE and sGATE projections agreed well. The RMSD averaged over the 64 projections were 0.02 for the SPECT benchmark and 0.09 for the clinical SPECT system when comparing sGATE and ARF_r. The RMSD were also 0.02 for the SPECT benchmark and 0.09 for the clinical SPECT system when comparing sGATE and ARF_a. As negligible differences were found between ARF–GATE simulations performed with either ARF_r or ARF_a tables in terms of both visual and quantitative agreements, all subsequent ARF–GATE simulations used the ARF_a table.

The images and x-axis profiles of the uniform source are presented in figure 6 for the SPECT benchmark and clinical SPECT systems. The RMSD for this emission geometry were 0.02 and 0.09 for the SPECT benchmark and clinical SPECT system, respectively. An RMSD of 0.09 was also found when repeating two independent sGATE simulations for the

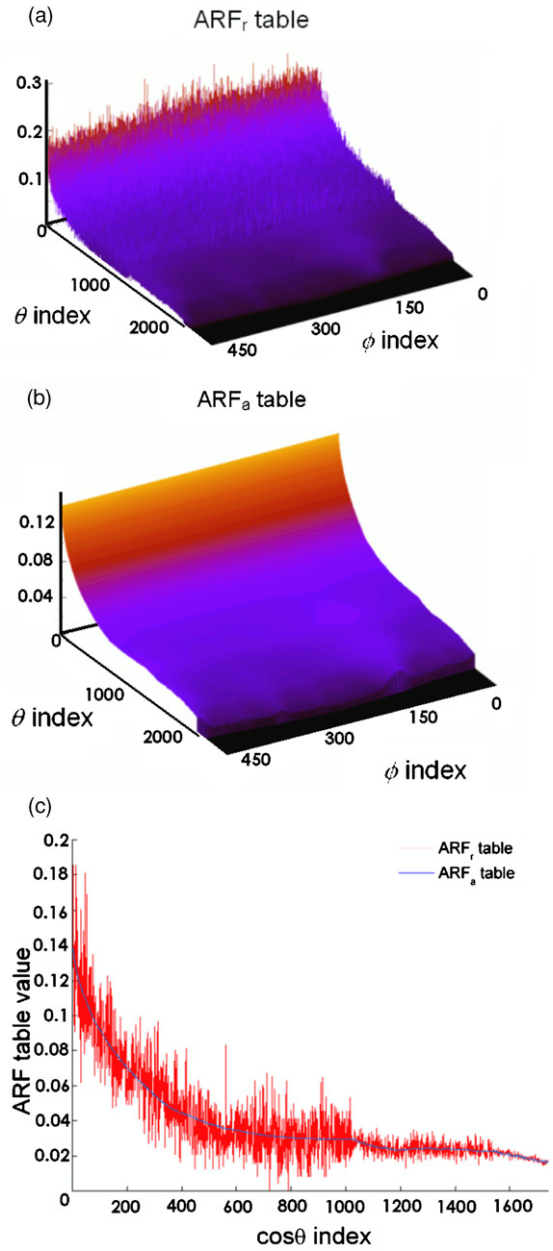

Figure 2. 2D ARF tables derived for the GATE benchmark SPECT system. (A) Raw ARF table, ARF_r; (B) averaged ARF table, ARF_a; (C) ARF profiles for a 0° polar angle: ARF_r versus ARF_a table for the GATE SPECT benchmark. The x-axis units are for the parameterization of $\cos\theta$ ($\cos\theta$ ranges from 0 to 1 and is binned in 2048 bins).

clinical SPECT system, suggesting that there are equivalent differences between two sGATE simulations and that obtained between an sGATE and an ARF–GATE simulation and that the observed RMSD is mostly due to statistical fluctuations.

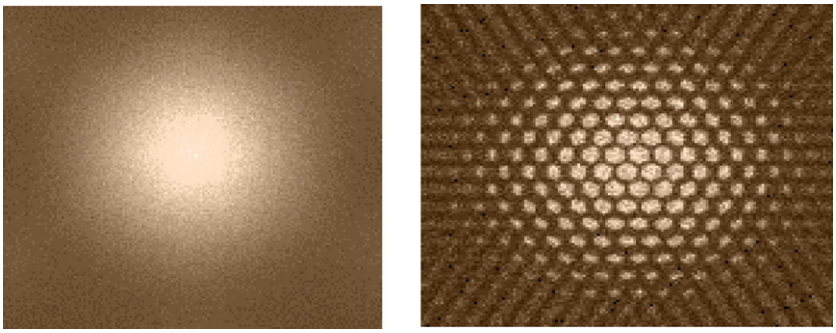

(a) (b)

Figure 3. Hole effect pattern on the collimator/detector response function (CDRF). Right: raw CDRF image, left: smoothed CDRF image.

Table 2. Computational efficiency for the GATE benchmark SPECT and clinical SPECT system simulations.

		sGATE	ARF–GATE	Noise level (%)
GATE SPECT benchmark	Number of photon for one run of simulation	5 millions	5 millions	3.8
	Duration time for one run	1148 s	1058 s	
	Number of runs to achieve the same noise level	10	1	
	Total duration time	11 220 s	922 s	
	Speed-up factor	12		
Clinical SPECT system	Number of photon for one run of simulation	20 millions	20 millions	9.8
	Duration time for one run	7520 s	1590 s	
	Number of runs to achieve the same noise level	38	1	
	Total duration time	285 760 s	1590 s	
	Speed-up factor	180		

Fifty million emitted photons were used in the simulation of the sGATE image of the uniform source for the SPECT benchmark simulation, and 7.6 million photons were detected in the 15% energy window. For the simulation of the uniform source in combination with the simulated clinical SPECT system, 760 million photons were emitted in the sGATE simulation and 0.5 million were detected in the 15% energy window. The sGATE simulation took approximately 11 000 s (2.6 GHz Intel core 2 duo) for the SPECT benchmark and 286 000 s for the Siemens Symbia (dual 2.5 GHz PowerPC G5). To achieve the same noise level in the simulated projections (table 2) as when using sGATE, only 5 million and 20 million photons were needed with the ARF–GATE simulation for the SPECT benchmark and the Siemens Symbia SPECT systems, respectively, corresponding to run times of 922 s and 1590 s, respectively, on the same computer specifications. The acceleration factors between ARF–GATE and sGATE were thus approximately 12 for the SPECT benchmark and 180 for the Siemens Symbia SPECT simulations. The same noise level could be reached with 10 and

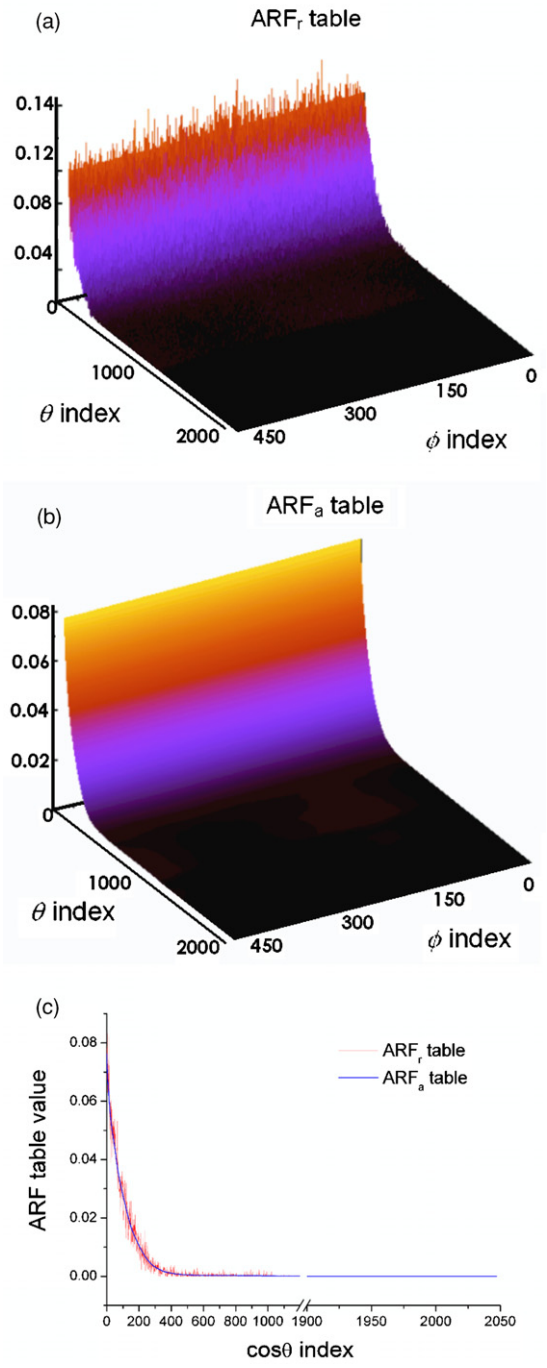

Figure 4. ARF tables generated for the high-energy collimator of the SIEMENS Symbia T clinical SPECT system when considering 364 keV emitted photons. (A) ARF$_r$ table. (B) ARF$_a$ table. (C) ARF profiles for a 0° polar angle: ARF$_r$ versus ARF$_a$ table for the clinical SPECT system. The x-axis units are for the parameterization of $\cos\theta$ ($\cos\theta$ ranges from 0 to 1 and is binned in 2048 bins but only the first 750).

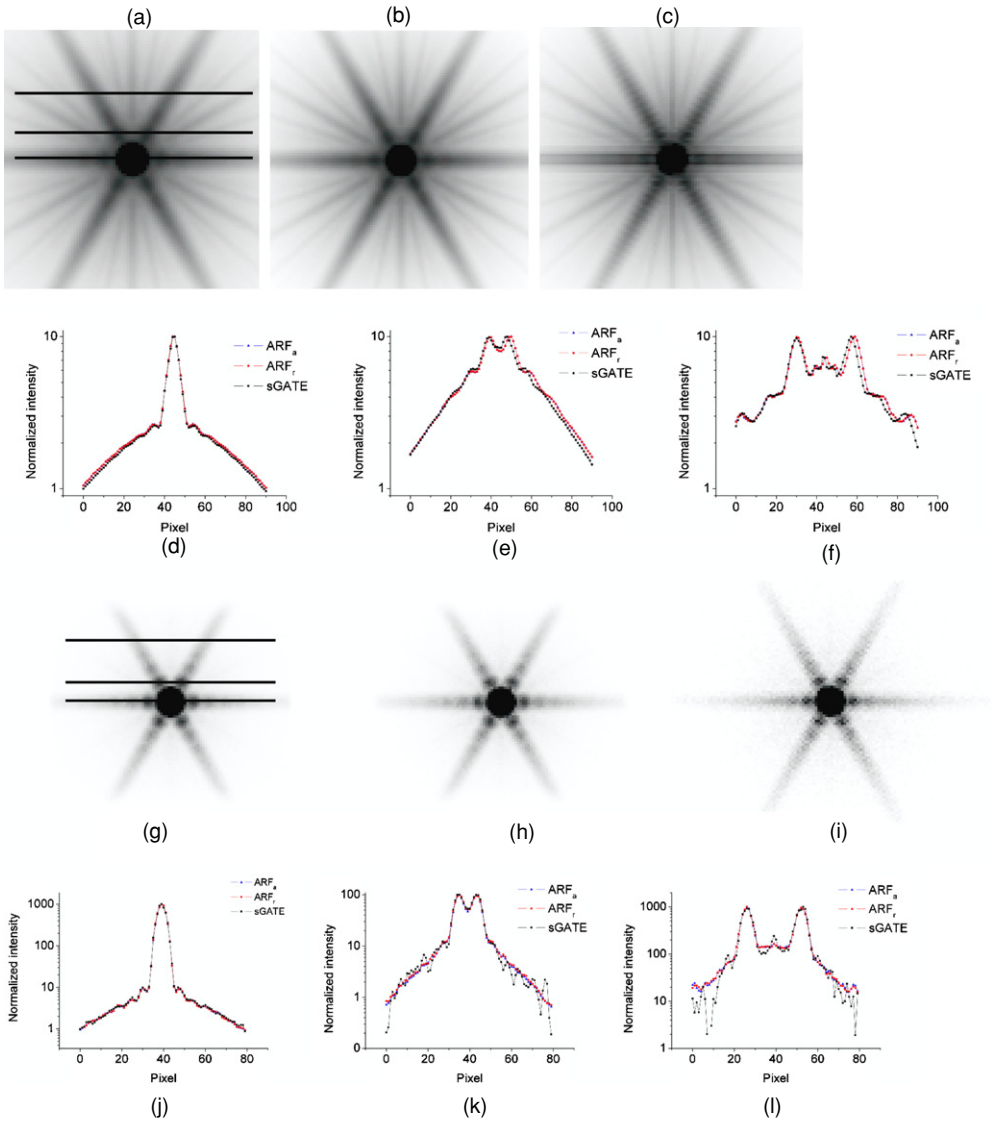

Figure 5. Projection images of a 364 keV point source in air for the collimator/detector of the GATE SPECT benchmark (A), (B) and (C), and the SIEMENS Symbia T SPECT system (G), (H) and (I). The image contrast was enhanced to highlight the common star structure. (A), (G) Images computed with the ARF_a table. (B), (H) Images computed with the ARF_r table. (C), (I) Images computed with sGATE. *X*-axis profile for ARF–GATE computed using the ARF_r table (red), the ARF_a table (blue) and sGATE (black) for the GATE SPECT benchmark (D), (E) and (F), and the SIEMENS Symbia T SPECT system (J), (K) and (L). The line profiles are drawn in black on the ARF_a projection for the GATE SPECT benchmark and the SIEMENS Symbia T SPECT system.

38 times less photons for the SPECT benchmark and the Siemens Symbia SPECT systems simulations, respectively, when ARF–GATE was used (table 2). The speed-up factor obtained when comparing ARF–GATE with sGATE for the tracking of photons inside the collimator only was also calculated based on a single simulation run considering the clinical SPECT

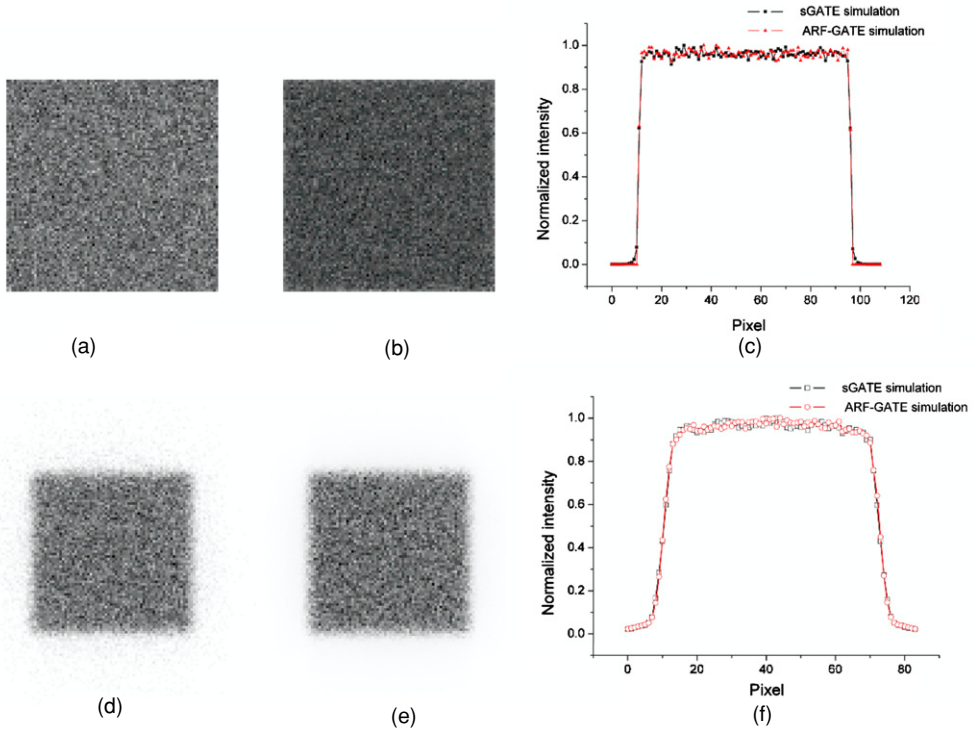

Figure 6. Simulation of the uniform source with 364 keV photons for the GATE SPECT benchmark (A) and (B), and the SIEMENS Symbia T SPECT system (D) and (E). (A), (D) sGATE images of the uniform source. (B), (E) ARF–GATE images of the uniform source. (C), (F) Profiles for ARF–GATE and sGATE.

system (table 2). In this case, the ARF approach lead to an acceleration factor of 11 for a same number of photons reaching the collimator.

The overall system sensitivity was similar for the ARF–GATE (41.9 $\pm$ 1.5 counts MBq^{-1} s^{-1}) and sGATE (41.8 $\pm$ 1.8 counts MBq^{-1} s^{-1}) simulations for the clinical SPECT system.

The complete SPECT simulation of the Jaszczak phantom with sGATE took 33 400 CPU hours. The same simulation with ARF–GATE took 341 CPU hours for the same level of noise in the projections, corresponding to an $\sim \times 100$ acceleration. With the use of ARF–GATE, the same image quality could be reached with 38 times less photons. The profiles of one projection for sGATE and ARF–GATE are shown in figure 7.

4. Discussion

This note describes the validation and evaluation of the implementation of the ARF modeling within the GATE simulation platform. The use of ARF tables within GATE is straightforward. First, the ROOT files produced by the simulation of a rectangular source with the model of the SPECT system of interest are stored. Second, the ARF tables are computed for a given energy window either using equation (1) or based on the computation of the averaged CDRF table.

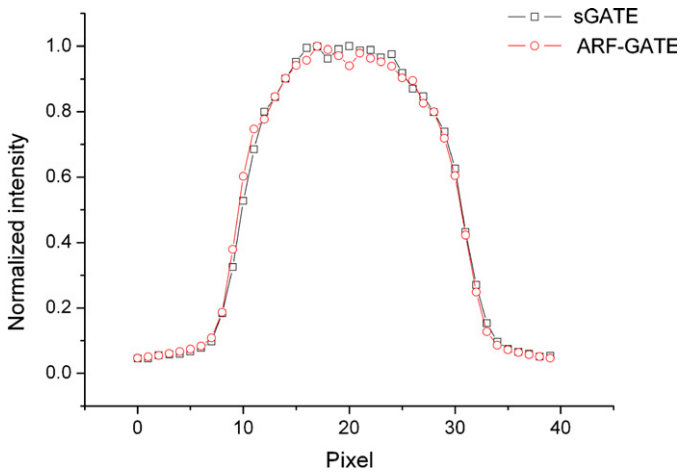

Figure 7. Profiles through a projection for the SPECT simulation of the Jaszczak phantom using ARF–GATE and sGATE.

The use of the averaged ARF tables reduced the local fluctuations introduced by the hole pattern at low azimuthal angles. No RMSD differences were found between the use of the raw and the averaged ARF tables for the simulation of the point source. This is because in the regions of the highest signal (>10% of the maximum value), the high uncertainties affecting the ARF values of the raw ARF table cancel out given that many photons are detected in these regions. No significant differences were found when comparing ARF-based GATE simulations and those using standard collimator/detector photon tracking for the two detection systems considered here (the hypothetical detector of the GATE SPECT benchmark and the Symbia T camera). This suggests that even for challenging acquisition conditions where septal penetration is high (like in the SPECT benchmark, where 364 keV photons are acquired with the low-energy high-resolution collimator), the results obtained using ARF–GATE simulations are consistent with those of the sGATE simulation. However, as it could be noted in figures 5(D)–(F) and 6(D) and (E), the projections computed with ARF–GATE tend to be more blurred than the one computed with sGATE. This is a direct consequence of the use of the ARF table without the effect of the hole pattern (figure 3(A)). In this case, the pixel size (4.8×4.8 mm^2) is of the same order of magnitude as the collimator hole diameter (4 mm for the clinical SPECT system considered). As the hole pattern is removed when using the ARF approach, the pixelized behavior of the projection due to the similarity between the pixel size and the collimator hole diameter is also removed compared with the projections simulated with sGATE.

The acceleration factors achieved with ARF–GATE were dependent on the type of collimator used, with a larger impact for the high-energy collimators associated with a larger number of photon interactions within the collimator. The computational efficiency increased by more than two orders of magnitude when ARF–GATE was used for 364 keV photons in air. In a more realistic situation, when considering the complete iodine-131 spectrum in a scattering medium, in combination with a camera equipped with a realistic high-energy collimator, a speed-up factor of ~100 was observed. This acceleration factor cannot be readily compared with those reported in Song *et al* (2005), which were derived only based on a visual comparison of the noise texture in the projection images. The comparison of acceleration factors and accuracy with those achieved using other acceleration methods such as CFD is

also difficult as almost no study deals with iodine-131. A recent work of Khosravi *et al* (2007) using the CFD methodology with iodine-131 showed a speed-up factor of roughly 10 without loss of accuracy when comparing with simulation including forced detection only, but this work does not include any detailed report regarding the validation of the simulated collimator response compared to real collimator response.

A major approximation involved in the ARF method is the assumption that the septal thickness is small compared to the intrinsic resolution (including the pixel size effect). For the clinical SPECT system considered here, the ratio of the intrinsic resolution to the septal thickness is 2.5 (and 10 for the GATE SPECT benchmark) compared to 5 for the medium energy collimator of the GE Millennium VG SPECT previously used by Song *et al* (2005). However, the low intrinsic resolution to septal thickness ratio did not have a significant effect on the quantitative results. A ratio of 2.5 could thus be considered as sufficient to compute reliable ARF tables for high-energy collimators.

5. Conclusions

The ARF model for SPECT simulations was implemented within GATE. This implementation reduces the computation time by a factor between 10 and 100, through a decrease of both the time needed to transport the photons and the number of photon decays necessary to obtain a given noise level in the simulated projections.

Acknowledgments

This work was supported by the Cancéropôle Grand Ouest (contract R05014NG) and the French National Research Agency (ANR) (ANR-06-CIS6-004-03).

References

Beekman F J, de Jong H W A M and Slijpen E T P 1999 Efficient SPECT scatter calculation in non-uniform media using correlated Monte Carlo simulation *Phys. Med. Biol.* **44** N183–92

Buvat I and Castiglioni I 2002 Monte Carlo simulations in SPET and PET *Q. J. Nucl. Med.* **46** 48–61

Carlier T, Moisan M, Ferrer L, Kraeber-Bodéré F, Barbet J and Bardies M 2008 Validation of a GATE model of the Siemens Symbia system for 99mTc, ^{111}In and ^{131}I acquisitions *J. Nucl. Med.* **49** 404P

Chen C L, Wang Y, Lee J J and Tsui B M W 2008 Integration of SimSET photon history generator in GATE for efficient Monte Carlo simulations of pinhole SPECT *Med. Phys.* **35** 3278–84

De Beenhouwer J, Staelens S, Vandenberghe S and Lemahieu I 2008 Acceleration of GATE SPECT simulations *Med. Phys.* **35** 1476–85

de Jong H W A M, Slijpen E T P and Beekman F J 2001 Acceleration of Monte Carlo SPECT simulation using convolution-based forced detection *IEEE Trans. Nucl. Sci.* **48** 58–74

Descourt P, Du Y, Song X, Frey E C, Tsui B M W and Visvikis D 2008 Angular response function parameterization for collimator/detector in SPECT simulations within the GATE toolkit *IEEE NSS-MIC Conf. Rec.* pp 4969–71

Descourt P and Visvikis D 2008 Acceleration techniques for new detector architecture simulations *J. Nucl. Med.* **49** 405P

Dewaraja Y K, Ljungberg M and Koral K F 2000 Characterization of scatter and penetration using Monte Carlo simulation in ^{131}I imaging *J. Nucl. Med.* **41** 123–30

Frey E C and Tsui B M W 2006 *Quantitative Analysis in Nuclear Medicine Imaging* ed H Zaidi (Berlin: Springer) pp 141–66

Jan S *et al* 2004 GATE: a simulation toolkit for PET and SPECT *Phys. Med. Biol.* **49** 4543–61

Khosravi H R, Sarkar S, Takavar A, Saghari M and Shahriari M 2007 Planar and SPECT Monte Carlo acceleration using a variance reduction technique in I^{131} imaging *Iran. J. Radiat. Res.* **4** 175–82

Liu S, King M A, Brill A B, Stabin M G and Farncombe T H 2008 Accelerated SPECT Monte Carlo simulation using multiple projection sampling and convolution-based forced detection *IEEE Trans. Nucl. Sci.* **55** 560–7

Rault E, Vandenberghe S, Van Holen R, De Beenhouwer J, Staelens S and Lemahieu I 2007 Comparison of image quality of different iodine isotopes (I-123, I-124 and I-131) *Cancer Biother. Radiopharm.* **22** 423–30

Rehfeld N S, Stute S, Apostolakis J, Soret M and Buvat I 2009 Introducing improved voxel navigation and fictitious interaction tracking in GATE for enhanced efficiency *Phys. Med. Biol.* **54** 2163–78

Rogers D W 2006 Fifty years of Monte Carlo simulations for medical physics *Phys. Med. Biol.* **51** R287–301

Song X, Segars W P, Du Y, Tsui B M W and Frey E C 2005 Fast modelling of collimator-detector response in Monte Carlo simulation of SPECT imaging using the angular response function *Phys. Med. Biol.* **50** 1791–804

Staelens S, de Wit T and Beekman F 2007 Fast hybrid SPECT simulation including efficient septal penetration modeling (SP-PSF) *Phys. Med. Biol.* **52** 3027–43

Verhaegen F and Seuntjens J 2003 Monte Carlo modelling of external radiotherapy photon beams *Phys. Med. Biol.* **48** R107–64

Visvikis D, Bardies M, Chiavassa S, Danford C, Kirov A, Lamare F, Maigne L, Staelens S and Taschereau R 2006 Use of the GATE Monte Carlo package for dosimetry applications *Nucl. Instrum. Methods* A **569** 335–40

Zaidi H 1999 Relevance of accurate Monte Carlo modeling in nuclear medical imaging *Med. Phys.* **26** 574–608

IOP Publishing | Institute of Physics and Engineering in Medicine Physics in Medicine & Biology

Phys. Med. Biol. **59** (2014) 6417–6430 doi:10.1088/0031-9155/59/21/6417

Clinical NECR in 18F-FDG PET scans: optimization of injected activity and variable acquisition time. Relationship with SNR

T Carlier[1,2], L Ferrer[2,3], H Necib[2,4], C Bodet-Milin[1,2], C Rousseau[2,3] and F Kraeber-Bodéré[1,2,3]

[1] Nuclear Medicine Department, University Hospital of Nantes, Nantes, France
[2] CRCNA, UMR 892 INSERM, Nantes, France
[3] Nuclear Medicine Department, Integrated Center of Oncology, St Herblain, France
[4] Department of Radiology, University Hospital of Nantes, Nantes, France

E-mail: thomas.carlier@chu-nantes.fr

Received 18 March 2014, revised 11 August 2014
Accepted for publication 29 August 2014
Published 8 October 2014

Abstract

The injected activity and the acquisition time per bed position for 18F-FDG PET scans are usually optimized by using metrics obtained from phantom experiments. However, optimal activity and time duration can significantly vary from a phantom set-up and from patient to patient. An approach using a patient-specific noise equivalent count rate (NECR) modelling has been previously proposed for optimizing clinical scanning protocols. We propose using the clinical NECR on a large population as a function of the body mass index (BMI) for deriving the optimal injected activity and acquisition duration per bed position. The relationship between the NEC and the signal-to-noise ratio (SNR) was assessed both in a phantom and in a clinical setting. 491 consecutive patients were retrospectively evaluated and divided into 4 BMI subgroups. Two criteria were used to optimize the injected activity and the time per bed position was adjusted using the NECR value while keeping the total acquisition time constant. Finally, the relationship between NEC and SNR was investigated using an anthropomorphic phantom and a population of 507 other patients. While the first dose regimen suggested a unique injected activity (665 MBq) regardless of the BMI, the second dose regimen proposed a variable activity and a total acquisition time according to the BMI. The NEC improvement was around 35% as compared with the local current injection rule. Variable time per bed position was derived according to BMI and anatomical region. NEC and number of true events were found to be highly correlated with SNR for the phantom set-up and partially confirmed in the patient study for the BMI subgroup under 28 $kg\,m^{-2}$ suggesting that for the scanner, the nonlinear

reconstruction algorithm used in this study and BMI < 28 kg m^{-2}, NEC, or the number of true events linearly correlated with SNR^2.

Keywords: PET, NECR, activity

S Online supplementary data available from stacks.iop.org/PMB/59/216147

(Some figures may appear in colour only in the online journal)

1. Introduction

PET image quality can be assessed with a metric proposed by Strother in the 90s, termed the noise equivalent count rate (NECR) (Strother *et al* 1990). This index is calculated as the ratio of the square of the true events (useful signal) to the total events (true, random and scatter coincidences). It has been shown that the NECR is directly proportional to the SNR in the reconstructed volume when a linear reconstruction algorithm is used (Watson 2004). The evaluation of the NECR is mostly performed using a test object described by the NEMA NU2-2007 standard (National Electrical Manufacturers Association 2007) consisting of a cylinder of 20 cm diameter and 70 cm long. The use of the NECR for the purpose of optimizing the patient injected activity has been investigated in several studies (Badawi *et al* 1996, Lartizien *et al* 2002, Watson *et al* 2005, Danna *et al* 2006, Walker *et al* 2009, Accorsi *et al* 2010, Chang *et al* 2011, de Groot *et al* 2013). These studies differ in the assumptions used to establish the relationship between the NECR and the injected activity for a patient. One study assumes a linear relationship between acquisitions acquired with a phantom and a patient (Lartizien *et al* 2002), while other models rely on the patient-specific NECR from a unique count rate measurement obtained at the time of acquisition (Watson *et al* 2005, Danna *et al* 2006, Walker *et al* 2009, Accorsi *et al* 2010). Whilst some of these model the dead time which has an impact on true and random coincidences (Danna *et al* 2006), others explicitly model the singles rate, which is directly related to the number of true and random coincidences (Watson *et al* 2005, Walker *et al* 2009, Accorsi *et al* 2010). The method proposed by Watson *et al* (2005) and implemented in this work is based on; 1) the measurement of scanner live-time functions, and 2) the computation of patient-dependent constants that yield true and random coincidence count rates according to singles rate modeling. Although this approach was explictly used in the context of ^{15}O–H_2O exams, it has been never applied, to our knowledge, with a large number of adults patients for ^{18}F-FDG exams.

The aim of this study was to assess this methodology in a large retrospective series of patients with a first objective of optimizing the activity injected for an ^{18}F-FDG PET scan using a latest generation PET system. The new dose regimen were derived using patient data acquired with a conventional protocol without considering any optimization.

The second objective was to use this model to derive a variable acquisition time per bed position. Only a few studies have addressed this and are based exclusively on the average attenuation correction factor assuming a uniform distribution of activity in each region of the body (Carney *et al* 2004, Krizsan *et al* 2011). While an increased NECR may be due to clinically irrelevant counts, such as heart uptake or accumulation of tracer in the bladder, we hypothesize that NECR could be a valuable index to adapt the scan time for each bed position if a suitable weighting factor is used for those regions.

The third objective was to assess the relationship between NEC (or true events) and SNR when using a non-linear reconstruction algorithm. Previous studies were mainly focused on experimental data (Watson 2004, Dahlbom *et al* 2005, Chang *et al* 2012) and there is a need to assess the

relationship between SNR and NEC with patient data. For this purpose, a phantom experiment and a patient study were performed and compared to recent findings (Chang *et al* 2011, Chang *et al* 2012).

2. Materials and methods

2.1. PNECR and NECR

NECR was calculated using the following equation

$$\mathrm{NECR} = \frac{T^2}{T + S_{\mathrm{in}} + kR_{\mathrm{in}}} \tag{1}$$

where T, S_{in} and R_{in} are respectively the true, scattered and random coincidence rates within the boundary of the patient in the projection space. The constant k was set to 1 since we used randoms smoothing (Panin 2011). A metric closely related to the NECR can be also used (Watson *et al* 2003). This index, called pseudo-NECR (PNECR) is defined as

$$\mathrm{PNECR} = \frac{(T+S)^2}{T + S + R/2} \tag{2}$$

where T, S and R are respectively the true, scattered and random coincidence rates registered for the entire field-of-view (FOV). PNECR could also be expressed considering the total number of prompt (P) and random coincidences that could be derived, in practice, directly from the sinogram:

$$\mathrm{PNECR} = \frac{(P-R)^2}{P - R/2} \tag{3}$$

With some reasonable assumptions, Watson and colleagues hypothesized that NECR and PNECR are proportional. They validated this assumption with experimental data and we showed that, for clinical data, the linear relationship held true over a wide range of body mass index (BMI) (supplemental data (stacks.iop.org/PMB/59/216147)). NEC and PNEC are the NECR and PNECR multiplied by the acquisition time. PNECR was used for the first two parts of this work whereas NECR was used for the third part.

The Biograph mCT PET system (Siemens Healthcare Molecular Imaging USA, Inc.) with an extended axial FOV (21.8 cm) was used throughout this work.

2.2. Optimization of injected activity for PET acquisition

A thorough explanation of the formalism for the clinical modeling of NECR (or PNECR) can be found in Watson *et al* (2005) or Walker *et al* (2009). The proposed methodology was first validated with three phantoms simulating different BMI. We found a good correlation between experimental and modeled NECR (mean error < 3.5%) for a wide range of activity in the FOV (10–400 MBq) (data not shown).

A total of 491 patient scans were evaluated retrospectively using the conventional protocol before any optimizations. These patients were divided into four BMI subgroups: [16–22], [22–28], [28–32] and more than 32 $\mathrm{kg\,m^{-2}}$. PNECR was computed for the bed position encompassing the whole liver. The other bed positions were not considered for consistency with the third part of the study (relationship between SNR and NEC) and because the PNECR values (excluding the brain and the head and neck bed positions) were found very similar between each bed position from the base of the neck to the mid thigh. Unlike the original work of Watson *et al* (2005), the ^{18}F-FDG excretion was also taken into account (International

Commission on Radiation Protection 2008). This refinement was found to improve the accuracy of clinical PNECR modeling by approximately 5%.

Two criteria were considered:

(a) For each patient, the PNECR versus injected dose for the bed position encompassing the liver was modelled using the methodology of Watson *et al* (2005) mentioned above. From this modelization, the injected activity that yielded 90% of the maximum PNECR value 60 min after injection was reported. This value was justified by the broad and flat peaks of the PNECR (Watson *et al* 2005),

(b) As the regimen proposed above yielded injected activity incompatible with a moderate patient exposure, a second scheme was proposed to find a reasonable compromise between exposure and PET raw data quality. In this regimen, the computed activity for each patient should lead to a predefined PNEC value ($PNEC_{target}$) 60 min after injection. From the 491 patients, those that met the criteria $24 < BMI < 26\,kg\,m^{-2}$ and $65 < mass < 75\,kg$ were selected (58 patients). The PNEC value (PNECR multiplied by 150 s which is conventional acquisition time for patients with a BMI less than $25\,kg\,m^{-2}$ before this study) that corresponded to 75% of the maximum PNEC was reported. This percentage was chosen given the trade-off between injected activity and total acquisition time as well as the maximum injected activity advised by our national regulatory. The mean PNEC value for these 58 patients was defined as $PNEC_{target}$. Then, for the whole database and a constant acquisition time of 150 s, the injected activity that yielded the $PNEC_{target}$ value was derived. However, in some cases, the $PNEC_{target}$ value could not be reached (for the heaviest patient) or led to an injected activity too high (the maximum allowed activity concentration was $4\,MBq\,mL^{-1}$ for economical consideration). In these cases, the $PNEC_{target}$ was achieved instead by modifying the acquisition time per bed position for each BMI subgroup. As Masuda *et al* (2009) found that increasing injected activity was unnecessary for increasing the image quality for patients above 90 kg and for LSO systems, a maximum activity was derived for patient with $BMI > 32\,kg\,m^{-2}$. For this purpose, we reported the 5% highest computed injected activity for those patients with $BMI > 32\,kg\,m^{-2}$. The mean value derived from those values was chosen as the maximum allowed injected activity regardless of the BMI. The acquisition time per bed position was modified accordingly to meet this requirement.

The PNECR or PNEC (depending on the dose regimen considered) achieved for each patient were then compared to the PNECR or PNEC obtained with our local routine practice ($3\,MBq\,kg^{-1}$) using a paired Wilcoxon test. A p-value less than 0.05 was considered significant.

2.3. Variable acquisition time per bed position

When the time for each bed position is constant and equal to the acquisition time found in section 2.2 for the bed position encompassing the liver (that only differed according to the BMI), then the total acquisition time T_{acq}^{BMI} for a complete scan can be expressed as: $T_{acq}^{BMI} = n \times t_L^{BMI}$, with n the number of bed position and t_L^{BMI} the acquisition time for the bed position encompassing the liver that is specific for each BMI.

Once the total time T_{acq}^{BMI} is fixed for each BMI subgroup, we vary the time for each bed position given that each PNEC multiplied by a weighting factor defined below must be equal. With this constraint:

$$t_i(P_i) = T_{acq}^{BMI} \frac{P_i}{PNECR_i} \left[\sum_j \frac{P_j}{PNECR_j} \right]^{-1} \quad (4)$$

where t_i is the time spent for bed position i and P_i a weighting factor for the bed position i. In this study, P_i was set to be identical for all bed positions, except for the whole body acquisition (from top of the head to the feet) where acquisition time for the legs was required to be 16% of $T_{\text{acq}}^{\text{BMI}}$ due in part to the difference of attenuation medium between the upper part of the body and the legs and, on the other hand, to a shared decision with the nuclear medicine specialists. Without this constraint, the time spent for imaging the legs would have been a significant percentage of the total time (>50%), that is clinically irrelevant.

Again, patients were classified in four subgroups according to BMI. The PNECR model made it possible to calculate the PNECR as if all acquisitions started at 60 min post-injection. Only patients with arms positioned alongside the body were analyzed due to clinically irrelevant signal when arms are above the head for the 'head and neck' bed position.

2.4. Relationship between NEC and SNR for nonlinear reconstruction algorithm

In this last part, the NEC was used in order to allow a direct comparison with other studies (Chang *et al* 2011, Chang *et al* 2012). The NEC was defined as

$$\text{NEC} \approx \left(1 - S_f\right)^2 \text{PNEC} \tag{5}$$

where S_f is the scatter fraction defined as

$$S_f = \frac{S}{T+S} \tag{6}$$

S_f was determined using an implementation of the single scatter simulation algorithm (Watson 2007) with time-of-flight (TOF) extension. As stated previously, this approximation has been found to be reliable over a wide range of activity in the FOV of the PET system and BMI.

This study was conducted in two steps:

(a) The relationship between NEC and SNR was first assessed with a phantom experiment with activity inside and outside the FOV (figure 1) that closely mimicked the ratio of clinical activity for the bed position around the step centered on the liver. An annular ring of water bags was added to match the $T + S$ rates derived in patient studies (Brambilla *et al* 2007). The activity concentration in the elliptical lung-spine body phantom™ (Data Spectrum Corporation), centered in the FOV, was set to 20 kBq mL^{-1} at the beginning of the acquisition. The acquisition was repeated 36 times over 12 h with the default acquisition parameters. Each acquisition was set to 150 s. All PET acquisitions were reconstructed using the 3D ordinary Poisson ordered-subset expectation maximization (OSEM) algorithm with TOF information and point-spread-function modeling (Panin *et al* 2006).

(b) A total of 507 patients, acquired with the standard protocol, divided in 4 BMI subgroups as before were retrospectively included. Among them, we selected those patients with no disease in the liver, serum glucose level less than 8 μmol L^{-1} and excluded patient scans with heterogeneous uptake in the liver. The population was thus reduced to 328 patients. The SNR was calculated within the range of 30 slices located at the center of the axial FOV that maximize the axial sensitivity to avoid any bias due to loss of sensitivity at the edge of the FOV.

For phantom and patient studies, we used varying reconstruction parameters: from two to three iterations and 21 subsets, and two 3D Gaussian post filters (2 mm and 4 mm FWHM) for a total of three different reconstructions. The SNR was computed by choosing randomly 200 non-neighbouring voxels in the uniform region for the phantom study (Chang *et al* 2012) and

Figure 1. Phantoms used to derive the experimental relationship between NEC and SNR. Only the central part was centered in the FOV of the PET system. The two phantoms located on both sides of the central phantom simulated activity outside the FOV.

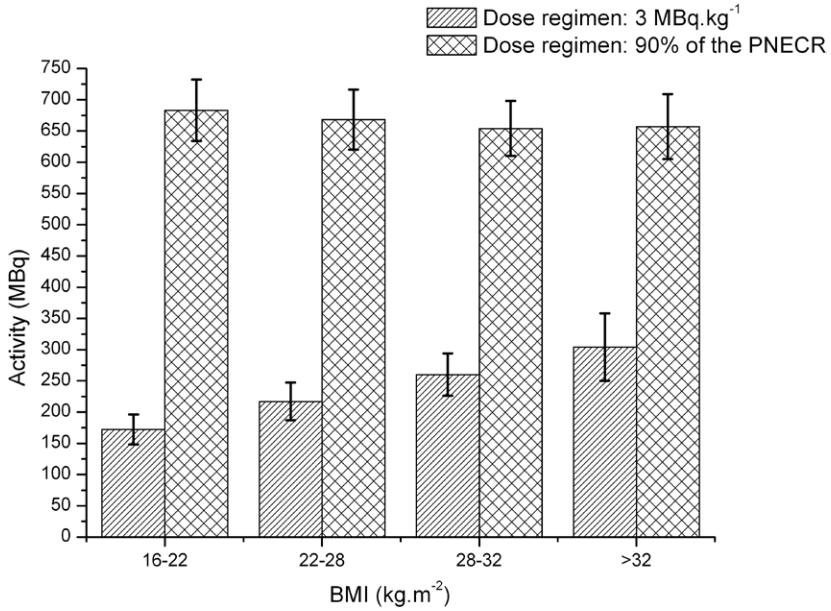

Figure 2. Activity computed for the first dose regimen (90% of the PNECR) and the routine practice ($3\,\mathrm{MBq\,kg^{-1}}$).

60 non-neighbouring voxels in the liver for the patient study. The SNR was defined as the ratio of the mean to standard deviation of the selected voxels.

3. Results

3.1. Comparison of different regimens of injected activity

Figure 2 shows that the activity to be injected to achieve 90% of the PNECR is almost constant (≈665 MBq), regardless of the BMI. The improvement in terms of PNECR or PNEC as

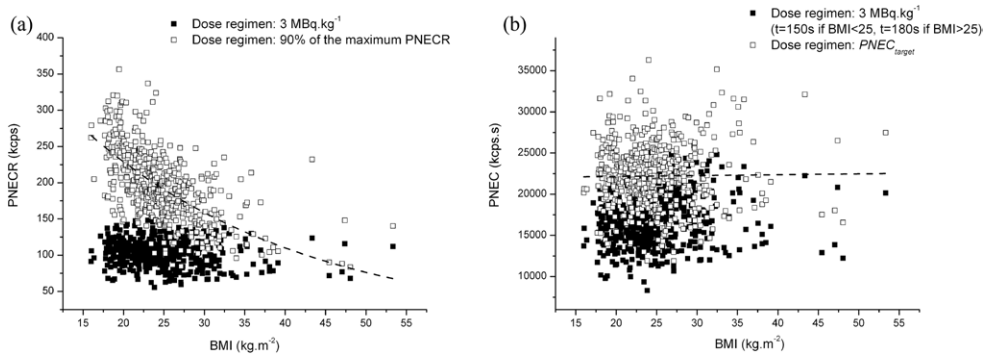

Figure 3. PNECR (*a*) and PNEC (*b*) versus patient BMI for the routine practice (3 MBq kg^{-1}) and the two proposed dose regimens, achieve 90% of the maximum PNECR and achieve the $PNEC_{target}$. Dotted lines are the exponential (R^2 = 0.41) (*a*) as suggested by Chang *et al* (2011) and linear (*b*) regression for the two evaluated dose regimens. Note that the second dose regimen (*b*) aimed at achieving a constant PNEC ($PNEC_{target}$ = 22 500 kcps.s) that corresponds well to the linear regression (PNEC = 22 300 kcps.s). Each dot represents a single patient.

Table1. Injected activity for the second dose regimen ($PNEC_{target}$) and percentage improvement compared with the standard dose regimen as a function of BMI.

BMI (kg m^{-2})	[16–22]	[22–28]	[28–32]	>32
Activity concentration (MBq kg^{-1})	4	4	3	3
Maximum activity (MBq)		400		
Time per bed position (s)	180	180	210	240
PNEC improvement (%)	38 ± 5*	30 ± 12*	16 ± 2*	34 ± 9*

*PNEC improvement statistically significant at the 0.05 level (paired Wilcoxon test)

compared with the standard dose regimen is illustrated in figure 3 for respectively the first (A) and the second dose regimen (B). The decreasing trend of PNECR versus injected activity for the first optimized dose regimen (90% of the maximum PNECR) highlighted in figure 3(*a*) confirms that image quality and hence PNECR for heavier patients could be only increased by scanning for longer periods and not by injecting more activity (Masuda *et al* 2009). While an exponential curve fitting was possible for the dose regimen that yielded 90% of the PNECR as suggested by Chang *et al* (2011), we did not find an exponential decrease for our routine dose regimen, unlike Chang *et al* (2011).

Table 1 summarizes the results for the second dose regimen ($PNEC_{target}$) and the improvement observed when comparing the PNEC achieved with the standard dose regimen (3 MBq kg^{-1} and t = 150 s if BMI < 25 kg m^{-2} or t = 180 s if BMI ≥ 25 kg m^{-2} for one bed position).

3.2. Variable acquisition time per bed position

An example of PNECR modelling for one patient and for each bed position and the corresponding PNECR values that were measured are shown in figure 4. The interest of varying the time per bed position is clearly highlighted when looking at the different PNECR values as a function of bed position (up to a factor 2) for this specific patient.

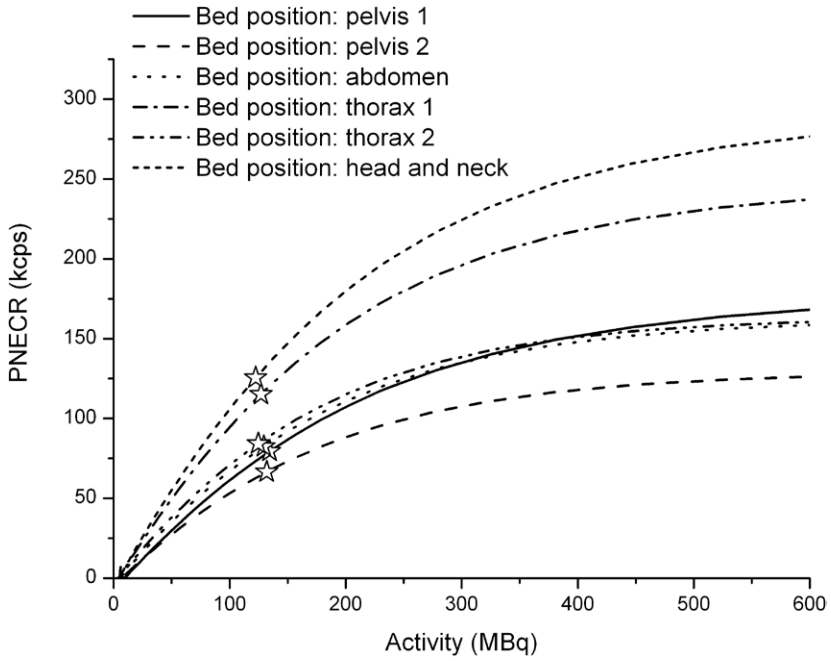

Figure 4. PNECR modelling for a patient and the different bed positions. The white stars show the PNECR values measured and used as the input for PNECR modelling.

The time per bed position was computed for each patient within each BMI subgroup and then averaged. Three different acquisition modes were considered: 1) whole body (13 steps), 2) from head to mid-thigh (7 steps), 3) from mid-head to mid-thigh (six steps). The rationale for distinguishing the last two acquisition modes was the high level of tracer in the brain. When the head was not completely included in the FOV (third acquisition mode), a significant part of the signal collected could be considered as out-of-FOV activity and the PNECR was modified accordingly. Figure 5 illustrates an example for the [22–28] $kg\,m^{-2}$ subgroup and the three acquisition modes. In this example, the weighting factors were identical for all bed positions, except for the whole body acquisition as described earlier. The impact of encompassing the full head within the FOV is highlighted when comparing the time spent for the 'head-and-neck' bed position (first step for acquisition mode 3 and second step for acquisition modes 1 and 2).

3.3. Relationship between NEC and SNR for a nonlinear reconstruction algorithm

SNR^2 versus NEC and true count rate are plotted in figure 6 for the phantom experiment and the patient studies. In the phantom data, while a linear function was previously reported as a good fit with linear reconstruction algorithms such as rebinned filtered back-projection (FBP) (Watson 2004, Dahlbom *et al* 2005, Chang *et al* 2012), the relationship between SNR^2 and NEC was best fitted with a quadratic function rather than a linear function albeit a linear trend is also consistent with the experimental data. It should be noted that a similar unexplained quadratic trend when using iterative algorithm was also reported in the study of Chang *et al* (2012) in figures 2(*b*) and (*c*) of their publication for two different type of PET scanners. On the other hand, SNR^2 and the number of true coincidences were linearly related as suggested

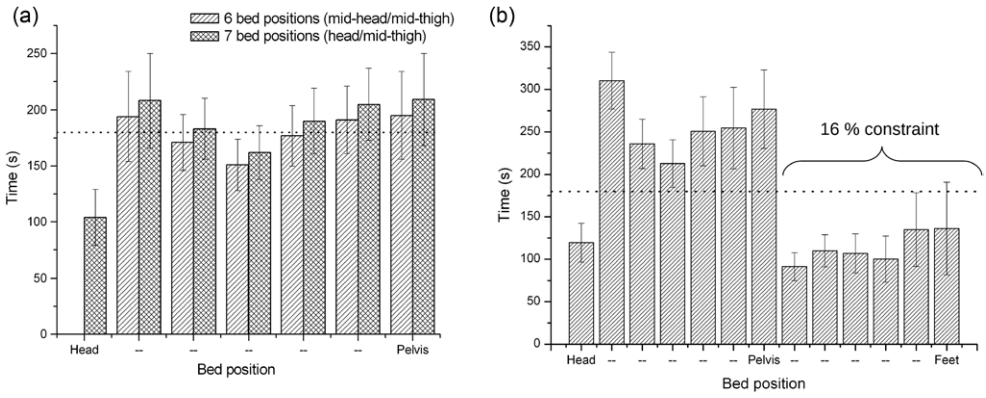

Figure 5. Time per bed position for six and seven steps (including the whole brain) (*a*) and for a whole body acquisition with 13 steps (*b*). These values were computed for the [22–28] kg m^{-2} BMI subgroup. The dotted line is for a constant time per bed position (180 s). The brace represents the steps constrained to 16% of the total time for a whole body acquisition (*b*).

by Chang *et al* (2012). However, the correlation was moderate for the patient-based study with BMI between 16 and 28 kg m^{-2}. In addition, no significant difference (Fisher's *z*-transformation: $p > 0.05$) between correlation coefficient found in the three first BMI subgroups could be demonstrated while the correlation coefficient for the last subgroup differed. For the two last subgroups (BMI > 28 kg m^{-2}), the quadratic trend between NEC and SNR^2 could not be confirmed. A linear fit was then performed instead of a quadratic fit. This approximation was supported by the fact that the quadratic term involved when fitting phantom and patient data (for BMI between 16 and 28 kg m^{-2}) was negligible (at least three orders of magnitude smaller) when compared with the linear term of the quadratic equation. However, the number of patients included in the last two subgroups (for those whose BMI was greater than 28 kg m^{-2}) was at least less than half of the number of patients in the first two subgroups. Hence, the statistical analysis power was not identical for each subgroup.

4. Discussion

The determination of ^{18}F-FDG injected activity differs significantly when considering the current EANM guidelines (Boellaard *et al* 2010), or routine practice in the USA (Graham *et al* 2011). Many authors have proposed optimizing the injected activity based on different figures of merit (FOM) involving phantom experiments or patient data. The studies based on analysis of patient data use either reconstructed images or raw data before reconstruction. In these cases, the metrics used for optimizing the dose regimen and/or acquisition parameters could be a visual assessment of image quality as a function of injected activity (Everaert *et al* 2003, Halpern *et al* 2005, Alessio *et al* 2011) or directly as a function of SNR computed in almost all cases in the liver (Masuda *et al* 2009, Chang *et al* 2011, de Groot *et al* 2013). NECR was also used as a metric for deriving the optimal dose regimen (Danna *et al* 2006, Walker *et al* 2009, Accorsi *et al* 2010). In this work, we used the methodology proposed by Watson *et al* (2005) that makes possible the modeling of the complete NECR by means of the actual measured number of singles events for each patient. This method has already been applied in the context of ^{15}O–H_2O (Walker *et al* 2009) but never, to our knowledge, to ^{18}F-FDG exams for a large number of adult patients. The robustness of the modeling was first

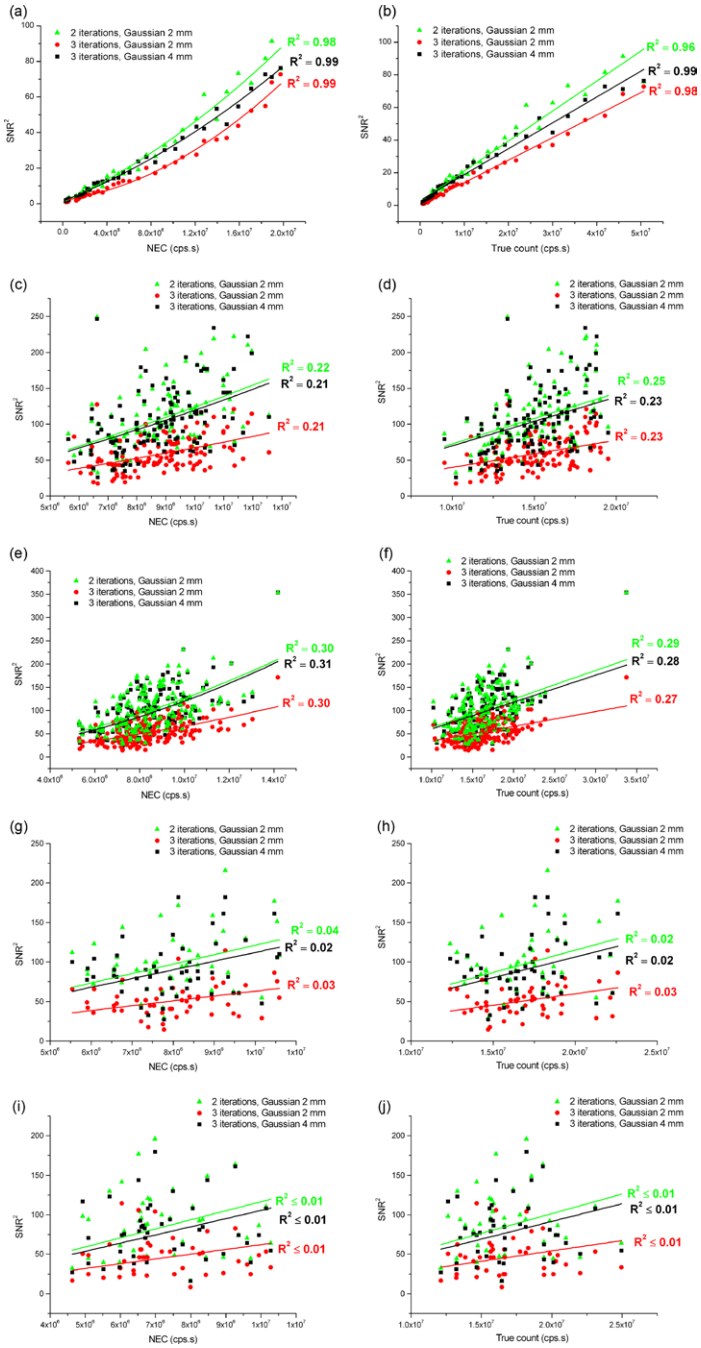

Figure 6. SNR^2 versus NEC (*a*,*c*,*e*,*g*,*i*) and true counts (*b*,*d*,*f*,*h*,*j*) for various reconstruction parameters for the phantom study (*a*,*b*) and the patient study: (*c*,*d*) for BMI [16–22] $kg\,m^{-2}$, (*e*,*f*) for BMI [22–28] $kg\,m^{-2}$, (*g*,*h*) for BMI [28–32] $kg\,m^{-2}$, and (*i*,*j*) for BMI > 32 $kg\,m^{-2}$. Each data point is a time-related (36 measurements over 12 h) measurement (*a*,*b*) while for (*c*,*d*,*e*,*f*,*g*,*h*) this represents one patient for the bed position encompassing the liver. The solid lines show the quadratic fit for NEC versus SNR^2 and the linear fit for true count versus SNR^2.

assessed with different phantoms for the Siemens Biograph mCT PET system and the difference between experimental and modeling was found to be no more than 3.5% for singles events, true, scattered and random coincidences and NECR for a wide range of activity in the FOV (10–400 MBq). Hence, this methodology was used to predict retrospectively the NECR for any given initial activity. As suggested by Watson *et al* (2005), we found that a unique activity of about 665 MBq, regardless of the BMI, is necessary to achieve 90% of the NECR. Obviously, this activity could be considered as excessive for dosimetric consideration (effective dose for an adult: 12.6 mSv based on ICRP 106 dose measurement). One possible way to overcome this limitation is to choose a constant value of a suitable metric that would be achieved for each patient. This metric can be the SNR in the liver measured on reconstructed images (de Groot *et al* 2013) or a value of the NEC (Accorsi *et al* 2010). We chose this latter solution by selecting a set of 58 patients (with the following criterion: $24 < \text{BMI} < 26\,\text{kg}\,\text{m}^{-2}$ and $65 < \text{mass} < 75\,\text{kg}$) from which we derived a constant PNEC value that corresponded to the mean value of 75% of the maximum NEC. This scheme led to a new dose regimen and acquisition time as a function of BMI (table 1). As already mentioned in several studies (Watson *et al* 2005, Masuda *et al* 2009), it is preferable to scan the patient longer for larger patients rather than increasing the injected activity. This conclusion held true in our population (see figure 3(*a*)) since PNECR tends to vanish for the first optimized dose regimen (90% of the maximum PNECR) when BMI increases. Hence, a maximum injected activity of 400 MBq was set for all patients while the total acquisition time was accordingly adapted (table 1). We should note that, for an identical acquisition time, the computed activity differed from those of de Groot *et al* (2013). For example, for a 77 kg patient ($\text{BMI} = 25\,\text{kg}\,\text{m}^{-2}$), they found an injected activity of 222 MBq and 314 MBq respectively for mass and BMI as the input variable in their equation although they stated that their was no significant difference between their two models that involved either the mass or the BMI as input variable. For this patient, our model gave a computed activity of 306 MBq, very similar to their model that uses the BMI. The exact opposite was found for a patient weighing 92 kg ($\text{BMI} = 30\,\text{kg}\,\text{m}^{-2}$) where our model was found to be very close to the model using mass in their equation and different from the one using BMI (our model: 275 MBq versus 277 MBq or 430 MBq for the model using respectively mass or BMI). These discrepancies underline the difficulty in choosing valuable metrics for optimizing injection rules when using patient data. It is important to note that our proposed injection rule fulfils the requirement specified in the EANM guidelines for injected activity and the Biograph mCT PET system (Boellaard *et al* 2010).

One benefit of our approach is the possibility to take advantage of NECR modelling for computing an acquisition time dependent on the bed position by setting the initial uptake time to 60 min post-injection for each patient. It is well known that scan duration is strongly related to detectability (Alessio *et al* 2011, Kadrmas *et al* 2012) especially when scanning the head and neck bed position where very small structures could be of clinical interest (Goethals *et al* 2010). The initial attempts to tackle this issue were based on the modelling of attenuation on clinical count rate (Krizsan *et al* 2011), or on the underlying relationship between the average attenuation correction factor and SNR (Carney *et al* 2004). While these two methods assume a uniform distribution of activity in the body, our method does not make any assumption on activity distribution as it is based on NECR. In order to make the implementation in routine clinical assessment easier, a constant total time was chosen, and equal to the number of bed position multiplied by the duration shown in table 1. The duration per bed position was then modulated by the NECR and a weighting factor that may semi-empirically take into account the difference of attenuating medium between upper and lower (legs) parts of the body, or the irrelevant signal from bed position corresponding to heart or bladder. In this work, the weighting factors have been chosen to be identical for all bed positions (except for the whole body

acquisition) so that the impact of NECR on time duration could be highlighted. Finally, the weighting factors may enable to focus on a bed position with a given clinical interest while preserving the benefit of using the NECR information. These weighting factors may also be computed using the approach proposed by Krizsan *et al* (2011) in an attempt to account for attenuation, which can be computed quickly based on the topogram, and the NECR that accounts for the distribution of activity. For example, the weighting factors could be computed as the ratio between the total attenuation factor (considering the whole acquisition) and the average attenuation factor for a given bed position. Indeed, Krizsan *et al* (2011) shown a strong relationship between average attenuation factor (ACF) and noise for a specific bed position (the larger the ACF, the larger the noise).

These developments make sense if the relationship between NEC and SNR in the reconstructed images with a non-linear algorithm hold true. Indeed, while SNR^2 and NEC were proven to be linearly related using linear reconstruction algorithms such as rebinned filtered back-projection (FBP) (Watson 2004, Dahlbom *et al* 2005, Chang *et al* 2012), the use of non-linear algorithms (mostly OSEM-like algorithms) requires special caution. Several authors have pointed out that image noise was not inversely proportional to NEC (Dahlbom *et al* 2005, Watson 2006), unlike in FBP reconstruction. Chang *et al* (2012) recently suggested that NECR might not always be predictive of SNR at high activity concentration and that a higher NEC is not always related to a better SNR. They conducted their study with both phantom and clinical data and showed, only with phantom data, that SNR^2 is instead related linearly to the number of true events. We investigated these relationships for an iterative algorithm with a larger population and a phantom experiment that fitted the range of count rate that is clinically relevant. For the PET system used in this work (Biograph mCT, Siemens), we found a clear relationship between SNR^2 and NEC or the number of true events with the phantom experiment data for an OSEM-based algorithm. However, unlike that reported by Chang *et al* (2012), we did not reach the peak NECR. Additional experiments at higher count rates for the Biograph mCT must be conducted to assess the possible dependence of count-rate on event mispositioning (Badawi *et al* 2004), and make possible a comparison with existing published data. Additionally, the quadratic relationship between SNR^2 and NEC found with the phantom data did not hold true when considering patient data, unlike the relationship between SNR^2 and the number of true events. Moreover, it is worth noting that the correlation between SNR^2 and NEC was found higher with phantom data than with patient data. The linear trend for both NEC and number of true events versus SNR^2 was more pronounced for the first two subgroups ($BMI < 28\,kg\,m^{-2}$) than the last two groups. The lack of significant difference between the two first BMI subgroups and the [28–32] $kg\,m^{-2}$ may be partly due to the lower number of patients included in this subgroup and the fact that the dose regimen used in this analysis corresponded to our previous routine practise ($3\,MBq\,kg^{-1}$) without variable time acquisition.

The choice of the bed position encompassing the liver for optimizing the injected activity for a whole body exam is a simplification. This is justified by the fact that the study was conducted in two steps: optimizing the injected activity using the bed position also used for the third part of the study (relationship between SNR and NEC) and then deriving suitable acquisition time for each bed position using PNECR. In that respect, it could be noted that the PNECR value were found very similar between bed position (figure 5(*a*)). Hence, we assumed that averaging the different bed position for deriving the injected activity would not change the conclusions when considering the part involving optimization of injected activity. The main limitation of our study is that the new dose regimen was not assessed and compared with our initial routine practise. However, this objective was not in the scope of the study as we initially focused on the derivation of an optimized dose regimen based on modelling the NECR and deriving the relationship between NECR and SNR. Hence, given our results, we can reasonably hypothesize

that a NEC enhancement for a given subgroup may translate into an SNR improvement. As an example, a 38% increase of NEC ([16–22] kg m^{-2} subgroup) may be equivalent to an increase of SNR^2 from 93 to 138 given the relationship between SNR^2 and NEC for this subgroup. Similarly, for the [22–28] kg m^{-2} subgroup, a 30% increase of NEC may be equivalent to an increase of SNR^2 from 82 to 119. However, as already mentioned, these results need to be confirmed for the two higher BMI subgroups given the limited number of patient enrolled compared to the two first BMI subgroups and the fact that the conventional protocol was used (the scan time was not adapted). We expect a potential relationship between NEC and SNR^2 using a larger population and the new dose regimen in addition to the conventional protocol since other groups (Watson 2006, Masuda *et al* 2009, de Groot *et al* 2013) showed a significant improvement of SNR^2 when the acquisition time increased for patient with high BMI.

Finally, it is worth noting that these results are only valid for an 18F-FDG acquisition and the PET system studied in this study. However the methodology could be easily adapted to other radiopharmaceuticals.

5. Conclusion

This study showed that clinical NECR modelling is a valuable alternative to phantom-based experiments for optimizing retrospectively acquisition protocols for PET 18F-FDG scans, including the determination of variable duration per bed position. For the typical count rates found in a clinical setting, both NEC and the number of true events count rate could be used as a predictive index of SNR with a non-linear reconstruction algorithm. Further studies are needed to confirm those results for patient with large BMI (>28 kg m^{-2}).

Acknowledgments

The authors wish to thank Dr Frédéric Schoenahl and Dr Ludovic Le Meunier of Siemens Medical Solutions, France, for their useful comments and help during this study. We also thank Dr Irène Buvat, IMNC, Orsay, France, for providing us with very constructive comments and suggestions.

References

Accorsi A, Karp J S and Surti S 2010 Improved dose regimen in pediatric PET *J. Nucl. Med.* **51** 293–300

Alessio A M, Sammer M, Phillips G S, Manchanda V, Mohr B C and Parisi M T 2011 Evaluation of optimal acquisition duration or injected activity for pediatric 18F-FDG PET/CT *J. Nucl. Med.* **52** 1028–34

Badawi R D *et al* 2004 Count-rate dependent event mispositioning and NEC in PET *IEEE Trans. Nucl. Sci.* **51** 41–5

Badawi R D, Marsden P K, Cronin B F, Sutcliffe J L and Maisey M N 1996 Optimization of noise-equivalent count rates in 3D PET *Phys. Med. Biol.* **41** 1755–76

Boellaard R *et al* 2010 FDG PET and PET/CT: EANM procedure guidelines for tumor PET imaging: version 1.0 *Eur. J. Nucl. Med. Mol. Imaging* **37** 181–200

Brambilla M, Matheoud R, Secco C, Sacchetti G, Comi S, Rudoni M, Carriero A and Inglese E 2007 Impact of target-to-background ratio, target size, emission scan duration, and activity on physical figures of merit for a 3D LSO-based whole body PET/CT scanner *Med. Phys.* **34** 3854–65

Carney J P J, Watson C C and Townsend D W 2004 Optimization of the relative acquisition duration for PET/CT imaging in oncology *IEEE Nuclear Science Symp. Conf. Record (Rome, Italy, 16–22 October 2004)* (Piscataway, NJ: IEEE) pp 2910–4

Chang T, Chang G, Clark J W, Diab R H, Rohren E and Mawlawi O R 2012 Reliability of predicting image signal-to-noise ratio using noise equivalent count rate in PET imaging *Med. Phys.* **39** 5891–900

Chang T, Chang G, Kohlmyer S, Clark J W, Rohren E and Mawlawi O R 2011 Effects of injected dose, BMI and scanner type on NECR and image noise in PET imaging *Phys. Med. Biol.* **56** 5275–85

Dahlbom M, Schiepers C and Czernin J 2005 Comparison of noise equivalent count rates and image noise *IEEE Trans. Nucl. Sci.* **52** 1386–90

Danna M, Lecchi M, Bettinardi V, Gilardi M C, Stearns C W, Lucignani G and Fazio F 2006 Generation of the acquisition-specific NEC (AS-NEC) curves to optimize the injected dose in 3D 18F-FDG whole body PET studies *IEEE Trans. Nucl. Sci.* **53** 86–92

de Groot E H, Post N, Boellaard R, Wagenaar N R L, Willemsen A T M and van Dalen J A 2013 Optimized dose regimen for whole-body FDG-PET imaging *EJNMMI Res.* **3** 63

Everaert H, Vanhove C, Lahoutte T, Muylle K, Caveliers V, Bossuyt A and Franken P R 2003 Optimal dose of 18F-FDG required for whole-body PET using an LSO PET camera *Eur. J. Nucl. Med. Mol. Imaging* **30** 1615–9

Goethals I, D'Asseler Y, Dobbeleir A, Deblaere K and Ham H 2010 The effect of acquisition time on visual and semi-quantitative analysis of F-18 FDG-PET studies in patients with head and neck cancer *Nucl. Med. Commun.* **31** 227–31

Graham M M, Badawi R D and Wahl R L 2011 Variations in PET/CT methodology for oncologic imaging at US academic medical centers: an imaging response assessment team survey *J. Nucl. Med.* **52** 311–7

Halpern B S, Dahlbom M, Auerbach M A, Schiepers C, Fueger B J, Weber W A, Silverman D H S, Ratib O and Czernin J 2005 Optimizing Imaging protocols for overweight and obese patients: a lutetium orthosilicate PET/CT study *J. Nucl. Med.* **46** 603–7

International Commission on Radiation Protection 2008 Radiation dose to patients from radiopharmaceuticals. A third amendment to ICRP publication 53 *Ann. ICRP* **38** 1–198

Kadrmas D J, Oktay M B, Casey M E and Hamill J J 2012 Effect of scan time on oncologic lesion detection in whole-body PET *IEEE Trans. Nucl. Sci.* **59** 1940–7

Krizsan A K, Czernin J and Dahlbom M 2011 Whole body PET imaging using variable acquisition times *MIC IEEE Nucl. Sci. Conf. Rec.* pp 3931–4

Lartizien C, Comtat C, Kinahan P E, Ferreira N, Bendriem B and Trébossen R 2002 Optimization of injected dose based on noise equivalent count rates for 2- and 3-dimensional whole-body PET *J. Nucl. Med.* **43** 1268–78

Masuda Y, Kondo C, Matsuo Y, Uetani M and Kusakabe K 2009 Comparison of imaging protocols for 18F-FDG PET/CT in overweight patients: optimizing scan duration versus administered dose *J. Nucl. Med.* **50** 844–8

National Electrical Manufacturers Association 2007 *Performance Measurements of Positron Emission Tomographs* (Rosslyn, VA: National Electrical Manufacturers Association)

Panin V Y 2011 Ordered subsets acceleration of iterative algorithm for variance reduction on compressed sinogram random coincidences *IEEE Nuclear Science Symp. Conf. Record (Valencia, Spain, 23–29 October 2011)* (Piscataway, NJ: IEEE) pp 2986–90

Panin V Y, Kehren F, Michel C and Casey M 2006 Fully 3D PET reconstruction with system matrix derived from point source measurements *IEEE Trans. Med. Imaging* **25** 907–21

Strother S C, Casey M E and Hoffman E J 1990 Measuring PET scanner sensitivity: relating count rates to image signal-to-noise ratios using noise equivalent counts *IEEE Trans. Nucl. Sci.* **37** 783–8

Walker M D, Matthews J C, Asselin M C, Saleem A, Dickinson C, Charnley N, Julyan P J, Price P M and Jones T 2009 Optimization of the injected activity in dynamic 3D PET: a generalized approach using patient-specific NECs as demonstrated by a series of ^{15}O–H2O scans *J. Nucl. Med.* **50** 1409–17

Watson C C 2004 Count rate dependence of local signal-to-noise ratio in positron emission tomography *IEEE Trans. Nucl. Sci.* **51** 2670–80

Watson C C 2006 Image noise variance in 3D OSEM reconstruction of clinical time-of-flight PET *IEEE Nuclear Science Symp. Conf. Record (San Diego, California, 29 October–4 November 2006)* (Piscataway, NJ: IEEE) pp 1736–9

Watson C C 2007 Extension of single scatter simulation to scatter correction of time-of-flight PET *IEEE Trans. Nucl. Sci.* **54** 1679–86

Watson C C, Casey M E, Bendriem B, Carney J P, Townsend D W, Eberl S, Meikle S and DiFilippo F P 2005 Optimizing injected dose in clinical PET by accurately modeling the counting-rate response functions specific to individual patient scans *J. Nucl. Med.* **46** 1825–34

Watson C C, Casey M E, Beyer T, Bruckbauer T, Townsend D W and Brasse D 2003 Evaluation of clinical PET count rate performance *IEEE Trans. Nucl. Sci.* **50** 1379–85

IOP Publishing | Institute of Physics and Engineering in Medicine Physics in Medicine & Biology

Phys. Med. Biol. **60** (2015) 2475–2491 doi:10.1088/0031-9155/60/6/2475

Assessment of a fully 3D Monte Carlo reconstruction method for preclinical PET with iodine-124

M Moreau[1,2], I Buvat[3], L Ammour[4], N Chouin[2,4], F Kraeber-Bodéré[1,4], M Chérel[1] and T Carlier[1,4]

[1] CRCNA, INSERM, University of Nantes, UMR 892, Nantes, France
[2] AMaROC, National Veterinary School ONIRIS, Nantes, France
[3] I2BM, CEA-SHFJ, Orsay, France
[4] Nuclear Medicine Department, University Hospital of Nantes, Nantes, France

E-mail: thomas.carlier@chu-nantes.fr

Received 22 September 2014, revised 30 January 2015
Accepted for publication 3 February 2015
Published 5 March 2015

Abstract

Iodine-124 is a radionuclide well suited to the labeling of intact monoclonal antibodies. Yet, accurate quantification in preclinical imaging with I-124 is challenging due to the large positron range and a complex decay scheme including high-energy gammas. The aim of this work was to assess the quantitative performance of a fully 3D Monte Carlo (MC) reconstruction for preclinical I-124 PET. The high-resolution small animal PET Inveon (Siemens) was simulated using GATE 6.1. Three system matrices (SM) of different complexity were calculated in addition to a Siddon-based ray tracing approach for comparison purpose. Each system matrix accounted for a more or less complete description of the physics processes both in the scanned object and in the PET scanner. One homogeneous water phantom and three heterogeneous phantoms including water, lungs and bones were simulated, where hot and cold regions were used to assess activity recovery as well as the trade-off between contrast recovery and noise in different regions. The benefit of accounting for scatter, attenuation, positron range and spurious coincidences occurring in the object when calculating the system matrix used to reconstruct I-124 PET images was highlighted. We found that the use of an MC SM including a thorough modelling of the detector response and physical effects in a uniform water-equivalent phantom was efficient to get reasonable quantitative accuracy in homogeneous and heterogeneous phantoms. Modelling the phantom heterogeneities in the SM did not necessarily yield the most accurate estimate of the activity distribution, due to the high variance affecting many SM elements in the most sophisticated SM.

Keywords: PET, iodine-124, Monte Carlo, reconstruction, system matrix

S Online supplementary data available from stacks.iop.org/PMB/60/062475

(Some figures may appear in colour only in the online journal)

1. Introduction

For more than two decades, monoclonal antibodies (MAbs) have been labeled with gamma-emitting radionuclides and subsequently used in planar or single photon emission tomography (Herbertson *et al* 2014, Lütje *et al* 2014). However, absolute quantification might be easier using MAbs positron emission tomography (PET), called immuno-PET (Poli *et al* 2013). In that context, Iodine-124 (^{124}I) is well suited to the labeling of large molecules such as intact MAbs (Knowles and Wu 2012, Wright and Lapi 2013). In radioimmunotherapy involving α-emitters, ^{124}I could be a substitute to astatine-211 for biodistribution and dosimetric studies, since the stability of the labeling is similar for these two radionuclides (Walte *et al* 2007).

Quantitative ^{124}I PET has been previously investigated in clinical (Vandenberghe *et al* 2006b, Herzog *et al* 2008, Gregory *et al* 2009, Jentzen *et al* 2010) and preclinical settings (Yao *et al* 2005, Sauerzapf *et al* 2011, Taleb *et al* 2012). Yet, accurate quantification in preclinical imaging with ^{124}I remains challenging due to the large positron range (maximum energy: 1.5 MeV (11.5%) and 2.1 MeV (11.5%), as compared to 0.6 MeV for ^{18}F) worsening the spatial resolution, and to a complex decay scheme including high-energy gamma (~60% at 603 keV and ~10% at 723 keV) partly emitted in cascade with the positrons (Disselhorst *et al* 2010). The cascade decays can produce non-annihilation true coincidences, called cascade-coincidences in this paper, when a high-energy photon creates a coincidence with a 511 keV photon. These cascade-coincidences contribute to the background activity in clinical (Surti *et al* 2009) and preclinical (Herzog *et al* 2002) settings, with a fraction of ~35% of the total measured coincidences when using a preclinical PET system (Yu *et al* 2009).

Several groups have already tackled issues that are of foremost importance in ^{124}I PET. Methods have been proposed to account for the positron range within the reconstructed algorithm for high energetic positrons (Rahmim *et al* 2013). Rahmim *et al* (2008a) described a space-invariant correction involving a 3D bi-exponential modelling of the annihilation distribution in a homogeneous media. Monte Carlo (MC) simulations have also been used to determine the convolution kernels to be introduced in the forward step of an OSEM (ordered subset expectation maximization) algorithm (Cal-Gonzalez *et al* 2009) or in the forward and back-projection steps using a MAP (maximum a posteriori) algorithm (Ruangma *et al* 2006). In addition, few studies used a truncated convolution kernel calculated in water to account for the soft tissue/air boundary (Bai *et al* 2003, Bai *et al* 2005). However, while an improvement in spatial resolution has been reported, these approaches may introduce artifacts in reconstructed images. Space-variant modelling of the annihilation distribution was also considered in heterogeneous media. One possibility is to compute the annihilation distribution for few materials in the human body (such as water, lung an bone) and take advantage of the CT scan to determine the annihilation distribution within different media (Alessio *et al* 2008, Rahmim *et al* 2008b). Quantitative improvements compared with a space-invariant positron range model strongly depend on the heterogeneities present in the propagation medium. Last, the use of MC simulations within the reconstruction for determining the annihilation distribution in heterogeneous media has been investigated but is computationally intensive (Fu and Qi 2010).

The spatially uncorrelated cascade-coincidences produce a slowly varying background activity in the sinogram. This background activity can be estimated and subsequently subtracted

from the initial sinogram. The estimation can be based on fitting the sinogram tails with either a uniform (Pentlow *et al* 2000), linear (Lubberink *et al* 2002) or quadratic (Kull *et al* 2004) function. Another approach estimates the cascade-coincidences sinogram using a spatially variant convolution-subtraction technique (Beattie *et al* 2003, Walrand *et al* 2003). In this approach, the cascade-coincidence sinogram results from the convolution of an analytically-computed kernel with an ideal activity distribution (i.e. without scatter nor attenuation). Alternatively, an approach similar to the single scatter simulation correction developed by Watson *et al* (2000) for scattered coincidences can be used (Cheng *et al* 2009, 2011, Laforest and Liu 2009). However, these methods require an initial estimate of the activity distribution. This estimate is usually obtained from a 2D analytical reconstruction of the original sinogram corrected for scatter and attenuation and assuming a uniform background subtraction for cascade distribution correction.

The full MC modelling of the system matrix (SM) used in iterative reconstruction makes it possible to precisely account for all physical effects occurring in the scanner and the object (Floyd *et al* 1986, Veklerov *et al* 1988). This approach was already investigated in SPECT accounting for the object and scanner (Lazaro *et al* 2005, Aguiar *et al* 2014). The performance of this approach in PET imaging relies partly on the accuracy of the SM elements R_{ij}, where each R_{ij} is the probability that an event emitted from a source voxel j in the object is assigned to a specific LOR i. Yet, when particle-matter interactions in the object are considered, the prohibitive MC modelling time is the main limitation of this approach. Up to now, when using a MC calculation of the SM in PET imaging, only the point spread function (PSF) of the detector has been modeled (Rafecas *et al* 2004, Vandenberghe *et al* 2006a, Aguiar *et al* 2010, Ortuño *et al* 2010, Cabello and Rafecas 2012) and the associated SM was sparse (Kontaxakis *et al* 2002). By taking advantages of the SM sparsity and of scanner symmetries, simulation time and memory requirement could be reduced (Johnson *et al* 1995).

It is also possible to factorize the SM as a product of independent contributions (geometry, particle interactions in the detectors and in the object) to reduce its size, and allow for an independent computation of each contribution (Qi *et al* 1998, Rahmim *et al* 2008a, Cecchetti *et al* 2013). However, these techniques often require simplifications since the SM can usually not be written as a product of sparse diagonal matrices (Ortuño *et al* 2010). For instance, there is no model in which the accolinearity effect is independent from the geometric projector.

The aim of this work was to assess the quantitative performance of a fully 3D MC reconstruction for preclinical ^{124}I PET. We investigated the benefits of using a complete description of the physics processes both in the PET scanner and in the object for calculating the SM and assessed the impact of different level of complexity and statistical properties of the SM on the resulting image features.

2. Methods

2.1. PET system

The high-resolution small animal Inveon PET system from Siemens was used. This scanner consists of 64 blocks of 20 × 20 lutetium-oxyorthosilicate (LSO) crystals (1.51 × 1.51 × 10 mm^3) readout by position sensitive photomultipliers tubes. The 25 600 crystals arranged in 16 modules of 4 blocks and 80 axial rings yield ~164 millions lines of response (LOR). The transaxial field of view (FOV) is 10.0 cm in diameter and the axial FOV is 12.7 cm.

2.2. Simulated acquisitions

A homogeneous thin water phantom P0 (30 × 30 × 2 mm^3, voxel size: 1 × 1 × 1 mm^3) with hot and cold inserts in a background was used: the hot and cold regions were 8 × 8 × 2 mm^3

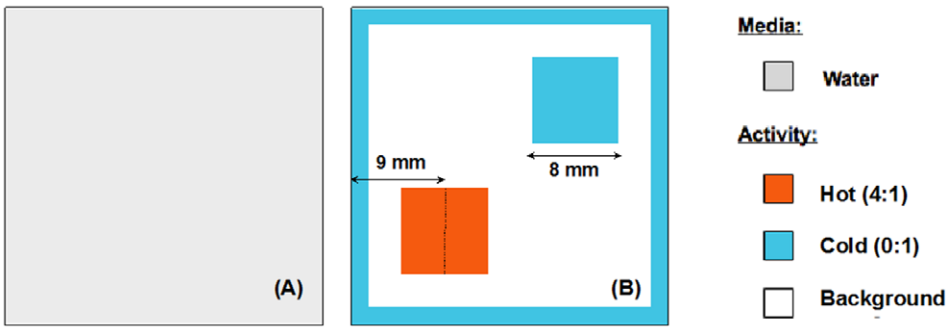

Figure 1. Axial slice of phantom P0: medium (*a*) and activity distribution (*b*).

(figure 1). Hot and background regions were filled with ^{124}I source. The activity concentration in the hot region was 4 times the activity within the background, while the cold region contained no activity. The background activity was only filled in the 26 × 26 × 2 centered voxels. The simulations were performed with GATE v6.1 (Jan *et al* 2011).

A heterogeneous phantom (30 × 30 × 2 mm^3, voxel size: 1 × 1 × 1 mm^3) composed of water, lung and bone (figure 2(*a*)) was also designed to produce three groups of heterogeneous projections.

Phantom P1 was filled with ^{124}I as shown in figure 2(*b*). In phantom P2, five hot regions mimicking tumors were added with dimensions ranging from 1 × 1 to 5 × 5 mm^2. The 'tumors' were located near the bone (figure 2(*c*)) and also filled with ^{124}I.

PET acquisitions were simulated so that the number of detected prompts was similar for all settings (2.32 × 10^6 for P0, 2.72 × 10^6 for P1 and 2.35 × 10^6 for P2).

2.3. System matrix computation

Given the simulated phantom and cylindrical geometry of the pre-clinical PET scanner, we took advantage of the symmetries in the phantom and in the PET system for reducing the number of particles needed for SM computation. Considering a transaxial plane in the Inveon FOV and the voxelized phantom in the center of the FOV, eight symmetries were used for voxels with the same x and y coordinates in the transaxial planes and sixteen symmetries for all others. As a result, only 7% of the initial volume was used for computing the different SM. Only non-zero elements of the SM were stored.

For each phantom, three different SMs were calculated to investigate the benefit of using a complete description of the physical processes for calculating the SM.

The first SM was created by simulating photon pairs in opposite directions (*Back-To-Back* source in GATE). Interactions in the object were not modeled as if photons propagated in vacuum. Only the system geometry and photon interactions in the PET system (crystal scattering and penetration) were modeled. This model was called *BtB-Vacuum* and the resulting SM modelling only the PSF of the scanner was used for all phantoms.

The second SM was calculated by simulating a ^{124}I source. The interactions in the object were explicitly modeled assuming the phantoms consisted of water only (instead of soft tissue, lung or bone encountered in real animals). This second SM accounted for attenuation, scatter, positron range and spurious coincidences (511 keV photon in coincidence with a gamma photon emitted in cascade) as occurring in a water medium. Cascade-γ of ^{124}I were included

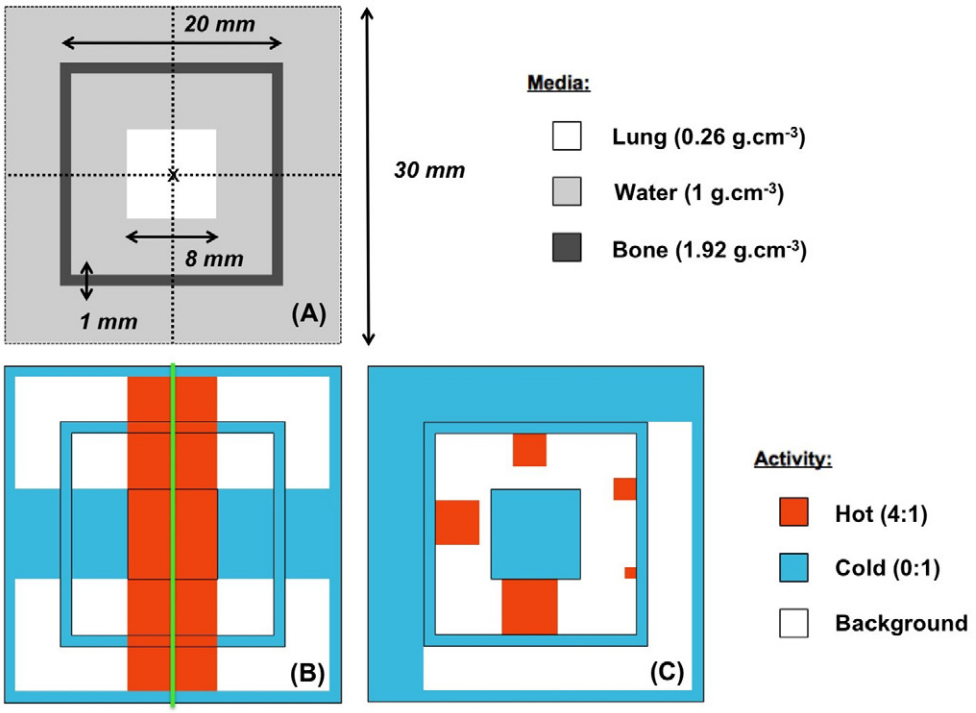

Figure 2. Description of phantoms P1 (*b*) and P2 (*c*) involving a heterogeneous medium (*a*). The green line (*b*) shows the location of the profile measured across the hot region.

because of the linear relationship between simulated activity and the number of coincidences involving cascade-γ. This model was called I124-*Uniform* and the resulting SM was used for all three phantoms described in section 2.2.

The third type of SMs was identical to I124-*Uniform* SM except that the medium heterogeneity was taken into account (water, lung and bone). This model was called I124-*Real*. Note that the object used to calculate I124-*Uniform* SM and I124-*Real* SM had the dimensions and composition of phantoms P1 and P2 described in the section 2.2.

Each of these SMs was computed with different statistical variances in the SM elements leading to 12 SMs, as shown in table 1.

Note that *BtB-Vacuum Large*, I124-*Uniform Large* and I124-*Real Small* SM have approximately (6% maximum difference) the same number of detected coincidences for comparison purpose. Therefore, *BtB-Vacuum Large* and I124-*Uniform* were used to reconstruct phantom P0 while *BtB-Vacuum Large*, I124-*Uniform Large* and I124-*Real Small* were used to reconstruct P1 and P2 phantoms so as to compare the performance of the SM when calculated from about the same number of prompts.

Random coincidences were not included in the computation of the SMs, and only coincidences involving two γ-photons (annihilation-γ or cascade-γ) emitted from the same event were used for SM computation.

A standard Siddon ray-tracing algorithm (Siddon 1985) was also implemented for comparison purpose, where each SM element R_{ij} was proportional to the line intersection between LOR i and voxel j.

Table 1. Number of detected prompts used for each system matrix, taking symmetries into account.

System Matrix	Size (Go)	Number of prompt coincidences
BtB-Vacuum Small	0.3	1.45×10^9
BtB-Vacuum Medium	0.7	8.61×10^9
BtB-Vacuum Large	1.2	2.78×10^{10}
I124-*Uniform Small*	2.1	7.31×10^9
I124-*Uniform Medium*	4.9	1.94×10^{10}
I124-*Uniform Large*	6.8	2.85×10^{10}
I124-*Real XX Small*	2.9	1.18×10^{10}
I124-*Real X Small*	4.6	2.07×10^{10}
I124-*Real Small*	6.2	2.95×10^{10}
I124-*Real Medium*	12.3	6.49×10^{10}
I124-*Real Large*	17.6	9.77×10^{10}

2.4. Reconstruction

The MLEM (Shepp and Vardi 1982) reconstruction algorithm was implemented using a histogrammed LOR-MLEM approach accounting for all symmetries mentioned in section 2.3:

$$f_j^{k+1} = f_j^k \frac{1}{\sum_i^I Rij} \sum_i^I Rij \frac{\mathrm{LOR}i}{\sum_j^J Rij f_j^k} \tag{1}$$

where f_j^{k+1} is the reconstructed activity in voxel j for iteration $k+1$, f_j^k is the reconstructed activity in voxel j for iteration k, J is the total number of initial voxels, I is the total number of non-zero element related to voxel j, and $(k+1)$ the current iteration.

2.5. Figures of merit

2.5.1. System matrix. The accuracy and statistical quality of an SM calculated using MC simulations are two key factors for reliable image reconstruction. The accuracy depends on the description of the physics processes used for SM computation. The statistical quality is related to the number of simulated events for SM computation.

We defined four figures of merit (FOM) related to the SM:

- *%NonZero:* percent number of non-zero SM elements;
- *%Ones*: percent number of non-zero SM elements computed with only one detected prompt;
- *Pmin, Pmax:* the minimal (non-zero) and maximal probability in the SM, respectively.

The sensitivity images (that intrisically takes into account the medium heterogeneities) were also analyzed for each MC-based SM. Profiles through the central slice of the sensitivity images were drawn to analyze the main differences between the SM.

2.5.2. Reconstructed images. The contrast recoveries for the hot and cold regions were defined as:

$$\mathrm{CR_{Hot}} = 100 \frac{(C_H - C_B)/C_B}{(A_H - A_B)/A_B} = 100 \frac{C_H - C_B}{3C_B} \tag{2}$$

$$\mathrm{CR}_{\mathrm{Cold}} = 100\frac{C_B - C_C}{C_B} \tag{3}$$

For P0, C_H, C_C and C_B were respectively the average counts in the hot region, in the cold region and in the background, and A_H and A_B the real average activity in the hot region and the background respectively.

For P2, C_H was the number of counts in the voxel with the highest signal in a 'tumor', according to the NEMA NU-4 recommendations (National Electrical Manufacturers Association 2008).

A profile throughout the hot region (green arrow in figure 2(*b*)) was drawn for phantom P1. Using I124-*Uniform* SM, absolute activity recovery for P0 projections was calculated as:

$$\mathrm{AR}_{\mathrm{ROI}} = 100\frac{A_{\mathrm{ROI}}^{\mathrm{Measured}}}{A_{\mathrm{ROI}}^{\mathrm{Theoric}}} \tag{4}$$

where $A_{\mathrm{ROI}}^{\mathrm{Measured}}$ is the reconstructed mean activity per voxel and $A_{\mathrm{ROI}}^{\mathrm{Theoric}}$ the mean activity simulated per voxel in the ROI. Similarly, activity recovery (AR) was also calculated in the five hot regions of P2 when using I124-*Real* SMs.

The average residual activity in cold regions (water and lung) for P2 was compared to the mean activity within the background using:

$$A_{\mathrm{Cold}} = 100\frac{\sum_{j}^{\mathrm{Cold\,ROI}} C(j)\Big|_J}{\sum_{k}^{\mathrm{Background}} C(k)\Big|_K} \tag{5}$$

where $C(j)$ and $C(k)$ are respectively the value of voxel j in the cold region (lung or water) and of voxel k in the background and J and K are the total number of voxel in those regions.

Last, the coefficient of variation was used as a surrogate of the noise level as follows:

$$\mathrm{CV} = 100\frac{\sigma}{CB} \tag{6}$$

where σ is the standard deviation measured in the background.

The computation time required for each SM was reported.

3. Results

3.1. Characteristics of the system matrices

The SMs were compared according to the total number of prompts used to generate them. Figure 3(*a*) shows the percentage of non-zero entries (*%NonZero*) in all SMs. It can be seen that *BtB-Vacuum* SMs are more sparse than I124 SMs. Moreover, the *%NonZero* for I124 SMs increases linearly with respect to the number of simulated prompts with a higher slope than the one found for *BtB-Vacuum* SMs. The *%Ones* for each SM (figure 3(*b*)) shows that for I124 *SMs*, the large majority of non-zero elements are computed only from one detected prompt compared to *BtB-Vacuum* SMs, and slightly increases with the number of detected prompts. Conversely, *%Ones* decreases with the number of detected prompts in the case of *BtB-Vacuum* SMs.

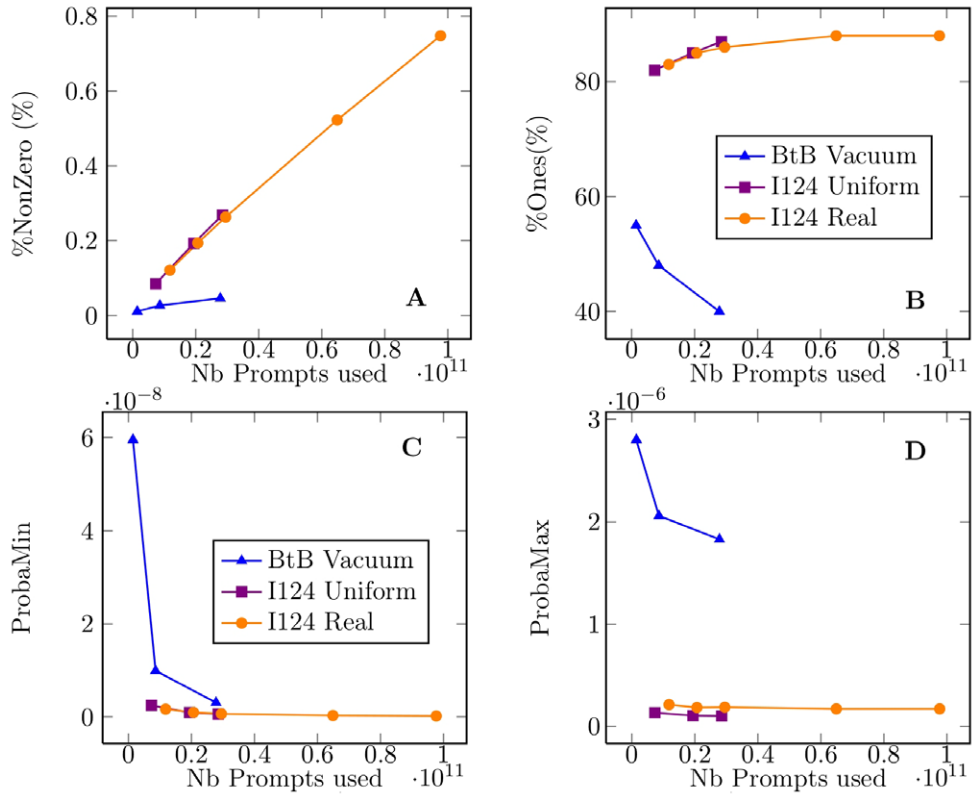

Figure 3. Number of non-zero SM elements (*a*), number of non-zero SM elements computed from only one detected prompt (*b*), and minimum (*c*) and maximum (*d*) probabilities as a function of the number of prompts used for computing each SM.

The minimum (figure 3(*c*)) and maximum (figure 3(*d*)) probabilities show that the probabilities computed for each I124 SMs are lower than those of *BtB-Vacuum* SMs, with a flat trend with respect to the detected number of prompts.

Figure 4 shows the profiles through the different sensitivity images for each SM computed by Monte Carlo. The strong impact of modelling the positron range can be clearly seen in the sensitivity image as a function of density heterogeneities while the profile of the *BtB-Vacuum* SM sensitivity image has a conventional shape in agreement with results reported by Aguiar *et al* (2010).

3.2. Image quality

3.2.1. Homogeneous P0 phantom. In the case of a homogeneous medium, for the same number of prompts used for calculating the SMs, the *BtB-Vacuum* and I124-*Uniform* SMs yielded a better contrast recovery for the hot and cold regions (figure 5) compared with a Siddon-based SM. Modelling the attenuation medium increased the contrast recovery compared to data reconstructed with *BtB-Vacuum* SM.

The absolute activity recoveries were 99 and 101% for the hot region and background respectively (CV = 6%) when using the SM I124-*Uniform Large*, with a number of prompts used to calculate this SM 12 000 times higher than the number of prompts recorded in the

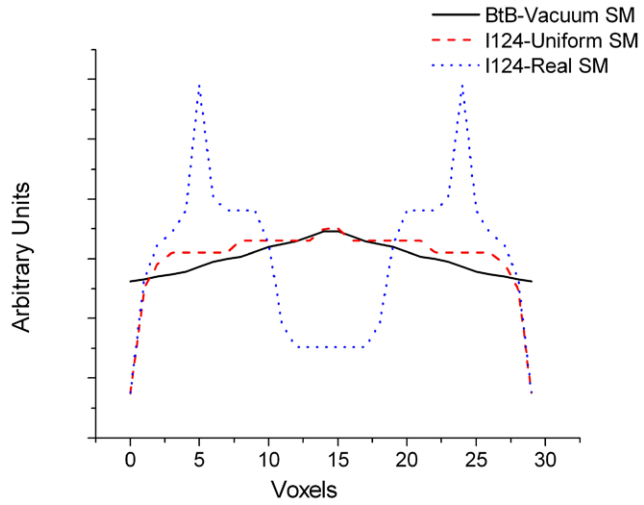

Figure 4. Profiles through the sensitivity images computed with three different Monte Carlo SMs (*BtB-Vacuum Large*, I124-*Uniform Large* and I124-*Real Small*).

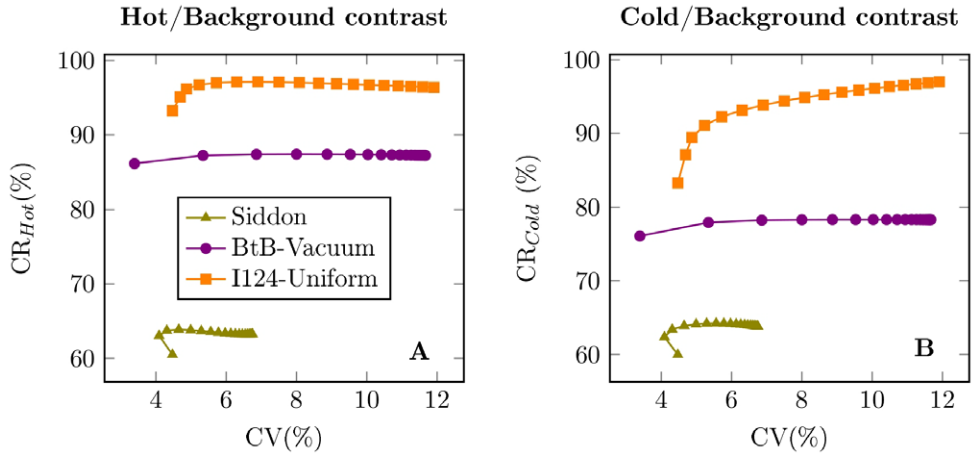

Figure 5. Contrast recovery in the hot (*a*) and cold (*b*) regions of phantom P0 as a function of the coefficient of variation (CV) for three SMs. About the same number of prompts was used for the two Monte Carlo SM (*BtB-Vacuum Large*, I124-*Uniform Large*). Each CV value corresponds to a number of MLEM iteration.

projections. Using the SM I124-*Uniform Small*, activity recovery decreases to 88% within the hot region for the same background noise level.

3.2.2. Heterogeneous phantoms. P1 phantom. Phantom P1 was reconstructed using the four SMs defined in section 2.3. For each SM, the iteration number was chosen so that CV = 12%. The reconstructed images and associated normalized profiles through the hot region are shown in figure 6. Due to the positron range, a high uptake in the bone region (hot and cold) and a low uptake for the hot lung region were observed when using the *BtB-Vacuum* SM and Siddon algorithm. These artifacts were reduced when using the I124-*Real* SM. Only the use of the

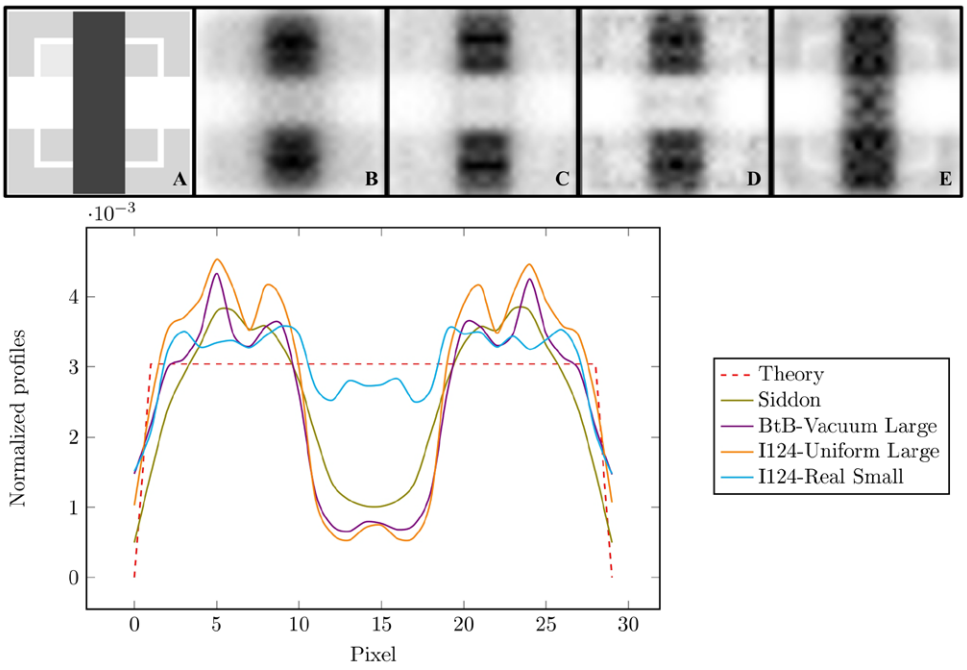

Figure 6. Top: reconstructed images of P1 (CV = 12%) with four SMs: (*b*) Siddon, (*c*) *BtB-Vacuum Large*, (*d*) I124-*Uniform Large* and (*e*) I124-*Real Small* (about the same number of prompt coincidences was used for computing the three Monte Carlo SM), compared to the theoretical distribution (*a*). Gray-scale is identical for all images. Bottom: Line profiles through the hot region of P1 phantom (see profile location in figure 2 (*b*)). Profiles were normalized by the total number of reconstructed counts in each image.

I124-*Real* SM with a precise modelling of the propagating medium allowed partial recovery of activity in the lung region (92%).

P2 phantom. P2 phantom was reconstructed using the four SMs described in section 2.3. For each SM, the iteration number was chosen so that CV = 6%. Reconstructed images are shown in figure 7. The contrast recovery for the smallest region ($1 \times 1\,\text{mm}^2$) was not reported as it was not distinguishable from the background.

The hot region contrasts were better recovered using the MC SMs regardless the background noise level (figure 8). For 'tumors' between 3 and 5 mm in size, the use of I124-*Uniform* SM improved the contrast recovery compared to *BtB-Vacuum* SM. The contrast recovery tended to be higher when using I124-*Uniform* SM (except for the largest tumor) than using the I124-*Real* SM.

Unlike the other MC SMs, the I124-*Real* SM failed to properly identify the cold lung region (figure 8(*f*)). The contrast in the cold water region was better recovered when using I124-*Uniform* and I124-*Real* SMs than with the Siddon and *BtB-Vacuum* SMs (figure 8(*e*)). Finally, it was more challenging to identify the absence of activity in the cold lung region than in the cold water region.

The impact of the number of detected prompts used for computing the I124-*Real* SM is illustrated in figures 8 and 9. Increasing the number of prompts used to compute the SM

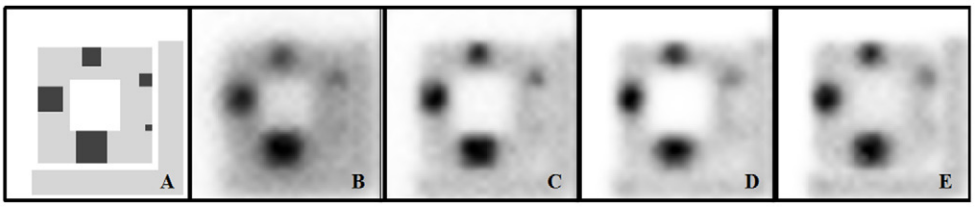

Figure 7. Reconstructed images of P2 phantom (CV = 6%) for four SMs: (*b*) Siddon, (*c*) *BtB-Vacuum Large*, (*d*) I124-*Uniform Large* and (*e*) I124-*Real Small* (about the same number of prompts was used for computing the three Monte Carlo SMs), compared to the theoretical distribution (*a*). Gray-scale is identical for all images.

yielded a better absolute activity recovery for all 'tumors' and for the cold lung region (figures 8(*a*)–(*f*) and figures 9(*a*)–(*d*) and (*f*)). The lack of activity in the cold water region was properly identified whatever the SM (figure 9(*e*)).

Table 2 shows the computation time needed for each SM computation.

4. Discussion

We developed and assessed a fully 3D MC reconstruction method for ^{124}I preclinical PET. Three different types of system matrices (SMs) were computed to study the impact of different levels of complexity and statistical properties. The first level of complexity was to simulate the PET system response using the *BtB-Vacuum* model. Then the model was refined by including the positron range and the spurious coincidences when particles propagated in a uniform medium (I124-*Uniform* SM). This intermediate step was chosen since it can be used regardless of the exact description of the propagation medium, for instance when no transmission scan is available. Finally, a full and complete description of the physics processes for computing the SM was used (I124-*Real SM*). As the SMs are calculated using the MC approach involving simulating a fixed number of possible particle histories, each SM entry is noisy. There is therefore a trade-off between the sophistication of the model (yielding many different particle trajectories) and the noise in each entry estimate.

Figure 3 shows that it is more challenging to get entries with low noise for the I124 SMs compared with *BtB-Vacuum* SMs. Indeed, for a given number of simulated prompts, accounting for all the physics processes (positron range, scattered and spurious coincidences) lead to a larger number of possible LOR through each voxel, which increases the total number of SM entries. These results are consistent with conclusions reported by other groups (Rafecas *et al* 2004, Cabello and Rafecas 2012). We also found that for I124 SMs, most non-zero entries were calculated only from a single detected event, involving a high statistical variance compared to *BtB-Vacuum* SMs entries.

As a result, the number of prompts used to calculate the SM plays an essential role and should be as high as possible when using a sophisticated description of the physics processes. As an example, a decrease of 13% in contrast recovery was observed when four times less coincidences were used to compute the I124-*Uniform Small* SM for P0. In P0, the number of prompts used to calculated the I124-*Uniform* SM has to be 12 000 times higher than the number of prompts recorded in the projections to achieve a contrast recovery higher than 99% in the background and in the hot region. Results presented in figures 8 and 9 advocate for the need to reduce the variance of the SM for achieving better quantitative results when using an SM that fully models the physics processes. With the most accurate I124-*Real* SM, absolute activity recovery was always higher than 85% for all structures larger than 2 mm (figure 9).

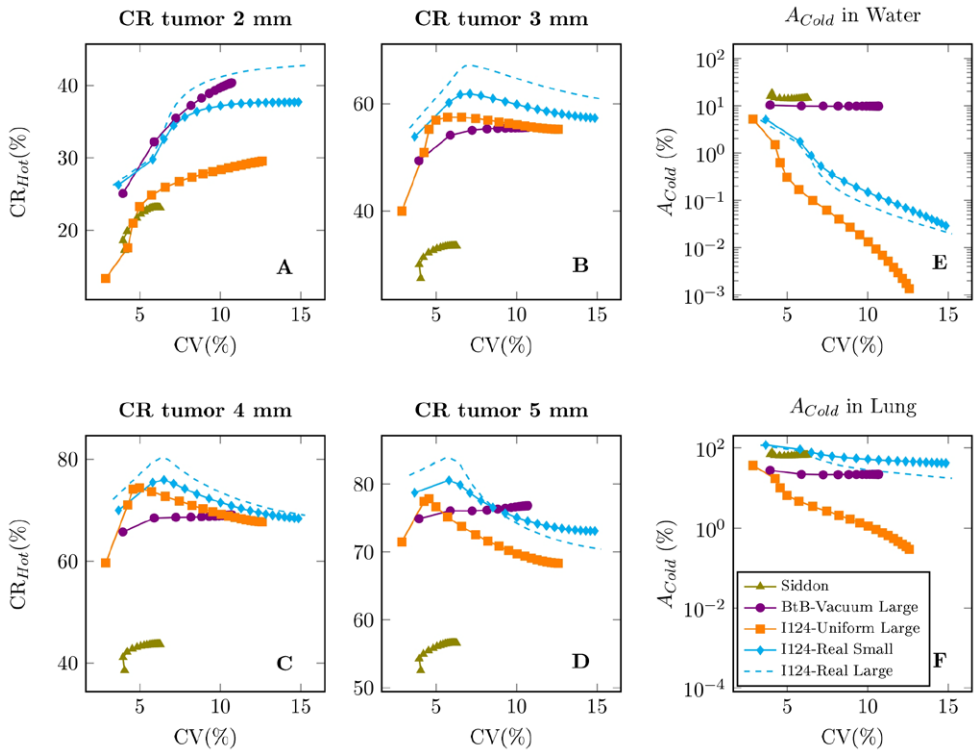

Figure 8. Contrast recovery for various tumors (P2 phantom, tumors size are: 2 mm (*a*), 3 mm (*b*), 4 mm (*c*) and 5 mm (*d*)) and average percentage of residual activity in cold regions (*e*): water, (*f*): lung) as a function of CV for four SMs. About the same number of prompt coincidences was used for computing the Monte Carlo SM (*BtB-Vacuum Large*, I124-*Uniform Large* and I124-*Real Small*). Results when using I124-*Real Large* SM are also presented for highlighting the impact of increasing the number of prompts used in the calculation of the most sophisticated SM.

However, it is worth mentioning that increasing the simulated number of prompts has obviously a significant cost in term of computation time.

Using I124-*Uniform* or I124-*Real* SMs allowed a better contrast recovery for hot and cold regions than simply taking into account the PSF in the SM as performed when using the *BtB-Vacuum* SM (figures 5 and 6). *BtB-Vacuum* SM increases the contrast recovery when compared to the use of the Siddon ray-tracing algorithm, but the improvement was found lower than that between *BtB-Vacuum* SMs and I124-*Uniform* SMs (figure 5) or between *BtB-Vacuum* and I124-*Real* SMs (figure 6). A complete modelling of the system (scanner and object) yielded better qualitative and quantitative results compared with the SM *BtB-Vacuum*, with around 50% improvement in contrast recovery for the hot lung and hot bone regions in P1 (figure 6) and 10 and 20% improvement in contrast recovery for the hot and cold regions respectively in P0 (figure 5). Results shown in figure 6 confirm that precisely accounting for the medium heterogeneity (water, lung and bone) for SM computation yields better quantitative results when activity is present in all regions (figure 2(*b*)), compared to the use of PSF only or PSF and soft tissue modelling only. The activity distribution in the object plays an essential role in the identification of the most appropriate SM. As expected, the use of *BtB-Vacuum* and I124-*Uniform* SMs did not make it possible to correctly locate positron decays

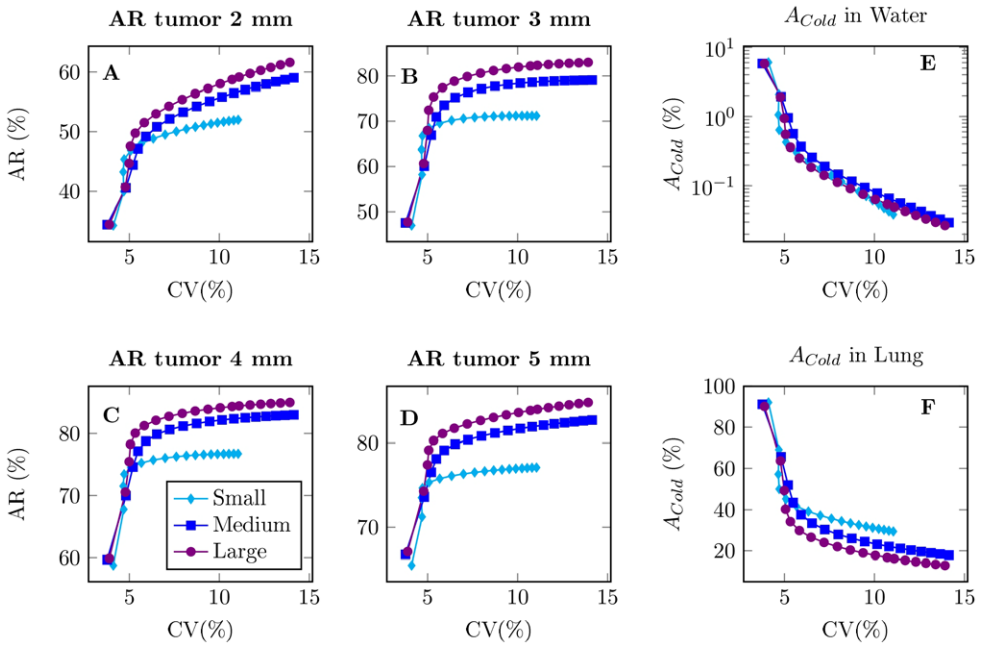

Figure 9. Activity recovery (AR) for various 'tumors' (P2 phantom) (tumors size are: 2 mm (*a*), 3 mm (*b*), 4 mm (*c*) and 5 mm (*d*)) and average percentage residual activity in the cold regions (*e*): water, (*f*): lung) as a function of the CV using the I124-*Real* SMs.

Table 2. Computation time for generating each SM (for one Intel Xeon CPU @ 2.4 GHz).

System Matrix	SM computation time (*h*)
BtB-Vacuum Small	6
BtB-Vacuum Medium	24
BtB-Vacuum Large	72
I124-*Uniform Small*	43
I124-*Uniform Medium*	108
I124-*Uniform Large*	168
I124-*Real Small*	168
I124-*Real Medium*	336
I124-*Real Large*	504

when activity was distributed in regions with large difference in density (lung versus water and bone versus water). The activity was overestimated in bone region while it was underestimated in lung region (figures 6(*c*) and (*d*)) because of the positron range. The impact of modelling all physics processes in the SM was especially visible for the P1 phantom where activity was present in all different media.

With a different activity distribution in the same heterogeneous object (figure 2(*c*)), where activity is only present in water, the reconstructions using MC-based SMs still yielded better contrast recovery than when using SM based on the Siddon ray-tracing algorithm (figure 8). Yet, using the I124-*Real* SM decreased the contrast recovery for all 'tumors' (except for the largest) when comparing with data reconstructed with *BtB-Vacuum* or I124-*Uniform* SMs (figure 8). These observations suggest that the use of SM that account for the different density

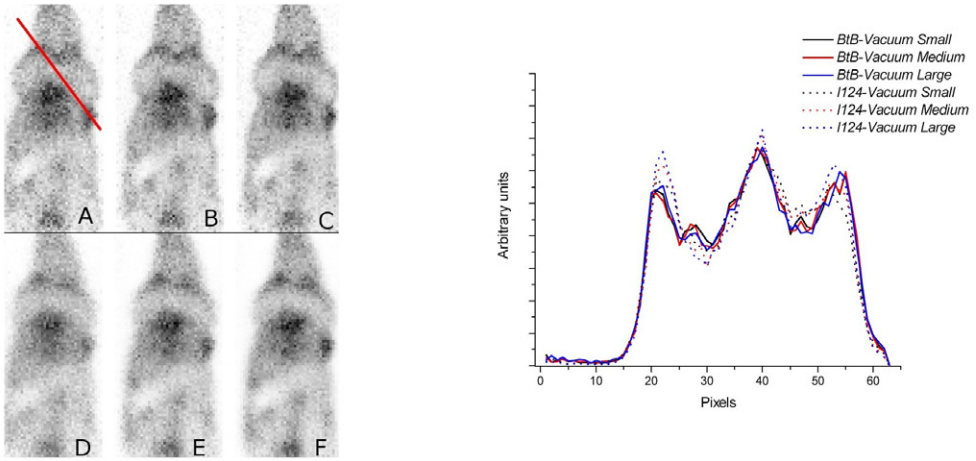

Figure 10. Reconstructed images using the *BtB-Vacuum* (*a*, *b*, *c*) and the I124-*Uniform* (*d*, *e*, *f*) SMs for a mouse that over-expressed CD138 in a breast carcinoma model injected with 3.5 MBq of 124I-labeled B–B4 mAb. Small (*a*, *d*), medium (*b*, *e*) and large (*c*, *f*) SMs have been used. Left: profiles through the red line shown in (*a*).

in the object did not necessarily lead to more accurate quantitative results compared to using an SM that assumed a uniform medium. In this case, for the same number of prompt coincidences used to compute all MC-based SMs, using the SM that precisely modeled the particle interactions within the scanner and the object can worsen the quantitative results compared to a less sophisticated SM because of insufficient statistics when calculating the most complex SM (figures 8(*a*)–(*c*)). However, the respective performance of the SM also highly depends on the activity and attenuation distributions of the object to be reconstructed (see supplemental data) (stacks.iop.org/PMB/60/062475) and makes very difficult to derive a general rule given a fixed number of prompt coincidences used for computing each SM.

We also noted that the smallest structure (e.g. 2 mm size, figure 8(*a*)) was more challenging to recover when the complexity of the SM increased (from *BtB-Vacuum* to I124-*Real*). This might be due to the fact that a small structure is present in a small number of voxels that are crossed by a higher number of LOR in I124-*Uniform* or I124-*Real* SM calculation compared to the ray-tracing algorithm or even the *BtB-Vacuum* SM), yielding many SM elements with high variance that complicate image reconstruction.

This work also suggests that the presence of low-density regions (e.g. lung) makes it even more difficult to get SM entries with a low variance compared to a phantom with a uniform medium of higher density. In the case of a cold lung region for example, the use of I124-*Real* SM actually decreased contrast recovery compared to the use of other MC-based SMs that do not account for those low density regions (figures 7 and 8(*f*)). Indeed, during the SM calculation, positron starting from a voxel located in a low-density region may be detected in a high number of LOR given their higher mean free path compared to their mean free path in a water region. For a same number of simulated decay per voxel used to compute the SM entries, the SM element variance associated to those voxels is thus higher than those computed for voxels located in water.

For illustration purpose only, figure 10 shows an application of the developed approach in a real pre-clinical setting using the high-resolution small animal Inveon PET system, demonstrating the practical feasibility of the approach.

Last, the SM computation times reported in table 2 suggest that without any optimization, the use of the proposed approach is still of limited interest. For the real mouse example shown in figure 10, 16 d (using 336 Intel Xeon CPUs @ 2.4 GHz) were needed for the I124-*Uniform Large* SM calculation (figure 10(*f*)). Yet, several strategies could be used to reduce computation time, including taking advantage of GPU as proposed in GATE v7.0.

5. Conclusion

We developed a fully 3D MC system matrix computation and reconstruction method for ^{124}I preclinical PET acquisitions. The trade-off between complexity (i.e. modelling all physics processes) and statistical robustness for the SM computation was studied. When activity was distributed in regions with different densities, only a precise modelling of the object made it possible to recover hot and cold regions with a maximum deviation in activity estimates of +/ − 20%. However, in a realistic case when activity was present only in soft tissue within a heterogeneous propagation medium, the use of an SM that fully modelled all physics processes in the object and in the PET scanner did not always improved the activity recovery. An SM that only accounted for particle propagation in soft tissue and for the system PSF yielded the most accurate results due to the lack of sufficient statistics in the most sophisticated SM modelling the different densities in the object.

Acknowledgments

The authors wish to thank Dr Simon Stute for valuable discussion. This work was supported by a grant from the Pays de la Loire Council called ‘Nucléaire pour la Santé’ (NucSan).

References

Aguiar P, Pino F, Silva-Rodríguez J, Pavía J, Ros D, Ruibal Á and El Bitar Z 2014 Analytical, experimental, and Monte Carlo system response matrix for pinhole SPECT reconstruction *Med. Phys.* **41** 032501

Aguiar P, Rafecas M, Ortuño J E, Kontaxakis G, Santos A, Pavía J and Ros D 2010 Geometrical and Monte Carlo projectors in 3D PET reconstruction *Med. Phys.* **37** 5691–702

Alessio A and MacDonald L 2008 Spatially variant positron range modelling derived from CT for PET image reconstruction *IEEE Nuclear Science Symp. Conf. Rec.* (*Dresden Germany, 19–25 October 2008*) pp 3637–40

Bai B, Laforest R, Smith A M and Leahy R M 2005 Evaluation of MAP image reconstruction with positron range modelling for 3D PET *IEEE Nuclear Science Symp. Conf. Rec.* (*Fajardo, 23–29 October 2005*) vol 5 pp 2686–89

Bai B, Ruangma A, Laforest R, Tai Y-C and Leahy R M 2003 Positron range modelling for statistical PET image reconstruction *IEEE Nuclear Science Symp. Conf. Rec.* (*Portland, 19–25 October 2003*) vol 4 pp 2501–5

Beattie B J, Finn R D, Rowland D J and Pentlow K S 2003 Quantitative imaging of bromine-76 and yttrium-86 with PET: a method for the removal of spurious activity introduced by cascade gamma rays *Med. Phys.* **30** 2410–23

Cabello J and Rafecas M 2012 Comparison of basis functions for 3D PET reconstruction using a Monte Carlo system matrix *Phys. Med. Biol.* **57** 1759–77

Cal-González J, Herraiz J K, España S, Desco M, Vaquero J J and Udías J M 2009 Positron range effects in high resolution 3D PET imaging *IEEE Nuclear Science Symp. Conf. Rec.* (*Orlando, FL, 24 October–1 November 2009*) pp 2788–91

Cecchetti M, Moehrs S, Belcari N and Del Guerra A 2013 Accurate and efficient modelling of the detector response in small animal multi-head PET systems *Phys. Med. Biol.* **58** 6713–31

Cheng J C, Agbeko N, O'Sullivan J and Laforest R 2009 Evaluation of an iterative cascade gamma ray correction algorithm for non-standard PET nuclides at various counting statistics in high resolution small animal PET imaging *IEEE Nuclear Science Symp. Conf. Rec.* (*Orlando, FL, 24 October–1 November 2009*) pp 2842–5

Cheng J C and Laforest R 2011 Incorporation of a cascade gamma ray correction into the SRW iterative reconstruction for non-standard PET nuclides: towards a unified correction weighted (UCW) scheme in the sensitivity image *IEEE Nuclear Science Symp. Conf. Rec.* (*Valencia, 23–29 October 2011*) pp 4059–62

Disselhorst J, Brom M, Laverman P, Slump C, Boerman O, Oyen W, Gotthardt M and Visser E 2010 Image-quality assessment for several positron emitters using the NEMA NU 4-2008 standards in the siemens inveon small-animal PET scanner *J. Nucl. Med.* **51** 610–7

Floyd C E, Jaszczak R J, Greer K L and Coleman R E 1986 Inverse Monte Carlo as a unified reconstruction algorithm for ECT *J. Nucl. Med.* **27** 1577–85

Fu L and Qi J 2010 A residual correction method for high-resolution PET reconstruction with application to on-the-fly Monte Carlo based model of positron range *Med. Phys.* **37** 704–13

Gregory R A, Hooker C A, Partridge M and Flux G D 2009 Optimization and assessment of quantitative 124I imaging on a Philips gemini dual GS PET/CT system *Eur. J. Nucl. Med. Mol. Imag.* **36** 1037–48

Herbertson R A *et al* 2014 Targeted chemoradiation in metastatic colorectal cancer: a phase I trial of ^{131}I-huA33 with concurrent capecitabine *J. Nucl. Med.* **55** 534–9

Herzog H, Tellmann L, Scholten B, Coenen H H and Qaim S M 2008 PET imaging problems with the non-standard positron emitters Yttrium-86 and Iodine-124 *Q. J. Nucl. Med. Mol. Imag.* **52** 159–65

Herzog H, Tellmann L, Qaim S M, Spellerberg S, Schmid A and Coenen H H 2002 PET quantitation and imaging of the non-pure positron-emitting iodine isotope 124I *Appl. Radiat. Isot.* **56** 673–9

Jan S *et al* 2011 GATE V6: a major enhancement of the GATE simulation platform enabling modelling of CT and radiotherapy *Phys. Med. Biol.* **56** 881–901

Jentzen W 2010 Experimental investigation of factors affecting the absolute recovery coefficients in iodine-124 PET lesion imaging *Phys. Med. Biol.* **55** 2365–98

Johnson C A, Yan Y C, Carson R E, Martino R L and Daube-Witherspoon M E 1995 A system for the 3D reconstruction of retracted-septa PET data using the EM algorithm *IEEE Trans. Nucl. Sci.* **42** 1223–7

Knowles S M and Wu A M 2012 Advances in immuno-positron emission tomography: antibodies for molecular imaging in oncology *J. Clin. Oncol.* **30** 3884–92

Kontaxakis G, Strauss L G, Thireou T, Ledesma-Carbayo M J, Santos A, Pavlopoulos S A and Dimitrakopoulou-Strauss A 2002 Iterative image reconstruction for clinical PET using ordered subsets, median root prior and a web based interface *Mol. Imag. Biol.* **4** 219–31

Kull T, Ruckbager J, Weller R, Reske S and Glatting G 2004 Quantitative imaging of yttrium-86 PET with the ECAT EXACT HR + in 2D mode *Cancer Biother. Radiopharm.* **19** 482–90

Laforest R and Liu X 2009 Cascade removal and microPET imaging with 76Br *Phys. Med. Biol.* **54** 1503–31

Lazaro D, El Bitar Z, Breton V, Hill D and Buvat I 2005 Fully 3D Monte Carlo reconstruction in SPECT: a feasibility study *Phys. Med. Biol.* **50** 3739–54

Lubberink M, Schneider H, Bergström M and Lundqvist H 2002 Quantitative imaging and correction for cascade gamma radiation of 76Br with 2D and 3D PET *Phys. Med. Biol.* **47** 3519–34

Lütje S, Rijpkema M, Franssen G M, Fracasso G, Helfrich W, Eek A, Oyen W J, Colombatti M and Boerman O C 2014 Dual-modality image-guided surgery of prostate cancer with a radiolabeled fluorescent anti-PSMA monoclonal antibody *J. Nucl. Med.* **55** 995–1001

National Electrical Manufacturers Association 2008 Performance measurements for small animal positron emission tomographs NEMA Standards Publication NU 4-2008

Ortuño J E, Kontaxakis G E, Rubio J L, Guerra P and Santos A 2010 Efficient methodologies for system matrix modelling in iterative image reconstruction for rotating high-resolution PET *Phys. Med. Biol.* **55** 1833–61

Pentlow K S, Finn R D, Larson S M, Erdi Y E, Beattie B J and Humm J L 2000 Quantitative imaging of Yttrium-86 with PET. The occurrence and correction of anomalous apparent activity in high density regions *Clin. Positron Imag.* **3** 85–90

Poli G L, Bianchi C, Virotta G, Bettini A, Moretti R, Trachsel E, Elia G, Giovannoni L, Neri D and Bruno A 2013 Radretumab radioimmunotherapy in patients with brain metastasis: a 124I-L19SIP dosimetric PET study *Cancer Immunol. Res.* **1** 134–43

Qi J Y, Leahy R M, Cherry S R, Chatziioannou A and Farquhar T H 1998 High-resolution 3D Bayesian image reconstruction using the MicroPET small-animal scanner *Phys. Med. Biol.* **43** 1001–13

Rafecas M, Mosler B, Dietz M, Pögl M, Stamatakis A, McElroy D and Ziegler S 2004 Use of a Monte Carlo-based probability matrix for 3D iterative reconstruction of MADPET-II data *IEEE Trans. Nucl. Sci.* **51** 2597–605

Rahmim A, Qi J and Sossi V 2013 Resolution modelling in PET imaging: theory, practice, benefits, and pitfalls *Med. Phys.* **40** 064301–16

Rahmim A, Tang J, Lodge M A, Lashkari S, Ay M R, Lautamäki R, Tsui B M W and Bengel F M 2008a Analytic system matrix resolution modelling in PET: an application to Rb-82 cardiac imaging *Phys. Med. Biol*. **53** 5947–65

Rahmim A, Tang J, Lodge M A, Lashkari S, Ay M R and Bengel F M 2008b Resolution modeled PET image reconstruction incorporating space-variance of positron range: Rb-82 cardiac PET imaging *IEEE Nuclear Science Symp. Conf. Rec.* (*Dresden, Germany, 19–25 October 2008*) pp 3643–50

Ruangma A, Bai B, Lewis J S, Sun X, Welch M J, Leahy R and Laforest R 2006 3D maximum a posteriori (MAP) imaging with radiopharmaceuticals labeled with three Cu radionuclides *Nucl. Med. Biol.* **33** 217–26

Sauerzapf S, Thomas L, Behe M, Weber W, Zakhnini A, Pietrzyk A and Mix M 2011 Using Monte-Carlo simulations to implement corrections for I-124 as a non-pure positron emitter in small animal and human PET imaging *IEEE Nuclear Science Symp. Conf. Rec.* (*Valencia, 23–29 October 2011*) pp 2688–91

Shepp L A and Vardi Y 1982 Maximum likelihood reconstruction for emission tomography medical imaging *IEEE Trans. Med. Imaging* **1** 113–22

Siddon R L 1985 Fast calculation of the exact radiological path for a three-dimensional CT array *Med. Phys.* **12** 252–5

Surti S, Scheuermann R and Karp J S 2009 Correction technique for cascade gammas in I-124 imaging on a fully-3D, time-of-flight PET scanner *IEEE Trans. Nucl. Sci.* **56** 653–60

Taleb D, Ali Bahri M, Warnock G, Salmon E, Luxen A, Plenevaux A, Anizan N and Seret A 2012 performance measurements of the microPET FOCUS 120 for iodine-124 imaging *IEEE Trans. Nucl. Sci.* **59** 1868–78

Vandenberghe S, Staelens S, Byrne C L, Soares E J, Lemahieu I and Glick S J 2006a Reconstruction of 2D PET data with Monte Carlo generated system matrix for generalized natural pixels *Phys. Med. Biol*. **51** 3105–25

Vandenberghe S 2006b 3D positron emission tomography imaging with 124I and 86Y *Nucl. Med. Commun.* **27** 237–45

Veklerov E, Llacer J and Hoffman E J 1988 MLEM reconstruction of a brain phantom using a Monte Carlo transition matrix and a statistical stopping rule *IEEE Trans. Nucl. Sci.* **35** 603–7

Walrand S, Jamar F, Mathieu I, De Camps J, Lonneux M, Sibomana M, Labar D, Michel C and Pauwels S 2003 Quantitation in PET using isotopes emitting prompt single gammas: application to yttrium-86 *Eur. J. Nucl. Med. Mol. Imag.* **30** 354–61

Walte A, Sriyapureddy S S, Korkmaz Z, Krull D, Bolte O, Hofmann M, Meyer G J and Knapp W H 2007 Preparation and evaluation of 211At labelled antineoplastic antibodies *J. Pharm. Pharm. Sci.* **10** 277s–85s

Watson C C 2000 New, faster, image-based scatter correction for 3D PET *IEEE Trans. Nucl. Sci.* **47** 1587–94

Wright B D and Lapi S E 2013 Designing the magic bullet? the advancement of immuno-PET into clinical use *J. Nucl. Med.* **54** 1171–4

Yao R, Balakrishnan S, Ambwani S, Rathod V and Shao Y 2005 Quantitative Iodine-124 Imaging on animal PET *IEEE Nuclear Science Symp. Conf. Rec*. (*Fajardo, 23–29 October 2005*) vol 3, pp 1649–52

Yu A R, Kim J S, Kim K M, Lee Y S, Woo S K, Lee W H, Kim J G, Park J A, Kim H J and Cheon G J 2009 Optimal PET acquisition setting of I-124 with siemens inveon PET: comparative simulation study with F-18 and microPET R4 *IEEE Nuclear Science Symp. Conf. Rec.* (*Orlando, FL, 24 October–1 November 2009*) pp 2666–8

^{90}Y-PET imaging: Exploring limitations and accuracy under conditions of low counts and high random fraction

Thomas Carlier[a)]
Department of Nuclear Medicine, University Hospital of Nantes, Place Alexis Ricordeau, Nantes 44093, France and CRCNA–UMR 892 INSERM 6299 CNRS, 8 quai Moncousu BP 70721, Nantes 44007, France

Kathy P. Willowson
Institute of Medical Physics, University of Sydney, Camperdown, New South Wales 2006, Australia

Eugene Fourkal
Department of Radiation Oncology, Allegheny General Hospital, Pittsburgh, Pennsylvania 15212

Dale L. Bailey
Faculty of Health Sciences, University of Sydney, Lidcombe 2141, Australia and Department of Nuclear Medicine, Royal North Shore Hospital, St Leonards, New South Wales 2065, Australia

Mohan Doss
Department of Diagnostic Imaging, Fox Chase Cancer Center, Philadelphia, Pennsylvania 19111

Maurizio Conti
Siemens Healthcare Molecular Imaging, 810 Innovation Drive, Knoxville, Tennessee 37932

(Received 28 October 2014; revised 4 June 2015; accepted for publication 7 June 2015; published 22 June 2015)

Purpose: ^{90}Y-positron emission tomography (PET) imaging is becoming a recognized modality for postinfusion quantitative assessment following radioembolization therapy. However, the extremely low counts and high random fraction associated with ^{90}Y-PET may significantly impair both qualitative and quantitative results. The aim of this work was to study image quality and noise level in relation to the quantification and bias performance of two types of Siemens PET scanners when imaging ^{90}Y and to compare experimental results with clinical data from two types of commercially available ^{90}Y microspheres.

Methods: Data were acquired on both Siemens Biograph TruePoint [non-time-of-flight (TOF)] and Biograph microcomputed tomography (mCT) (TOF) PET/CT scanners. The study was conducted in three phases. The first aimed to assess quantification and bias for different reconstruction methods according to random fraction and number of true counts in the scan. The NEMA 1994 PET phantom was filled with water with one cylindrical insert left empty (air) and the other filled with a solution of ^{90}Y. The phantom was scanned for 60 min in the PET/CT scanner every one or two days. The second phase used the NEMA 2001 PET phantom to derive noise and image quality metrics. The spheres and the background were filled with a ^{90}Y solution in an 8:1 contrast ratio and four 30 min acquisitions were performed over a one week period. Finally, 32 patient data (8 treated with Therasphere® and 24 with SIR-Spheres®) were retrospectively reconstructed and activity in the whole field of view and the liver was compared to theoretical injected activity.

Results: The contribution of both bremsstrahlung and LSO trues was found to be negligible, allowing data to be decay corrected to obtain correct quantification. In general, the recovered activity for all reconstruction methods was stable over the range studied, with a small bias appearing at extremely high random fraction and low counts for iterative algorithms. Point spread function (PSF) correction and TOF reconstruction in general reduce background variability and noise and increase recovered concentration. Results for patient data indicated a good correlation between the expected and PET reconstructed activities. A linear relationship between the expected and the measured activities in the organ of interest was observed for all reconstruction method used: a linearity coefficient of 0.89 ± 0.05 for the Biograph mCT and 0.81 ± 0.05 for the Biograph TruePoint.

Conclusions: Due to the low counts and high random fraction, accurate image quantification of ^{90}Y during selective internal radionuclide therapy is affected by random coincidence estimation, scatter correction, and any positivity constraint of the algorithm. Nevertheless, phantom and patient studies showed that the impact of number of true and random coincidences on quantitative results was found to be limited as long as ordinary Poisson ordered subsets expectation maximization reconstruction algorithms with random smoothing are used. Adding PSF correction and TOF information to the reconstruction greatly improves the image quality in terms of bias, variability, noise reduction, and detectability. On the patient studies, the total activity in the field of view is in general accurately

measured by Biograph mCT and slightly overestimated by the Biograph TruePoint. © *2015 American Association of Physicists in Medicine.* [http://dx.doi.org/10.1118/1.4922685]

Key words: ^{90}Y-PET, radioembolization, quantification

1. INTRODUCTION

Selective internal radionuclide therapy (SIRT) is a treatment modality for liver cancer based on in the intra-arterial catheter injection of ^{90}Y-loaded-microspheres. The principle is to saturate the tumor with ^{90}Y microspheres (20–50 μm) through selective lodgment in its hypervascular network. Microspheres are blocked in the capillaries and deliver the therapeutic effect of ^{90}Y ionizing radiations (β^- disintegration) locally ($E_{\beta_{\max}}$ = 2.2 MeV, maximum range in water: 11 mm).[1] SIRT is indicated in nonresectable liver cancer with or without portal vein thrombosis, which makes it a good alternative to liver directed procedures such as transarterial chemoembolization.[2,3]

There is considerable interest in performing SIRT dosimetry.[4–6] The ability to compute dose volume histograms (DVHs) in the tumor or the nontumor liver allows for a concise representation of the 3D absorbed dose distribution. 3D dosimetry requires an accurate voxel-based quantification through emission tomography[7] feeding into a realistic voxel by voxel modeling of the energy deposition.[8] For this purpose, ^{90}Y-based bremsstrahlung single photon emission computed tomography (SPECT) could be used but it is complicated by the poor spatial correlation of the signal to the site of deposition and lack of an appropriate collimator[9] and requires specific reconstruction algorithms that are still under development.[10] The resulting images have a poor spatial resolution and are not quantitatively accurate, particularly for small lesions.[10]

The ^{90}Y nucleus decays (half-life: 64 h) to the fundamental level of ^{90}Zr by beta emission (99.99%), but a lower probability branch (0.01%) follows another beta decay to a ^{90}Zr excited state. The following 0^+–0^+ transition (1.78 MeV) of ^{90}Zr can happen via a pair creation β^+/β^- with an even smaller branching ratio (31.86×10^{-6}), which results in a weak but detectable positron emission tomography (PET) signal [Fig. 1(a)]. Hence, the first clinical applications of PET imaging with ^{90}Y have been proposed recently, mainly in the context of SIRT (Refs. 11–13) and peptide receptor radionuclide therapy.[14,15] Thus, ^{90}Y-PET imaging might be a valuable alternative to derive quantitative information with a high spatial resolution based on state-of-the-art PET/CT systems including resolution modeling and time-of-flight (TOF) capability.

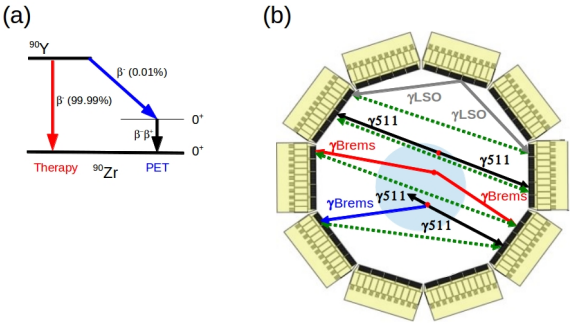

F . 1. Simplified decay scheme of ^{90}Y (a). Different types of true coincidences (b). γ511-γ511: two 511-keV photons in coincidence; γBrems-γBrems: two Bremsstrahlung photon that could yield a coincidence; γ511-γBrems: Bremsstrahlung photon that could yield a coincidence with an annihilation photon; γLSO-γLSO: two LSO-based events that could yield a true coincidence. The dotted lines are for the resulting LOR for all coincidences.

Studies were initially focused on the quantitative performance of ^{90}Y-PET imaging using clinical reconstruction algorithms and standard acquisition parameters. Several authors reported satisfactory quantitative performance using phantom experiments[16–20] and the benefit of acquiring data with TOF information was also addressed.[21] However, concerns remain when comparing ^{90}Y-PET imaging accuracy with ^{18}F-FDG-PET accuracy. Indeed, contrast recovery for small features is lower in ^{90}Y-PET imaging than in ^{18}F-FDG-PET imaging, as reported by several authors and this still remains at least partly unexplained.[10,16,17] The accuracy and reproducibility of the PET measurement of total injected activity need also to be assessed, as this may be a reliable method for confirming total delivered activity to patients in situations where vascular backpressure from the liver during the procedure limits the dose that can be delivered to less than prescribed.

PET imaging of ^{90}Y is challenging because of several factors inherent to the physics of the decay. First of all, the high flux of bremsstrahlung photons from the prevalent therapeutic β^- decay branch [Fig. 1(a)], which are reduced by collimation in SPECT, could overwhelm the PET detectors. From the point of view of the random coincidences, the same high flux of time-uncorrelated bremsstrahlung photons is responsible for a very high random fraction (defined as the ratio between the number of random coincidences and the number of prompt coincidences) in the PET coincidence data; if LSO or LYSO scintillators are used, these random coincidences add to the random coincidences generated by the photons resulting from natural ^{176}Lu present in the crystals. Indeed, the LSO is a scintillator typically containing 2.6% of ^{176}Lu, a radioactive isotope that decays β^- into ^{176}Hf with a cascade of γ photons in coincidence, with 307, 202, and 88 keV energy.

Finally, given the small branching ratio of true coincidences from pure annihilation 511 keV photons, the contribution of spurious events in time coincidence cannot be *a priori* ignored.

In Fig. 1(b), all possible true events are shown: (a) the true coincidence of back-to-back 511 keV photons from the pair production, (b) the coincidences from LSO background, (c) the coincidences from two bremsstrahlung photons emitted simultaneously by the therapeutic β^-, and (d) the coincidences from an annihilation 511 keV photon and a bremsstrahlung photon emitted simultaneously.

The only significant contribution to true coincidence counts is the 511 keV photons from pair production from ^{90}Y decay: given the time and energy window of a typical PET scanner,

there is a very low probability of two high energy bremsstrahlung photons being recorded in coincidence, or even lower for one high energy bremsstrahlung and one 511 keV photon given the half time (62×10^{-9} s) of the excited state of ^{90}Zr.[22] Scatter correction, random correction, and algorithm bias at low counts are key issues for ^{90}Y PET imaging.

This study aims to establish a new full comprehensive analysis of ^{90}Y-PET imaging as a function of the random fraction and the number of true coincidences for two PET systems (both from Siemens Healthcare Molecular Imaging) of different generations: the Biograph TruePoint (previous) and the Biograph mCT (current). To the best of our knowledge, no studies have been thoroughly focused on the impact of variable random fraction and number of true coincidences on quantitative results for different reconstruction algorithms and PET scanners. For this purpose, the study was divided into three parts: (1) assessment of ^{90}Y-PET quantification and bias for different reconstruction methods, random fraction, and number of true coincidences, (2) recovered activity (RA) in lesions, variability, and image roughness study, and (3) comparison of activity derived by PET imaging with the theoretical injected activity in patients as a function of reconstruction algorithm.

2. METHODS AND MATERIALS

This work is aimed at establishing the quantification and image quality performance for ^{90}Y on the Siemens Biograph TruePoint and Biograph mCT PET/CT scanners. The study was based on the use of a 4-ring Biograph mCT (Ref. 23) and 3-ring Biograph TruePoint 16 (Ref. 24) scanner. They are representative of the two main Siemens PET scanners used for ^{90}Y imaging, and the different reconstruction methods available are tested and discussed in this paper.

After a preliminary evaluation of the effect of bremsstrahlung and LSO background on the data, the investigation consists of three parts: (a) a first study with a uniform water phantom containing a large uniform ^{90}Y insert, aimed to assess quantification performance and reproducibility of the measurement, (b) a second study with a PET image quality phantom, aimed to assess capability to detect and quantify local concentration of activity of the order of a few centimeters and to measure noise level, and (c) a third study consisting of the analysis of the relationship between injected and measured activities in patient images. The two phantoms used in parts (a) and (b), the NEMA 1994 PET phantom and the NEMA/IEC 2001 PET phantom, are shown in Fig. 2.

2.A. PET scanners and reconstruction details

Both PET scanners are made of detector rings on a cylindrical geometry. Each ring incorporates 48 detector blocks, 5.2×5.2 cm in cross section. Each block comprises a 13×13 matrix of $4\times4\times20$ mm^3 LSO crystal elements. The Biograph TruePoint used in this work is a 3-ring scanner, covering 3×5.2 cm^2 axial field of view (FOV), and the Biograph mCT is a 4-ring scanner, covering 4×5.2 cm^2 axial FOV. The NEMA sensitivity is 4.2 cps/kBq for the 3-ring Biograph TruePoint[24] and 9.5 cps/kBq for the 4-ring mCT.[23] The time coincidence window, for prompt and delayed coincidences, is 4.1 ns for both scanners. The Biograph mCT is a TOF-capable scanner, with a TOF reconstruction kernel of 580 ps, while the Biograph TruePoint does not have TOF capability.

At the time of this experiment, ^{90}Y was not available in the list of acquisition radioisotopes provided. Data could be acquired using any of the radioisotopes in the database, and two methods are typically used to obtain correct quantification: (1) the sinogram header is edited and the branching ratio and half-life are modified according to ^{90}Y values before reconstruction and (2) the scan is reconstructed and the resulting values are modified accounting for the correct branching ratio and half-life. For this work, we used a ^{22}Na acquisition setting (as ^{90}Y was not available) and activity branching ration was corrected *a posteriori*.

The reconstruction methods available on both or either one of the two PET scanners are filtered backprojection (FBP), in conventional and TOF mode, 2D attenuation weighted ordered subsets expectation maximization (AW-OSEM2D), 3D ordinary Poisson-OSEM (OP-OSEM3D) in conventional and TOF mode (OP-OSEM3D+TOF), and OP-OSEM3D with point spread function correction (OP-OSEM3D+PSF) in conventional and TOF mode (OP-OSEM3D+PSF+TOF). The 2D reconstructions, FBP and AW-OSEM2D, are preceded by Fourier rebinning to reassign 3D data into 2D format for reconstruction. All reconstruction methods available are listed in Table I, with the "label" used in the user interface.

During reconstruction, data are normalized, corrected for attenuation, scatter, and random coincidences. The randoms are measured as delayed coincidences. In FBP and AW-OSEM2D, the delayed coincident events are unsmoothed.

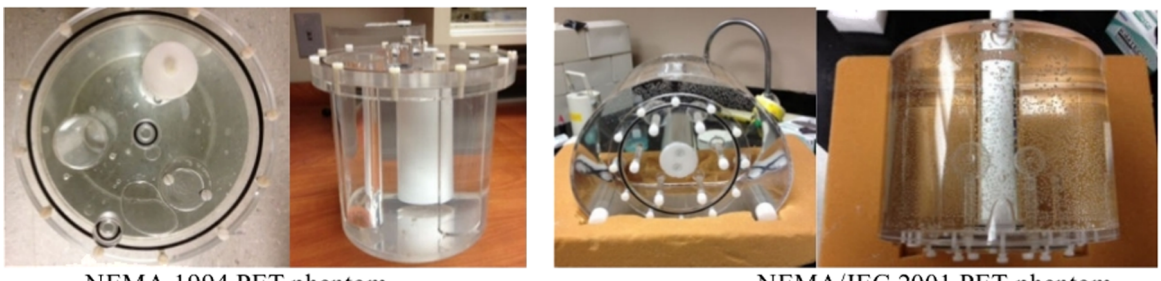

F . 2. Phantoms used.

T I. Reconstruction methods used and labels with which they are available on the Siemens scanners.

Reconstruction method	Image pixel size, iteration, subsets, 3D Gaussian post-reconstruction filter (FWHM)	Biograph TruePoint label	Biograph mCT label
FBP	4×4×2 mm^3, N/A, N/A, 5 mm	Backprojection	Backprojection
AW-OSEM2D	4×4×2 mm^3, 3i, 24ss, 5 mm	Iterative	N/A
OP-OSEM3D	4×4×2 mm^3, 3i, 24ss, 5 mm	Iterative	Iterative
OP-OSEM3D+TOF	4×4×2 mm^3, 2i, 21ss, 5 mm	N/A	Iterative+TOF
OP-OSEM3D+PSF	4×4×2 mm^3, 3i, 24ss, 5 mm	TrueX	TrueX
OP-OSEM3D+PSF+TOF	4×4×2 mm^3, 2i, 21ss, 5 mm	N/A	TrueX+TOF

In all reconstruction based on OP-OSEM3D methods, the delayed coincident events are smoothed in order to have a noiseless estimate.[25] In order to be able to smooth the random coincidences, a separate prompt coincidence and random coincidence acquisition mode is used in the Biograph TruePoint (it is the default for Biograph mCT).

Scatter correction is also a sensitive part of the reconstruction process in a situation of count limitation such as ^{90}Y imaging. The single scatter simulation with tail fitting and scaling is used.[26,27] The scatter scaling, or fitting of the tails of the sinogram, was not used for the first study on the cylindrical phantom, in order to reduce this uncertainty and to obtain a more consistent scatter correction across variable random fraction and count statistics. Scatter scaling was still used for the image quality phantom and for the patient studies, to be closer to the clinical practice.

A larger 4-mm image pixel size was used, in order to reduce the noise due to the low number of counts, and a 3D 5 mm-full width at half maximum (FWHM) Gaussian filter was applied post-reconstruction. Subsets and iteration number for iterative methods were selected based on typical clinical parameters, but also a preliminary assessment was done to verify that an acceptable level of convergence was reached. TOF reconstruction needs fewer iterations because of the faster convergence rate. In Table I, the reconstruction parameters are listed. Finally, it must be noted that the correctness of quantification does depend on the convergence level, and more iterations could offer better recovery. The bias is also affected by the number of iterations.

2.B. Quantification and bias experiments

The NEMA 1994 PET phantom was used for assessing the quantification performance of the different reconstruction methods. The NEMA 1994 PET phantom is a water phantom (inner diameter: 19 cm) with 3 inserts: two fillable with water (inner diameter: 4.5 cm) and the third is a Teflon cylinder typically used to simulate bone. The Teflon insert was removed, one of the inserts was left empty (air), and one insert was filled with a water solution of ^{90}Y. This phantom is simple but particularly interesting to test reliability and bias of reconstruction algorithms: the cold water background is particularly challenging, since it is populated by a high level of random and scatter coincidences and no true coincidences.

This phantom represents a more realistic simulation of a liver in abdomen, where no background activity is present, compared to a classic image quality phantom with background activity.

The initial activity used for the Biograph mCT experiment was 4183 MBq and for the Biograph TruePoint was 2845 MBq. The insert, 19 cm long, was fully contained within the axial FOV of the 4-ring mCT, but it was only partially covered by the 3-ring Biograph TruePoint. Therefore, the initial activity estimated in the FOV for the 3-ring scanner was corrected by the axial coverage (5.2 cm × 3)/19 cm (5.2 cm is the size of a block): initial activity in the FOV was 2845 MBq × 0.82 = 2332 MBq. The phantom was scanned for 60 min in the PET/CT every one or two days, in list mode. For each scan, a CT was acquired for attenuation and scatter correction. In Table II, the scan details for each experiment are reported.

The prompt and random coincidence emission sinograms acquired in this experiment were used in a preliminary investigation on the impact of the bremsstrahlung photons. Prompt, random, and net true coincidence sinogram profiles at different random fractions were compared.

Then, activity quantification accuracy, activity variability, and algorithm bias in the background were studied. The list mode files were used to extract data for two studies: (a) quantification and bias as a function of the random fraction and (b) quantification and bias as a function of the number of true counts in the scan.

The total number of net true coincidences (e.g., the number of prompts minus the number of random coincidences) in the scan selected for the study of quantification vs random fraction was 0.16×10^6 for the 4-ring Biograph mCT and the 3-ring Biograph TruePoint. The number of net trues selected is representative of a typical patient scan. Each list mode data set was rebinned into a sinogram and reconstructed using

T II. Acquisition delay and activity in the PET FOV in different frames for the NEMA 1994 PET phantom.

	Biograph mCT		Biograph TruePoint	
	Delay	MBq	Delay	MBq
Frame 0	0	4183	0	2332
Frame 1	23 h 7 min	3256	—	
Frame 2	—		1 day 20 h 36 min	1439
Frame 4	3 days 13 h 26 min	1658	3 days 22 h 6 min	842
Frame 6	5 days 13 h 19 min	987	5 days 15 h 33 min	537
Frame 8	7 days 13 h 15 min	587	7 days 22 h 50 min	295

selected reconstruction methods. The corresponding images were analyzed. Total activity in the whole FOV and in the insert was plotted as a function of the estimated injected activity.

One of the first frames was used for the study of quantification as a function of true coincidences: frame 0 for the Biograph TruePoint (random fraction 68%) and frame 1 for the Biograph mCT (random fraction 71%). Files with increasing number of net true events were extracted, covering a range from 80 kcts to over 1 Mcts. Each of these list mode files was rebinned into a sinogram and reconstructed using selected reconstruction methods. The corresponding images were analyzed. Three regions in the FOV were identified: the insert with ^{90}Y activity, the cold water region in the cylindrical phantom (including the air insert), and the rest of the FOV outside the phantom, basically air and the scanner bed. In each region, 25 central slices, 2 slices apart to reduce the pixel correlation, were selected, and 3 regions of interest (ROIs) were placed in each plane: (a) "insert," a circle including the insert filled with ^{90}Y (5 cm diameter), (b) "water," a circle around the phantom (20 cm diameter) including the air insert (5 cm diameter) but excluding the insert filled with ^{90}Y, and (c) "air," a 60-cm diameter circle centered in the FOV, but excluding the phantom. The residual activity in air [region (c)] was minimal and is therefore discussed further in this work.

Mean values in the 25 ROIs were used to compute a mean value for the activity concentration in each of the three regions. The standard deviation of the activity concentration in the insert region was also derived for assessing the quantification variability and estimating the error on the activity density measurement.

In addition, total activity in the FOV was computed by adding the activity in all image voxels. In order to estimate the reproducibility of the measurements, five noise realizations of the same sinogram were obtained when possible, extracting data randomly from the original long file. The standard deviation of the total activity over the five realizations was used as an estimate of the reproducibility. These five sinograms were extracted from the original list mode file with an identical number of net true events for each of the five sinograms ranging from 81 920 to 573 440 net true events for the Biograph mCT and 81 920 to 245 760 for the Biograph TruePoint, given the reduced amount of data available for this system.

2.C. Image quality and noise level experiments

The NEMA 2001 PET phantom (total volume: 9.7 l) used is a water phantom with six fillable spheres (of diameter 10, 13, 17, 22, 28, and 37 mm) and a Styrofoam cylindrical insert in the center. The spheres and the background were filled with a ^{90}Y solution in an 8:1 contrast ratio. The initial activity instilled for the Biograph mCT experiment was 3785 MBq, and for the Biograph TruePoint, it was 2879 MBq. The phantom was acquired with one bed position for the Biograph mCT and two bed positions for the Biograph TruePoint. Acquisition time was 30 min for the Biograph mCT and 15 min for each bed position for the Biograph TruePoint; acquisition was repeated every one or two days. For each scan, a CT was acquired for attenuation and scatter correction.

All frames were reconstructed using the methods described in Sec. 2.A, with the exception of AW-OSEM2D, which had previously demonstrated an extremely high bias, and hence unreliable quantitative results. The total activity in the phantom (obtained by summing all activity in the FOV) in each frame, corrected for decay, was studied as a function of the assayed activity.

Across all frames, the contrast to noise ratio (CNR) in the 22-mm sphere was studied as a function of the decaying activity. The CNR was assumed to be related to the visual ability to detect a small lesion, in a noisy background.[17,28] It was defined as

$$\mathrm{CNR} = \frac{C_L - C_B}{\sigma_B} \times \sqrt{N} \times \mathrm{PVE}, \tag{1}$$

where C_L and C_B are the sphere and the background intensity, respectively, N is the number of voxels within the sphere, σ_B is the background variability as calculated in the numerator of Eq. (3), and PVE (0–1) is the recovery coefficient due to the partial volume effect for the 17-mm sphere. The recovery coefficient was evaluated with a ^{18}F-based acquisition using a contrast ratio identical to that of the ^{90}Y-based acquisitions. A list mode file acquired with ^{18}F was split into ten independent files with the same number of net true events. The mean recovery coefficient was derived and defined as the PVE.

Of all the available frames, the frame with total true events and random fraction closer to a clinical condition was chosen, namely, frame 3 for the Biograph mCT and frame 0 for the Biograph TruePoint. The selected scan had 0.4×10^6 net trues and 86.5% random fraction for the 4-ring Biograph mCT and 0.4×10^6 net true events and 77% random fraction for the 3-ring Biograph TruePoint. For this frame, the recovered activity concentration as a function of sphere size was studied, for all reconstruction methods, using a volume of interest corresponding to the entire sphere volume.

Background variability and image roughness were also studied as a function of the reconstruction method. The background variability represents the local nonuniformity and could be affected by systematic local bias; the image roughness is a measure of the pixel to pixel variability or the level of noise in a single image and affects the visual ability to detect small objects in the noisy background.[29] The image roughness can be expressed as the coefficient of variation (COV) measured as standard deviation in large uniform ROIs and averaged over the number of ROIs (using the ROIs definition proposed in the NEMA 2007 protocol).

Background variability (BV) was defined as

$$\mathrm{BV} = 100 \cdot \frac{\sqrt{\sum_{k=1}^{K} \left(\frac{(m_k - \bar{m})^2}{K-1} \right)}}{\bar{m}}, \tag{2}$$

where m_k is the mean value inside a ROI_k and $\bar{m}$ is the mean value of m_k across the $K = 60$ ROIs.

The COV was defined as

$$\mathrm{COV} = \sum_{k=0}^{K} \frac{1}{K} \frac{\sqrt{\sum_{i \in \mathrm{ROI}_k}^{I} \left(\frac{(\mathrm{img}_i - m_k)^2}{I-1} \right)}}{m_k}, \quad (3)$$

where img_i is an image element value inside a ROI_k (I image elements) and m_k is the mean value in the ROI_k ($K = 60$ ROIs). The ROI size was equal to the sphere considered for the computation.

2.D. Quantification in patients

Finally, the quantification characteristics of the different reconstruction methods were verified on 32 patient data sets collected from 3 hospital sites: 10 patients from the Fox Chase Cancer Center (Philadelphia) equipped with a Biograph TruePoint, 10 patients from the University Hospital of Nantes (Nantes, France) equipped with a Biograph mCT, and 12 patients from the Royal North Shore Hospital (Sydney, Australia) equipped with a Biograph mCT. Patients enrolled in the Fox Chase Cancer Center and the Royal North Shore Hospital were acquired over 20 min (two bed positions), while patients enrolled at the University Hospital of Nantes were acquired over 30 min (one bed position).

OP-OSEM+PSF with 2 iterations and 21 subsets for Biograph TruePoint and OP-OSEM+PSF+TOF with 2 iterations and 21 subsets for Biograph mCT were used. FBP reconstruction is added as a reference. Pixel size was $4\times4\times2$ mm^3 and $4\times4\times3$ mm^3 for the Biograph TruePoint and Biograph mCT, respectively. A 5 mm-FWHM post-reconstruction Gaussian filter was applied to all images.

All data were analyzed using a dedicated nuclear medicine workstation (DOSIsoft, Cachan, France). Total activity in the image was plotted as a function of the estimated injected activity. The coregistered CT data were also used to segment whole liver volumes and the total activity in the segmented liver was plotted as a function of the estimated injected activity.

3. RESULTS

3.A. Effect of bremsstrahlung and LSO background

The ^{176}Lu natural background spectrum contributes to the single detected events, measured to be about 5000 s^{-1}/block in a Biograph mCT, and therefore to the delayed coincidences, measured to be about 1100 s^{-1} in a 4-ring Biograph mCT. There is also a very weak contribution to true coincidences: it was measured to be about 1–5 counts/s in a 4-ring mCT. While the contribution to the true coincidences is negligible compared to the true coincidences from ^{90}Y 511-keV photon pairs, the random coincidences from LSO are a strong component of the total detected random coincidences.[17]

The relative contribution to randoms from LSO and bremsstrahlung can be seen in Fig. 3, where the radial profile of the delayed coincidences is shown for the Biograph TruePoint. We used the sinograms acquired for the experiment described in Sec. 2.B. Each scan was 30 min long; all planes and angles

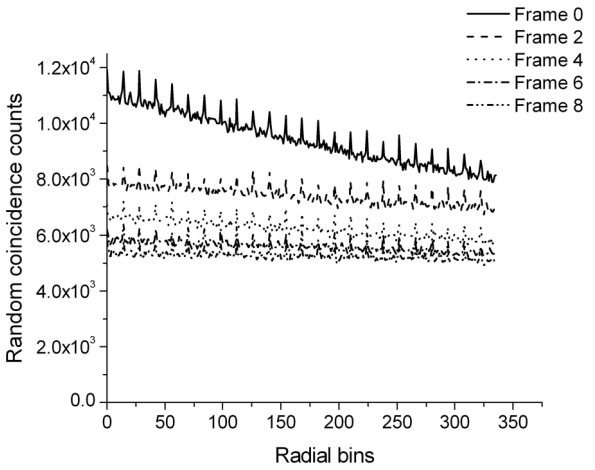

F . 3. The sinogram radial profile of the delayed coincidences measured in each of the scans acquired on the Biograph TruePoint in eight consecutive days using the NEMA 1994 PET phantom. Each scan is 30 min long; all planes and angles are added.

of the delayed sinogram were added and plotted, from top to bottom, for frames 0, 2, 4, 6, and 8. Clearly there are two contributions to the delayed events: the bremsstrahlung randoms with some spatial distribution (see slope left–right) and the LSO random coincidences that are uniform across the FOV. Overtime the bremsstrahlung random events disappear and the distribution becomes flat (only LSO). As can be seen in Fig. 4, the measured delayed curve fits well the prompt coincidences outside the phantom, and a random estimate based on the delayed coincidences should be reliable and able to subtract random coincidences from both sources, provided that a smoothed estimate can be obtained.

3.B. Quantification and bias experiments

The analysis of the quantification in the images vs random fraction is presented in Fig. 5, and the random fraction for all data points is presented in Table III. All data are decay corrected to the assay time. LSO background true counts were

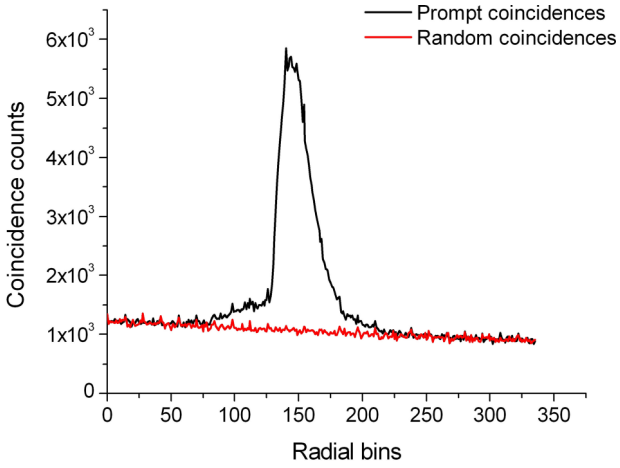

F . 4. The radial profile of the prompt and delayed coincidences in the sinogram, measured on the Biograph TruePoint, frame 0, using the NEMA 1994 PET phantom. All planes and angles are added.

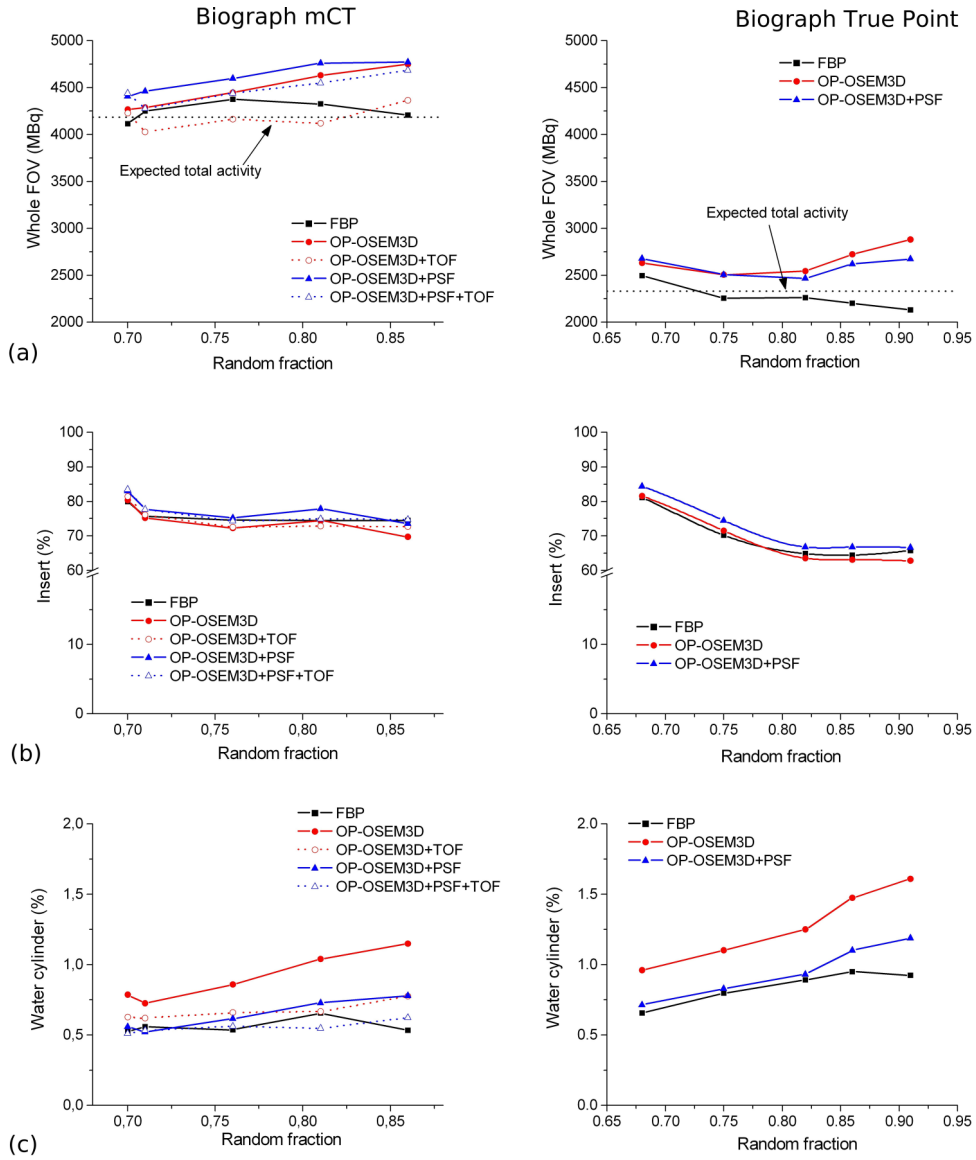

F . 5. Decay corrected total activity and activity concentration in three regions vs random fraction: (a) total activity, (b) hot insert (5 cm diameter), and (c) water background (20 cm diameter) including the air insert (5 cm diameter). Plots (b) and (c) are normalized by the expected activity concentration in the hot insert. Results from Biograph mCT (left) and Biograph TruePoint (right). Each data point has 0.16×10^6 trues for mCT and Biograph TruePoint data.

always below 3% in all data sets and were therefore neglected in the decay correction.

The total activity measured in the FOV according to the random fraction is shown in Fig. 5(a), for all reconstruction methods. For the Biograph mCT scanner, the FBP reconstruction yields a very stable value in the covered range, while for iterative reconstructions, a small algorithm bias is visible at higher random fraction. The Biograph TruePoint data have a similar behavior in terms of algorithm bias but there is some uncertainty on the expected input activity due to the axial coverage of the scanner.

The AW-OSEM2D images, available only in the Biograph TruePoint, are not shown in Fig. 5. In fact, they are consistently characterized by a strong positive bias in the background, much larger than all other methods. For example, even at a relatively small random fraction of 68%, the measured activity is 5344 MBq, compared to an expected total activity of 2332 MBq. Because of this strong positive bias at low counts, AW-OSEM2D is clearly not recommended for ^{90}Y imaging, and it will not be considered and presented in the following results.

T III. Random fraction, defined as random divided by prompt coincidences, in different acquisition frames. All frames contain 0.16×10^6 net true counts (prompts–randoms).

	Random fraction	
	Biograph mCT	Biograph TruePoint
Frame 0	0.70	0.68
Frame 1	0.71	—
Frame 2	—	0.75
Frame 4	0.76	0.82
Frame 6	0.81	0.86
Frame 8	0.86	0.91

In Fig. 5(b), the activity concentration in the insert is plotted, corrected for decay, and normalized to the expected value. For the Biograph mCT, the recovery in the insert is stable over the random fraction range, and it is about 80%. Increasing the number of iterations would probably increase the recovery. For the Biograph TruePoint, the recovery is similar, but it seems to have a decreasing trend with increasing random fraction.

A linear relationship between expected and measured activities is observed for all reconstruction method used (plots not shown), considering either the whole FOV (Table IV) or the total activity in the insert (Table V). The Biograph TruePoint slightly overestimates the total activity.

The bias in the water background is studied and reported in Fig. 5(c), corrected for decay, and normalized to the expected value in the insert. Bias is within a few percent. Much higher bias is observed in AW-OSEM2D reconstruction, as pointed out already. Some artifact bias is also observed in the air around the phantom, and it contributes to the total bias in the FOV, but it is much lower than in the water phantom, closer to the source, and associated with more scatter events. In general, bias is higher for iterative algorithms and increases with random fraction. PSF correction and TOF reconstruction reduce the bias.

In Fig. 6, the activity is studied as a function of the counts in the scan. One can observe that total activity and activity concentration in the insert are very stable with decreasing counts [Figs. 6(a) and 6(b)]. In Fig. 6(c), the bias is presented as a function of the number of counts. While for the Biograph mCT the background bias is almost stable over the range, a trend of growing bias with decreasing counts can be observed in the Biograph TruePoint. Nevertheless, the effect of the background bias on the measured total activity is limited, as can be seen in Fig. 6(a). In general, PSF correction and TOF reconstruction reduce the bias.

Over all measurements in Figs. 5 and 6, one can observe an average bias in the water background of the order of 10^4 Bq/ml. FBP reconstruction and reconstructions with PSF correction have the lowest bias in water background, but it must be stressed that here we report the average bias in the large volume: the FBP reconstruction might show strong local bias and does have a highly structured noise pattern.

In Fig. 7, the standard deviation of whole FOV activity as a function of the number of net true events in the sinogram is shown, for both scanners. Only three data sets were available for the Biograph TruePoint experiment, given the reduced amount of data available in the list mode.

T IV. Proportionality coefficient and goodness of fit, for total activity in the whole FOV (R^2 in parenthesis).

	Biograph mCT	Biograph TruePoint
FBP	0.98 ± 0.02 (0.99)	1.08 ± 0.08 (0.98)
OP-OSEM	0.99 ± 0.01 (0.99)	1.11 ± 0.03 (0.99)
OP-OSEM+TOF	0.99 ± 0.02 (0.99)	—
OP-OSEM+PSF	1.03 ± 0.01 (0.99)	1.14 ± 0.04 (0.99)
OP-OSEM+PSF+TOF	1.04 ± 0.02 (0.99)	—

T V. Proportionality coefficient and goodness of fit, for total activity in the insert (R^2 in parenthesis).

	Biograph mCT	Biograph TruePoint
FBP	0.88 ± 0.01 (0.99)	0.96 ± 0.12 (0.96)
OP-OSEM	0.86 ± 0.01 (0.99)	0.93 ± 0.11 (0.96)
OP-OSEM+TOF	0.88 ± 0.03 (0.99)	—
OP-OSEM+PSF	0.90 ± 0.01 (0.99)	0.99 ± 0.11 (0.96)
OP-OSEM+PSF+TOF	0.92 ± 0.03 (0.99)	—

The normalized variability of the mean concentration activity in the hot insert is shown in Fig. 8, according to the random fraction and true counts. The variability, or standard deviation of the mean activity concentration in each ROI, was measured across slices in the insert. FBP reconstruction yields the lowest variability for the two scanners whether random fraction or number of net true events is considered: the FBP reconstruction is preceded by 2D Fourier rebinning, which provides some smoothing across planes, thus reducing variability. The variability for iterative reconstructions was found to be similar for both scanners. As expected, for all reconstructions and methods, the variability increases with decreasing total counts in the scan. For the Biograph TruePoint, the variability also increased with the increase of random fraction. The Biograph mCT variability appears not to be sensitive to increasing random fraction, at least in the range studied.

3.C. Image quality and noise level experiments

A transverse slice through the center of the spheres is shown in Fig. 9 for the different reconstruction methods and for the two PET systems using the first day of imaging. The total activity measured in the FOV for the image quality phantom experiment is shown in Fig. 10 as a function of the random fraction. A trend very similar to that of the quantification and bias experiments is observed: estimated total activity is fairly constant, but increases at high random fraction, particularly for the Biograph TruePoint.

The CNR for the 22-mm sphere for all the reconstruction methods according to the theoretical activity in the sphere is shown in Fig. 11. The FBP reconstruction, reported as a reference here, is clearly inferior to the iterative methods, in terms of CNR. The benefit of using TOF information for detectability purpose is visible for the mCT data. The use of PSF-based reconstruction is found to increase the detectability as compared to algorithms without PSF correction in the mCT data, but PSF-based reconstruction apparently does not improve detectability in the Biograph TruePoint, at least with the number of iterations and subsets used.

Recovered concentration for all the spheres, COV, and BV are summarized in Table VI for the Biograph TruePoint and Table VII for the Biograph mCT. The 10-mm sphere is not included in the computation as it is not visible even for the first frame with the highest activity concentration. The 13-mm is also not visible in the Biograph TruePoint images, but it is still included in the table. The high background variability and the high COV, directly related to noise level, are responsible for the difficulty to recover activity in small spheres,

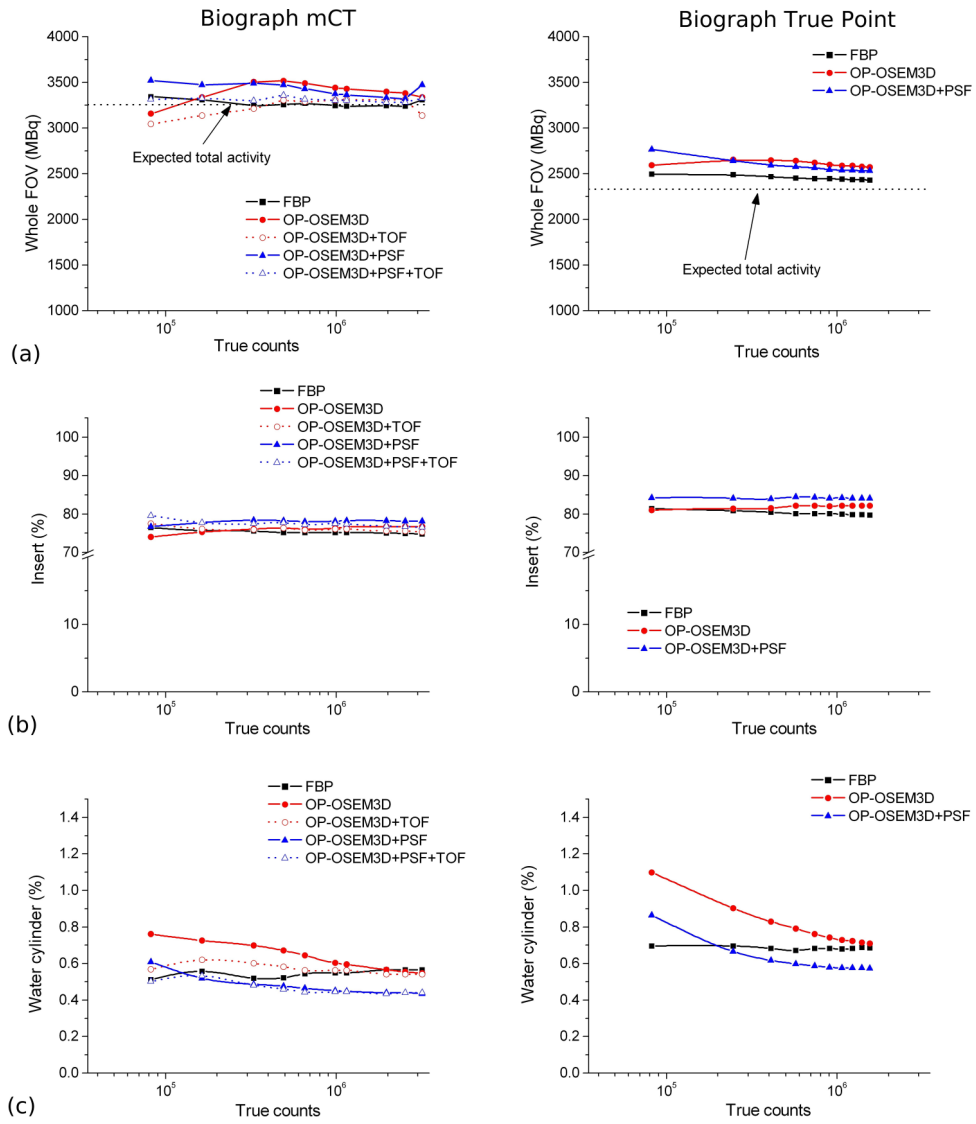

F . 6. Total activity and activity concentration in three regions vs number of trues in the sinogram: (a) total activity, (b) hot insert (5 cm diameter), and (c) water background (20 cm diameter) including the air insert (5 cm diameter). Plots (b) and (c) are normalized by the expected activity concentration in the hot insert. Results from Biograph mCT (left) and Biograph TruePoint 16 (right). Random fraction 71% for Biograph mCT data and 68% for Biograph TruePoint data.

compared to standard ^{18}F measurements in the NEMA standard.[24] As expected, FBP reconstruction has the higher COV and BV. TOF-based reconstruction reduces COV and BV and increases recovered concentration: this is a general performance of TOF information for all reconstruction methods, as can be seen comparing TOF and non-TOF results for recovered activity concentration, COV, BV for each sphere, and noise metric. The benefit of using PSF correction is similar, improving estimated activity concentration and decreasing BV and COV, in almost all cases. Recovered activity concentration generally increases with sphere size and advanced algorithms.

3.D. Quantification in patients

Measures of total activity measured in the FOV and in the segmented liver volume against estimated injected activity in the patient are represented in Figs. 12(a) and 12(b), respectively.

Good agreement between expected and measured activities is observed for all reconstruction methods used. The proportionality coefficient is found to be close to one, as shown in Tables VIII and IX for the total measured activity in the whole FOV. The Biograph TruePoint slightly overestimates the total activity.

An average bias over all patients was estimated: the average injected activity was 1153 ± 634 MBq and average total measured activity in the segmented liver was 967 ± 505 MBq for the Biograph mCT, resulting in an average underestimate of -186 MBq (-16%); the average injected activity was 1220 ± 618 and average total measured activity in the segmented liver was 1080 ± 453 MBq for the Biograph TruePoint, resulting in an average underestimate of -140 MBq (-11%). No account has been allowed for here due to lung

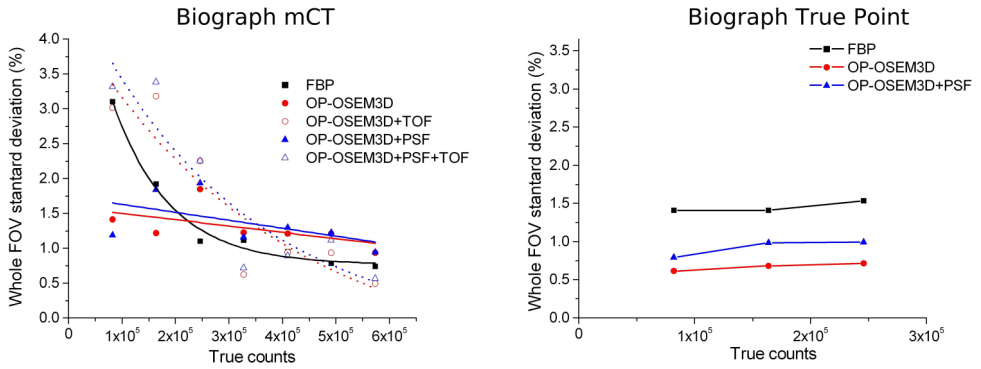

F . 7. Standard deviation of whole FOV activity vs number of trues in the sinogram. Results from Biograph mCT (left) and Biograph TruePoint 16 (right). Only three data sets were available for the Biograph TruePoint experiment, given the reduced amount of data available in the list mode. Experimental data points were fitted for the Biograph mCT data to highlight the relationship between standard deviation and true counts.

shunting or any residual radioactivity remaining in the catheter lines and other associated infusion hardware.

4. DISCUSSION

Given the therapeutic dose of ^{90}Y injected to a typical patient, of the order of thousands of MBq, a very high flux of bremsstrahlung photons is generated. Since no septa or collimators are used in contemporary PET scanners, this could result in detector saturation due to excessive count rates. In fact, no saturation was observed in the detectors. This is likely due to the relatively small size of the block detector as a function of overall detector surface area (5.2×5.2 cm^2 in cross section) that limits the count rate seen from each electronic channel, the front-end lower pulse height analyzer (PHA) energy threshold, between 100 and 200 keV, and the narrow and high PHA energy window used (425 or 435 to 650 keV). Nevertheless, even the reduced qualified bremsstrahlung singles can contribute significantly to random coincidences, particularly if the PET scan is performed soon after the injection. The preliminary measurements show that the high flux of bremsstrahlung radiation does not have a strong effect on detector saturation or a measurable contribution to true coincidences, at least in the two PET scanners studied in this work. On the other hand, the bremsstrahlung radiation, together with the LSO background radiation, greatly increases the random fraction in the PET study. As a consequence, we can assume that the branching ratio of 31.86×10^{-6} and the half-life of

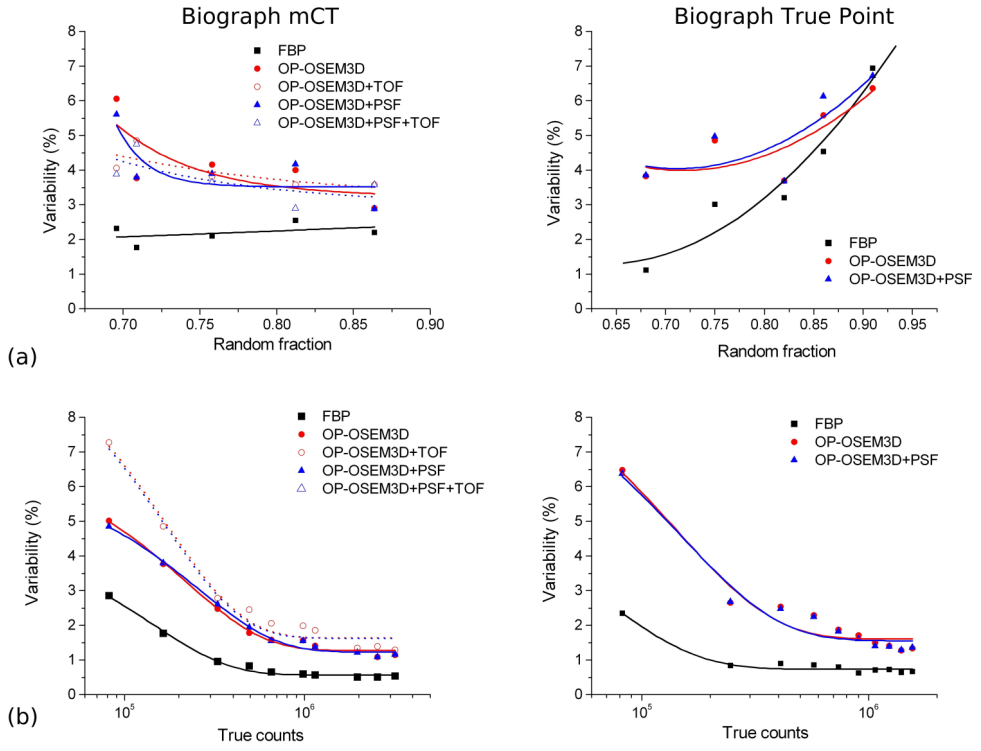

F . 8. Variability of mean activity concentration inside the hot insert across 25 slices vs random fraction (a) and number of trues in the sinogram (b). Results from Biograph mCT (left) and Biograph TruePoint (right). Plots are normalized by the expected activity concentration in the hot insert. Experimental data points were fitted to highlight the relationship between variability and both random fraction and true counts.

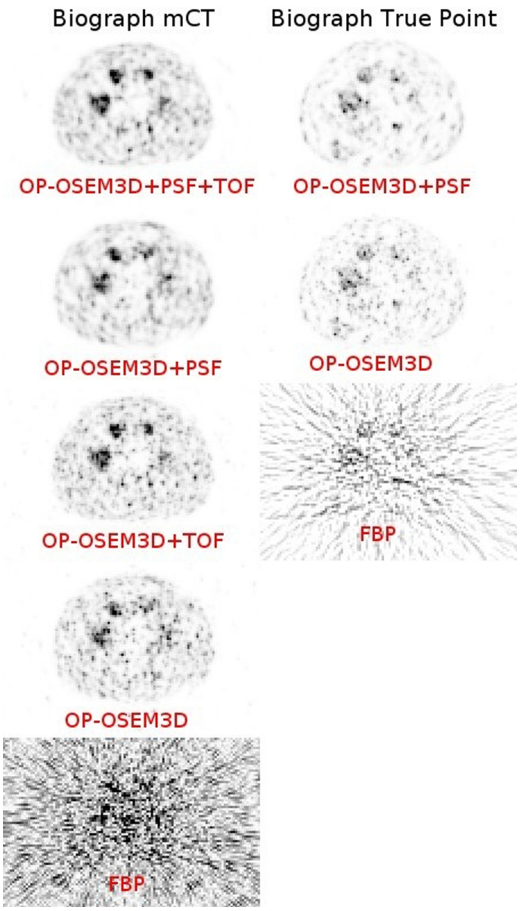

F . 9. Central slice of the NEMA/IEC 2001 PET phantom for different reconstruction algorithms and the two PET systems. The selected scan had 0.4×10^6 day true coincidences for both PET systems. Gray scale is identical between each reconstruction algorithm for a given PET system.

2.3×10^5 s can be correctly applied to the measured true counts in order to obtain correct quantification, neglecting LSO trues and bremsstrahlung trues.

The combination of high random fraction and extremely low true coincidences poses a serious challenge to the reconstruction.

The quantitative bias observed by several groups in ^{90}Y images is related to the interplay of low counts, high random fraction, and scatter correction: when total counts are extremely low, as in ^{90}Y imaging, both scatter and random estimates are noisy, and correction for both scatter and randoms (often close to 90% of the data) generates a very noisy true coincidence sinogram, with large fraction of negative counts. Algorithm positivity constraints result in bias in the final images.

Given the low number of true events in ^{90}Y imaging, the LSO and bremsstrahlung random coincidences[18] are often a large fraction of the prompt coincidences (>90%), and it is a necessity to apply some smoothing technique on the measured delayed coincidences. This is possible only if separate prompt and random events are acquired. Where random smoothing is not available, as in the implementation of AW-OSEM2D, a dramatic bias is observed. In addition, AW-OSEM2D is also characterized by an update equation using positivity constraint both on the fully corrected sinogram and the image space. In conclusion, AW-OSEM2D cannot be used for ^{90}Y imaging on the Biograph TruePoint scanner.

Scatter correction is also a sensitive part of the reconstruction process in a situation of count limited as ^{90}Y imaging. Using single scatter simulation with tail fitting and scaling,[26,27] both simulation and tail fitting can fail to reproduce the correct scatter at very low event counts. The single scatter simulation is based on a preliminary image reconstructed without scatter subtraction. At very low counts, this image is very noisy and the resulting scatter might be inaccurate. Moreover, the scaling of such scatter based on the noisy tails of the sinogram is prone to inaccuracy and can result in heavy under- or overestimates of the scatter contribution. When possible, it is probably safer not to use scatter scaling or fitting of the tails of the sinogram: some scatter from outside the FOV might be underestimated, but erratic and dramatically incorrect scaling could be prevented. Similarly, van Elmbt suggested an additional component of true coincidences affecting the ends of the profile tails in rebinned sinograms.[21] They assumed that this signal may come from pair production in the LSO crystals by the x-ray bremsstrahlung above 1.022 MeV. This component might also bias the scaling of the scattered sinogram needed to correct the data.

In term of the algorithm bias, the first phantom study showed that if using OP-OSEM and its advanced variation (PSF and TOF), the bias is less than 10% in a wide range of random fraction (up to 95%) and down to a very small number of counts (80 000 net trues). However, the decreasing trend

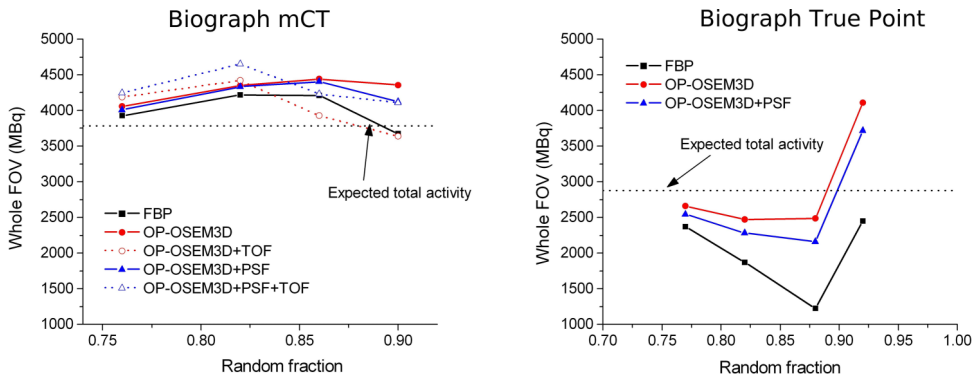

F . 10. Total activity in image quality phantom vs random fraction, for all reconstruction methods. Results from Biograph mCT (left) and Biograph TruePoint (right).

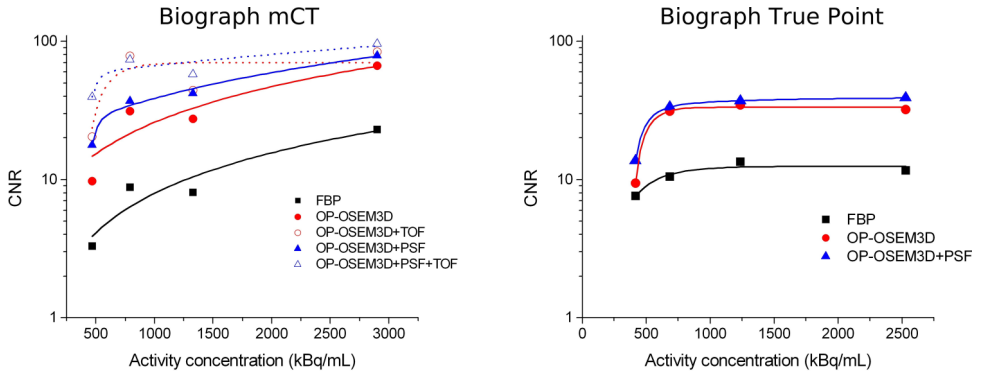

F . 11. CNR for the 22-mm sphere as a function of activity concentration in the sphere and for different reconstruction algorithms. Results from Biograph mCT (left) and Biograph TruePoint (right). Experimental data points were fitted to highlight the relationship between CNR and activity concentration.

with increasing random fraction for the Biograph TruePoint needs still to be understood.

The reproducibility of the measurement and variability are also areas of concern, but again they can be contained within 10%, in the range of the experiment. As expected, the standard deviation over five realizations was lower when the number of net true events increased (Fig. 7). This represents a higher reproducibility of the measurements at higher counts. One can also note that the standard deviation is found to be higher when using TOF information combined with an iterative algorithm and a number of net true events less than approximately 3×10^5. This is unexpected but can be attributed to the particular implementation of the TOF data organization and reconstruction, which might be more sensitive to very sparse data.

Overall, the iterative methods show a positive bias at low counts and high random fraction, but PSF correction and TOF reconstruction reduce such bias. In this experiment, all iterative methods performed fairly well in measuring activity in a large uniform hot region, and using PSF correction and PSF+TOF reconstruction was best at reducing bias in the background and therefore allowing a better estimate of the total activity in the FOV.

It was observed that the FBP reconstruction does not show an increasing bias with high random fraction and low counts. It must be noted that in more critical experimental conditions, FBP reconstruction could be more sensitive to inaccurate scatter correction, while iterative methods, particularly with TOF information, can partially correct inconsistent data during the iteration process.[30]

Contrast recovery in ^{90}Y hot spheres measured in this work is lower than what typically measured with ^{18}F sources, and high background variability and noise level are responsible for such loss of contrast. The 10 mm sphere could not be seen over the background noise in either scanner. This is to be expected, given the extremely low number of counts in the scan. High image noise (COV) and variability (BV) are observed. Improved recovered activity concentration and reduced noise and background variability are observed when more advanced reconstruction methods (PSF and TOF) were used. The experiment confirmed that PSF correction and TOF information improve CNR for both scanners. This is similar to previous observations in the literature.[17,19]

Regarding the contrast recovery measurements on the NEMA 2001 sphere phantom, it must be observed that while this phantom is the standard in PET for assessing image quality and contrast recovery, it might not be the best phantom for a realistic simulation of ^{90}Y patient scans: the contrast ratio is typically higher in a patient, and almost all the activity is concentrated in a smaller volume in part of the liver. Nevertheless, this experiment allows the reader to compare results with a model used by many, even in the ^{90}Y imaging community.

Overall, all methods could be used as a good estimate of the total activity in the FOV, but iterative reconstruction with PSF correction even though based on ^{18}F measurements is clearly associated with lower noise, lower background variability, and improved recovered activity concentration of small features which is further improved when using TOF data in the reconstruction.

The improved contrast recovery (see Table VII) due to TOF reconstruction is to be expected, since there is ample evidence of the benefits of TOF reconstruction, in terms of signal to noise ratio (SNR). SNR improves if TOF is used, and such improvement or gain depends on the time resolution of the scanner, the size of the patient, and also the random fraction: it has been shown that the TOF gain in SNR is greater for large random fraction.[31,32]

T VI. Biograph TruePoint: RA concentration for five spheres, BV, and COV for all reconstruction methods. Frame 0 (0.4×10^6 net true coincidences and 77% random fraction) was chosen.

Reconstruction method	RA (13 mm) (%)	RA (17 mm) (%)	RA (22 mm) (%)	RA (28 mm) (%)	RA (37 mm) (%)	BV (%)	COV (%)
FBP	40	24	49	60	66	72	215
OP-OSEM3D	37	21	42	51	61	23	109
OP-OSEM3D+PSF	35	26	49	56	68	30	90

T VII. Biograph mCT: RA concentration for five spheres, BV, and COV for all reconstruction methods. Frame 3 (0.4×10^6 net true coincidences and 86.5% random fraction) was chosen.

Reconstruction method	RA (13 mm) (%)	RA (17 mm) (%)	RA (22 mm) (%)	RA (28 mm) (%)	RA (37 mm) (%)	BV (%)	COV (%)
FBP	43	66	62	71	85	49	438
OP-OSEM3D	31	35	46	59	75	24	84
OP-OSEM3D+TOF	45	48	62	72	92	16	73
OP-OSEM3D+PSF	31	44	58	68	84	25	63
OP-OSEM3D+PSF+TOF	51	54	66	77	99	17	58

All performance parameters are dependent not only on the reconstruction methods but also on the specific reconstruction parameters used: subsets, iterations, and post-reconstruction filter size. In order to keep the noise level at an acceptable level, it is better to use a lower number of maximum likelihood expectation maximization (MLEM) iterations, typically <50 (for example 2 iterations × 21 subsets = 42 MLEM-equivalent iterations), and large filter, typically >4 mm. On the other hand, small filter size and high number of iteration should reduce bias.

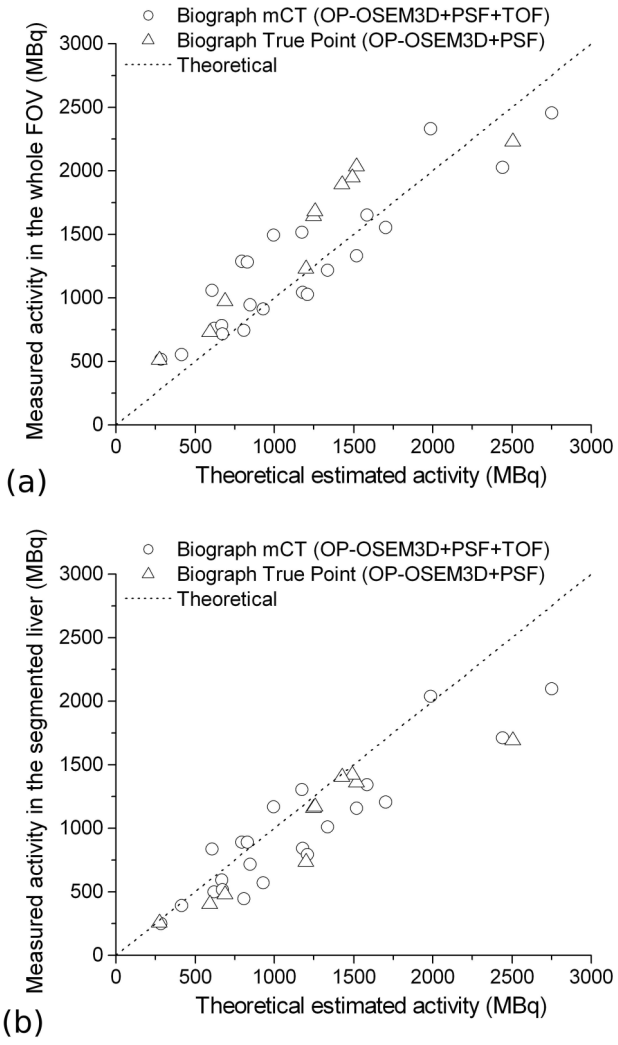

F . 12. For both the Biograph TruePoint and Biograph mCT, total activity in patients vs expected activity (a) and total activity in segmented liver vs expected activity (b), for all reconstruction methods.

In general it was observed that the local recovery in the 50 mm hot cylindrical insert for the first phantom experiment, and in largest spheres for the second experiment (22–37 cm), reached about 80%. While the total activity in the field of view is in general close to the expected value, the appearance of bias in the background translated into loss of counts in the region of true activity concentration. This could be partially due to convergence, and local recovery might improve with more iterations, with a high cost in terms of noise.

Quantification of patient data demonstrated that both the Biograph TruePoint and Biograph mCT can give clinically acceptable estimates of total activity injected during treatment. While the FBP and OP-OSEM3D reconstruction methods in conjunction with PSF and TOF corrections give comparable results for measures of activity in the total FOV, FBP reconstructions should not be used to analyze activity measures in spatially defined volumes of interest, as the distribution of counts within the FOV is not necessarily correct. It must be noticed, based on the experience of phantom experiments, that the local recovery of activity in the sites of the treated lesions is not full, but in general it about 80%, for all reconstruction methods: some of the data are spread as background bias in the nontreated liver and the rest of the body. Such an underestimate may not be unreasonable. Indeed, it was expected that a ±20% uncertainty applied to the estimated injected activity, which was a result of the initial calibration uncertainty in the delivery vial of labeled microspheres, in combination with the inability to accurately measure the initial and residual activities in the delivery apparatus due to the difficulties associated with beta emitters. Nevertheless, the total activity can be correctly estimated adding all the activity in the FOV: for the reconstruction methods used, a linearity coefficient of 1.00 ± 0.05 was observed on the Biograph mCT, and 1.15 ± 0.07 was observed on the Biograph TruePoint. For the activity in the liver, the linearity coefficient was 0.89 ± 0.05 for the Biograph mCT, and 0.81 ± 0.05 for the Biograph TruePoint. Additionally, we must point out that, while the estimated lung shunt for each patient, acquired as part of the standard work up

T VIII. Proportionality coefficient and goodness of fit, for total activity in the whole FOV (R^2 in parenthesis).

	Biograph mCT	Biograph TruePoint
FBP	0.81 ± 0.04 (0.80)	0.84 ± 0.04 (0.91)
OP-OSEM+PSF	—	1.15 ± 0.07 (0.74)
OP-OSEM+PSF+TOF	1.00 ± 0.05 (0.72)	—

T IX. Proportionality coefficient and goodness of fit, for activity in liver (R^2 in parenthesis).

	Biograph mCT	Biograph TruePoint
FBP	0.90 ± 0.05 (0.76)	0.86 ± 0.05 (0.85)
OP-OSEM+PSF	—	0.81 ± 0.05 (0.84)
OP-OSEM+PSF+TOF	0.89 ± 0.05 (0.69)	—

procedure for radioembolization therapy, was recorded, it was not taken into account through subtraction from the expected activity in the segmented liver. This was due to the fact that the study was retrospective with each of the three contributing centers having variations in methodology for calculation of the shunt fraction. The shunt fraction itself is not thought to be a quantitative measure of the actual fraction of activity present in the lungs, due to the nonquantitative approach to measurement (lack of attenuation and scatter correction), in combination with the questionable reciprocity of the ^{99m}Tc-MAA and ^{90}Y microsphere distributions. Finally, it is worth noting that since the shunt was not subtracted from the injected activity, the coefficients could be slightly underestimated, as found.

Overall, both in patient and phantom studies, we consistently observed a deficit of the activity measured in a volume of interest surrounding the expected focus of activity, either a hot insert or the patient liver, if compared with what was theoretically injected. This is likely due to the low-count data that are currently reconstructed with an iterative algorithm such as MLEM and its accelerated version, OSEM. As these algorithms are based on the Poisson model and intrinsically include a non-negativity constraint, they are positively biased in regions without any activity and in low-activity regions.[5] The non-negativity constraint, depending on the reconstruction method used, can be applied both in the sinogram space, forcing the content of each sinogram bin to be positive after subtraction of randoms and scatter, and in the image space, forcing the content of each image voxel to be positive. Amplification of noise clusters and average positive bias in extremely low or zero activity regions are the consequences of the positivity constraint.

5. CONCLUSIONS

This work is a comprehensive study of ^{90}Y-PET quantitative performance when using LSO-based PET scanners. Due to the low total counts and high random fraction when imaging ^{90}Y, an accurate image quantification is affected by random events and its estimation, scatter correction, and positivity constraints of the algorithm.

Nevertheless, phantom and patient studies showed that the impact of number of true and random coincidences on quantitative results was found to be limited as long as OP-OSEM reconstruction algorithms with random smoothing are used. Adding PSF correction and TOF information to the reconstruction greatly improves the image quality in terms of bias, variability, noise reduction, and detectability.

On the patient studies, the total activity in the field of view is in general accurately measured by Biograph mCT and slightly overestimated by the Biograph TruePoint. A linear relationship between the expected and the measured activities in the organ of interest is observed for all reconstruction methods used.

ACKNOWLEDGMENTS

The authors wish to thank the DOSIsoft company (Cachan, France) for their valuable input in analyzing patient data. The authors would also like to thank Sirtex (Sydney, Australia) for allowing the use of the NEMA 2001 PET phantom data, acquired as part of a larger Sirtex-supported integral study.

[a]Author to whom correspondence should be addressed. Electronic mail: thomas.carlier@chu-nantes.fr

[1]B. Lambert, E. Sturm, J. Mertens, R. Oltenfreiter, P. Smeets, R. Troisi, H. Van Vlierberghe, and L. Defreyne, "Intra-arterial treatment with 90Y microspheres for hepatocellular carcinoma: 4 years experience at Ghent University Hospital," Eur. J. Nucl. Med. Mol. Imaging **38**, 2117–2124 (2011).
[2]R. Salem and K. Thurston, "Radioembolization with 90Yttrium microspheres: A state-of-the-art brachytherapy treatment for primary and secondary liver malignancies," J. Vasc. Interv. Radiol. **17**, 1251–1278 (2006).
[3]R. Salem, V. Mazzaferro, and B. Sangro, "Yttrium 90 radioembolization for the treatment of hepatocellular carcinoma: Biological lessons, current challenges, and clinical perspectives," Hepatology **58**, 2188–2197 (2013).
[4]A. Dieudonné, E. Garin, S. Laffont, Y. Rolland, R. Lebtahi, D. Leguludec, and I. Gardin, "Clinical feasibility of fast 3-dimensional dosimetry of the liver for treatment planning of hepatocellular carcinoma with 90Y-microspheres," J. Nucl. Med. **52**, 1930–1937 (2011).
[5]Y. H. Kao *et al.*, "Post-radioembolization yttrium-90 PET/CT - Part 2: Dose–Response and tumor predictive dosimetry for resin microspheres," EJNMMI Res. **3**, 57 (2013).
[6]E. Fourkal, I. Veltchev, M. Lin, S. Koren, J. Meyer, M. Doss, and J. Q. Yu, "3D inpatient dose reconstruction from the PET-CT imaging of ^{90}Y microspheres for metastatic cancer to the liver: Feasibility study," Med. Phys. **40**, 081702 (10pp.) (2013).
[7]Y. K. Dewaraja, E. C. Frey, G. Sgouros, A. B. Brill, P. Roberson, P. B. Zanzonico, and M. Ljungberg, "MIRD Pamphlet No. 23: Quantitative SPECT for patient-specific 3-dimensional dosimetry in internal radionuclide therapy," J. Nucl. Med. **53**, 1310–1325 (2012).
[8]A. Dieudonné *et al.*, "Study of the impact of tissue density heterogeneities on 3-dimensional abdominal dosimetry: Comparison between dose kernel convolution and direct Monte Carlo methods," J. Nucl. Med. **54**, 236–243 (2013).
[9]X. Rong and E. C. Frey, "A collimator optimization method for quantitative imaging: Application to Y-90 bremsstrahlung SPECT," Med. Phys. **40**, 082504 (9pp.) (2013).
[10]M. Elschot, M. G. E. H. Lam, M. A. A. J. van den Bosch, M. A. Viergever, and H. W. A. M. de Jong, "Quantitative Monte Carlo-based 90Y SPECT reconstruction," J. Nucl. Med. **54**, 1557–1563 (2013).
[11]R. Lhommel, L. van Elmbt, P. Goffette, M. Van den Eynde, F. Jamar, S. Pauwels, and S. Walrand, "Feasibility of 90Y TOF PET-based dosimetry in liver metastasis therapy using SIR-Spheres," Eur. J. Nucl. Med. Mol. Imaging **37**, 1654–1662 (2010).
[12]V. L. Gates, A. A. H. Esmail, K. Marshall, S. Spies, and R. Salem, "Internal pair production of 90Y permits hepatic localization of microspheres using routine PET: Proof of concept," J. Nucl. Med. **52**, 72–76 (2011).
[13]T. Chang, A. C. Bourgeois, A. M. Balius, and A. S. Pasciak, "Treatment modification of yttrium-90 radioembolization based on quantitative positron emission tomography/CT imaging," J. Vasc. Interv. Radiol. **24**, 333–337 (2013).
[14]S. Walrand, F. Jamar, L. van Elmbt, R. Lhommel, E. B. Bekonde, and S. Pauwels, "4-step renal dosimetry dependant on cortex geometry applied to 90Y peptide receptor radiotherapy: Evaluation using a fillable kidney phantom imaged by 90Y PET," J. Nucl. Med. **51**, 1969–1973 (2010).
[15]C. Fabbri *et al.*, "Quantitative evaluation on [90Y] DOTATOC PET and SPECT imaging by phantom acquisitions and clinical applications in locoregional and systemic treatments," Q. J. Nucl. Med. Mol. Imaging **56**, 522–528 (2012).

[16]K. Willowson, N. Forwood, B. W. Jakoby, A. M. Smith, and D. L. Bailey, "Quantitative 90Y image reconstruction in PET," Med. Phys. **39**, 7153–7159 (2012).
[17]T. Carlier, T. Eugène, C. Bodet-Milin, E. Garin, C. Ansquer, C. Rousseau, L. Ferrer, J. Barbet, F. Schoenahl, and F. Kraeber-Bodéré, "Assessment of acquisition protocols for routine imaging of Y-90 using PET/CT," EJNMMI Res. **3**, 11 (2013).
[18]A. Goedicke, Y. Berker, F. A. Verburg, F. F. Behrend, O. Winz, and F. M. Mottaghy, "Study-parameter impact in quantitative 90-Yttrium PET imaging for radioembolization treatment monitoring and dosimetry," IEEE Trans. Med. Imaging **32**, 485–492 (2013).
[19]K. N. Tapp, W. B. Lea, M. S. Johnson, M. Tann, J. W. Fletcher, and G. D. Hutchins, "The impact of image reconstruction bias on PET/CT ^{90}Y dosimetry after radioembolization," J. Nucl. Med. **55**, 1452–1458 (2014).
[20]J. M. Martí-Climent, E. Prieto, C. Elosúa, M. Rodríguez-Fraile, I. Domínguez-Prado, C. Vigil, M. García-Velloso, J. Arbizu, I. Peñuelas, and J. A. Richter, "PET optimization for improved assessment and accurate quantification of ^{90}Y-microsphere biodistribution after radioembolization," Med. Phys. **41**, 092503 (10pp.) (2014).
[21]L. van Elmbt, S. Vandenberghe, S. Walrand, S. Pauwels, and F. Jamar, "Comparison of yttrium-90 quantitative imaging by TOF and non-TOF PET in a phantom of liver selective internal radiotherapy," Phys. Med. Biol. **56**, 6759–6777 (2011).
[22]D. Burch, P. Russo, H. Swanson, and E. G. Adelberger, "Lifetime of the first excited state in ^{96}Zr*," Phys. Lett. B **40**, 357–359 (1972).
[23]B. W. Jakoby, Y. Bercier, M. Conti, M. E. Casey, C. Hayden, B. Bendriem, and D. W. Townsend, "Physics performance and clinical investigation of the mCT time-of-flight PET/CT scanner," Phys. Med. Biol. **56**, 2375–2389 (2011).
[24]Y. S. Lee, J. S. Kim, K. M. Kim, J. H. Kang, S. M. Lim, and H. J. Kim, "Performance measurement of PSF modeling reconstruction (True X) on Siemens Biograph TruePoint TrueV PET/CT," Ann. Nucl. Med. **28**, 340–348 (2014).
[25]V. Y. Panin, "Iterative algorithms for variance reduction on compressed sinogram random coincidences in PET," in *IEEE Nuclear Science Symposium Conference Record* (IEEE, Dresden, Germany, 2008), pp. 3719–3725.
[26]C. C. Watson, "New, faster, image-based scatter correction for 3D PET," IEEE Trans. Nucl. Sci. **47**, 1587–1594 (2000).
[27]C. C. Watson, M. E. Casey, C. Michel, and B. Bendriem, "Advances in scatter correction for 3D PET/CT," in *IEEE Nuclear Science Symposium Conference Record* (IEEE, Rome, Italy, 2004), Vol. 5, pp. 3008–3012.
[28]Q. Bao and A. F. Chatziioannou, "Estimation of the minimum detectable activity of preclinical PET imaging systems with an analytical method," Med. Phys. **37**, 6070–6083 (2010).
[29]S. Tong, A. M. Alessio, and P. E. Kinahan, "Noise and signal properties in PSF-based fully 3D PET image reconstruction: An experimental evaluation," Phys. Med. Biol. **55**, 1453–1473 (2010).
[30]M. Conti, "Why is TOF PET reconstruction a more robust method in the presence of inconsistent data?," Phys. Med. Biol. **56**, 155–168 (2011).
[31]M. Conti, "Effect of randoms on signal-to-noise-ratio in TOF PET," IEEE Trans. Nucl. Sci. **53**, 1188–1193 (2006).
[32]L. Eriksson and M. Conti, "Randoms and TOF gain revisited," Phys. Med. Biol. **60**, 1613–1623 (2015).